A Biophysical Mechanism for Modulating Kv2 Channel Activation Uncovered with Tarantula Toxin-Based Tools

By

REBECKA JANE SEPELA
DISSERTATION

Submitted in partial satisfaction of the requirements for the degree of

DOCTOR OF PHILOSOPHY

in

Biochemistry, Molecular, Cellular, and Developmental Biology

in the

OFFICE OF GRADUATE STUDIES

of the

UNIVERSITY OF CALIFORNIA

DAVIS

Approved:

Jon Sack, Chair

Karen Zito

James Trimmer

Tsung-Yu Chen

Committee in Charge

2022

Dedication

This thesis and the work within would not have been possible without the abundance of support that I have received from my advisor, family, friends, and colleagues.

With much gratitude, I dedicate this dissertation to those who have elevated my scientific exploration in lab (Jon, Parashar, Robin, Matt, and Tsung-Yu), to those who have kept me grounded outside of lab (Emma, Hannah, Lauren, Bobby, Prema, Yulong, Anastasia, Mattie, Christina, Katie, Mary Allison, and Carlie), to those who have encouraged me to pursue my passions (Karen and Jim), and finally, to those whose love and constant support fuels my chasing of these goals (Mom, Dad, Jake, Grandma Patti, Grandpa Brandon, Grandma Janet, and Grandpa Mike). Thank you all.

Table of Contents

Preface

I am interested in understanding how ionic conductances integrate during pathophysiological and physiological signaling events. Ion channels are specialized proteins that can form a passageway through the cellular membrane for charged ions to move down their electrochemical gradient. Since the electrochemical gradient is dictated by both the difference in ionic concentration and charge across a membrane, any ionic flux readjusts the driving force that defines how ionic conductances flow. As such, ion channels feed back on their own activities and on the activities of other proximal ion channel populations, both promoting and partaking in complex electrical cascades. A subclass of ion channels further defines electrical activity through characteristic voltage dependence such that ionic flux is gated to only occur in response to certain membrane potentials. The mechanisms that define the gating of these voltage-gated ion channels are ingrained within the protein sequence and structure of that individual channel. However, factors not directly dictated by ion channel protein sequence can redefine the voltage dependence of ion channel activity, further modulating how that ion channel participates in complex electrical cascades. Deciphering the role of a single ion channel subtype during these symphonic signaling events is very difficult. But since many of life's processes depend on maintaining a harmonious and regulated flow of ions, understanding the role of each player will better prepare us for addressing the cacophonous consequences when ionic flow goes awry.

One such example of ionic flow gone awry is in ischemic stroke. Stroke is the 5th leading cause of death and a major contributor to disability in the USA (1). Of all stroke cases, ischemic stroke accounts for 87% (1). During ischemia, the voltage-gated potassium ion channels of subtype 2 (Kv2), are heavily modulated and their expression and their K^+ conductance is linked to neuronal death. Characterizing the actions of Kv2 channels during ischemia is important for understanding stroke-induced neuronal death and future development of therapeutics.

Kv2 ion channels are highly expressed in most central neurons (2) in distinct punctate clusters (3). These channels respond to cellular depolarization to regulate the efflux of potassium and control electrical excitability (4–7). Kv2's electrical properties are dynamically regulated by intracellular ionic composition (8), expression level (9), phosphorylation state (10), expression morphology (11–15), and subcellular expression patterns (16). Due to this dynamism, identifying the precise role Kv2 channels play in shaping an electrical signal is difficult. Kv2 channels are hypothesized to modulate their activity in excitotoxic insults, like ischemic attack (17). During a cerebral ischemic stroke, decline in blood flow and oxygen deprivation lead to dysregulation of ionic homeostasis within the brain (18). Neurons become hyperexcitable, intracellular calcium drastically increases, and excitotoxic cascades are initiated (19) resulting in neurodegeneration. Previous studies suggest that Kv2 ion channels become very active during ischemia (17), suppress electrical excitability (5–7), and provide neural protection from excitotoxic signaling. However, there has also been evidence that excessive efflux of potassium through Kv2 channels during ischemia can trigger apoptotic cascades leading to neuronal death (20–22). Both proposed responses assume a dramatic increase in the number of active Kv2 channels. However, due to technological limitations, the hypothesized mass activation has never been observed in real time or *in vivo*. *In vitro* studies propose a putative mechanism for mass activation. Increases in intracellular Ca^{2+} during ischemia lead to biochemical modification of Kv2 channels, changed expression morphology from clustered punctate to diffuse, and cause a heightened sensitivity to voltage (23). Lowering the threshold for voltage-activation could lead to mass activation of Kv2 channels (17). However, the biophysical mechanism through which Kv2 channels can shift their voltage-dependence is unknown.

The pathophysiological modification of Kv2 channels presupposes an integral electrophysiological role in the ischemic response. However, gaps in understanding the actions of Kv2 channels during ischemic insult limit our comprehension of how the channels participate in complex electrical cascades.

Filling in the knowledge gaps of how Kv2 ion channels contribute to neuronal circuitry, respond to ischemic insult, and modulate their function is technically difficult *in vivo*. Neurons possess a variety of electrical signaling patterns ranging in shape, size, and frequency. The summed conductance from the dynamic and distinct collection of ion channels present in any particular neuron creates this diversity. Despite advances made with patch-clamp recording and heterologous expression of cloned channels, our understanding of how different ionic conductances form a unified electrical signal is still incomplete, even in the best-studied neurons (24). Because ionic currents can be controlled-by and are effectors-of voltage change, the role of any singular ion channel is crucially dependent on the other conductances present in a cell. Adding or removing a particular channel can have counter-intuitive effects, potentially limiting the interpretability of classical genetic or technological approaches (24). Specifically, prior conclusions regarding the basal functions of Kv2 channels based on studies using channel blockers or genetic manipulation (6, 25–28) are not obviously reconcilable with recent electrophysiology studies (29). Moreover, techniques that exist to catalog the channels expressed in a neuron or to record the ensemble ionic flux are problematic when studying live Kv2 dynamics which are regulated by Ca^{2+} dependent mechanisms. Altogether, technological limitations have restricted our ability to probe Kv2 channel activation during signaling events, especially in native tissue.

This goal of this thesis research is two-fold, to (1) develop technologies for live, cellular and subcellular resolution of subtype-specific ion channel activation in native systems, and (2) describe the biophysical mechanism through which Kv2 channels shift their voltage-dependence. During ischemic conditions, Kv2 channels shift their voltage-dependence through a phosphorylation-dependent mechanism (17). However, since phosphorylation status is subject to the whims of cell regulation (30, 31), phenomena that depend on phosphorylation can be challenging to control. To similarly interrogate the biophysical mechanisms that could underlie the shifting of Kv2 voltage-dependence by a method that does not directly depend on phosphorylation, this thesis explores the Kv2.1-AMIGO1 interaction.

AMIGO1 is an extracellular adhesion molecule that is also an auxiliary subunit to Kv2 channels (32, 33). AMIGO1 modulates ionic conductances of Kv2 channels, yet the underlying mechanism is unknown (33).

Within this thesis, I will introduce a family of ion channel auxiliary subunits and discuss how these proteins mediate the flux through their voltage-gated ion channel partners. This group of auxiliary subunits also exhibit adhesion-type functions and I will review these roles as well, discussing the possible interplay between auxiliary and adhesive functions (Chapter 1). I then describe the development of a family of tools that deciphers changes in Kv2 ion channel activity (Chapter 2 and Appendix A). Next, I will convey how these tools can be deployed to interrogate the biophysical mechanism through which AMIGO1 modulates Kv2.1 voltage dependence to change ion channel activity (Chapter 3 and Appendix B). Finally, I present concluding ideas and open questions that can be further investigated to better understand how ionic conductances integrate during pathophysiological and physiological signaling events (Chapter 4).

Abstract

Voltage-gated potassium (Kv) channels sense voltage and facilitate transmembrane flow of K+ to control the electrical excitability of cells. The Kv2.1 channel subtype is abundant in most brain neurons and its conductance is critical for homeostatic regulation of neuronal excitability. Kv2.1 channel must progress through a series of conformational changes, including consecutive voltage-sensor activation and pore opening, to permit the flux of this potassium conductance. Many forms of regulation modulate Kv2.1 conductance, yet the biophysical mechanisms through which the conductance is modulated are unknown. In my thesis research, I helped develop two molecular tools to track and control Kv2.1 ion channel conformational change to interrogate which conformational changes are modulated to alter Kv2.1 conductance.

For the first method, I synthesized GxTX–594, a variant of the peptidyl tarantula toxin guangxitoxin-1E (GxTX-1E), conjugated to a fluorophore (AlexaFluor-594) optimal for two-photon excitation imaging through light-scattering tissue. GxTX–594 targets the voltage sensors of Kv2 proteins and dynamically labels cell surface Kv2 proteins, responding to voltage stimulation and the conformational state of the voltage sensor. To interpret dynamic changes in fluorescence intensity, we developed a statistical thermodynamic model that relates the conformational changes of Kv2 voltage sensors to degree of labeling. This tool permitted us to visually determine the conformational state of endogenous Kv2 voltage sensors in live hippocampal tissue. For the second method, we synthesized GxTX Ser13Pra(JP) and GxTX Lys27Pra(JP), different variants of guangxitoxin-1E conjugated to an fluorophore, JP (julolidine phenoxazone), that has an inherent response to the polarity of its immediate surroundings. GxTX–JP variants offer site-specific structural insight into Kv2.1 voltage sensing domain allostery that occurs during membrane depolarization. Using voltage-clamp spectroscopy to collect emission spectra as a function of membrane potential, we found that emission spectra of these tools vary with toxin labeling site, the presence of Kv2 channels, and changes in membrane potential. With a high-

affinity conjugate in which the fluorophore itself interacts closely with the channel, the emission shift midpoint is 50 mV more negative than the Kv2.1 gating current midpoint. This suggests that substantial conformational changes at the toxin−channel interface are associated with early gating charge transitions and these are not concerted with voltage sensing domain motions at more depolarized potentials.

I then deployed these tools to investigate a biophysical mechanism through which Kv2.1 conductance could be modulated by its auxiliary binding partner, AMIGO1. The neuronal adhesion protein AMIGO1 associates with and modulates the voltage-dependence of Kv2.1 channel activation, yet the underlying mechanism for this or any other modulator of Kv2 conformational change was unknown. With voltage clamp recordings and spectroscopy of heterologously expressed Kv2.1 and AMIGO1 in mammalian cell lines, I demonstrated that AMIGO1 modulates Kv2.1 voltage sensor movement to change Kv2.1 conductance. AMIGO1 speeds early voltage sensor movements and shifts the gating charge–voltage relationship to more negative voltages. From the gating charge–voltage relationship I found that AMIGO1 exerts a larger energetic effect on voltage sensor movement than apparent from the conductance–voltage relationship, which is largely dependent on pore opening. I propose that the mechanistic separation between early voltage sensor movements and pore opening makes the magnitude of the AMIGO1 impact dependent on modulation of Kv2 gating. Conductance-voltage measurements made in the presence of GxTX–594 reveal an increased impact of AMIGO1 on Kv2.1 conduction compared to conditions lacking Kv2 gating modulators. Finally, fluorescence measurements from GxTX Lys27Pra(JP) and GxTX Ser13Pra(JP) bound to Kv2.1 indicate that the voltage sensors enter their earliest resting conformation, yet this conformation is less stable upon voltage stimulation. From this work I concluded that AMIGO1 modulates the Kv2.1 conductance activation pathway by destabilizing the earliest resting state of the voltage sensors. Based on a series of thermodynamic calculations, I speculate that removal of AMIGO1 could be functionally equivalent to blocking the majority of Kv2 current in neurons, which would suggest that AMIGO1 plays a supporting role in controlling the electrical

excitability of cells. This work has contributed to the greater understanding of the allosteric mechanisms through which ion channel voltage-dependence can be modulated and raises new questions about the molecular interactions that occur during these early resting conformations.

Chapter 1: Why are ion channels sticky? A review examining the curious coupling of voltage-gated ion channels with cell adhesion molecules.

Preface

A major focus of this thesis is the Kv2 voltage-gated potassium channel and the single transmembrane pass auxiliary subunit, AMIGO1. To provide context for these studies, this introduction chapter is a review of structural and functional aspects of single transmembrane pass auxiliary subunits with cell adhesion molecule-like extracellular domains that modulate voltage-gated ion channels. Here, I define what constitutes an ion channel auxiliary subunit and compare the mechanisms through which auxiliary subunits act on their ion channel partners. I also discuss the cell adhesion molecule-like properties of these auxiliary subunits and consider whether these properties could be influenced by ion channel activity. This chapter is unpublished. I conceptualized and wrote this chapter. Jon Sack provided organizational feedback and constructive criticism for revisions.

Abstract

Voltage-gated ion channels (VGICs) proteins respond to changes in membrane potential to mediate ionic flux through cell membranes. VGICs can form complexes with non-conducting, auxiliary subunits that modify VGIC expression and function. Auxiliary subunits range in structure from globular intracellular proteins, to single-pass transmembrane proteins, to multi-pass transmembrane proteins, to secreted proteins, many of which have roles that are ancillary to the modulation of VGIC expression and function. In this review, I highlight a subset of single transmembrane pass, auxiliary proteins that have cell adhesion molecule (CAM)-like ancillary functions. CAMs are transmembrane proteins composed of three domains: an intracellular domain that anchors the protein to the cytoskeleton, a transmembrane domain, and an extracellular domain capable of making contacts with other extracellular proteins. Here, I first discuss the shared structural topology of this group of proteins and present the evidence that led to their classification as VGIC auxiliary subunits. I highlight a few key examples to demonstrate the different mechanisms of action through which these auxiliary subunits modulate ionic flux and the molecular regions important for mediating this interaction. I then discuss the requisites for defining a protein as a CAM and give key examples showcasing the range of adhesive activities exhibited within this group of auxiliary proteins. Finally, I review select instances where the auxiliary and adhesive functions of these proteins coalesce to influence ion channel activity in a tissue- or niche-specific manner. The purpose of this review is not to be comprehensive, but instead to highlight structural similarities within this group of 20 proteins, to suggest an overarching hypothesis on the commonality of functions these proteins might share, and to suggest gaps where more research could be done. This review proposes that viewing ion channel interactors through a wholistic lens, and not just as an auxiliary subunit *or* an adhesion molecule, could result in a more nuanced understanding of how ion channel conductances function in physiological and pathophysiological signaling events.

Introduction

Voltage-gated ion channels (VGICs) are multi-pass transmembrane proteins that are selectively permeable to specific ions and control the flux of that ion across the cell membrane. VGICs play important roles in the electrical signaling of excitable cells. Thus far nearly 40 K^+ channel genes (34), 10 Ca^{2+} channel genes (35), 9 Na^+ channel genes (36), and 9 Cl^- channel genes (37) have been found in mammals. The cationic VGICs (K^+, Ca^{2+}, and Na^+ channels) are composed of four voltage sensitive domains (VSD), which consist of 4 transmembrane helices (S1-S4), and a pore domain (PD), which is lined by transmembrane helices (S5 and S6) and an intervening reentrant P-loop. Changes in membrane potential are detected by charged residues, or gating charges, that exist within the VSD. Movement of gating charges triggers a cascade of conformational rearrangements throughout the protein that then causes the PD to open, permitting ionic flux across the membrane. The PD is responsible for the ion selectivity and conduction, permitting the passive flow of ions down their electrochemical gradients at near rates of diffusion (~10^{-8} ions/sec). The coupling between the gating charge movement of voltage sensor domains and opening of the pore domain varies between channel types (38–43).

Much of our understanding of VGIC function has been defined by isolated studies of these proteins in heterologous systems; however, VGICs are commonly expressed in multimeric complexes and found with auxiliary proteins *in vivo* (44). Though nonconducting themselves, auxiliary proteins are capable of altering VGIC-pharmacological interactions (45), influencing VGIC trafficking and expression (46–48), modifying the post-translational status of their VGIC partner (49), and/or modifying VSD voltage sensitivity of activation or inactivation (50). Auxiliary subunits of voltage-gated ion channels can be intracellular, secreted, or transmembrane proteins. Transmembrane auxiliary subunits can be single-pass or multi-pass proteins. This review will highlight a select subset of single-pass transmembrane auxiliary subunits (Fig. 1.1). While the proteins examined here are not closely related in sequence, they were chosen to be examined as a group because they meet two criteria (1) they are single transmembrane pass

auxiliary partners of VGICs and have "auxiliary" functions in modulating channel conductance and (2) they have (or one of their closest homologs has) "adhesive" functions and carry out cellular adhesion molecule-like (CAMs) roles.

CAMs can regulate cell differentiation, inhibit cell growth and apoptosis, mediate mechanical adhesion between cells or with the extracellular matrix, and propagate intracellular signals (51). Additionally, CAMs have been studied for their ability to coordinate cellular responses through adhesion-independent mechanisms such as interacting with growth factor receptors, transcription cofactors, or even through immobilizing cytosolic partners at the membrane preventing further downstream signaling (51).

Prior to 2010, only a short list of proteins with cellular adhesion molecule-like adhesive domains were known to have auxiliary roles as ion channel partner proteins: Navβ, α2δ, and DPPL. However, since then, the list of validated auxiliary proteins with these adhesive domains has expanded to include proteins in the γ, AMIGO, LINGO, and HEPACAM families[1,2]. Much work has been done to classify the various effects of these auxiliary proteins on their ion channels partners, see (50, 52–68), and some work has been done to characterize the adhesive properties of these proteins (69–73). However, the auxiliary and adhesive properties of these proteins have largely remained disparate. This review highlights this interesting group of proteins that seem to lead a double life. A previous review discussed how the adhesive and auxiliary roles of some auxiliary subunits coalesce in the context of cancer pathophysiology (73). Here, I examine more broadly how the auxiliary and adhesive properties of these proteins pertain to

[1] Chloride channel accessory proteins, CLCA1-4 (461), are also auxiliary (462, 463) and adhesive (464) subunits. Some proteins in this family are single-pass transmembrane proteins (465) while others are secreted (466, 467). CLCA-1 and CLCA-2 are auxiliary subunits to the TMEM16A Cl- channel (462, 463).
[2] Osteopetrosis associated transmembrane protein 1 (Ostm1) has a single transmembrane, a short cytoplasmic tail and a large luminal domain with many glycosylation sites (468). Ostm1 modulates the electrogenic $2Cl^-$-H^+ exchanger (468, 469) that is located in the late endosome and lysosome compartments (470).

physiological function. I identify 20 different proteins that meet the two-part criteria, possessing both auxiliary functions that modulation ion channel conductance and adhesive functions, to be included within this review. I aim to present the dual roles of these proteins as a means to highlight an intersection of the disparate fields of ion channel physiology and cell adhesion, where ion channel function might affect adhesion and adhesion might affect ion channel function. Since the study of this auxiliary-adhesion intersection is in its infancy, my goal is to identify research in this area and suggest interesting directions for future study. Understanding the relationship between cell adhesion molecules and VGIC function will help further our understanding the physiological implications of auxiliary protein-VGIC association in physiological and pathophysiological settings (53, 73–83).

Defining a molecule as an auxiliary subunit

Specific criteria have been established to categorize proteins as ion channel auxiliary subunits (50, 59, 84–88).

(1) An auxiliary subunit is not a pore-forming subunit.

The putative auxiliary subunit should not show any ion channel activity. This facet can be assessed by expressing the subunit alone assessing and electrophysiological activity with voltage clamp (89, 90). However, the absence of current does not mean a protein is not a channel, only that any conductance has not been observed. While there are many reasons that could lead to a lack of a detectable conductance, one possible explanation is that some auxiliary subunits only traffic to the surface membrane with coexpression of an ion channel partner[3]. Without a structure, it is difficult to assess if a transmembrane protein is a channel.

[3] LRRC52 trafficking is reorganized by BK (120) and KSper (115, 471). Similarly, AMIGO1/2/3 trafficking is dependent on Kv2.1 (33, 121) or Kv2.2 (33, 121). HEPACAM(1) trafficking is not dependent on ClC-2 (90).

(2) Direct and stable interaction with a pore-forming subunit.

The putative auxiliary subunit should have a sustained interaction with a pore-forming subunit. There are many ways to assess direct and stable interactions and the experimental preparation from which this interaction is probed might change depending on the scientific motivation for interrogating a particular auxiliary subunit. Physiologists, or those interested in recapitulating biological functions of an auxiliary subunit interaction, might only classify a protein as an auxiliary subunit if the stable interaction persists in native samples. On the other hand, biophysicists, or those interested in studying mechanistic phenomena, might be satisfied with stability studies done in heterologous preparations. Regardless of the system of interest, stable interactions can be by verified by binding experiments of two purified recombinant proteins *in vitro* (88) or by native polyacrylamide gel electrophoresis. Co-immunoprecipitation with properly validated antibodies (91) and/or co-crystallization/co-vitrification[4] are also valid approaches. Other methods to evaluate protein-protein interactions take advantage of recent advances in microscopy and can include imaging of protein co-diffusion or reorganization, functional imaging techniques like Forster resonance energy transfer, fluorescence recovery after photobleaching, proximity ligation assay, tryptophan quenching, and voltage-clamp fluorometry, and colocalization (Table 1.1). When considering evidence from imaging studies, it is important to consider the limits of resolution for a particular approach.

(3) Modulation of channel properties and/or trafficking in heterologous cells.

Auxiliary subunits modulate channel properties and/or trafficking when co-expressed with ion channels in heterologous cells. This facet can be assessed by electrophysiological approaches that measure the voltage-dependence or the total amount of current in conditions with and without the

[4] Techniques used for atomic scale structure determination.

putative auxiliary subunit. Protein quantitation approaches, including immunoblots, or protein imaging approaches, like fluorescent-tagging or immunolabeling, can be used to validate changes in channel trafficking.

(4) Demonstrate interaction with channels in vivo.

This final criterion is that auxiliary subunits impact native ion channel function or expression *in vivo* (46, 88). Since it is possible that regulatory effects of a putative auxiliary subunit observed under high expression conditions differ with what is seen in native systems, this criterion can be of paramount importance to physiologists, but is not necessary for those interested in biophysical interactions. This criterion has been developed more recently than the former three and is likely a reflection of the increased accessibility of genetic and native tissue approaches. Genetic approaches to disrupt putative auxiliary proteins *in vivo* can be paired with an electrophysiological or imaging tests to assess if the channel expression, channel properties, and/or localization of ion channels changes with this manipulation. This criterion will distinguish native auxiliary subunits from proteins behaving as auxiliary subunits only in heterologous cells (88).

Structural aspects of VGIC auxiliary subunits

While not all the auxiliary subunits reviewed here have met all of these four criteria (mainly criteria #1 and #4), these proteins impact ion channel function when coexpressed in heterologous expression systems (Table 1.1)[5]. In the coming section, I introduce this group of auxiliary subunits and highlight the extracellular structural features that contribute to their adhesive qualities. I also highlight when homology to other validated cell adhesion molecules has been found.

[5] This list is not exhaustive.

Nav β1-4

Nav β auxiliary subunits interact with voltage gated Na^+ (Nav) channels (59, 66, 92–95), and some voltage gated K^+ (Kv) channels (96–98). The Nav β family of single transmembrane pass auxiliary subunits is comprised of four members, Nav β1 (92), Nav β2 (99), Nav β3 (100), Nav β4 (101), and one embryonic splice variant of Nav β1 that is secreted, Nav β1B (72). All four auxiliary subunits with transmembrane segments have Type I[6] topology and contain a single extracellular immunoglobulin (Ig) domain that is highly conserved within the Ig superfamily of cell adhesion molecules. Overall, Nav β1 and Nav β3 are most similar to each other (100), and share some homology to the myelin P0 family of cell adhesion molecules, which form antiparallel dimers to stabilize membrane-membrane structures such as the myelin intraperiod line (100, 102). Nav β2 and Nav β4 are homologous to each other and their extracellular Ig domain[7] contains regions with similarity to contactin CAMs, which can create *cis* and

[6] Type I membrane protein topology indicates that the auxiliary subunit contains an extracellular N-terminal domain that is glycosylated, a single transmembrane domain, and an intracellular C-terminal tail (472). An N-terminal sequence directs the protein to the endoplasmic reticulum and an internal stop-transfer membrane-anchor sequence that becomes the membrane-spanning α helix (473). In mature proteins, the NH_2 terminal sequence is an amino-terminal cleavable signal peptide necessary for extracellular localization of the remainder of the N-terminal domain (289).

[7] **Ig domain**: A large collection of CAMs are members of the immunoglobulin superfamily and contain Ig domains in their extracellular segment. Ig domains are found in 765 genes within the human genome (474), making them one of the most populous domain families. Ig domains are characterized by a globular structure composed of 70-110 amino acids (193). This sequence creates a sandwich-like fold structure composed of two sheets of antiparallel β stands (195). On the interior of the Ig domain are in-pointing hydrophobic residues while the exterior is lined with out-pointing hydrophilic residues. The two β sheets are connected by a disulfide bond between well-conserved cysteine residues that stabilize the domain structure (193). Ig-CAMs can form complexes in cis and in trans, creating zipper like arrays (194) and facilitating protein-protein interactions (475).

trans cell adhesion interactions (99). Nav β subunits exhibit tissue-dependent expression (47, 99, 103–110) and development-dependent expression (111, 112).

LRRC/γ1-4

LRRC/γ auxiliary subunits interact with large-conductance Ca^{2+}-activated K^+ (BK) channels (113). The LRRC/γ family of auxiliary subunits is comprised of four members, LRRC26/γ1 (114), LRRC52/γ2 (113), LRRC55/γ3 (113), and LRRC38/γ4 (113). All four auxiliary subunits have a single-transmembrane domain and belong to the Type I single-span membrane protein family. They contain a N-terminal cleavable signal peptide that is necessary for proper trafficking but is cleaved in mature proteins to promote the extracellular localization of a N-terminal Leucine Rich Repeat (LRR) domain[8] (113). The LRR domain contains six LRR units and two cysteine-rich regions: the LRRNT capped on the N-terminal side and the LRRCT capped on the C-terminal side (68). Within the LRR domains, the LRRC/y subunits also contain consensus N-glycosylation sites (113). This family of auxiliary subunits also has a short C-terminal tail. Overall, the four family members share an overall sequence similarity of 35-40%, with the most sequence similarity in the structurally determinant residues of the LRR domains and sequence

[8] **LRR domain**: Leucine-rich repeat (LRR)-containing proteins are also key regulators of cell adhesion, extracellular matrix assembly, cell-signaling and synaptic organization (476, 477). LRR domains are found in 188 genes, the 16th most populous domain (474). LRRs are 20-29 amino acid motifs that are comprised of an 11 amino acid consensus sequence of LxxLxLxxN (113) or LxxLxLxxNx(L/I)xx(a)xxxx(F/L/I) (69), where x can be any residue, a is an aliphatic residue, and L and Asp can be replaced with other hydrophobic residues (192). Leucine rich repeat units are often capped at the N and C terminal sides by two-cysteine-rich sequences of variable length (LRRNT and LRRCT respectively). This sequence creates a horseshoe-shaped structure with a short α-helix connected by loops flanking the outer circumference and a concave β-sheet lining the inner circumference (192). The concave surface of the β-sheet structure provides an effective ligand binding site while the convex surface consists of α helices that can vary substantially among LRR proteins and affect the curvature of the LRR domain (196).

divergence in the transmembrane and intracellular C-terminal tail regions (68). LRRC/γ subunits exhibit tissue-dependent expression (113, 115–120) and development-dependent expression (115).

AMIGO1-3

AMIGO auxiliary subunits interact with the voltage gated K^+ channels of family 2 (Kv2) (32, 33, 121). The AMIGO family of auxiliary subunits comprises three members, AMIGO1 (alivin-2)(32), AMIGO2 (alivin-1, DEGA) (33), and AMIGO3 (alivin-3)(33). All three members are Type I single-span transmembrane proteins (69). The AMIGOs contain a putative N-terminal cleavable signal peptide (69). The extracellular domain contains six LRR units, flanked on each side by cysteine-rich LRRNT and LRRCT domains, and one Ig domain close to the transmembrane domain (69). The cytosolic portion of the AMIGOs does not contain any known domains (69). Within the LRR domains, the AMIGO subunits also contain consensus N-glycosylation sites (69). Overall, the three family members share an overall amino acid sequence similarity of 48-50% (69), with the most conserved regions being the LRRs, the transmembrane region, and some parts of the cytosolic tail. Interestingly, the entire transmembrane domain and the cytoplasmic tail are 100% identical between the murine and human AMIGOs (69). The extracellular region of AMIGO shares some homology with the Slit family of extracellular axon guiding proteins and the Nogo-66 receptor (69). AMIGO subunits exhibit tissue-dependent expression (69, 122) and development-dependent expression (123, 124).

LINGO

The LINGO1 auxiliary subunit interacts with BK channels (125). The LINGO family contains homologs 1-4 (122), however since only LINGO1 has a verified interaction with a VGIC, LINGO1 will be the focus of this section. LINGO1 is a single-transmembrane domain proteins that belongs to the Type I

single-span membrane protein family. LINGO1 contains a putative N-terminal cleavable signal peptide (126). The extracellular LINGO1 domain contains one Ig domain, 12 complete LRR units, one partial LRR unit, and two cysteine-rich regions: the LRRNT capped on the N-terminal side and the LRRCT capped on the C-terminal side (126). LINGO1 contains eight consensus N-glycosylation sites, two within the IgI1 domain and six within the LRR domain (126). Like the other auxiliary subunits, LINGO1 also contains a short C-terminal tail. Between species, LINGO1 has a high degree of evolutionary conservation with 92.7-99.8% sequency identity of the extracellular sequence between monkey, mouse, rat, and chicken (126). The IgI1 domain of LINGO1 shares sequence homology with the third Ig3 modules of the neural cell adhesion molecule, NCAM (126). LINGO subunits exhibit tissue-dependent expression (122) and development-dependent expression (127).

HEPACAM

The HEPACAM family of auxiliary subunits is comprised of two members HEPACAM(1) (GlialCam) (90) and HEPACAM2 (Miki) (128). HEPACAM(1) interacts with the voltage-gated Cl^- channel ClC-2 (90). To date, there is no known interacting VGIC partner for HEPACAM2 (90). Both members are Type I single-span transmembrane proteins (56). The HEPACAMs contain a putative, N-terminal cleavable, signal peptide (90, 128). The putative extracellular domain of HEPACAM(1) contains two Ig-like domains, one V-set and another one of the C2-type (56), while HEPACAM2 contains one additional Ig-like domain. The C-terminus of HEPACAM(1) is intracellular and contains a low-complexity proline-rich tail that can be phosphorylated (56). Within the extracellular domains, the HEPACAM(1) subunit also contains consensus glycosylation sites (56, 129). HEPACAM subunits exhibit tissue-dependent expression (70, 90, 130) and development-dependent expression (131).

α2δ-1-4

The α2δ family interacts with Cav channels (54, 132). The α2δ family includes four variants, α2δ-1 (133), α2δ-2 (134), α2δ-3 (135), α2δ-4 (136)[9]. While other α2δ family variants have been identified by bioinformatic means (137), they have yet to be validated as auxiliary subunits and will not be discussed here. The topology of α2δ-1 has been solved biochemically and is thought to be shared with the other α2δ subunits (54). The α2δ protein is a Type I transmembrane protein that is proteolytically cleaved post translationally into two separate segments, α2 and δ, that remain coupled by a disulfide bond (138). The NH_2-terminal signal sequence targets the α2 to the extracellular space, while the short C-terminal δ region tethers the protein to the membrane by a glycosyl-phosphatidylinositol (GPI)-anchoring motif. Both the α2 and δ segments are highly glycosylated (139). The extracellular domain of α2 domain contains a Von Willebrand Factor A (VWA) domain[10]. Within the VWA domain of both α2δ-1 and α2δ-2, the MIDAS motif within the VWA domain contains all 5 co-coordinating amino acids essential for binding divalent cations (140) and for interacting with the partner ion channel (141). VWA domains are

[9] Cachd1 is predicted to be a single transmembrane protein with homology to the α2δ family (478). Cachd1 interacts with Cav2.2 (478), Cav3.1, Cav3.2, and Cav3.3 (479) Cachd1 has a VWA domain with a disrupted MIDAS motif and multiple Cache domains. Unlike the α2δ, Cachd1 is predicted to have a large intracellular C-terminal tail.

[10] **VWA domain:** The majority of well-characterized von Willebrand factor type A (VWA) domains are found in cell adhesion and extracellular matrix (ECM) proteins, which are or could be involved in protein–protein interactions (137). VWA domains are found in 81 genes of the human genome, the 36th most populous family (474). VWA domains are ~200 amino acids that come together to make a Rossmann fold with a metal ion adhesion site (MIDAS motif) that mediates divalent-cation-dependent interactions with ligands. It has been suggested that VWA domains with a perfect MIDAS motif undergo divalent-cation-dependent structural rearrangements upon ion binding (137). VWA domains are often found in integrin-like adhesion molecules (137).

also found in cell adhesion molecules including integrin β-subunit (140). Immediately following the VWA domain, there are also two bacterial chemosensory-like Cache domains, that could mediate binding to small ligands like amino acids. α2δ subunits exhibit tissue-dependent expression (133–135, 142–144).

DPPL

The family of dipeptidyl-peptidase-like (DPPL) proteins interact with Kv4 channels (145). This family includes DPP6 (DPPX, BSPL, KAF) and DPP10 (DPPY). Alternative splicing of the DPPL transcripts creates a set of DPPL proteins with variable N-terminal regions attached to a set of common C-terminal cores. Thus far five DPP6 (DPP6a, DPP6K, DPP6L, DPP6D, DPP6S) and four DPP10 (DPP10a, DPP10b, DPP10c, DPP10d) N-terminal variants have been isolated in mammals (46). All these proteins are Type II[11] transmembrane proteins that have a cytoplasmic NH_2 terminus, a single transmembrane helix and a large extracellular COOH terminal domain. The extracellular domain has many with N-glycosylation sites (146), a cysteine-rich domain, and an aminopeptidase-like domain, which justifies the classification of these proteins in the family of prolyl oligopeptidase serine proteases (147). This domain takes on the conformation of an eight-bladed β-propeller domain[12] with an α/β hydrolase domain (146). Other proteins within the DPPL family (ie. CD-26) use an active aminopeptidase domain to remove

[11] Type II membrane proteins have an intracellular N-terminal tail, a single transmembrane domain, and an extracellular C-terminal domain (472). Type II proteins are targeted to the endoplasmic reticulum and anchored in the membrane with a signal-anchor sequence that also functions as a stop-transfer sequence. Membrane orientation is typically defined by both the length of the hydrophobic transmembrane segment, (long, > 20 amino acid hydrophobic segments tend to adopt type I topology and short < 20 amino acid segments tend to adopt type II topology) and by whichever membrane-flanking segment has the greatest net positive charge (the side with more positive charge will remain on the cytosolic face of the membrane) (473).

[12] **β-propeller domain:** β-propeller domains are characterized by 4-8 symmetrical blade-shaped, beta sheets arranged around a central axis. Beta propellers often surround an active site for ligand binding but protein-protein interactions can also occur at multiple areas around the domain.

dipeptides from regulatory proteins and peptides (9,10), however DPP6 and DPP10 have amino acid substitutions (aspartic acid and glycine, respectively) at the catalytic serine, which renders them inactive as proteases (8,13). DPP6 shares homology with this known cell-adhesion molecule CD-26 (148). DPPL subunits exhibit tissue-dependent expression (149–154) and development-dependent expression (155).

The formerly listed group of auxiliary subunits are distinct from other known VGIC auxiliary subunits in that they (1) are single-transmembrane pass proteins and (2) have a defined extracellular topology that is known to accommodate adhesive-like interactions[13]. While an intracellular or multi-pass topology does not preclude a molecule from participating in adhesive interactions (e.g., (156)), I chose to limit the review to this group of proteins because I am additionally interested in how single-transmembrane pass auxiliary subunits alter VGIC conductance (Chapter 3). Since cationic VGICs are generally considered to have similar architecture, it is intriguing to hypothesize that they might interact with auxiliary subunits of a similar topology in a similar manner. However, based on the limited number of available atomistic structures available for CAM-like single-transmembrane pass auxiliary subunits (157–162)[14], it is not yet clear if this group adopts a uniform binding pose with their partner channel (Fig. 1.4). However, it is clear that these structures are distinct from the binding poses seen with other intracellular (160–163)[15], multi-pass[16] (161, 164), or non-adhesive single-transmembrane pass proteins (165)[17]. Will the elucidation of more structures show similar binding poses for this group of subunits?

[13] OSTM1, CLCA1-4, and Cachd1 are similar in their single transmembrane topology and potential to facilitate adhesive-like interactions. However, these auxiliary subunits were excluded from the review due to the limited amount of current research on these proteins.

[14] Notably, there are no structures detailing the channel binding mode for AMIGO, LINGO, HEPACAM, or LRRC/γ. The structure for α2δ lacks resolution of the transmembrane segment (161, 162)

[15] Intracellular auxiliary VGIC subunits include Cav β 1-4, KChIP, Kv β 1.1- 3, and LRRC10.

[16] Multi-pass auxiliary VGIC subunits include BK β 1-4, Barttin, and Cav γ 1-8.

[17] Single-transmembrane pass auxiliary VGICs subunits not yet documented to have adhesive-like functions include KCNE1 (MinK/IsK), KCNE2 (MiRP1), KCNE3 (MiRP2), KCNE4 (MiRP3), and KCNE5(KCNE1L/AMMERCR2,

Does the localization of the auxiliary subunit to the channel determine the mechanisms through which a subunit can modulate ion channel conductance? These are questions that warrant further investigation.

Modulation of channel function by single transmembrane pass auxiliary subunits

Auxiliary subunit expression can influence many properties of ion channel function. Ion channel current can be increased or decreased by modulating trafficking and stability or by altering the post translational decorations. Here, I categorize the manner in which different single transmembrane pass auxiliary subunits affect channel conductance (Table 1.2), and then compare different mechanisms through which these effects could be incurred. The conductance of a cell (G) is related to the measured current in that cell (I) (Eqn. A) which can be experimentally determined with whole-cell voltage-clamp electrophysiology experiments. The conversion factor between current and conductance is unique to the experimental preparation and for each conducting ion is dictated by the electrochemical driving force, which is determined at a certain membrane potential (V_m), the valence of the conducting ion (z) and the concentration gradient of the ion (C_{out} / C_{in}).

$$I = G\ x\ (V_m - \frac{RT}{zF}\ x\ ln\left(\frac{C_{out}}{C_{in}}\right)) \qquad \text{Eqn. A}$$

To frame the mechanisms that auxiliary subunits affect to change cell conductance, we can similarly analyze the mechanisms that are used to alter cell current. The total amount of current (I_{Total}) measured from a cell during a whole-cell voltage-clamp experiment is determined by Eqn. B.

$$I_{Total} = N\ x\ P_o\ x\ i \qquad \text{Eqn. B}$$

Here, the number of channels expressed on the cell surface (N), the probability of each channel to be open and conductive at certain test potential (P_o) and the amount of current that a single channel passes at that same test potential (i) determine the total amount of current that can be expected from the cell when stimulated to the same test potential. Thus, to change channel conductance, auxiliary subunits

may alter the number of channels, the single channel conductance, and/or the open probability. To link these biophysical parameters to the conformations that are responsible for their properties, we will adopt language used in the Horrigan-Aldrich models for channel conductance (166). Modifications that are expected alter the single channel open probability will be described as effects that alter either pore opening, voltage sensor movement, or voltage sensor-pore coupling.

Change the number of conducting channels

Many auxiliary subunits are associated with increasing the number of conducting channels. One mechanism to effect this change is by increasing channel expression in the plasma membrane, either through helping channels traffic to the surface or by stabilizing channel expression at the surface without changing the proportion of intracellular to plasma membrane expression. Imaging approaches with the capacity to isolate thin optical sections of the cell membrane are sufficient to assess cases where auxiliary subunit expression helps channels traffic from the cytosol to the cell surface, especially when paired with a cell surface marker. Such methods have identified changes in channel localization driven by auxiliary subunit including: LRRC52(γ2), which directs the localization of BKα in mammalian inner hair cells (167); DPP6 and DPP10, which help traffic Kv4.2 from its intracellular localization in transiently transfected CHO cells (147, 151) and COS-7 cells (145) to the cell-surface; HEPACAM(1), which redirects ClC-2 expression to cell-to-cell junctions in HeLa cells and in cotransduced cultured rat astrocytes (90). Complementarily, surface channel expression can be quantified by protein content measurements that isolate surface and intracellular proteins. Changes in surface expression can be affected by auxiliary subunits including: DPP6, which increases Kv4.2 surface protein content in cotransfected CHO cells (147), Nav β1 which increases surface Nav1.5 in cotransfected CHO cells (77) and surface Kv4.2 in cotransfected HEK293 cells (96). Notably, not all ion channels require their auxiliary subunit to direct localization[18], not

[18] Kv2 channels traffic to cell surface clusters without AMIGO1 coexpression (121)

all auxiliary subunits increase the expression of their ion channel partner[19], and measurement of surface expression density by voltage clamp can be misleading, as not all surface expressing ion channels are conducting[20]. When increases in channel expression or surface localization do lead to an increase in number of conducting channels, this effect may manifest as an increase in current density in response to voltage steps (Table 1.2) [21]. Current density is typically normalized by cell capacitance, which approximates cell surface area.

Change single channel conductance

Changes in current density can originate from changes in the unitary conductance of individual channels. The unitary conductance of a channel is defined by the rate of ion permeation. While permeation is defined by interactions in the selectivity filter, the pore helix and the C-terminus of S6, which localizes near the internal cavity of the channel, can further influence ion permeation rates (173). DPP6 is one example of an auxiliary subunit that modulates channel conductance, in part, by altering the unitary conductance of its partner channel, Kv4.2 (174). Single channel recordings from TSA-201 cells coexpressing DPP6 and Kv4.2 exhibit three distinct open levels, each nearly twice as large compared to those recorded from cells expressing Kv4.2 only (174)[22]. Charge neutralization of two negatively charged amino acid side chains (D18 and E20) in the juxtamembrane cytoplasmic N-terminal region of DPP6 abolished the effect of DPPVI on Kv4.2 channel unitary conductance but preserved the ability of DPP6 to

[19] LINGO1 expression suppresses BK α surface expression in HEK293 cells (125).
[20] Conductance through Kv2 channels depends on the density of expression (345).
[21] Current density is another means to distinguish an increase the number of conducting channels, however this measurement alone is unable to distinguish between increases in surface expression, increases in single channel conductance, or increases in channel open probability.
[22] Similarily, Kv4 recordings from mammalian neurons exhibit a unitary conductance that is 1.5-2 fold larger (5, 7, 480, 481) than the unitary conductance from mammalian Kv4 α subunits expressed alone (482–484). Single channel recordings from native cerebellar granule neurons, which likely express DPP6 (150, 485, 486), are also ~2 fold greater than unitary conductances from primary neurons in *dpp6*-/- mice (174).]

shift the *G-V* by -30 mV [23]. This result suggests that the effects of DPP6 on pore conductance are separable from other effects that DPP6 has on voltage sensor movements. Further, these differential effects could be explained by an electrostatic mechanism where the cytoplasmic N-terminal region of DPP6 influences conduction (174) while the transmembrane segment interacts with the channel core to mediate additional effects on Kv4 gating[24] (175, 176). While recent structures could not resolve most of the intracellular interactions to structurally validate this pore interaction, the structures do confirm that the transmembrane segment of DPP6 hydrophobically associates with the voltage sensor of Kv4.2 between the S1 and S2 helices localizing the extracellular region of DPP6 above the channel core (160).

Change open probability

Changes in the probability that a channel is open can arise by many means. Here we discuss several mechanisms by which auxiliary subunits have been found to act, including blocking the pore, a shift in the conductance–voltage (*G–V*), or steady state inactivation–voltage (*SSI–V*) relations. While blocking the pore decreases open probability shifts in voltage dependence can increase or decrease open probability. A hyperpolarizing shift of the *G–V* or a depolarizing shift of the *SSI–V* can result in more open channels. *G–V* and *SSI–V* relations can be shifted by modulating pore opening (125, 166, 168), voltage sensor movement (169, 170), or voltage sensor-pore coupling (114, 171, 172).

Block the pore: diminish open probability

Auxiliary subunits also decrease channel current densities by blocking the channel pore. Similar to 'ball-and-chain' N-type inactivation seen in K^+ channels, a cytosolic region of auxiliary subunits can

[23] Alternative hypotheses to explain DPP6 effects on unitary conductance including a significant contribution of the KChIP (K^+ channel interacting proteins, a cytoplasmic auxiliary subunit) to Kv4 unitary conductance (483, 484), exacerbated outward rectification and/or reduced K^+ selectivity were ruled out through macroscopic recordings (147, 175, 486).

[24] Gating current recordings revealed that DPP6 destabilized the resting and intermediate states of the voltage-dependent activation pathway (175).

physically occlude the pore[25]. The auxiliary subunit LINGO1 seems to act on BK channel conductance in this manner. Coexpression of LINGO1 with BK channels drastically alters channel inactivation, transforming sustained outward BK currents into fast-inactivating currents that begin activating at more negative potentials (125). Trypsin application to the cytosolic side of a patches containing LINGO1 and BK increases current amplitudes and abolishes this inactivation. Macroscopic current recordings made from C-terminal truncation mutants of LINGO1 reveal that this effect of LINGO1 is conferred by the 8 most distal amino acids of the intracellular domain, and that exogenous application of a synthetic peptide with these amino acids could reconstitute the drastic inactivation. Interestingly, even with the removal of these amino acids and the mitigation of inactivation, the hyperpolarizing effect of LINGO1 on the voltage-dependence of BK conductance persisted, suggesting that similar to DPP6, different regions of the auxiliary subunit are important for mediating different biophysical effects (125).

Change voltage sensor movement: shift the G-V

Another way auxiliary subunits change channel open probability is to alter the voltage-dependence of channel activation. Distinct from altering the current density at any one voltage, shifting the voltage-dependent range of channel activation changes the voltages which open the channel. Most of the auxiliary subunits reviewed here confer hyperpolarizing shifts in channel activation (Table. 1.3)[26], such that channels are more active at more negative voltages. One example of an auxiliary subunit that shifts the voltage-dependence of channel activation to more hyperpolarized voltages is AMIGO1. When coexpressed with Kv2.1 channels, AMIGO1 increases the amount of Kv2.1 current elicited with voltage-steps near the threshold for channel activation but does not alter detectably increase current elicited at

[25] The intracellular Kv β auxiliary subunits (487) and the multi-pass transmembrane BK β subunits (488) similarly affect 'ball and chain' inactivation.

[26] Some of the auxiliary subunits reviewed here (Nav β and DPPL) to shift the voltage-dependence of channel activation to more positive voltages in certain experimental preparations (Table. 1.3).

voltages which already maximally activate the conductance (32, 33, 177). I would expect that at negative voltages where very little Kv2 conductance is activated that AMIGO would increase that small current.

In Chapter 3, I describe the biophysical mechanism through which AMIGO1 alters the voltage-dependence of Kv2.1 conduction and show that the presence of AMIGO1 shifts the voltage-dependence of gating charge movement to hyperpolarized voltages and accelerates voltage sensor activation. While the region of interaction responsible for this biophysical effect of AMIGO1 is not known, in Appendix B I present preliminary data suggesting that the intracellular regions of the channel are important interactors for mediating the effects of AMIGO1 on voltage sensor activation.

Change voltage sensor movement: shift the SSI-V

Another mechanism auxiliary subunits use to alter channel open probability is shifting the voltage-dependence of channel inactivation (Table. 1.4). Inactivated channels enter a conformation that prevents them from passing permeant ions through the channel irrespective of the membrane potential. When the voltage dependence of channel inactivation is shifted to more depolarized voltages, the window current, or the range of voltages at which the channel is in a conductive state, is increased[27]. For instance, Nav β1 and Nav β3 both shift the voltage dependence of Nav1.5 inactivation to more depolarized potentials, creating a larger window current. Gating charge measurements and voltage-clamp fluorometry experiments reveal that both Nav β1 and Nav β3 shift the voltage-dependence of some gating charge activation to more depolarized potentials[28]; while Nav β1 alters the movement of the 4th

[27] Conversely, shifting the threshold of channel inactivation to more negative potentials causes channels to enter an inactive and nonconductive state at lower voltages and can lead to decreased channel conductance.

[28] The effects of the +5-+10 mV shift in the $V_{1/2}$ of gating charge-voltage curve are more apparent in the voltage-dependence of inactivation curve than the voltage-dependence of activation curve, suggesting that not all conformational changes incurred upon voltage sensor movement are directly translated to the pore opening conformational step. Such an effect is similarly seen with AMIGO1, which exhibits preferential effects on voltage sensor movement compared to pore opening, as described in Chapter 3.

domain voltage sensor, Nav β3 alters the movement of both the 3rd and 4th domain voltage sensors. Experiments with protein chimeras designed to reveal which domain of the subunits interact with the channel reveal that the extracellular and transmembrane regions of Nav β3 are essential for modulating the 3rd domain voltage sensor (169).[29] Experiments carried out in different systems aimed at answering the same question for Nav β1 suggest that the Nav β1 extracellular domain is critical for modulating channel gating and the voltage dependence of activation of brain and skeletal muscle sodium channels (178–180), while the transmembrane and intracellular regions[30] are responsible for determining the voltage-dependence of inactivation (179, 181). Congruently, recent atomic structures localize Nav β1 near the 3rd domain voltage sensor of EeNav1.4(182), hNav1.4 (183), and hNav1.7 (184) (Fig. 1.2), such that the transmembrane region of Nav β1 is nestled between the S0 and S2 helices of the 3rd domain voltage sensor (182–184) and the extracellular Ig domain interacts with extracellular loop domains, S5 from the 1st domain and S6 from the 4th domain. While these structures did not resolve the C-terminal domain (183, 184), a previous atomic structure collected without the presence of auxiliary subunits, shows the globular C-terminal domain interacting with the 3rd and 4th domain linker, the 4th domain voltage sensor, the 4th domain S4-S5 segment, the 4th domain S6 segment, and the 3rd domain S6 segment of the channel (185). Such interactions suggest that the C-terminal domain could also affect channel function by sequestering the S3-S4 linker and preventing it from inactivating (185)[31].

---

[29]While Nav β1 and Nav β3 associate with voltage-gated sodium channels through a noncovalent interaction (92, 100), Navβ2 and β4 form covalent disulfide bonds with the α subunit (99, 101). Cys55 in β 2 form a disulfide bridge with Cys910 in the 2nd domain pore loop (93, 94). As such, the mechanism of interaction may vary for these two subunits.

[30] The intracellular region of Nav β1 facilitates binding to the C-terminus of Nav1.1 (181) or the S5-S6 linker of the 4th domain of Nav1.4 (489).

[31] Biophysical studies on DPP10-Kv4.2 interactions suggest that DPP10 alters Kv4.2 conductance by accelerating the time course of inactivation and recovery (145). In these studies, the cytoplasmic N-

Change voltage sensor-pore coupling

Another mode to alter channel conductance is through modulation of the coupling between the voltage sensor conformational change and the pore opening conformational change.

Selective conduction of ion permeation through a channel pore requires a conversion from potential energy created by the membrane electric field (and sensed by voltage sensors), to the mechanical work needed to open the pore (186). Increasing the energy conversion of this process could increase the responsiveness of ion permeation to voltage, and foreseeably increase channel conductance. One example of an auxiliary subunit that modulates this process is the LRRC26/γ1 subunit of the BK channel (114). BK channels have both a dependency on the intracellular calcium concentration and a voltage-dependence. Without modulating BK calcium sensitivity, coexpression of BK with LRRC26/γ1 induces a large negative shift in the $V_{1/2}$ (~-140 mV) of activation. This large negative shift in $V_{1/2}$ is accompanied by reduced deactivation speed, and an increase in the rate of activation, yet the voltage-dependence of pore opening and open probability at extreme negative voltages is unaffected (114). These combined effects on BK activation can be accounted for by a great enhancement of the allosteric coupling factor, which stabilizes the channels open state when the voltage sensor is activated and reciprocally stabilizes the activated voltage sensor when the channel is open. While it is not known how LRRC26/γ1 assembles with BK, or the structural region through which voltage sensor-pore coupling is enhanced, several functional studies suggest that interactions between the S4-S5 linker and the distal S6 region of the pore domain are important for transmission of conformational changes from the voltage sensors to the pore (186). Electrophysiological analyses reveal that many regions of LRRC26/γ1 protein are important for the

terminal domain of DPP10 determines the rate of inactivation (145). The intracellular region of DPP6 is unresolved in the most recent atomic structure of Kv4.2-DPP6 (160).

modulatory function of LRRC26/γ1 on BK $V_{1/2}$, however only the putative transmembrane region is necessary for LRRC26/γ1 to associate with BK by co-immunoprecipitation (187).

The mode of action of α2δ on increasing Cav current could also be through increased voltage sensor-pore coupling (132). The available atomic structures of α2δ-1 in complex with a channel (Cav1.1(188) or Cav2.2(162)) lack a transmembrane density (161). However, the structure does reveal that the channel interacts with α2 through its extracellular loops, particularly the L5 loops of the 1st, 2nd, and 3rd domain and the intervening loop between S1 and S2 of the 1st domain (188)[32]. Interestingly, from this structure the MIDAS motif is seen localized immediately above the L1-2 loop in the 1st domain voltage sensor, suggesting that conformational changes of MIDAS could be directly coupled to the modulation of VSD.

Defining a molecule as CAM-like

In addition to functionalities as auxiliary subunits, the proteins discussed in this review also have properties similar to cell adhesion molecules. The term "cell adhesion molecule" was coined in the mid-1970s where it was used to describe molecules that form bonds between cells (189). Adhesion molecules are now defined more broadly as cell surface proteins that mediate the interaction between cells or between cells and the extracellular matrix (190). Cell adhesion is mediated by a variety of molecules, but is often broadly grouped into immunoglobulin-like CAMs, integrins, cadherins, selectins, or nectins (51, 191). Many different structural motifs are responsible for mediating the adhesive properties of cell adhesion molecules, but generally these proteins are grouped based on their extracellular domains (70,

[32] The structure also reveals intracellular interactions between the C-terminal, the S3-S4 linker, the 4th domain voltage sensor, the 4th domain S4-S5 segment, the 4th domain S6 segment, and the 3rd domain S6 segment of the channel, similar to those seen in the NavPaS channel (185).

118, 123, 137, 192–195). The proteins highlighted within this review possess extracellular domains associated with adhesion: immunoglobulin-like (Ig) domain(s) (193–195), leucine rich repeat (LRR) domain(s) (118, 192, 196, 197), von Willebrand Factor-A (VWA) domain(s) (137), or β-propeller domain(s)[33] (198, 199) (Fig. 1.1).

Functions of CAM-like molecules

As implied by this definition, CAMs create cell-cell interactions, which can arise from CAM-mediated homo- or heterophilic *trans* interactions. CAMs can also be responsible for *cis* interactions with other proteins anchored in the same cell. Further, they can interact with intracellular components to affect intracellular signal transduction, cytoarchitecture, and gene transcription. Because of these functionalities, CAMs often have roles in cell outgrowth, proliferation, and migration.

Structures of the following molecules indicate the capacity[34] of these proteins to form dimers, trimers, or tetramers, a prerequisite to forming homophilic or heterophilic interactions: Nav β3 (95), Nav β4 (200), AMIGO1 (201), LINGO1 (202), HEPACAM(1) (126), DPP6 (146, 160), DPP10 (203). Further, Navβ (73, 204, 205) HEPACAM (206, 207) AMIGO (69) LINGO (126) LRRC/γ (208–210) DPPL (148) α2δ (211, 212) all have documented roles in cell outgrowth, proliferation, and/or migration. Does this group of auxiliary subunits similarly take on some of the other classical roles of CAMs?

[33] β-propeller domains are seen integrin molecules (198, 199), which have binding properties distinct from cadherins and Ig Cams; see (490) for a helpful info graphic.

[34] Whether oligomerization between auxiliary subunits occurs in the presence of an ion channel partner is still an open question. The following structures lacked obvious oligomerization: α2δ (146, 203), Nav β1 (182), Nav β2 (252), and Nav β4 (158). However, an atomic structure indicates that DPP6 is able to form *cis* dimers while associated with its partner channel (160).

Homophilic trans interactions

One functional role of cell adhesion molecules is to foster adhesion in *trans*, or between cells. The potential for CAM auxiliary subunits to create homophilic *trans* adhesions is commonly assessed by separately transfecting cultured cells with auxiliary subunits tagged with distinct tags for biochemical identification (Myc, GFP, HA, etc). After leaving sufficient time for expression, the separate populations of cells are then mixed in a confluent coculture where cells are touching. If both populations of auxiliary subunit are coprecipitated from cell lysates incubated with only one tag binder, then there is strong evidence that the extracellular domain of the auxiliary subunit can interact with a compliment of itself when expressed in a neighboring cell. Alternatively, bead aggregation assays can also test for *trans* interactions; if bead populations functionalized with interacting domains readily aggregate, then *trans* interactions are likely present. A third approach is to add a molecule predicted to compete with the domains that participate in a *trans* interaction; if the competition molecule abrogates a cell-to-cell interaction, then it is likely preventing a *trans* interaction. Nav β1 (213), Nav β2 (214), Nav β3 (215), Nav β 4 (216), AMIGO1-3 (69), and HEPACAM(1) (217) all have the capacity to facilitate *trans* homophilic binding.

Heterophilic trans interactions

Cell adhesion molecules can also foster *trans* adhesions between cells by mediating heterophilic interactions. Heterophilic t*rans* interactions can be assessed through similar techniques to those used to assess homophilic *trans* interactions, except a different adhesion molecule is used for bait or competition. Independent of ion channel presence, AMIGO1, AMIGO2, and AMIGO3, Nav β1 (215, 218), Nav β2 (218), and secreted Nav β3 (215) are all able to support heterophilic *trans* interactions.

The physiological ramifications of *trans* interactions are seen in adhesion experiments carried out with AMIGO1. Exogenous application of the AMIGO1 ectodomain has a dominant negative effect and is able to inhibit AMIGO1-mediated adhesion and fasciculation in brain neurons *in vitro* (69). Further, when tested *in vivo,* zebrafish injected with antisense AMIGO1 mRNA or AMIGO1-ectodomain mRNA demonstrated disturbed development of the early neuronal fiber tracts (124). This fiber tract defective phenotype could be recused by co-injection with the full-length AMIGO1 mRNA or AMIGO1-ectodomain mRNA, but not with co-injection of Kv2.1 mRNA (124). This data supports a role for AMIGO1-facilitated adhesion that is independent of its role as an auxiliary protein. While I expect heterophilic *trans* interactions to mediate similar adhesive roles as homophilic *trans* interactions, whether this is the case is unclear.

Cis interactions between auxiliary subunits

As opposed to interacting with fellow adhesion proteins across cell junctions, CAMs also meditate *cis* interactions between proteins within a single cell. *Cis* interactions can be interrogated by proximity-dependent imaging (219, 220) or labeling techniques. For instance, bioluminescence resonance energy transfer (BRET) can be used to probe molecular interactions when two proteins labeled with either an energy donor domain or an energy acceptor domain localize 10-100A of each other. Alternatively, cis interactions can sometimes be detected in cryo-EM atomistic structures. Independent of ion channel coexpression[35], Nav β3 (95, 221, 222), Nav β4 (200), HEPACAM(1) (206, 217). and LINGO1 (202) can interact in *cis*; further, LINGO1 can form *cis* homo- and heterooligomers with itself or its homologs

[35] DPP6 subunits interact in *cis* while bound to Kv4.2 channels (160).

(202)[36]. *Cis* interactions can facilitate intra-membranous interactions in a conformation dependent manner, suggesting that the physiological role of these interactions might be context dependent (223).

Interactions with the extracellular matrix

Cell adhesion molecules can also interact with extracellular matrix proteins, which can occur in *trans* or in *cis*. A prime example of this in Nav β1, which interacts with other cell adhesion molecules including neurofascin-155, N-cadherin, connexin, contactin, neuronal CAM, and neurofascin-186 (214, 218, 224, 225). Further, both Nav β1 and Nav β2 interact with the extracellular matrix molecule tenascin-R (226, 227). Nav β2 also interacts with laminin (228). Similarly, α2δ interacts with thrombospondins to mediate excitatory synaptogenesis (229).

Interactions with the cytoskeleton

Another function of cell adhesion molecules it to interact with cytoskeletal proteins. HEPACAM(1) was found to colocalize and coimmunoprecipitate with the actin cytoskeleton (206). Nav β1 subunits bind to ankyrin G and ankyrin B (230, 231), which are known for linking Nav channels to the cytoskeleton[37].

[36] Co-immunoprecipitation experiments with LINGO1 and its homologs conducted from mouse brain confirmed the presence of physiological heterocomplexes, but do not differentiate whether these complexes are formed in *cis* or in *trans* (202).
[37] Nav β1 subunit promotes direct binding of ankyrin G to the pore forming Nav1.2 alpha subunit (230, 231).

Recruiter of intracellular interacting partners

Cell adhesion molecules can also be involved in localizing intracellular interacting partners and facilitating intracellular signaling cascades. For instance, Nav β1 directly binds with the receptor protein tyrosine kinase B (232), a molecule which participates in intracellular signaling cascades[38].

Additionally, AMIGO2 directly interacts with 3-phosphoinositide-dependent kinase 1 to activate the phosphoinositide 3-kinase-Akt pathway to control cell survival and angiogenesis (233). While these functions are independent of ion channel association, it is intriguing to speculate about if these functions overlap or are modulated with ion channel coexpression.

Participation in downstream signaling cascades

An additional mode through which CAM molecules can affect intracellular signaling is by participating in signaling cascades. Such an effect has been documented for Navβ subunits, which are substrates for proteolytic processing by BACE1 (β-site amyloid precursor protein-cleaving enzyme) and γ -secretases (234, 235). In *in vitro* cell experiments, Navβ2 can be sequentially cleaved by ADAM10 (an ectodomain sheddase) (234) or BACE1 (which similarly cleaves the ectodomain) (235) and then by γ-secretase, which acts on the intracellular C-terminal fragment[39]. These enzymatic actions can have downstream impacts [40].

---

[38] Tyrosine phosphorylation of Nav β1 influences how the auxiliary protein interacts with ankyrin (224, 491) and tyrosine phosphorylation of sodium channels alters the voltage-dependence, rate of inactivation, and current levels (232). Similarly, digestion of the GPI anchor of α2δ-3 by prokaryotic phosphatidylinositol-phospholipase C releases α2 from the membrane and decreases Ca^{2+} current (492).

[39] Application of a γ-secretase inhibitor prevented cell-cell aggregation and migration in a wound healing assay and negatively affected migration of neuroblastoma cells (234).

[40] Interestingly, the presence of the intracellular domain of Nav β2 positively affects Nav1.1 mRNA and protein levels in cell-based assays, however BACE1 activity caused this increase in channel production to

Implications of auxiliary-adhesion duality

I have presented a few select examples of the ion channel-dependent auxiliary roles of these subunits and the ion channel-independent, CAM-like activities. While the auxiliary and adhesive roles of these proteins are interesting in their own right, I am particularly intrigued by the potential convergence between auxiliary and adhesive functions. This group of proteins has the potential to bring ion channels to the site of certain adhesions, change the behavior of ion channels specifically at sites of adhesions, create adhesions in response to ion channel activity and could even couple channel activity to extracellular adhesion formation or intracellular signaling cascades. I discuss a few specific examples where this seems to be the case (see footnotes 35, 37, 38, and 40). To date there are only a few studies on this topic.

Is auxiliary subunit adhesion dependent on ion channel activity?

Auxiliary proteins change ion channel conductances and their adhesive properties can influence channel localization, might these disparate functions overlap through activity-dependent adhesion? Such a phenomena has been explored with HEPACAM(1), which forms a ternary complex with ClC-2 and MLC-1, a multi-pass membrane protein. In oligodendrocytes, HEPACAM(1) is necessary for targeting ClC-2 localization to cell-to-cell junctions and for the modification of ClC-2 rectification. Interestingly, a recent study found that in cultured astrocytes, ClC-2 function and localization showed no signs of HEPACAM(1) influence under basal conditions. However, when the astrocytes were exposed to depolarizing conditions, ClC-2 trafficked to cell–cell junctions and exhibited currents similar to those

---

accumulate intracellularly (493). Together, Nav β2 processing controls Nav1.1 current densities and regulates gene expression of the alpha subunit (493).

expected from HEPACAM(1) co-association. Immunoprecipitation followed by mass spectrometry revealed that ClC-2 only associated with HEPACAM(1) under depolarizing conditions. Interestingly, ClC-2 depolarization-induced reorganization was inhibited by the calcium chelator BAPTA, the calcium channel blocker nifedipine, and by blocking calpain proteases (236). While these results do not suggest that the conductive activity of the ClC-2 channel directly regulates HEPACAM(1) adhesive functions, they do suggest that HEPACAM(1) adhesive properties are dependent on signals that are integrated by a different ion channel[41]. These results could have intriguing ramifications for pathophysiological conditions where extracellular potassium is increased. Under these depolarizing conditions, ClC-2 would be expected to associated with HEPACAM(1) at cell-to-cell junctions, exhibit increased rectification activity, and could facilitate the necessary chloride influx needed to mediate potassium siphoning (236). Such reorganization could be concomitant with rearrangements in cytoskeleton. Do auxiliary subunits help mediate these transmembrane signaling and cytoskeletal reorganizing events?

Do trans junctional electrical signaling domains enable ephaptic coupling?

Another potential ramification of adhesion-protein mediated coupling of ion channels is the formation of intercellular signaling domains. By facilitating *trans* homophilic and heterophilic interactions, auxiliary subunits could localize their ion channel partners into regions closely opposed to other ion channels. A recent study explored this possibility in the context of cardiac conduction, which computer models have suggested may involve ephaptic coupling[42]. Ephaptic coupling is a type of

[41] Kv2.1 channels are known to undergo activity-dependent changes in localization. Ischemic insults and glutamate exposure transforms clustered Kv2.1 localization into diffusion localization (23, 27, 374) . While AMIGO1 follows Kv2.1 during these stimuli (32), this reorganization event occurs independently of AMIGO1 function and instead is mediated by dephosphorylation of a Kv2.1 C-terminal residue that abrogates the interaction with ER-resident proteins (349).

[42] While controversial (237), theoretical studies suggest that ephaptic coupling could represent a functional means of signal transduction due to (1) the close proximity between membranes of adjacent myocytes, (2) the high density of sodium channels localized at points of membrane apposition, and (3)

coupling that involves the intercellular transmission of action potentials via ion accumulation/depletion transients that occur within the narrow extracellular clefts between closely opposed cells. This study tested the hypothesis that Nav β1 could mediate adhesion scaffolds necessary for *trans*-activating Nav1.5 channels within the perinexal clefts adjacent to gap junctions in myocytes. Super-resolution revealed preferential colocalization of Nav β1 and Nav1.5 at the clefts and smart patch clamp[43] revealed that there was a greater sodium current density at the perinexi compared to non-junctional sites. Application of a peptide designed to selectively inhibit Nav β1 widened perinexi in guinea pig ventricles. Further, this peptide reduced perinexal sodium currents without altering whole cell sodium currents in myocyte monolayers, and precipitated arrhythmogenic conduction in Langendorff-perfused guinea pig hearts (237). Though the smart-patch experiments within this study were conducted on a scale that was too large to directly assess the presence of ephaptic signaling, these results suggest a plausible role for Nav β 1 in adhesion and ephaptic action potential propagation. Due to the paradigm-shifting nature of the hypothesis that action potentials propagate through extracellular ion accumulation or depletion, additional research on this topic is certainly warranted. Ephaptic coupling has also been observed in neural tissues (238), another context in which roles of auxiliary subunit adhesion could be assessed.

Do intramembranous clustering domains enable channel oligomerization?

Because some auxiliary-adhesion subunits can facilitate *cis* oligomerization, another potential implication of VGIC-CAM pairing could be to create *cis* ion channel oligomers or heterogenous intramembranous clustering domains. While some VGICs form clusters through pathways independent of their auxiliary partner (10, 17, 222, 239–243), some channels do need coexpression of their auxiliary

---

experimental findings that knockout mice lacking a principle ventricular gap junction protein (494) and humans with dominant negative mutations in the same protein still conduct (495).

[43] Smart patch clamp is an approach that uses a high resistance patch electrode to record electrical events that are localized at a specific site within a narrow region of the cell (496).

subunit to localize into clusters (90, 167). In either instance, the adhesive properties of these ion channel auxiliary subunits could mediate *cis* interactions and further reinforce or tighten already clustered ion channels or create new clusters in instances where clustering is not mediated by the channel. Nav β3 could be playing such a role. Super resolution, atomic force images have documented Nav1.5 trimers[44], a structure that increases in prevalence with Nav β3 coexpression (95). Additionally, super-resolution STORM imaging of fixed Nav1.5 channels suggests that larger radii Nav1.5 clusters are more prevalent with Nav β3 coexpression (222). Further, the number of Nav1.5 channel signals illuminated by proximity ligation assay increase with Nav β3 coexpression (222). While this data seems to be consistent with oligomerization, there are experimental caveats that could lead to data artifacts (222). Accordingly, recent atomistic structures of full length Nav β1 in complex with Nav1.4 (183) have permitted the superposition of modeled/assembled Nav β3 monomeric structures on to this homologous scaffold (244)[45]. For channel trimers to form, molecular dynamics simulations suggest that Nav β3 Ig domains must adopt conformations that are briefly and infrequently sampled *in silico*. As such, trimerization would likely be a very slow process (244) and more research is warranted to confirm the presence of these structures *in*

[44] In an atomic-resolution crystal structure lacking a sodium channel alpha subunit, the Ig domain of Nav β3 forms a trimeric oligomer (95). Analysis of individual protomers showcased that adjacent faces of the Nav β3-Ig fold are stabilized by disulfide bonds and an intramolecular salt bridge. This slightly unusual Ig fold leaves key hydrophobic residues and hydrogen bonding residues free to interact with other protomers and create/stabilize a trimer interface (222).

[45] Molecular dynamics simulations suggest the extracellular domain of Nav β3 monomers have increased conformational freedom and enter orientations amenable for trimer formation. This is in comparison to the more conformationally restricted Nav β1 subunits, which were used as the scaffold for modeling oligomerization (244). Further, even though the Nav β3 primary sequence is most closely related to that of Nav β1 and most of the residues of the Nav β3 trimer interface, including two critical cysteines, are fully conserved (95), select residues necessary for trimerization are unique to Nav β3 (Arg115 and Pro6) (95).

vivo. What would be the electrophysiological or physiological implication of such oligomers? An independent report suggests Nav1.5 channels dimerize through a mechanism independent of auxiliary subunits and exhibit altered gating (245, 246), however, more research is still needed. Whether oligomerization occurs with other auxiliary subunits and VGICs is still an open question[46].

Do auxiliary subunits recruit other intracellular interacting partners that affect ion channel function?

Aside from forming clustering domains composed of ion channel oligomers, the adhesive roles of auxiliary proteins could also facilitate the formation of heterogenous clustering domains by localizing other intracellular or intramembranous ancillary interactors. Does the presence of auxiliary subunit-mediated interactions change ion channel function? Curious results from LRRC52/γ2 knockout mice suggest that this might be the case. While heterologous expression of LRRC52 in oocytes shifts the activation of BK channel gating by ~ -90 mV, the absence of LRRC52/γ2 in LRRC52 knockout mice, results in a BK gating shift of about ~210 mV in inner ear hair cells and disrupted BK localization (167). The drastic disparity in shifts in voltage-dependence suggests that the effect of LRRC52/γ2 on BK gating alone is insufficient to account for the BK gating phenotype seen in inner ear hair cells. Maybe the disrupted BK localization and clustering also disassembles a part or all of a BK macromolecular complex that could contain other elements necessary to confer a full 210 mV gating shift (167)? Do auxiliary subunit

[46] Nav β2 and Nav β4 do not seem to share this capability for oligomerization as there is little sequence similarity between the trimer interface of Nav β3 and the equivalent regions on Nav β2 and Nav β4 (94). Structures of the extracellular domains of AMIGO1 (201) and LINGO1 (126) demonstrate a potential to assemble into higher order oligomers, however these structures were acquired in conditions lacking a channel subunit.

interactions with the extracellular matrix proteins or intracellular proteins affect ion channel function? More research is required to address this possibility and disentangle the closely coupled adhesive and auxiliary roles these proteins.

Is auxiliary subunit adhesion responsive to ion channel activity?

Though still largely unexplored, a few additional studies have attempted to broach the question of how ion channel signaling affects the adhesive properties of their auxiliary subunits. For instance, MCF-7 cells transfected with a silencing RNA targeted to Nav β1, exhibited reduced adhesion and increased migration. However, when treated with tetrodotoxin (a sodium channel pore blocker), adhesion could be increased and the increased in migration could be reversed (71). While there are many mechanisms that could explain this phenomena, the observation that a sodium channel pore blocker could influence adhesive properties either directly or indirectly (maybe by mediating the expression of other proteins involved in adhesion), suggests that electrical cues could be important for patterning (71). AMIGO2 expression in cultured cerebellar granule neurons is regulated by neuronal activity, which can be induced either by KCl depolarization or NMDA (247). Interestingly, AMIGO2 expression is regulated at the transcriptional level by Ca^{2+} influx through voltage-dependent L-type Ca^{2+} channels, which in some cell types, the Ca^{2+} influx through these channels is facilitated by Kv2 channel-mediated organization (248). Conversely, application of tetrodotoxin to cultured cortical neurons inhibits both spontaneous electrical activity and increases in AMIGO2 mRNA expression (247). Both AMIGO1 and AMIGO2 are proteins that enhance cell adhesion (69, 249). While the mechanisms through which electrical activity are coupled to the expression of these adhesion proteins are unclear, these experiments suggest that the activities of electrically conductive ion channels and adhesive subunits may be more intertwined than currently understood.

Conclusion

Thus far I have reviewed the defining characteristics of auxiliary proteins and the mechanisms through which auxiliary subunits alter ion channel function. I have also reviewed the adhesive functions of these same proteins and, while more research is needed, I put forth some examples where the adhesive properties of these subunits seem to alter ion channel function.

By the principle of microscopic reversibility, if the adhesive functions of the auxiliary subunits were to affect ion channel function, then ion channel function would affect the adhesive properties. However, whether the conductive status of the ion channel partner modulates cell adhesion properties is an open question. While structural coupling between adhesion proteins and ion channels is well-established, the degree to which the disparate activities of these two molecules are intertwined is unknown and experimentally difficult to disentangle.

Ion channels play key roles in both interpreting electrical signals and integrating information into patterns of neural activity. Ion channels feedback on their own activities as well as on the activities of other neighboring channel populations, both promoting and partaking in complex, symphonic electrical cascades. Life's processes depend on maintaining a harmonious and regulated flow of ions and such signaling can only be accomplished with a high degree of spatial and temporal precision. Molecular dissection of the ion channel interactome and detailed analyses of the functional impacts that auxiliary subunits have on ion channel proteins has greatly expanded our understanding of how such precision may be achieved. Moving forward, it will be important to take these same approaches in considering how the adhesive properties of auxiliary subunits similarly contribute to signaling and if signaling contributes to cell adhesion properties. Understanding the role of each ion channel complex will better prepare us for addressing the cacophonous consequences when ionic flow goes awry, as in pathophysiological states. By integrating these two perspectives and utilizing holistic approaches, we may discover new and unexpected mechanisms the define our physiology.

Figures and Tables

Figure 1.1

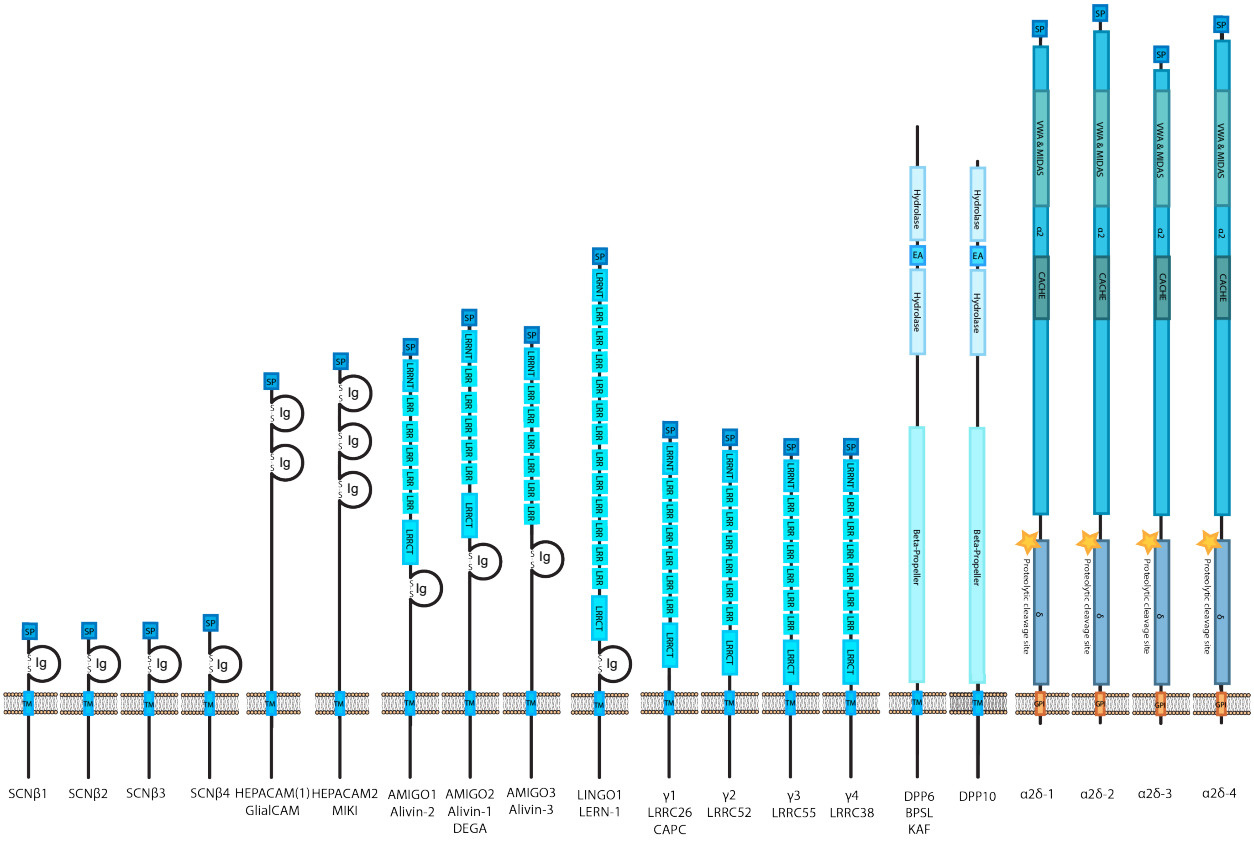

Figure 1.1

The topology of the different auxiliary subunits reviewed here. TM: Transmembrane domain. Ig: Immunoglobulin domain. SP: Signal peptide. LRR: Leucine rich repeat domain (+CT: C-terminal, +NT: N-terminal). EA: Extended arm (203). VWA: Von Willebrand A Factor. MIDAS: Metal ion-dependent adhesion site. GPI: Glycosylphosphatidylinositol anchor. The length of the different proteins represents their rank order total number of amino acids as reported for the human homolog by Uniprot. Within a protein, the different domains are ordered sequentially, but the size of the domain does not necessarily reflect the number of amino acids dedicated to forming that domain. Information regarding structures can be found at https://alphafold.ebi.ac.uk.

Figure 1.2

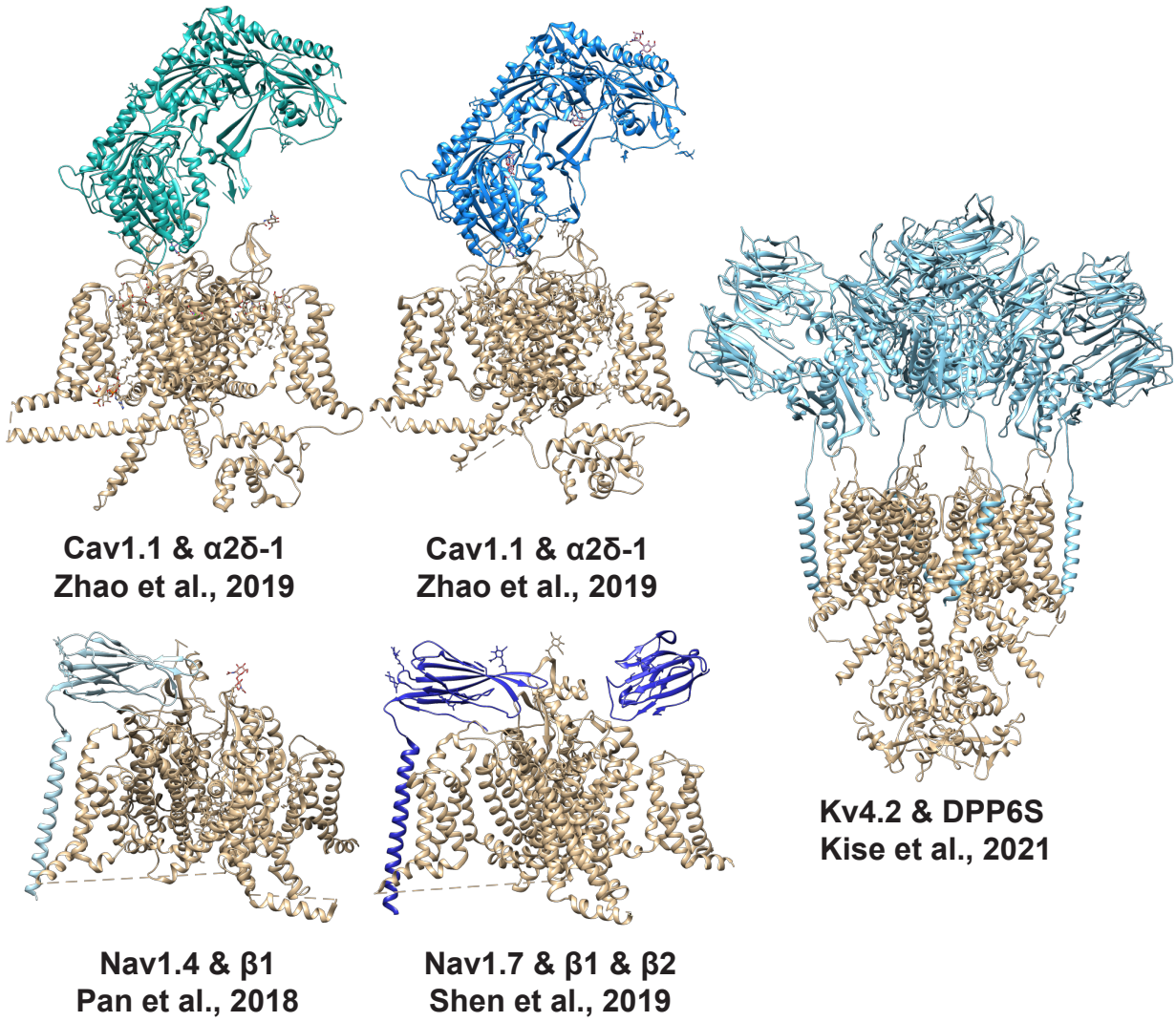

Figure 1.2

Atomistic structures of different auxiliary subunit-ion channel pairs. More information regarding the structures can be found in the references listed.

Table 1.1

Subunit	Native Tissue	Heterologous Expression	Subunit	Native Tissue	Heterologous Expression
Nav β1	Nav1.1: Co-IP (47), Coloc (47) Nav1.5: Co-IP (47), Coloc (250) Kv4.2: Co-IP (97), IP-MS (96) Kv4.3: Co-IP (97)	Nav1.4: Co-vit (182, 183) Nav1.5: FRET (169) Nav1.7: Co-vit (184) Kv4.2: Co-IP (96)	AMIGO3		Kv2.1: Co-IP (33), Reorg (33, 177), Coloc (33, 177) Kv2.2: Co-IP (33), Reorg (33), Coloc (33)
Nav β2	Nav1.1: Co-IP (47), Coloc (47) Nav1.2: IP-MS (251) Nav1.5: Co-IP (47), Coloc (250)	Nav1.2: Co-vit (252) Nav1.7: Co-vit (184)	LINGO1	BKα: Co-IP (125)	
Nav β3	Nav1.5: Co-IP (253) Nav1.7: Co-IP (254)	Nav1.5: Co-IP (253),FRET (169), Coloc (253) Nav1.7: Co-IP (254)	HEPACAM(1)	ClC-2: Co-IP (90, 236), IP-MS (90, 236), PLA: (236), Coloc: (90)	ClC-2: Co-IP (90), Reorg: (90), Coloc: (90)
Nav β4		Nav1.1: Co-vit (158) Nav1.2: Co-IP (101)	HEPACAM2		
LRRC26/ γ1	BKα: Co-IP (114, 116, 255, 256), IP-MS (114), FRET (255), Coloc (255, 256)	BKα: Co-IP (114)	α2δ-1	Cav1.1: Co-AP (257) Cav2.1: IP-MS (258) Cav2.2: IP-MS (258) Cav2.3: IP-MS (258)	Cav1.1: Co-vit (188) Cav2.2: Co-vit (162)
LRRC52/γ 2	BKα: Reorg (167), PLA (120), Coloc (120)	KSper: Co-IP (115)	α2δ-2	Cav2.1: IP-MS (258) Cav2.2: IP-MS (258) Cav2.3: IP-MS (258)	
LRRC55/γ 3			α2δ-3	Cav2.1: IP-MS (258) Cav2.2: IP-MS (258) Cav2.3: IP-MS (258)	
LRRC38/γ 4			α2δ-4		Cav1.2: Co-IP (136)
AMIGO1	Kv2.1: Co-IP (32, 124), Reorg (32), Coloc (32, 121) Kv2.2: Coloc (121)	Kv2.1: Co-IP (33), Reorg (33, 121, 177), Coloc (32, 33, 121, 177) Kv2.2: Co-IP (33), Reorg (33, 121), Coloc (33, 121)	DPP6	Kv4.2: Co-IP (147, 151), IP-MS (96, 147)	Kv4.1: Co-IP (152)* Kv4.2: Co-vit (160), Co-IP (152)*, Reorg (147, 151, 259) Kv4.3: Co-IP (152)
AMIGO2		Kv2.1: Co-IP (33), Reorg (33, 177), Coloc (33, 177) Kv2.2: Co-IP (33), Reorg (33), Coloc (33)	DPP10	Kv4.2: Co-IP (151, 260), IP-MS (96, 151) Nav1.5: Co-IP (261)	Kv4.1: Co-IP (152)* Kv4.2: Co-IP (145, 152, 260), Reorg (151)(145) Kv4.3: Co-IP (152) Nav1.5: Co-IP (261)

Table 1.1

Key: Co-IP = coimmunoprecipitation. IP-MS = immunopurification followed by mass spectrometry identification. Reorg = imaging data suggests that localization of one protein is dependent on the other. FRET = Forster resonance energy transfer. Coloc = colocalization (resolution of confocal imaging ~250 nm). Co-vit = co-vitrification. PLA = proximity lifation assay (resolution </= 40nm). Co-AP = co-affinity purification. *= data not shown in the publication.

Table 1.2

	Effect of coexpression on current density	
Subunit	Native cell systems	Heterologous expression systems
Nav β1	↑ (I_A, cortical neurons) (96).	↑ ($I_{Nav1.2}$) (230, 262)– ($I_{Nav1.4}$)(263). ↑–($I_{Nav1.5}$) (47, 77). – ($I_{Nav1.6}$) (264). ↑ ($I_{Nav1.7}$) (265). ↑ ($I_{Nav1.8}$) (264).
Nav β2	↑ (I_{Na}, ventral cardiomyocytes) (266). – (I_{Na}, artial cardiomyocytes) (266).	– ($I_{Nav1.5}$) (47). – ($I_{Nav1.6}$) (264). – ($I_{Nav1.7}$) (265). – ($I_{Nav1.8}$) (264).
Nav β3		– ($I_{Nav1.2}$)(230). – ($I_{Nav1.5}$) (221, 253). – ($I_{Nav1.6}$)(264). ↑ ($I_{Nav1.7}$) (265). ↓ ($I_{Nav1.8}$) (264, 267).
Nav β4	↓ (I_{Na}, purkinjie cells) (268).	– ($I_{Nav1.6}$) (264). – ($I_{Nav1.7}$) (265). – ($I_{Nav1.8}$) (264).
LRRC26/γ1	– (I_K, parotid cells) (116). – ($I_{BK\alpha}$, parotid cells) (116). – ($I_{BK\alpha}$, inner hair cells) (167).	
LRRC52/γ2	↑ ($I_{BK\alpha}$, inner hair cells) (167).	↑ $I_{BK\alpha}$ (167).
HEPACAM(1)		↑ (I_{ClC-2}) (90).
α2δ-1	↑ ($I_{Ca,L\text{-}type}$, cardiomyocytes) (269).	
α2δ-2	↑ (I_{Ba}, purkinjie cells) (134).	
α2δ-3		– ($I_{Cav2.1}$) (135).
DPP6	– (I_K, hippocampal CA1 neurons) (270).	↑ ($I_{Kv4.3}$) (152).
DPP10		↑ ($I_{Kv4.2}$) (260). ↑ ($I_{Kv4.3}$) (152).

Table 1.2

Auxiliary subunit effects on current density in native systems is assessed by comparing currents in cells isolated from knockout or knockdown to those in wild type cells. Here, ↑= a proportional relationship between subunit present and current density, where knockout currents were smaller than wildtype ones. – = no effect was seen in the knockout animal compared to wildtype. ↓ = an inverse relationship where currents in the knockout animal were larger than the wildtype animal. The effects in heterologous cells systems were assessed by coexpression and compared to singular expression of the channel. Here, ↑= an increase in current density with subunit coexpression. – = no effect. ↓ = a decrease in current density with subunit coexpression.

Table 1.3

	+ Subunit Boltzmann		Channel	Channel Boltzmann		Ref	ΔG Kcal
	$V_{1/2}$	z		$V_{1/2}$	z		/mol
Nav β1	-19.1	-6.5	Nav1.1	-18.3	-7.5	(271)	-0.3
	-23.2	4.4		-27	5.4	(181)	0.4
	-18.4	6.5	Nav1.2	-24.3	5.3	(272)	1.8
	-20.1	-7.8		-18.8	-6.9	(271)	-0.5
	-22.6	4.9	Nav1.3	-15.8	5.2	(72)	-0.8
	-33.3	5.2	Nav1.4	-28.6	4.5	(183)	-0.5
	-23.9	6.3		-22.8	6.4	(273)	-0.4
	-33.4	3.1		-25.9	1.8	(274)	-0.4
	-22	4.1		-25	4.6	(275)	0.3
	-23.9	6.3		-22.8	6.4	(273)	-0.2
	-70.9	4.4		-75.5	4.8	(263)	0.5
	-48.9	8.5	Nav1.5	-38.7	7.7	(276)	-1.9
	-36	4.4		-48	4.7	(275)	1.3
	-43	6.7		-36	6.4	(77)	-1.1
	-41.8	5.8		-36.4	6.7	(277)	-1.8
	-24.9	5.9		-25.6	6.0	(47)	0.1
	-36.7	8.2		-37.8	8.2	(278)	0.2
	-20.3	-8.4		-17.4	-8.7	(157)	-0.6†
	-50.6	7.3		-46.1	7.8	(279)	-1.9
	-34.6	7.2		-35.8	6.8	(169)	0.2
	-34.3	4.9		-35.2	5.1	(280)	0.1
	-20.7	6.4		-25.3	8.0	(281)	0.8
	-57.6	6.3		-58	7.5	(282)	0.1
	-34.8	-5.8	Nav1.6	-36.7	-5.6	(264)	0.3†
	-17.4	5.8	Nav1.7	-18.6	6.8	(265)	0.2
	1.6	-6.3	Nav1.8	10.3	-6.6	(267)	-1.3†
	6.5	7.2		13.0	8.0	(283)	-1.1
	-16.5	-7.5		-12.5	-10.5	(264)	-0.8†
Nav β2	-19.4	5	Nav1.1	-19.6	4.6	(284)	0.0
	-20.7	6.4	Nav1.2	-24.3	5.3	(272)	1.2
	-18.8	4.5		-22.5	5.4	(285)	0.5
	-23.2	5.9	Nav1.5	-25.6	6	(47)	0.3
	-38	6.2		-39.6	7.6	(276)	0.3
	-34.7	6.5		-39.8	4.6	(285)	0.7
	-35.3	-5.6	Nav1.6	-36.7	-5.6	(264)	0.2†
	-18.2	6.2	Nav1.7	-18.6	6.8	(265)	0.1
	9.5	-5.7	Nav1.8	10.3	-6.6	(267)	-0.1†
	0.9	6.4		13	8.0	(283)	-2.0
	-13.9	-9.7		-12.5	-10.5	(264)	-0.3†
Nav β3	-12.1	8.3	Nav1.2	-24.3	5.3	(272)	4.7
	-17.2	9.3	Nav1.3	-24.1	7.8	(286)	1.4
	-20.6	-6.1		-12.3	-4.8	(108)	-1.0†
	-20.7	-8.2	Nav1.5	-17.4	-8.7	(157)	-0.6†
	-42.6	9.4		-42.6	7.3	(221)	0.0
	-30.4	7.4		-35.8	6.8	(169)	0.9
	-23.7	9.6		-25.3	8.0	(281)	0.3
	-36	5.1		-34	4.8	(253)	-0.2
	-39	4.7		-36	4.7	(253)	-0.3
	-37.3	-5.9	Nav1.6	-36.7	-5.6	(264)	-0.1†
	-22.3	5.4	Nav1.7	-18.6	6.8	(265)	-0.5
	11.5	-6	Nav1.8	10.3	-6.6	(267)	0.2†
	4.1	7.3		13	8.0	(283)	-1.6
	-14	-9.8		-12.5	-10.5	(264)	-0.4†

	+ Subunit Boltzmann		Channel	Channel Boltzmann		Ref	ΔG Kcal
	$V_{1/2}$	z		$V_{1/2}$	z		/mol
Nav β4	-22.1	5.7	Nav1.1	-20.5	6.3	(285)	-0.2
	-21.8	5.2		-16.8	4.9	(287)	-0.6
	-20.6	5.7		-15.6	5.7	(287)	-1.7
	-21.9	5.1	Nav1.2	-22.5	5.4	(285)	0.1
	-43.7	3.6	Nav1.5	-43.8	3.1	(288)	0.0
	-35.6	5.7		-39.8	4.6	(285)	0.5
	-44.3	-5.6	Nav1.6	-36.7	-5.6	(264)	-1.0†
	-16.1	7.1	Nav1.7	-18.6	6.8	(265)	0.4
	9.9	8.1	Nav1.8	13	8.0	(283)	-0.6
	-29.2	-7.2		-12.5	-11	(264)	-3.4†
LRRC26	23	1.6	BK	164	1.3	(289)	-3.6
	22	1.8		167	1.3	(290)	-4.8
	18	1.8		165	1.3	(113)	-5.1
	-64	1.7		76	1.5	(113)	-5.1
LRRC52	61	1.2	BK	164	1.3	(289)	-2.4
	61	1.2		167	1.3	(290)	-3.0
	64	1.4		165	1.3	(113)	-3.0
	47	1.3		106	1.5	(113)	-1.9
	9	1.5		76	1.5	(113)	-2.3
	-22	1.7		41	1.6	(113)	-2.4
	-69	1.7		-2	1.6	(113)	-2.6
LRRC55	115	1.4	BK	164	1.3	(289)	-1.3
	115	1.4		167	1.3	(290)	-1.6
	114	1.8		165	1.3	(113)	-1.8
	93	1.6		106	1.5	(113)	-0.5
	55	1.6		76	1.5	(113)	-0.7
	17	1.5		41	1.6	(113)	-0.9
	-6	1.7		-2	1.6	(113)	-0.2
LRRC38	154	1.3	BK	164	1.3	(289)	-0.3
	154	1.3		167	1.3	(290)	-0.4
	146	1.1		165	1.3	(113)	-0.5
	61	1.6		76	1.5	(113)	-0.5
	24	1.7		41	1.6	(113)	-0.6
	-25	1.6		-2	1.6	(113)	-0.9
AMIGO1	-7.4	7.8	Kv2.1	-1.7	7.2	(177)	-0.9
	-7.6	5.6		-1.8	5.6	(177)	-0.8
	10.2	6.7		17.6	6	(177)	-1
	-8.5	8.7		-2.4	9.6	(33)	-1.3
	-7.8	7.1	Kv2.1	-2.2	7.7	(33)	-1
AMIGO2	-8.7	9.0	Kv2.1	-2.0	5.9	(177)	-1.1
	-10.3	6.5		-2.4	9.6	(33)	-1.5
	-9.2	4.6	Kv2.2	-2.2	7.6	(33)	-1.0
AMIGO3	-7.8	7.5	Kv2.1	-2.0	5.9	(177)	-0.9
	-9.1	7.1		-2.4	9.6	(33)	-1.3
	9	5.3	Kv2.2	-2.2	7.6	(33)	-1.0
α 2 δ -1	-6.2	5.7	Cav1.2	2.2	7.4	(144)	-1.7
	2.3	6.0		12	7.8	(144)	-2.1
	6.9	4.4	Cav2.1	6.1	4.7	(144)	0.1
	-3.9	4.9	Cav2.3	-3.1	5.0	(144)	-0.1
	-28.1	4.4	Cav3.1	-28.4	4.0	(291)	0.0
	-23.4	4.3		-24.9	3.9	(144)	0.2

Table 1.3 continued

α2δ-2	-7.1	5.2	Cav1.2	2.2	7.4	(144)	-2.1
	3.0	6.4		12	7.8	(144)	-2.4
	-6.1	5.7		2.2	7.4	(144)	-2.1
	3.8	6.9		12	7.8	(144)	-2.4
	4.2	4.2	Cav2.1	6.1	4.7	(144)	-0.3
	3.0	4.1		6.1	4.7	(144)	-0.6
	-12.2	4.1	Cav2.3	-3.1	5	(144)	-1.7
	-9.1	4.1		-3.1	5.0	(144)	-1.2
	-22.3	4.1	Cav3.1	-24.9	3.9	(144)	0.5
	-21.9	4.2		-24.9	3.9	(144)	0.5
α2δ-3	4.9	5.9	Cav1.2	10.6	6.2	(291)	-1.6
	-29.8	4.1	Cav3.1	-28.4	4.0	(291)	-0.3
DPP6	-31.9	16.1	Kv4.1	-16	14	(145)	-14.1
	-22.1	16.2	Kv4.2	-0.1	20.6	(145)	-24.3
	-25.8	17		-0.1	20.6	(145)	-29.5
	-33.4	16.5		-5.3	17.6	(147)	-11.0
	-25.1	18.6		-4.1	21.5	(150)	-9.7
	-24.9	16.1		-4.1	21.5	(150)	-9.0
	-31.5	17.2		-4.1	21.5	(150)	-12.2
	-44	7		-20	8.0	(260)*	-11.4
	-22	16		2.0	22	(260)*	-29.2
	-26.9	22.2		-6.6	26.7	(292)	-32.3
	-30.3	16.3	Kv4.3	-15.4	19.9	(147)	-6.2
	-23.3	17.4		-6.2	21.5	(152)	-7.7
	-36.7	17		-6.0	23	(174)	-14.2
DPP10	-39	2.4	Nav1.5	-44	2.3	(261)	0.3
	-59.9	11	Kv1.4	-55	15.6	(293)	-1.5
	-1.3	19.4	Kv4.1	-16	14	(145)	5.7
	-18.9	17.5	Kv4.2	-0.1	20.6	(145)	-8.3
	-28.6	18.2		-0.1	20.6	(145)	-34.3
	-36	6		-20	8.0	(260)*	-7.4
	-26	20		2.0	22	(260)*	-39.4
	-26.9	19.7		0.5	21	(149)	-12.9
	-29.1	12.6		0.5	21	(149)	-11.5
	-30.7	15.6		0.5	21	(149)	-13.2
	-41.8	22	Kv4.3	-31.7	19.7	(293)	-4.9
	-17.4	19.4		-6.2	21.5	(152)	-5.3

Table 1.3

Estimation of energy that auxiliary subunit association confers onto shifting the voltage-dependence of channel activation. $\Delta G = \Delta V z F$, where $\Delta V = \Delta V_{1/2}$ as reported directly by a 1st order Boltzmann or calculated if 4th order Boltzmann relations were used to approximate data; z = the average slope derived from the Boltzmann fits for control *G–V* curves and *G–V* curves with the subunit (z was multiplied by 4, if derived from a 4th order Boltzmann); F = Faraday's constant. All data presented here was combined from different cell expression systems and different recording solutions; all of these parameters have unique effects on the recorded modulatory properties of the auxiliary subunit with respect to the channel. * = Boltzmann fit parameters for this analysis was estimated from a graphical representation provided by the original publication. † = Boltzmann fit for the original data was carried out in an inverse fashion, the signage was reversed for consistency within this report. A negative ΔG represents a left- or hyperpolarizing-shift in voltage–dependence. The opposite is represented by a positive ΔG.

Table 1.4

	+ Subunit Boltzmann		Channel	Channel Boltzmann		Ref	ΔG Kcal/ mol
	$V_{1/2}$	z		$V_{1/2}$	z		
Nav β1	-54.2	4.6	Nav1.1	-55.5	4.7	(271)	0.1
	-41.5	8.1		-32	6.6	(181)	-1.6
	-49.7	8.3	Nav1.2	-53.4	8.9	(272)	0.7
	-58.1	7.2		-51.7	10	(271)	-1.3
	-49.1	5.9		-45.1	9.8	(100)	-0.7
	-64	-6	Nav1.3	-51.8	-5.5	(72)	-1.6†
	-64.9	9.5	Nav1.4	-68.9	10	(183)	0.9
	-70.9	4.4		-75.5	4.8	(263)	0.5
	-66.5	6.3		-66.1	6.4	(273)	-0.1
	-61.8	4.7		-54.5	5.0	(274)	-0.8
	-59	5.5		-67	7.0	(275)	1.2
	-73	5.8	Nav1.5	-96	6.9	(275)	3.4
	-85	8.3		-77	8.3	(77)	-1.5
	-78.4	-7.7		-81.4	-9.2	(277)	0.6†
	-72.9	4.7		-77.1	4.9	(47)	0.5
	-90.9	-6.6		-95.2	-7.3	(278)	0.7†
	-70.7	5.9		-61.1	5.7	(157)	-1.3
	-92.6	6.4		-85.1	7.3	(279)	-1.2
	-74	-5.7		-84.8	-8.9	(169)	1.8†
	-77.2	-5.7		-83.7	-5.9	(280)	0.9†
	-95.5	4.7		-96.1	4.5	(281)	0.1
	-105	-4.9		-113	-5.3	(282)	1.0†
	-72.2	6.6	Nav1.6	-74.3	6	(264)	0.3
	-65.7	7	Nav1.7	-70.9	8.1	(265)	0.9
	-58.4	7.1	Nav1.8	-52.9	8.9	(267)	-1.0
	-47.2	-11		-30.3	-12	(283)	-4.4†
	-47.8	7.7		-43.2	6.0	(264)	0.7
Nav β2	-44.4	-6.7	Nav1.1	-44.1	-5.2	(284)	0.0
	-44.9	7.6	Nav1.2	-53.4	8.9	(272)	1.6
	-34.9	9.3		-37.7	9.0	(285)	0.6
	-77.1	5.1	Nav1.5	-77.1	4.9	(47)	0.0
	-67.2	7.9		-73.8	8.0	(285)	1.2
	-73.3	6.4	Nav1.6	-74.3	6	(264)	0.1
	-70.9	7.5	Nav1.7	-70.9	8.1	(265)	0.0
	-49	9.9	Nav1.8	-52.9	8.9	(267)	0.8
	-37.7	-15		-30.3	-12	(283)	-2.3†
	-43.7	5.4		-43.2	6.0	(264)	-0.1
Nav β3	-41.5	8.6	Nav1.2	-53.4	8.9	(272)	2.4
	-49.3	6.1	Nav1.3	-45.1	9.8	(100)	-0.8
	-70.1	5.6		-71.9	7.4	(286)	0.3
	-72.6	5.9		-61.1	5.7	(108)	-1.5
	-90.6	-6.5	Nav1.5	-96.1	-7.2	(221)	0.9†
	-75.2	-6.2		-84.8	-8.9	(169)	1.7†
	-85.2	4.2		-96.1	4.5	(281)	1.1
	-75.8	6.5	Nav1.6	-74.3	6	(264)	-0.2
	-67.4	7	Nav1.7	-70.9	8.1	(265)	0.6
	-47.9	9.0	Nav1.8	-52.9	8.9	(267)	1.0
	-48.1	-7.9		-30.3	-12	(283)	-4.1†
	-45.9	6.0		-43.2	6.0	(264)	-0.4
Nav β4	-31.4	7.3	Nav1.1	-32.3	7.6	(285)	0.2
	-45.7	8.1		-42.1	6.4	(287)	-0.6
	-44.4	7.4		-43.6	6.4	(287)	-0.1
	-34.9	7.1	Nav1.2	-37.7	9.0	(285)	0.5
	-74.4	9.6	Nav1.5	-73.8	8.0	(285)	-0.1
	-77.1	5.7	Nav1.6	-74.3	6.0	(264)	-0.4
	-70.8	7.2	Nav1.7	-70.9	8.1	(265)	0.0
	-34.7	-14	Nav1.8	-30.3	-12	(283)	-1.3†
	-52.5	7.3		-43.2	6.0	(264)	-1.4

	+ Subunit Boltzmann		Channel	Channel Boltzmann		Ref	ΔG Kcal/ mol
	$V_{1/2}$	z		$V_{1/2}$	z		
α2δ-1	-28.3	10	Cav1.2	-18.3	15	(144)	-2.9
	-19.8	9.8		-10.5	15	(144)	-2.7
	-6.5	6.9	Cav2.1	5.1	5.8	(144)	-1.7
	-61.4	7.7	Cav2.3	-56.5	7.7	(144)	-0.9
	-55.9	4.2	Cav3.1	-57.3	5.6	(291)	0.2
	-52	4.3		-54.9	4.3	(144)	0.3
α2δ-2	-28.2	9.0	Cav1.2	-18.3	15	(144)	-2.8
	-20.7	9.9		-10.5	15	(144)	-2.9
	-26.1	9.0		-18.3	15	(144)	-2.2
	-20.5	11		-10.5	15	(144)	-3.0
	1.0	6.2	Cav2.1	5.1	5.8	(144)	-0.6
	0.3	6.4		5.1	5.8	(144)	-0.7
	-45.9	7.2	Cav2.2	-42.4	11	(140)	-0.7
	-63.2	8.3	Cav2.3	-56.5	7.7	(144)	-1.2
	-62.7	7.8		-56.5	7.7	(144)	-1.1
	50.4	4	Cav3.1	-54.9	4.3	(144)	10.1
	50.1	4.2		-54.9	4.3	(144)	10.3
α2δ-3	-57.2	4.6	Cav3.1	-57.3	5.6	(291)	0.0
DPP6	-83.6	6.8	Kv4.1	-66.9	4.8	(145)	-2.2
	-71.2	4.1	Kv4.2	-63.9	5.1	(145)	-0.8
	-65.6	3.5		-63.9	5.1	(145)	-0.2
	-83.3	4.6		-66.9	5.8	(147)	-2.0
	-76.9	4.7		-64.1	7.5	(150)	-1.8
	-74.6	4.9		-64.1	7.5	(150)	-1.5
	-78.8	4.6		-64.1	7.5	(150)	-2.1
	-71	4.1		-62.5	4.8	(260)*	-0.9
	-65	3.9		-64	6.6	(260)*	-0.1
	-71.4	6.7	Kv4.3	-63	6.3	(147)	-1.3
	-65.8	-8.3		-41.9	-7.8	(152)	-4.4†
DPP10	-72	7.9	Nav1.5	-78	7.1	(261)	1.0
	-60	3	Kv1.4	-52.3	3.6	(293)	-0.6
	-70.7	7.1	Kv4.1	-66.9	4.8	(145)	-0.5
	-70.2	4.8	Kv4.2	-63.9	5.1	(145)	-0.7
	-69.6	3.7		-63.9	5.1	(145)	-0.6
	-74	4.8		-62.5	4.8	(260)*	-1.3
	-67	4.0		-64	6.6	(260)*	-0.4
	-74.1	4.7		-64.1	4.6	(149)	-1.1
	-71	3.9		-64.1	4.6	(149)	-0.7
	-72.9	4.4		-64.1	4.6	(149)	-0.9
	-59.7	4.2	Kv4.3	-43.4	5.1	(293)	-1.7
	-62.2	-9.5		-41.9	-7.8	(152)	-4.0†

Table 1.4

The approximate amount of energy that auxiliary subunit association confers onto shifting the voltage-dependence of channel steady-state inactivation. Values were calculated the same as for Table 1.3. Similarly, a negative Δ*G* represents a left- or hyperpolarizing-shift in voltage–dependence. The opposite is represented by a positive Δ*G*. * = Boltzmann fit parameters for this analysis was estimated from a graphical representation provided by the original publication. † = Boltzmann fit for the original data was carried out in an inverse fashion, the signage was reversed for consistency within this report

Chapter 2: Fluorescent tarantula toxins to track and control conformational change of Kv2 ion channels.

Preface

This chapter details my contributions to the development and characterization two labeled toxins used to track and control conformational change of the Kv2.1 voltage-gated ion channel. The first half of this section has been adapted from work published as research article in the *Journal of General Physiology* in 2021 as: *Thapa, P., *Stewart, R.G., Sepela, R.J., Vivas, O., Parajuli, L.K., Lillya, M., Fletcher-Taylor, S., Cohen, B.E. Zito, K., and Sack, J.T. EVAP: A two-photon imaging tool to study conformational changes in endogenous Kv2 channels in live tissues. *JGP* 153(11): e202012858. While the entirety of this work includes contributions from many authors, for this thesis chapter I distilled this body of work down into a smaller synopsis to better encapsulate my contributions. Regarding the work presented in this thesis, I conjugated and purified GxTX594 (Fig. 2.1) and patched CHO cells with and without GxTX–594 to assess activity (Fig. 2.3). Parashar Thapa patched CHO cells to determine the voltage-dependence of the off rate (Fig. 2.4) and this data was analyzed by both Parashar Thapa and Robert Stewart. Parashar Thapa, Robert Stewart, Jon Sack and I all contributed to the conceptualization of the statistical model of EVAP binding (Fig. 2.5); Robert Stewart and Jon Sack were instrumental in finalizing this model (Fig. 2.6). The writing for this section was largely adapted from the *JGP* article, which was drafted by Parashar Thapa, Robert Stewart, Jon Sack and I (with feedback from Oscar Vivas, Laxmi Parajuli, Sebastian Fletcher-Taylor, Bruce Cohen, Karen Zito, and Jon Sack). Minor changes to layout and organization were made to best fit this thesis.

The second half of this section has been adapted from work published as research article in the *American Chemical Society Journal for Chemical Neuroscience* in 2020 as: Fletcher-Taylor, S., Thapa, P., Sepela, R.J. Kaakati, R., Yarov-Yarovoy, V., Sack, J.T and Cohen, B.E. Distinguishing potassium channel resting state conformations in live cells with environment-sensitive fluorescence. *ACS Chem. Neurosci* 11 (15): 2316-2326. While the entirety of this work includes contributions from many authors, for this thesis chapter I distilled this body of work down into a smaller synopsis to better encapsulate my contributions. Regarding the work presented in this thesis, Jon Sack imaged the hippocampal neuron stained with GxTX Lys27Pra(JP) and I processed the image (Fig. 2.8A), Sebastian Fletcher-Taylor and Parashar Thapa imaged the selectivity of GxTX–JP conjugates (Fig. 2.8B), Sebastian Fletcher-Taylor acquired and analyzed data regarding the spectral emission of GxTX-JP conjugates in solution (Fig. 2.8C) and bound to cells (Fig. 2.8D). Parashar Thapa conducted voltage-clamp fluorometry experiments to determine the voltage-dependence of the GxTX Lys27Pra(JP) spectral response (Fig. 2.9 red) and I conducted gating current recordings to characterize voltage sensor movement in the presence of GxTX Lys27Pra(JP) (Fig. 2.9 black). Some work conducted by my colleagues is included within this chapter for context.

Abstract

A primary goal of molecular physiology is to understand how regulated conformational changes of proteins affect the function of cells, tissues, and organisms. Here, I describe two imaging methods for measuring the conformational changes of the voltage sensors of endogenous ion channel proteins within live tissue, without genetic modification. For the first method, I synthesized GxTX–594, a variant of the peptidyl tarantula toxin guangxitoxin-1E, conjugated to a fluorophore optimal for two-photon excitation imaging through light-scattering tissue. GxTX–594 targets the voltage sensors of Kv2 proteins, which form potassium channels and plasma membrane–endoplasmic reticulum junctions. GxTX-594 dynamically labels Kv2 proteins on cell surfaces in response to voltage stimulation. To interpret dynamic changes in fluorescence intensity, we developed a statistical thermodynamic model that relates the conformational changes of Kv2 voltage sensors to degree of labeling. Two-photon excitation imaging of Kv2 proteins in rat brain slices revealed puncta of GxTX–594 on hippocampal CA1 neurons that responded to voltage stimulation and retained a voltage response roughly similar to heterologously expressed Kv2.1 protein.

For the second method, we synthesized GxTX Ser13Pra(JP) and GxTX Lys27Pra(JP), different variants of guangxitoxin-1E conjugated to an fluorophore, JP (julolidine phenoxazone), that has an inherent response to the polarity of its immediate surroundings. GxTX–JP variants offer site-specific structural insight into Kv2.1 voltage sensing domain allostery that occurs during membrane depolarization. Using voltage-clamp spectroscopy to collect emission spectra as a function of membrane potential, we find that spectra vary with toxin labeling site, the presence of Kv2 channels, and changes in membrane potential. With a high-affinity conjugate in which the fluorophore itself interacts closely with the channel, the emission shift midpoint is 50 mV more negative than the Kv2.1 gating current midpoint. This suggests that substantial conformational changes at the toxin−channel interface are associated with early gating charge transitions and these are not concerted with voltage sensing domain motions at more

depolarized potentials. Both of these fluorescent probes enable study of conformational changes that can be correlated with electrophysiology, putting channel structures and models into a context of live-cell membranes and physiological states[47].

[47] A third method to track conformational change through photoacoustic imaging is described in Appendix A.

Introduction

To move the field of voltage-sensitive physiology forward, we need new tools that indicate when and where voltage-sensitive conformational changes in endogenous proteins occur. Many classes of transmembrane proteins have been found to be voltage sensitive (295). One important class of voltage-sensitive proteins is the voltage-gated potassium (Kv) ion channels. Kv channels are highly polymorphic (i.e., able to adopt many functional conformations), and electrophysiological studies have long shown that changes in channel structure underlie voltage-gated K^+ flux. The voltage sensors of proteins in this superfamily comprise a bundle of four transmembrane helices termed S1–S4 (163, 296). The S4 helix contains positively charged arginine and lysine residues, gating charges, that respond to voltage changes by moving through the transmembrane electric field (297–299). When voltage sensor domains encounter a transmembrane voltage that is more negative on the inside of the cell membrane, voltage sensors are biased toward resting conformations, or down states, in which gating charges are localized intracellularly. When voltage becomes more positive, gating charges translate toward the extracellular side of the membrane, and voltage sensors are progressively biased toward up states in a process of voltage activation (159, 300–302).

In some voltage-gated ion channel proteins, voltage sensor movement is also coupled to nonconducting protein functions (303, 304). These nonconducting protein functions are largely inaccessible to study by electrophysiology and are more poorly understood. Novel approaches are needed to learn more about voltage sensing in intact tissues and could be used to unlock the mysterious realm of nonconducting voltage-sensitive physiology. One important class of Kv proteins that has documented nonconducting functions is the Kv2 subtype. Kv2 proteins form voltage-gated K^+ channels (2) that are capable of integrating their response to voltage with many other cellular processes, including phosphorylation (305), SUMOylation (306), oxidation (307), membrane lipid composition (308), and auxiliary subunits (32, 33, 309). Additionally, Kv2 proteins bind endoplasmic reticulum proteins to form

plasma membrane–endoplasmic reticulum junctions (242, 243) and regulate a wide variety of physiological responses in tissues throughout the body (310). To study the functional outputs of voltage sensors, both conducting and nonconducting, it is essential to measure voltage sensor activation itself.

Attempts to understand dynamic changes in Kv voltage sensors have spanned decades and have included electrophysiological measurements of gating currents (295, 300, 301, 311, 312), site-directed mutagenesis (313, 314), side chain reactivity studies (315–317), and optical measurements from fluorophores inserted near voltage sensors by genetic encoding (315, 318) or chemical modification (319). However, the following experimental limitations prevent these existing techniques from measuring conformational changes of voltage sensors of most endogenous proteins: gating currents can only be measured when the proteins are expressed at high density in a voltage-clamped membrane; engineered proteins differ from endogenous channels; most chemical modification strategies result in off-target labeling; and conjugation of fluorophores into voltage sensors irreversibly alters structure and function.

Here, we develop a different strategy to reveal conformational states of Kv2 proteins. To image where in tissue the voltage sensors of Kv2 proteins adopt a specific resting conformation, we exploited the conformation-selective binding of the tarantula peptide guangxitoxin (GxTX)-1E, which can be conjugated to fluorophores to report Kv2 conformational changes (320–322). Venomous species commonly target ion channels with peptidyl gating-modifying toxins that preferentially bind to specific channel conformations, trapping them in particular physiological states (323). This conformational specificity has made GMTs critical tools for understanding channel allostery and physiology. GxTX-1E, a lipophilic cystine-knot peptide from the Chinese hissing bronze wolf tarantula C. *guangxiensis*, (29, 324, 325) targets the Kv2.1 closed state VSD with 5400-fold greater affinity than its open state (321), shifting channel opening to more depolarized potentials and effectively closing the channel without directly occluding its pore. Synthetic analogues of GxTX have been functionalized with optical probes and preferentially bind to closed, wild-type Kv2.1 channels in cells and tissue (320–322).

Here, we synthesize GxTX–594 and variants of GxTX–JP. GxTX–594 is a Ser13Cys GxTX variant conjugated to Alexa Fluor 594, a fluorophore compatible with two-photon excitation imaging through light-scattering tissue. GxTX–594 dynamically binds Kv2 channels in living tissue. When GxTX-594 binds, it becomes immobilized and fluorescently labels Kv2 proteins at the cell surface. When Kv2 channels become voltage activated, GxTX–594 unbinds, resulting in unlabeling (Fig. 1.2). This labeling/unlabeling dynamic is similar to a recently reported point accumulation for imaging of nanoscale topology superresoluton imaging method (326), yet the method reported here is sensitive to changes in protein conformation. GxTX–594 labeling of Kv2 proteins equilibrates on the time scale of seconds, revealing the probability (averaged over time) that unbound voltage sensors are resting or active. Here, we develop a method to calculate the average conformational status of unlabeled Kv2 proteins from images of GxTX–594 fluorescence and deploy the GxTX–594 probe in brain slices to image voltage-sensitive fluorescence changes that reveal conformational changes of endogenous neuronal Kv2 proteins. With standard fluorescent reporters such as AlexaFluor 594, labeled GxTX can be used to image endogenous Kv2.1 gating but offers no molecular insight into the toxin-VSD structure or channel allostery. To meet this need, we also synthesized GxTX–JP variants. GxTX–JP variants incorporate an environment-sensitive fluorophore into different sites on the GxTX peptide to gain information about protein motion at single amino acid level resolution. Environment sensitive fluorophores respond to the polarity of their immediate surroundings with large shifts in excitation and emission peaks (327–329) and are particularly well-suited for reporting protein allostery (330, 331). Voltage-clamp spectroscopy and collection of full emission spectra of JP−GxTX conjugates as a function of membrane potential reveals that different labeling sites on the toxin vary have varied environmentally-sensitive responses to Kv2.1 voltage activation. We use these varied responses to understand voltage sensor conformational status. One GxTX–JP variant with high affinity is especially useful in interrogating early gating charge transitions that are not concerted with later voltage sensor domain motions. These approaches provide an imaging

technique to study conformational changes of endogenous voltage-sensitive Kv2 proteins in samples that have not (or cannot) be genetically modified.

Results

GxTX–594 retains bioactivity for Kv2.1 after chemoselective modification

To monitor activation of Kv2 proteins in heterologous cells or tissue slices, I synthesized GxTX–594 (Fig. 2.1), which is compatible with two-photon imaging. Here GxTX is conjugated to Alexa Fluor 594, a persulfonated Texas Red analogue with a large two-photon excitation cross section and ample spectral separation from GFP, making it well suited for multiplexed, two-photon excitation imaging experiments (332). I performed electrophysiological analyses to determine whether GxTX–594 retains the ability to allosterically modulate Kv2.1 following conjugation (Fig. 2.3). GxTX is a partial inverse agonist of Kv2.1, which lowers channel open probability by stabilizing voltage sensors in a resting conformation. Consequently, more positive intracellular voltage is required to activate voltage sensors and achieve the same open probability as without GxTX (320). Previously, it was estimated that a Kv2.1 voltage sensor with GxTX bound is 5,400-fold more stable in its resting conformation and requires more positive intracellular voltage to become activated (320). To characterize the efficacy of GxTX–594 in allosterically modulating Kv2.1 gating, I voltage clamped Kv2.1-CHO cells and measured K^+ currents in GxTX–594. The Kv2.1 conductance–voltage (*G–V*) relation was analyzed by fitting with a fourth power Boltzmann function. The voltage at which the conductance of the fitted function is 50% of maximum, V_{Mid}, was +73 ± 13 mV for 100 nM GxTX–594 (Fig. 2.3G). For comparison, the V_{Mid} of 100 nM GxTX was +67 ± 6 mV (320). This shift of the *G–V* indicates that GxTX–594 retains an efficacy similar to GxTX.

The relationship between GxTX-594 cell-surface fluorescence and Kv2.1 voltage activation

To understand the relationship between channel gating and GxTX–594 fluorescence, my colleagues determined how fluorescence intensity on cells expressing Kv2.1 responds to changes in membrane voltage (methods found in (321)). My colleagues incubated Kv2.1–CHO cells for 5 min in a bath solution (CEG) containing 100 nM GxTX–594, which was then diluted with extracellular solution to

9 nM. Once GxTX–594 fluorescence intensity stabilized at the cell membrane (at least 9 min), cells were voltage clamped in whole-cell mode. The fluorescence response of GxTX–594 was measured while the membrane voltage of Kv2.1-CHO cells was stepped from a holding potential of −80 mV to more positive voltages that ranged from −40 mV to +80 mV (Fig. 2.4A). ROIs corresponding to the cell surface were manually identified and average fluorescence intensity quantified from time-lapse sequences. To compare voltage response properties between cells, fluorescence was normalized to analyze only the voltage-sensitive fraction of the total fluorescence from each cell, which was defined as the fluorescence that changed between −80 mV and +80 mV. The initial fluorescence at a holding potential of −80 mV was normalized to 100% F/F_{init}, and residual fluorescence after a +80-mV step was normalized to 0% F/F_{init}, (Fig. 2.4D). To characterize the voltage dependence of the Kv2.1–GxTX–594 interaction, fluorescence–voltage (*F–V*) responses were fit with a Boltzmann distribution. This fit had a half maximal voltage midpoint ($V_{1/2}$) of −27 mV and a steepness (z) of 1.4 e_0 (Fig. 2.4D, bottom panel, black line). This is similar to voltage sensor movement in Kv2.1-CHO cells without any GxTX present: $V_{1/2}$ = −26 mV, z = 1.6 e_0 (320). These results suggest that at 9 nM GxTX–594, the *F–V* appears to be a good surrogate for the gating current–voltage (*Q–V*) response of unlabeled Kv2 channels.

To determine the voltage dependence of the kinetics of GxTX–594 labeling and unlabeling, $k_{\Delta F}$ was compared at varying step potentials. $k_{\Delta F}$ was quantified by fitting the average fluorescence from voltage-clamped cells with a monoexponential function. In response to voltage steps from a holding potential of −80 mV to more positive potentials, $k_{\Delta F}$ increased progressively as step potential was increased above −40 mV and appeared to begin to saturate at higher voltages (Fig. 2.4E). Upon return to −80 mV, $k_{\Delta F}$ was similar to −40 mV. While the $k_{\Delta F}$ did not clearly display saturation at positive voltages that would justify fitting with a Boltzmann function, a model of GxTX594 dynamics, which we develop later in this study, indicated that Boltzmann fitting could yield physical insight (Fig. 2.4E, bottom panel, black line). We noted that the degree of variability in $k_{\Delta F}$ measurements became greater at more positive

potentials (Fig. 2.4E, top and bottom panels). At −80 mV, there was a twofold range in $k_{\Delta F}$ values and a ninefold range at +80 mV. The relatively low variation in $k_{\Delta F}$ at −80 mV suggests that despite variance in fluorescence intensity after rebinding, $k_{\Delta F}$ from fits of the upward relaxation at −80 mV are relatively consistent. The average $k_{\Delta F}$ equilibration at 10 nM GxTX–594 in concentration–effect experiments was comparable to Kv2.1-CHO cells incubated in 9 nM GxTX–594 and voltage clamped at −80 mV (0.0011 s^{-1} and 0.0014 s^{-1}, respectively; Supplemental Fig 2.5). This suggests that the Kv2 voltage sensors in the unclamped cells for concentration–effect experiments are in the same early resting conformation as voltage-clamped cells at −80 mV.

The relation between voltage sensor activation and GxTX-594 dynamics can be recapitulated by rate theory modeling

To enable translation of the intensity of fluorescence from GxTX–594 on a cell surface into a measure of Kv2 conformational change, we developed a model, a series of equations derived from rate theory that relate cell labeling to voltage sensor activation. The framework of the model is generalizable to fluorescent molecular probes that report conformational changes by a change in binding affinity. In the model, the proportion of labeled versus unlabeled Kv2 in a membrane is determined by the proportion of voltage sensors in resting versus activated conformations. The model assumes that the innate voltage sensitivity of the Kv2 subunit is solely responsible for controlling voltage dependence. GxTX labeling is voltage dependent because the binding and unbinding rates are different for resting and activated conformations of voltage sensors. Voltage activation of Kv2 channels involves many conformational changes (320, 333, 334). However, models that presume independent activation of a voltage sensor in each of the four Kv2.1 subunits accurately predict many aspects of voltage activation and voltage sensor toxin binding (320, 335). For simplicity, we model Kv2 proteins as having only resting and activated conformations that are independent in each voltage sensor and developed a rate theory model consisting of four interconnected states (Fig. 2.5, Scheme 1).

When voltage sensors change from resting to activated conformations, the binding rate of the GxTX–594 decreases, and the unbinding rate increases. When the membrane voltage is held constant for sufficient time, the proportions of labeled and unlabeled proteins reach an equilibrium. GxTX–594 labeling requires seconds to equilibrate (Fig. 2.4), whereas Kv2 channel gating equilibrates in milliseconds (320), three orders of magnitude more quickly. These distinct time scales of equilibration suggest an approximation to model the reversible GxTX–594 labeling response: voltage sensor conformations achieve equilibrium quickly such that only their distribution at equilibrium is expected to greatly impact the kinetics of labeling and unlabeling, allowing Scheme 1 to collapse into Scheme 2 (Fig 2.5), which depicts the structure of the GxTX–594 model used for calculations.

We constrained the GxTX–594 model with measurements of GxTX–594 binding kinetics and GxTX impacts on Kv2.1 gating (see Fig 2.6 and Table 2.1). We tested the viability of model predictions by comparison with GxTX–594 labeling measurements. The model predicts that the *F–V* for GxTX–594 labeling will conform to a Boltzmann distribution. The *F–V* prediction in 9 nM GxTX–594 had a $V_{1/2}$ and z that differ by only −4 mV and 0.06 e_0, respectively, from the Boltzmann fit of experimental data (Fig. 2.4D, bottom panel, black and green lines). The model also predicts that the $k_{\Delta F}$–*V* will conform to a Boltzmann distribution. The $k_{\Delta F}$–*V* prediction differs by only 3 mV and 0.05 e_0 from the Boltzmann fit of experimental data (Fig. 2.4E, bottom panel, black line). However, this fit was poorly constrained as we failed to obtain sufficient data at voltages above +80 mV where $k_{\Delta F}$–*V* is predicted to saturate. In our attempts, the durations required at more positive voltages irreversibly increased membrane leak. The $V_{1/2}$ and z values from the GxTX–594 *F–V* and $k_{\Delta F}$–*V* were not used as constraints of the model, and the similarity between the predictions and empirical findings seemed remarkable enough to warrant further exploration of the model predictions.

We used the model to investigate general principles of the relation between voltage sensor activation and reversible labeling. The model predicts that as GxTX–594 concentration decreases, the

change in labeling ($\Delta F/\Delta F_{Max}$) approaches the probability that unlabeled voltage sensors are resting (Fig. 2.6A). This prediction explains the similarity between the *F–V* in 9 nM GxTX–594 ($V_{1/2}$ = −27 ± 3mV, z = 1.4 ± 0.1 e_0; Fig. 2.4D) and the *Q–V* of Kv2.1 ($V_{1/2}$ = −26 ± 1 mV, z = 1.6 ± 0.1 e_0; (320)). As the concentration of GxTX–594 is increased, the *F–V* shifts to more positive voltages such that the fractional change in fluorescence intensity is always less than the fraction of unlabeled voltage sensors that are active. As GxTX–594 concentration increases and approaches the activated state K_d (1790 nM), voltage sensor activation becomes less effective at dissociating GxTX–594 due to binding to activated voltage sensors (Fig. 2.6B). The model predicts that at any concentration, this simple interpretation will be valid: A decrease in GxTX–594 surface fluorescence indicates activation of unlabeled voltage sensors.

The model also yields a simple interpretation of labeling kinetics, it predicts that as GxTX–594 concentration decreases, the rate of fluorescence change ($k_{\Delta F}$) approaches the probability that labeled channels are active (Fig. 2.6C). This prediction explains the similarity between the $k_{\Delta F}$–*V* in 9 nM GxTX–594 ($V_{1/2}$ = 38 ± 15 mV, z = 1.4 ± 0.4 e_0; Fig. 2.4D) and the *Q–V* of Kv2.1 in saturating GxTX ($V_{1/2}$ = 47 ± 1 mV, z = 1.6 ± 0.1 e_0; (320)). At low concentrations, the dependence of $k_{\Delta F}$ on the conformation of channels bound to GxTX594 is due to the rate of unbinding dominating $k_{\Delta F}$, with the rate of unbinding being solely determined by the conformation of channels bound to GxTX–594.

GxTX–JP labels Kv2 proteins

To measure voltage-dependent Kv structural changes in live cell membranes, we synthesized conjugates of GxTX-1E with a novel far-red fluorophore whose emission is responsive to changes in the polarity of its environment. Single substitutions with the alkynyl amino acid propargylglycine (Pra) were introduced at Ser13 and Lys27 positions of GxTX for fluorophore conjugation by Cu-catalyzed click chemistry (336). To conjugate to these alkynyl toxins, azide-functionalized fluorophores were synthesized (Fig. 2.7) with an aminophenoxazone (AP) ring system, which has shown large polarity-based spectral

shifts both in vitro and when conjugated to membrane proteins (331). To reduce rotation of the exocyclic nitrogen, which reduces fluorophore brightness and stability, the dimethylamine of AP was replaced with the julolidine ring system found in Texas Red (337).

To assess whether JP−GxTX conjugates are able to selectively label endogenous Kv2 channels, we stained dissociated rat hippocampal neurons with Lys27Pra(JP) GxTX (Fig. 2.8A). JP fluorescence is observed in clusters in the plasma membrane surrounding neuronal cell bodies and proximal dendrites, consistent with known patterns of Kv2.1 localization (338). Kv2.1-specific JP fluorescence was also observed in Kv2.1-expressing Chinese hamster ovary (CHO) cells co-plated with Kv2-free CHO cells and treated with JP conjugated at Ser13 and Lys27 (322). JP emission appears predominantly as clusters at the glass-adhered basal surface, which is a hallmark of Kv2.1 channel localization in neurons and other mammalian cells grown on glass (242, 243).

Spectra of resting cells stained with JP−GxTX conjugates were fit using split pseudo-Voigt functions, which are commonly used to fit asymmetric peak shapes (339, 340). Full JP emission spectra from resting CHO cells (Fig. 2.8C) show that JP conjugates at Ser13 have emission peaks of ~650 nm, consistent with JP−GxTX conjugates in buffer (Fig. 2.8D) and aqueous localization of AP fluorophores on membrane proteins (331). Relative to these aqueous JP conjugates, the emission peak from GxTX Lys27Pra(JP) is blue-shifted by 40 nm, similar to nonpolar environments like hydrocarbon solvents (322). In cell membranes without Kv2 channels, GxTX Lys27Pra(JP) emission is ~50-fold weaker and significantly red-shifted compared to membranes with Kv2.1 (Fig. 2.8D). My colleague also observed that GxTX Lys27Pra(JP) washes out far more slowly than unlabeled GxTX from resting Kv2.1-expressing cells (322). At a holding potential of −100 mV, the channels are in resting states, and the affinity of this JP conjugate is 3-fold higher than that of unlabeled GxTX. A Rosetta-generated homology model of the Kv2.1 VSD in its activated state in complex with GxTX shows the Lys27 side chain residing in the polar

region of the membrane adjacent to S4, sitting within roughly 8 A° of Arg296 and Arg299 (termed R2 and R3, based on homology to Shaker Kv channels) (322).

GxTX Lys27Pra(JP) tracks voltage-dependent conformational changes

To determine the voltage-dependent changes in the GxTX–voltage sensing domain structure, my colleagues measured full emission spectra from Lys27Pra(JP) on Kv2.1-expressing cells at membrane potentials from −100 to +100 mV (Fig. 2.9). Unlike GxTX conjugates with lipophobic fluorophores (341), there was no substantial dissociation of Lys27Pra(JP) from cell membranes in response to the 1−5 s depolarization steps for spectral measurement, consistent with its slow k_{off} rate (322). Raw emission data were fitted with split pseudo-Voigt functions, with 2-component fits more accurate than single component fits or other line shape functions. At all voltages, fit functions consistently show nonpolar (~610 nm) and polar (~640 nm) peaks, with gradual increases in the polar component as the voltage sensing domain moves from its resting to activated states (322). This suggests that multiple JP−GxTX–voltage sensing domain species are present and that depolarization changes the dominant JP species from a lipid/protein environment to a more polar one (although less polar than the fully aqueous positions in Fig. 2.8). In contrast to GxTX Lys27Pra(JP), emission maxima of JP−GxTX conjugates substituted at Lys10 or Ser13 show no significant voltage dependence (322). Control cells not expressing Kv2 channels showed weaker GxTX Lys27Pra(JP) emissions that are also independent of voltage. These emissions are not satisfactorily fit by 2-component split pseudo-Voigt functions, suggesting nonspecific interactions with cell membranes (325). We emphasize that the 2-component fits are optimal line shapes for the data but do not necessarily mean there are exactly 2 species or that the weightings of the fit components reflect percentages of particular conformations.

GxTX Lys27Pra(JP) tracks conformational changes that occur before gating charge movement

To better understand the conformational changes of the GxTX-voltage sensing domain complex, we compared voltage-dependent changes in GxTX Lys27Pra(JP) fluorescence with Kv2.1-gating currents

that I recorded (Fig. 2.9). Mean emission spectra calculated from integrations of 2-component fittings show a red shift fit well by a two-state Boltzmann function with a midpoint ($F_{1/2}$) of −15 mV and that plateaus above +40 mV. This two-state Boltzmann function may hide more subtle transitions within the data but is better constrained than more complex functions. By comparison, gating currents (Q_{OFF}) of the Kv2.1-Lys27Pra(JP) GxTX complex, which reflect the activation of S4 and movement of its 3 Arg through the membrane electric field, have a midpoint of +36 mV, similar to those of Kv2.1 with unlabeled GxTX (320, 322). At the $F_{1/2}$ of −15 mV, Q_{OFF} is at ~5% of its maximal value. This large discrepancy between voltage-dependent fluorescence shifts and gating currents suggests a complex voltage sensing domain allostery. While high-resolution resting state Kv channel structures have not been reported, one structural hypothesis for this voltage sensing domain allostery that the solvatochromic shift of Lys27Pra(JP) GxTX emission occurs at voltages far more negative than the majority of Kv2.1-gating currents (Fig. 2.9) or subsequent channel opening, suggesting that the conformational changes that alter the chemical environment of the JP are early voltage sensor domain motions in the closed channel. The mean emission wavelength plateaus by +40 mV, giving no indication of a component corresponding to the +37 mV midpoint of Q_{OFF} and suggesting that the conformational changes at the GxTX-voltage sensing domain interface are distinct from later S4 motions.

Discussion

The molecular targeting, conformation selectivity, and spatial precision of fluorescence from GxTX tools enable identification of where, both in tissue and cells, the conformational status of Kv2 voltage sensors becomes altered. However, the utility of GxTX-based tools is limited by several factors including emission intensity, variability between experiments, and inhibition of Kv2 proteins. We also discuss the potential utility and limitations of the model for Kv2 activity reporting by GxTX unlabeling.

Unique capabilities of GxTX-based tools

GxTX-based tools offer the only imaging method we are aware of for measuring voltage-sensitive conformational changes of a specific, endogenous protein. As GxTX binding selectively stabilizes the fully resting conformation of Kv2.1 voltage sensors , reversible GxTX labeling is expected to bind with highest affinity specifically to the fully resting conformation of the Kv2 voltage sensor, in which the first gating charge of the Kv2 S4 segment is in the gating charge transfer center (302). Images of GxTX–594 and GxTX–JP fluorescence reveal this conformation's occurrence, with subcellular spatial resolution. Importantly, the model we develop for GxTX–594 dynamics allows deconvolution of the behavior of unlabeled Kv2 proteins. This enables the subcellular locations where Kv2 voltage sensing occurs to be seen for the first time.

Since the original Hodgkin and Huxley description of voltage-gated K^+ channel gating in squid giant axons, channels have been proposed to adopt multiple conformations before opening in response to depolarizing voltage stimuli (342). Over half a century later, advances in membrane protein X-ray crystallography and single particle cryo-EM have enabled determination of full structures of voltage-gated K^+ channels (296, 302, 343) and analogous voltage-gated channels (159, 184) which have offered insight into the allostery of voltage gating. While structures of channels that are gated or modulated by ligands can be determined in apo and ligand-bound states, channels that are gated primarily by voltage

present an added challenge of determining the corresponding physiological state of a particular structure in the absence of functional cell membranes with clearly defined potentials. For example, in cryo-EM analysis of Nav1.7 bound to the GMT ProTxII, the "deactivated" structure may show a partially or fully down S4 (159), but these cannot be distinguished on the basis of structure alone. For these and Kv structures, making sense of conformational heterogeneity and dynamics requires novel techniques able to characterize channel allostery with correlated electrophysiological recording in live cell membranes. The observed voltage-dependent solvatochromic shifts (Fig. 2.9) demonstrate that JP-conjugated GxTX (GxTX Lys27Pra(JP)) detects conformational changes in the Kv2.1−GxTX complex.

Electrophysiological approaches can detect the voltage-sensitive K^+ conductance of Kv2 channels. However, the majority of Kv2 proteins on cell surface membranes do not function as channels and are nonconducting (344, 345), and Kv2 proteins dynamically regulate cellular physiology by nonconducting functions(242, 243, 338, 346–350). GxTX tools reports on the conformation of Kv2 voltage sensors independently from ion conductance, enabling the study of voltage sensor involvement in Kv2's nonconducting physiological functions.

During our initial testing of GxTX–594, we observed that the majority of Kv2 protein detected at discrete individual clusters was voltage sensitive. While it may not sound surprising to find that voltage-gated ion channel proteins are voltage sensitive, the voltage sensors of surface-expressed proteins can be immobilized. For example, gating charge of the L-type Ca^{2+} channel Cav1.2 is immobilized until it is bound by an intracellular protein (351). Kv2.1 channel function is extensively regulated by neurons. In rat CA1 neurons the clustered Kv2 channels are proposed to be nonconducting (352). Our results show that clustered Kv2 proteins in rat CA1 neurons remain voltage-sensitive. Interestingly, when Kv2.1 is expressed in CHO cells, a fraction of the GxTX–594 fluorescence is voltage insensitive. This observation is consistent with voltage sensor immobilization of some surface-expressed Kv2.1 protein, although it could be due to intracellular Kv2.1–GxTX–594 proteins that appear to be at the cell surface.

We used images of GxTX–594 fluorescence to measure the coupling between endogenous Kv2 proteins and membrane potential at specific, subcellular anatomical locations. Similarly, GxTX–594 imaging should detect changes of voltage sensor status when Kv2 proteins become engaged or disengaged from nonconducting functions such as formation of plasma membrane–endoplasmic reticulum junctions (243, 338, 348), regulation of exocytosis (346, 347), regulation of insulin secretion (353), interaction with kinases, phosphatases and SUMOylases (23, 354–357), formation of specialized subcellular calcium signaling domains (350), and interactions with astrocytic end feet (16). GxTX–594 could potentially reveal conformational changes in organs throughout the body where Kv2 proteins are expressed, which include muscle, thymus, spleen, kidney, adrenal gland, pancreas, lung, and reproductive organs (310).

Limitations of GxTX-based tools

There are important limitations to the GxTX approach, and of the underlying mechanism generally. We discuss several limitations which are worth considering in the design of any studies with GxTX-based tools.

GxTX–594 labeling is slower than channel gating and GxTX Lys27Pra(JP) measures conformational changes that occur prior to gating

The kinetics of reversible GxTX–594 labeling are limited to measuring changes in Kv2 activity on a time scale of tens of seconds. While the temporal resolution of GxTX–594 is compatible with live imaging and electrophysiology experiments, labeling kinetics do not provide sufficient time resolution to distinguish fast electrical signaling events. The response time of GxTX–594 is far slower than the kinetics of Kv2 conformational change, limiting measurements to the probability, averaged over time, that voltage sensors are resting or active. It is worth noting that the probability of a conformation's occurrence can be

a valuable measure, and is the ultimate quantitation of many biophysical studies of ion channels (e.g., open probability, steady state conductance and gating charge-voltage relation).

GxTX Lys27Pra(JP) however is not limited by labeling kinetics and instead is limited by the fundamental limits of obtaining spectral images with appropriate resolution for necessary deconvolution of the voltage-induced spectral shift. With the advent of dyes with greater polarity sensitivities that require less spectral resolution for deconvolution and faster imaging technologies, this limit will decrease. Yet, the conformational state information that can be gleaned from GxTX–JP tools is limited by where JP can be conjugated to GxTX without reducing GxTX activity and by where JP localizes with respect to the channel. For instance, GxTX Lys27Pra(JP) only detects early conformational changes that occur prior to gating charge translocation. If other transitions were to be detected, a whole different GxTX–JP would have to be designed and validated.

GxTX-594 dynamics are variable between CHO cells

The variability of GxTX–594 response rates and amplitudes and GxTX–JP spectral profiles between CHO cells limited the precision of results. Some of this variability is expected from technical imprecisions: fits poorly approximating the data, small changes due to variations of room temperature, photobleaching, and other potential sources. However, we often found that results were more consistent between stimuli of the same cell and the variability was greatest between cells. We suspect that cell-to-cell differences in Kv2.1 conformational equilibria are responsible for much of the variability in GxTX responses. The Kv2.1 conductance-voltage relation is regulated by many cellular pathways including kinases, phosphatases, and SUMOylases (23, 354, 355, 357, 358). Large cell-to-cell variation in Kv2.1 conductance-voltage, and gating charge-voltage relations have been reported in CHO cells by our group and others (320, 341, 359, 360). For instance, in the GxTX–594 study, when we predicted the voltage sensor $V_{1/2}$ of Kv2.1 from electrophysiology, we observed a 6.4 mV standard deviation with a range of 19

mV, and this variance appeared to be exacerbated by GxTX–594 having a 9.7 mV standard deviation and range of 36 mV (Fig 2.3). A similar increase in standard deviation with GxTX Lys27Pra(JP) was seen in *F–V* measurements. As GxTX dynamics and the *G–V* are both determined by voltage sensor activation, variability in the GxTX response is expected.

The hypothesis that cell-to-cell variation in fluorescence dynamics is due to the inherent variability of Kv2.1 voltage sensor activation could be more definitively tested by identifying if a correlation exists between the $V_{1/2}$ of the *Q–V* and fluorescence–voltage relationship from individual cells labeled with GxTX-based tools. While we have not attempted this, the structure of the variance in GxTX–594 fluorescence–voltage relationships is informative. For instance, the fluorescence–voltage relationships compiled from many cells exposed to GxTX–594 become more variable near the midpoint of relevant voltage sensor movements. The response amplitude, F/F_{init}, (Fig. 2.4D), is determined by unlabeled voltage sensor activation, and appears most variable near the $V_{1/2}$ of the unlabeled *QV* relation, -32 mV (320). The response kinetics, $k_{\Delta F,}$ are determined by activation of voltage sensors which have GxTX–594 bound and appear to become increasingly variable at voltages higher than -20 mV (Fig. 2.4E bottom panel). Despite this variability, the $V_{1/2}$ and *z* from the Boltzmann fit of the $k_{\Delta F}$–*V* relationship from many cells were remarkably close to the *Q–V* of the GxTX–Kv2.1 complex with a $V_{1/2}$ and *z* that differ by 3.3 mV and 0.07 e_0 respectively (320).

Fluorescence Intensity

Optical noise limits interpretation of GxTX imaging. Though the GxTX–594 signal from CA1 neurons was sufficient to identify voltage sensing of endogenous Kv2 protein (321), fluorescence signal to noise issues limit interpretation with all GxTX-based tools. This signal to noise ratio is influenced by the density of GxTX binding sites, the fluorescence intensity from each binding site, characteristics of the imaging system, and background fluorescence from unbound GxTX molecules or other sources. As the concentration of fluorophore is lowered, background fluorescence from unbound GxTX molecules will

decrease, and the percentage of labeled binding sites will decrease. In theory, fluorescence measurements from a single GxTX molecule immobilized by binding to a single voltage sensor could be informative, as fluorescence from a single binding site is eliminated altogether after unbinding and diffusion away. Yet, we have not been able to obtain single molecule resolution, so the density of EVAP binding sites can limit the signal to noise.

CA1 hippocampal neurons express Kv2 proteins at a density typical of central neurons (23, 25, 361), and we expect that GxTX-594 imaging will have similar signal to noise characteristics in most brain regions. Improved signal to noise would be expected from such cells that express higher densities of Kv2 proteins, such as neurons of the subiculum, or the inner segment of photoreceptors (13). Kv2 proteins are also expressed by many other cell types throughout the body (310), where GxTX labeling techniques may reveal Kv2 activity, if protein densities are sufficient.

GxTX-594 inhibits Kv2 proteins

GxTX-based probes inhibit the Kv2 proteins they label by stabilizing the resting conformation of Kv2 voltage sensors. The Kv2.1–GxTX complex does not open to conduct K^+ ions in the physiological voltage range (Fig. 2.3). Thus, GxTX depletes the population of Kv2 proteins responding normally to physiological stimuli, which could alter Kv2 signaling. The concentration of GxTX can be lowered such that only an inconsequential minority of proteins are bound, with the trade-off being dimmer fluorescence. With a related probe, we explored the impact of decreasing concentration on fluorescence response of a GxTX-based tool, and saw substantial fluorescence responses to voltage while inhibiting only ~10% of Kv2.1 current (341). Here, we demonstrate that lower concentration and physiological stimuli are not always required for scientifically meaningful implementation of a GxTX-based tool. Even when GxTX inhibits most Kv2 proteins, the behavior of unlabeled Kv2 proteins can be calculated using

the model we have developed. Of course, the electrical feedback within cells will be altered by such protocols.

The GxTX model is oversimplified

Another limitation of the analysis developed here is that the model of Kv2 voltage sensor conformational change is an oversimplification. The gating dynamics of Kv2 channels are more complex than our model (299, 320, 333, 334). Under some conditions the assumption of voltage sensor independence will limit the model's predictive power.

Conformation-selective probes reveal conformational changes of endogenous proteins

Measurements of dynamic reversible labeling by a conformation-selective probe such as GxTX-594 can enable deduction of how unlabeled proteins behave. This is perhaps counterintuitive because GxTX inhibits voltage sensor movement of the Kv2 protein it binds, and thus only bound proteins generate optical signals. This approach is analogous to calcium imaging experiments, which have been spectacularly informative about physiological calcium signaling (362), despite the fact that no optical signals originate from the physiologically relevant free Ca^{2+}, but only from Ca^{2+} that is chelated by a dye. In all such experiments, fluorescence from Ca^{2+}-bound dyes is deconvolved using the statistical thermodynamics of Ca^{2+} binding to calculate free Ca^{2+}. Similarly, GxTX-based probes dynamically bind to unlabeled Kv2 proteins, and the binding rate is dependent on the probability that unlabeled voltage sensors are in a resting conformation (Fig. 2.6). Thus, the conformations of unlabeled Kv2 proteins influence the dynamics of labeling with GxTX-based probes. Consequently, the dynamics of labeling reveal the conformations of unlabeled Kv2 proteins.

Deployment of GxTX-based tools to report conformational changes of endogenous proteins demonstrates that conformation-selective ligands can be used to image occurrence of the conformations they bind to. The same principles of action apply to any conformation-selective labeling reagent,

suggesting that probes for conformational changes of many different proteins could be developed. Probes could conceivably be developed from the many other voltage sensor toxins or other gating modifiers that act by a similar mechanism as GxTX, yet target the voltage sensors of different ion channel proteins (323, 363–365). Conformation-selective binders have been engineered for a variety of other proteins, and methods to quantify conformational changes from their fluorescence are needed. For example, fluorescently-labeled conformation-selective binders have revealed that endocytosed GPCRs continue to remain in a physiologically activated conformation. A means to determine the conformational equilibria of GPCRs from fluorescence images has not yet been developed. We suggest that the statistical thermodynamic framework developed here could provide a starting point for more quantitative interpretation of other conformation-selective molecular probes.

Acknowledgements

I thank Jim Trimmer (University of California, Davis) for numerous discussions, and constructive critical reading of an early version of the manuscript. I thank Georgeann Sack (Afferent LLC) for critical reading, editing, and feedback. This research was supported by US National Institutes of Health grants R01NS096317 (JTS, BEC), U01NS090581 (JTS), R21EY026449 (JTS), R01NS062736 (KZ), U01NS103571 (KZ), T32GM007377 (RJS), and American Heart Association 17POST33670698 (PT). GxTX variants were synthesized at the Molecular Foundry, supported by the Director, Office of Science, Office of Basic Energy Sciences, Division of Materials Sciences and Engineering, of the U.S. Department of Energy under contract DE-AC02-05CH11231.

I thank Victor Mann and Robert Stewart for helpful discussions, Kenneth Eum, Mark Lillya, and Michael Kirmiz for contributions to the early phases of this project, and Olivia Buonarati in the laboratory of Mary Horne and Johannes Hell for preparation of dissociated hippocampal neurons. This work was supported by National Institutes of Health award R01NS096317 (B.E.C. and J.T.S.), R21EY026449 (J.T.S), T32GM007377 (R.J.S.), F31NS108614 (R.J.S.), the UC Davis Senate (J.T.S), and American Heart Association award 17POST33670698 (P.T.). Work at the Molecular Foundry was supported by the Director, Office of Science, Office of Basic Energy Sciences, Division of Materials Sciences and Engineering of the U.S. Department of Energy under Contract No. DE-AC02- 05CH11231.

Methods and Materials

GxTX–594 synthesis

We used solid-phase peptide synthesis to generate a variant of GxTX, an amphiphilic 36-amino acid cystine knot peptide. We synthesized the same peptide used for GxTX–550, GxTX Ser13Cys, where a free thiolate side chain of cysteine 13 is predicted to extend into extracellular solution when the peptide is bound to a voltage sensor (341). GxTX–1E folds by formation of three internal disulfides, and cysteine 13 was differentially protected during oxidative refolding to direct chemoselective conjugation. Following refolding and thiol deprotection, Alexa Fluor 594 C_5 maleimide was condensed with the free thiol, and Ser13Cys (Alexa Fluor 594) GxTX–1E (called GxTX–594) was purified.

The Ser13Cys GxTX peptide was synthesized as previously described (341). Methionine 35 of GxTX was re-placed by the oxidation-resistant noncanonical amino acid norleucine to avoid complications from methionine oxidation, and serine 13 was replaced with cysteine to create a spinster thiol. GxTX Ser13Cys was labeled with a Texas Red derivative (Alexa Fluor 594 C_5 maleimide, cat. #10256; Thermo Fisher Scientific) to form GxTX-594. Ser13Cys GxTX lyophilisate was brought to 560 μM in 50% acetonitrile (ACN) + 1 mM Na_2EDTA. 2.4 μl of 1M Tris (pH 6.8 with HCl), 4 μl of 10 mM Alexa Fluor 594 C_5 maleimide in DMSO, and 17.9 μl of 560 μM Ser13Cys GxTX were added for a final solution of 100 mM Tris, 1.6 mM Alexa Fluor 594 C_5 maleimide, and 0.4 mM GxTX in 24 μl of reaction solution. Reactants were combined in a 1.5-ml low- protein–binding polypropylene tube (LoBind, cat. #022431081; Eppendorf) and mixed at 1,000 rpm at 20°C for 4 h (Thermo-mixer 5355 R; Eppendorf). After incubation, the tube was centrifuged at 845 RCF for 10 min at room temperature. A purple pellet was observed after centrifugation. The supernatant was transferred to a fresh tube and centrifuged at 845 RCF for 10 min. After this second centrifugation, no visible pellet was seen. The supernatant was injected onto a reverse-

phase HPLC C18 column (Biobasic 4.6-mm RP-C18 5 μm, cat. #2105-154630; Thermo Fisher Scientific) equilibrated in 20% ACN, 0.1% trifluoroacetic acid (TFA) at 1 ml/min, and eluted with a protocol holding in 20% ACN for 2 min, increasing to 30% ACN over 1 min, then increasing ACN at 0.31% per minute. HPLC effluent was monitored by fluorescence and an absorbance array detector. 1-ml fractions were pooled based on fluorescence (280-nm excitation, 350-nm emission) and absorbance (214 nm, 280 nm, and 594 nm). GxTX–594 peptide–fluorophore conjugate eluted at ~35% ACN, and mass was confirmed by mass spectrometry using a Bruker ultrafleXtreme matrix-assisted laser desorption ionization time-of-flight (MALDI-TOF; Fig. 2.1). Samples for identification from HPLC eluant were mixed 1:1 in an aqueous solution of 25% MeOH and 0.05% TFA saturated with α-cyano-4- hydrocinnamic acid, pipetted onto a ground-steel plate, dried under vacuum, and ionized with 60–80% laser power. Molecular species were detected using a reflector mode protocol and quantitated using Bruker Daltonics flexAnalysis 3.4 software. Lyophilizate containing GxTX–594 conjugation product was dissolved in cell external (CE) buffer (defined below) and stored at −80°C. GxTX–594 concentration was determined by 280-nm absorbance using a calculated molar attenuation coefficient of 18,900 $M^{-1}cm^{-1}$.

CHO cell culture and transfection for gating current and ionic current recordings

The CHO-K1 cell line (American Type Culture Collection) and a subclone transfected with a tetracycline-inducible rat Kv2.1 construct (Kv2.1-CHO; (366)) were cultured as described previously (341). To induce Kv2.1 expression in Kv2.1-TREx-CHO cells, 1 μg/ml minocycline (cat. #ALX-380-109-M050; Enzo Life Sciences), prepared in 70% ethanol at 2 mg/ml, was added to the maintenance media to induce Kv2.1 expression. Minocycline was added 40–48 h before imaging and voltage-clamp fluorometry experiments. Minocycline was added 1–2 h before whole-cell ionic current recordings to limit K^+ conductance such that voltage clamp could be maintained.

Kv2.1 ionic current recordings with GxTX–594

Prior to patching, Kv2.1-CHO cells were washed in divalent-free PBS and then harvested in Versene (cat. #15040066; Gibco-BRL). Cells were scraped and transferred to a polypropylene tube, pelleted, and washed three times at 1,000 g for 2 min and then resuspended in the same external solution as used in the recording chamber bath. Cells were rotated in a polypropylene tube at room temperature (22–24°C) until use. Cells were then pipetted into a 50-µl recording chamber (RC-24N; Warner Instruments) prefilled with external solution and allowed to settle for ≥5 min. After adhering to the bottom of the glass recording chamber, cells were thoroughly rinsed with external solution using a gravity-driven perfusion system. Cells showing uniform intracellular GFP expression of intermediate intensity were selected for patching.

Voltage clamp was achieved with a patch clamp amplifier (Axon Axopatch 200B; Molecular Devices) run by Patchmaster software. Borosilicate glass pipettes (BF150-110-7.5HP; Sutter Instruments) were pulled with blunt tips, coated with silicone elastomer (Sylgard 184; Dow Corning), heat cured, and tip fire-polished to resistances <4 MΩ. Capacitance and ohmic leak were subtracted using a P/5 protocol. Recordings were low-pass filtered at 10 kHz using the amplifier's built-in Bessel function and digitized at 100 kHz.

For whole-cell ionic current measurements in Kv2.1-CHO cells, the external patching solution contained (in mM) 3.5 KCl, 155 NaCl, 10 HEPES, 1.5 CaCl2, and 1 MgCl2, adjusted to pH 7.4 with NaOH. The internal (pipette) solution contained (in mM) 70 KCl, 5 EGTA, 50 HEPES, 50 KF, and 35 KOH, adjusted to pH 7.4 with KOH. The osmolality was 315 mOsm/liter for the external solution and 310 mOsm/liter for the internal solution measured by a vapor pressure osmometer. Following establishment of the whole-cell seal, ionic K+ current recordings were taken in the presence of a vehicle, which consisted of 100 nM tetrodotoxin, 10 mM glucose, and 0.1% BSA prepared in external solution. Cells were held at

−100 mV with channel activation steps ranging from −80 mV to +120 mV in increments of +5 mV (100 ms) before being returned to 0 mV (100 ms) to record tail currents. The intersweep interval was 2 s. To determine the bioactivity of GxTX594, Kv2.1 ionic currents were recorded once more, 5 min following the wash-in of bath solution also containing 100 nM GxTX–594. Wash-ins were performed while holding at −100 mV; 100 μl was washed through the chamber and removed distally through vacuum tubing to maintain constant bath fluid level.

Ionic current analysis

The average current in the 100 ms before voltage step was used to zero subtract the recording. Outward current taken as the mean value between 90 and 100 ms of the channel activation step was used to calculate and correct for series resistance-induced voltage error. Tail current values were derived from the mean value between 0.2 and 1.2 ms of the 0-mV tail current step. Tail current was normalized by the mean activation step current from 50 to 80 mV and plotted against the estimated membrane potential, which had been corrected for voltage error and the calculated liquid junction potential of 8.5 mV. These tail $G–V$ plots were fit with a fourth-power Boltzmann function (364), and the fit parameters were used for statistical analysis.

Gating Current Measurements with GxTX Lys27Pra(JP)

Channel expression was achieved by 48 h incubation with minocycline during culture. The external gating current recording solution contained 150 mM TEA-Cl, 41 mM HEPES, 1 mM MgCl2·6H2O, 1.5 mM CaCl2, adjusted to pH 7.3 with NMDG; measured osmolarity was 311 mOsm. The internal (pipette) solution contained 90 mM NMDG, 1 mM NMDG-Cl, 50 mM HEPES, 5 mM EGTA, 50 mM NMDG-F, 0.01 mM CsCl, adjusted to pH 7.4 with methanesulfonic acid, with a measured osmolarity of 303 mOsm. To avoid monovalent cation contamination of the recording solution, the pH was

determined from small aliquots that were discarded. Osmolarity was measured with a VAPRO vapor pressure osmometer 5520. Recording pipettes were pulled from thin-walled borosilicate glass (1.5 mm outer diameter, 1.1 mm inner diameter, with filament; Sutter Instruments). Pipette resistances with gating current solutions were 6−14 MΩ. Cultured cells were dissociated with 0.48 mM EDTA in PBS for 30 s and then harvested by scraping. Cells were pelleted by centrifugation (2 min × 1500g) and washed three times in NE. Following the final pelleting, cells were resuspended in the gating current external solution and left to sit in a 1.5 mL polypropylene tube. Prior to patching, 100 μL of cell suspension was added to the <100 μL recording chamber (Warner R-24N). Cells were given 4 min to adhere before gently washing with 10 mL of the gating current recording solution to dilute any monovalent cation contamination. GxTX Lys27Pra(JP) (100 μL of 100 nM) with 1% BSA was pipetted into the bath with vacuum line suctioning of the fluid surface to maintain constant bath volume. Seals with GΩ resistances were formed either before (n = 3) or after (n = 2) the addition of toxin. In all cases, the cell was incubated in GxTX Lys27Pra(JP) for at least 4 min before the gating current measurements were recorded. Patched cells were stepped from a −100 mV holding potential to the indicated potential for 100 ms and then to −140 mV to record OFF gating currents. Cell series resistances were 14−30 MΩ (before compensation), and 50% compensation was used when series resistance exceeded 10 MΩ. Cell capacitances were 6−10 pF. Remaining capacitance and ohmic leak were subtracted offline using the average of five traces recorded during P/5.9 voltage protocols from a −133 mV holding potential. In sequences of voltage steps, at least 2 s elapsed between the start times of each recording. Q_{off}-gating charge movement was quantified by integrating the area under the OFF-gating currents in a 10.5 ms window following the end of any obvious fast capacitative artifacts created from the voltage step to −140 mV. Currents were baseline-subtracted with the average current elicited during a 10 ms long period after current decay had ceased. This window began 10 ms following the −140 mV voltage step stimuli. Each Q_{off} curve was normalized using the average Q_{off} value elicited with 100−120 mV steps. The mean of the normalized data set is plotted with the standard error of

the mean, which was computed following normalization. Fitting with a Boltzmann distribution was as described previously, where V_{Mid} is the voltage where the function reaches half maximal conductance and z is valence in units of elementary charge (e_0). The calculated liquid junction potential of 13.5 mV between bath and pipette was corrected post hoc.

Hippocampal Neuron Imaging with GxTX Lys27Pra(JP)

All animal procedures were approved by the University of California at Davis Animal Care and Use Committee following NIH guidelines. Dissociated hippocampal neurons were prepared from embryonic day 18 rats of both sexes (Sprague−Dawley, Charles River Laboratories) as described previously (367).). Surface localization of Kv2.1 protein in similar cultures has been found to be maximal after 2 weeks in vitro (338), and neurons were imaged after 17 days. Neurons were rinsed with NEG solution and imaged during incubation at room temperature in NEGB with 100 nM GxTX Lys27Pra(JP) (from 73 μM stock) and 200 nM tetrodotoxin (diluted from a 10 mM stock in 50 mM HEPES-free acid, stored at −20 °C). Spectral images were acquired on a Zeiss 880 laser scanning confocal microscope run by ZEN black v2.1. Images were collected using a 63x 1.4 NA Plan-Apochromat DIC oil objective. GxTX Lys27Pra(JP) was excited using a 561 nm laser set to 4.0% power. Emission spectra were collected using 34 different PMT detectors. Two detectors binned emission signals from 371−410 and 697−758 nm. The remaining detectors used 8.9 nm wide bins to detect emission signals from 410−694 nm. A final detector collected TPMT/brightfield images. Images were analyzed with Zen Blue Desk. The JP signal was isolated from broadband autofluorescence signals using Zeiss linear unmixing methods, with the autofluorescence ROI taken from a region outside of the cell boundary. Unmixed images were further processed in ImageJ as max intensity stack projections.

Model for determining Kv2 activity based on GxTX–594 unlabeling

In the GxTX model, at any given voltage, there is a probability that a voltage sensor is either in its resting conformation ($P_{resting}$) or in its activated conformation ($P_{activated}$) such that $P_{activated} = (1 - P_{resting})$. The equilibrium for voltage sensor activation is then a ratio of activated-to-resting voltage sensors ($P_{activated}/P_{resting}$) in which

$$\frac{P_{activated}}{P_{resting}} unlabeled = e^{(V - V_{1/2,unlabeled})\frac{zF}{RT}} \quad \text{(Eqn. 1a)}$$

$$\frac{P_{activated}}{P_{resting}} labeled = e^{(V - V_{1/2,labeled})\frac{zF}{RT}} \quad \text{(Eqn. 1b)}$$

Where $V_{1/2}$ is the voltage where $P_{activated}/P_{resting} = 1$. In a prior study, our analysis of the conductance-voltage relation of Kv2.1 yielded a $V_{1/2} = -32$ mV with $z = 1.5$ elementary charges (e_0) for the early movement of four independent voltage sensors, and we found that with a saturating concentration of GxTX, the $V_{1/2} =$ +42 mV (Fig. 2.3C; (320)). These values were used for $V_{1/2,unlabeled}$, z, and $V_{1/2,labeled}$, respectively. To relate voltage sensor activation to transient labeling and unlabeling, we used microscopic binding (k_{on}[GxTX–594]) and unbinding (k_{off}) rates that are distinct for resting and activated voltage sensors. We estimated values for these rates assuming

$$k_{\Delta F} = k_{on}[EVAP] + k_{off} \quad \text{(Eqn. 2)}$$

And

$$K_d = \frac{k_{off}}{k_{on}} \quad \text{(Eqn, 3)}$$

To calculate the $k_{on,resting}$ and $k_{off,resting}$ values, we used the saturating value at negative voltages of the $k_{\Delta F}$–voltage relation (see Fig. 2.4E), and K_d from concentration–effect imaging (Supplemental Fig. 3.5). In 9 nM GxTX–594, at greater than +40 mV, voltage-dependent unlabeling was nearly complete, indicating that $k_{off,activated} >> k_{on,activated}$[GxTX–594]. The model does not include GxTX–594 signal that is insensitive to voltage (Fig. 2.4C). We input the saturating amplitude of the Boltzmann fit to the $k_{\Delta F}$ at positive voltages as $k_{off,activated}$ (Fig. 2.4E). The slow labeling of activated voltage sensors confounded attempts to measure

$k_{on,activated}$ directly, and we used the statistical thermodynamic principle of microscopic reversibility to constrain $k_{on,activated}$:

$$\frac{\frac{P_{activated}}{P_{resting}},labeled}{\frac{P_{activated}}{P_{resting}},unlabeled} = \frac{\frac{k_{off,resting}}{k_{on,resting}}}{\frac{k_{off,activated}}{k_{on,activated}}} \quad \text{(Eqn. 4)}$$

The GxTX–594 model depicted in Scheme 2 has only a single microscopic binding rate, $k_{on,total}$[GxTX–594], and unbinding rate, $k_{off,total}$. $k_{on,total}$ is a weighted sum of both $k_{on,resting}$ and $k_{on,activated}$ from Scheme 1. The weights for $k_{on,total}$ are the relative probabilities that unlabeled voltage sensors are resting or activated, which is determined at any static voltage by an equilibrium constant, $P_{activated}$ unlabeled:

$$k_{on,total} = k_{on,resting}[EVAP] \cdot \frac{1}{1+\frac{P_{activated}}{P_{resting}}unlabeled} + k_{on,active}[EVAP] \cdot \frac{1}{1+\frac{1}{\frac{P_{activated}}{P_{resting}}unlabeled}} \quad \text{(Eqn. 5)}$$

Similarly, $k_{off,total}$ is determined by the unbinding rate from resting voltage sensors ($k_{off,resting}$) and the unbinding rate from activated voltage sensors ($k_{off,activated}$) and weighted such that

$$k_{off,total} = k_{off,resting} \cdot \frac{1}{1+\frac{P_{activated}}{P_{resting}}labeled} + k_{off,active} \cdot \frac{1}{1+\frac{1}{\frac{P_{activated}}{P_{resting}}labeled}} \quad \text{(Eqn. 6)}$$

Using $k_{on,total}$ and $k_{off,total}$, we compute $k_{\Delta F}$ using Eqn. 2. The GxTX–594 model was also used to predict the magnitude of GxTX–594 fluorescence changes on cell surfaces. In theory, the ratio of fluorescence at a test voltage to fluorescence at a prior voltage (F/F_{init}) is equal to the probability that a Kv2 subunit is reversibly labeled by GxTX–594 ($P_{labeled}$):

$$\frac{F}{F_{init}} = \frac{P_{labeled}}{P_{labeled,init}} \quad \text{(Eqn. 7)}$$

The equilibrium $P_{labeled}$ at any voltage can be determined from microscopic binding rates associated with Scheme 2 where

$$P_{labeled} = \frac{1}{1+\frac{K_{d,total}}{[EVAP]}} = \frac{1}{1+\frac{k_{off,total}}{k_{on,total} \cdot [EVAP]}} \quad \text{(Eqn. 8)}$$

Predictions of F / F_{init} and $k_{\Delta F}$ during trains of 2-ms voltage steps from −80 mV to +40 mV were made from the model by summing the products of time-averaged probability of being at each voltage (P_{Vn}) and the fluorescence change predicted at that voltage (ΔF_{Vn}) :

$$F/F_{init} = (P_{V1} \cdot \Delta F_{V1}) + (P_{V2} \cdot \Delta F_{V2}) + \ldots + (P_{Vn} \cdot \Delta F_{Vn}) \quad \text{(Eqn. 9)}$$

For voltage steps from -80 to +40 mV, Eqn. 9 is:

$$F/F_{init} = (P_{40mV} \cdot \Delta F_{40mV}) + (P_{-80mV} \cdot \Delta F_{-80mV}) \quad \text{(Eqn. 9)}$$

We predicted EVAP kinetics responses as

$$k_{\Delta F} = \left(P_{V1} \cdot k_{\Delta F,V1}\right) + \left(P_{V2} \cdot k_{\Delta F,V2}\right) + \ldots + (P_{Vn} \cdot k_{\Delta F,Vn}) \quad \text{(Eqn. 10)}$$

where P_{Vn} is as in Eqn. 9 and $k_{\Delta F,n}$ is $k_{\Delta F}$ at that particular voltage. For voltage steps from -80 to +40 mV Eqn. 10 is:

$$k_{\Delta F} = (P_{40mV} \cdot k_{\Delta F40mV}) + (P_{-80mV} \cdot k_{\Delta F-80mV})$$

Figures and Tables

Figure 2.1

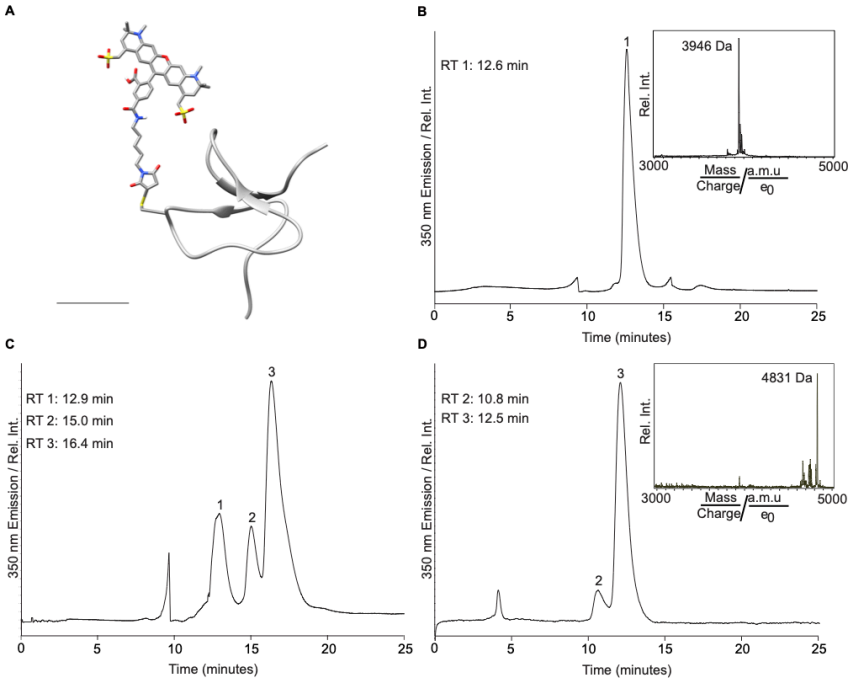

Figure 2.1 Synthesis of GxTX–594

(**A**) Molecular model of GxTX-594. Scale bar is 10 angstroms. Backbone of GxTX peptide depicted with ribbon. Cys13(maleimide-Alexa 594) depicted with CPK coloring. (**B**) HPLC chromatogram of Ser13Cys GxTX. Gradient described in Materials and Methods - GxTX Synthesis. GxTX Ser13Cys eluted at 12.6 minutes, peak 1, which corresponds to 33% acetonitrile. MALDI-TOF MS profile of peak 1 (Inset). Rel. Int. is Relative Intensity. (**C**) HPLC chromatogram of GxTX–594 conjugation reaction between Alexa Fluor 594-maleimide and GxTX Ser13Cys. Peak 1 is GxTX Ser13Cys (Retention time: 12.8 minutes, 33% acetonitrile), peak 2 is a minor product from conjugation, and peak 3 is GxTX–594, the major product from conjugation (Retention time: 16.4 minutes, 35% acetonitrile). The fractions corresponding to peak 3 were combined. (**D**) HPLC chromatogram of the combined peak 3 fractions from panel C, a GxTX–594 preparation used in this study. 2 uL of 13.1 μM GxTX–594 diluted in 200 uL of 0.1% TFA was injected. MALDI-TOF MS profile of the combined peak 3 fractions (Inset).

Figure 2.2

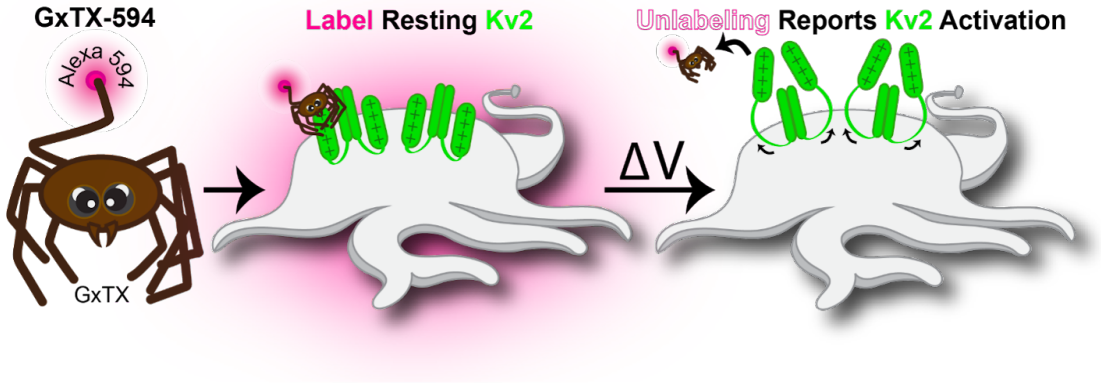

Figure 2.2 Schematic of the GxTX–594 tool

Schematic detailing the conceptual mode of action for GxTX–594.

Figure 2.3

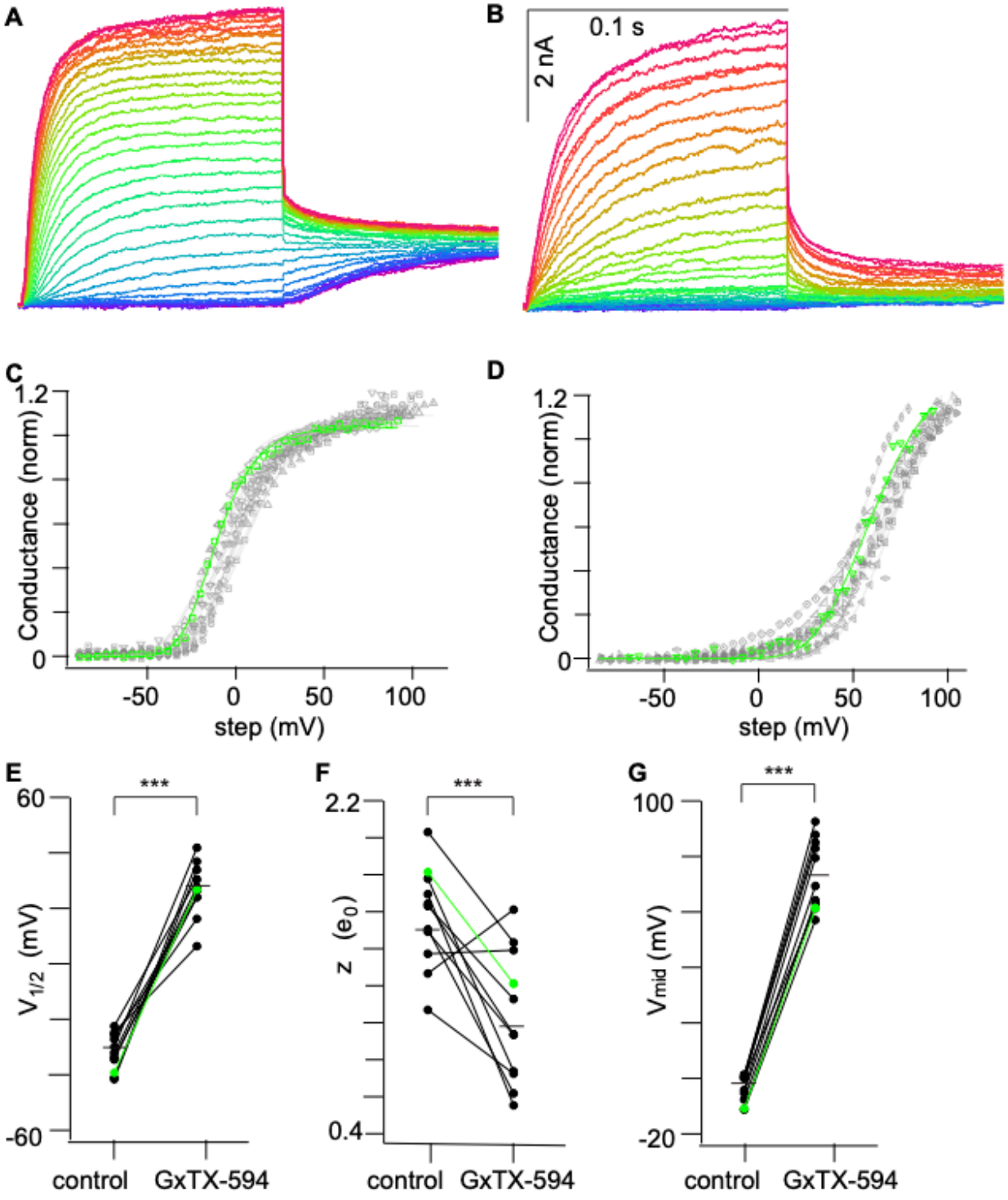
A
B
0.1 s
2 nA
C
Conductance (norm)
1.2
0
-50
0
50
100
step (mV)
D
Conductance (norm)
1.2
0
-50
0
50
100
step (mV)
E
***
60
-60
$V_{1/2}$ (mV)
control
GxTX-594
F
***
2.2
0.4
z (e_0)
control
GxTX-594
G
***
100
-20
V_{mid} (mV)
control
GxTX-594

Figure 2.3 GxTX-594 modulates Kv2.1 conductance.

(**A**) Representative Kv2.1-CHO current response under whole cell voltage-clamp. Cells were given 100-ms, 5-mV increment voltage steps ranging from -80 mV (blue) to +120 mV (red) and then stepped to 0 mV to record tail currents. The holding potential was -100 mV. (**B**) Kv2.1 currents from the same cell 5 minutes after the addition of 100 nM GxTX-594. Scale bars are the same for panels A and B. (**C**) Normalized conductance–voltage relationships from Kv2.1 tail currents before application of GxTX-594 (n = 13). Different symbols correspond to individual cells and the green corresponds to cell in panel A. (**D**) Normalized conductance–voltage relationships in 100 nM GxTX–594 (n = 11). (**E**) Mean midpoint of each of four independent voltage sensors in the fourth-power Boltzmann fit ($V_{1/2}$) before (-31 ± 6 mV SD) and after (+27 ± 10 mV SD) 100 nM GxTX–594. $p < 0.0001$ by Mann-Whitney *U* test. (**F**) Mean elementary charge associated with Boltzmann fit (*z*) before (1.5 ± 0.3 e_0 SD) and after (1.0 ± 0.4 e_0 SD) 100 nM GxTX-594. ***, P = 0.0007 by Mann-Whitney *U* test. (**G**) Mean midpoint of conductance change in the fourth-power Boltzmann fit (V_{Mid}) before (-2 ± 6 mV SD) and after (+73 ± 13 mV SD) 100 nM GxTX–594. ***, $p < 0.0001$ by Mann-Whitney *U* test.

Figure 2.4

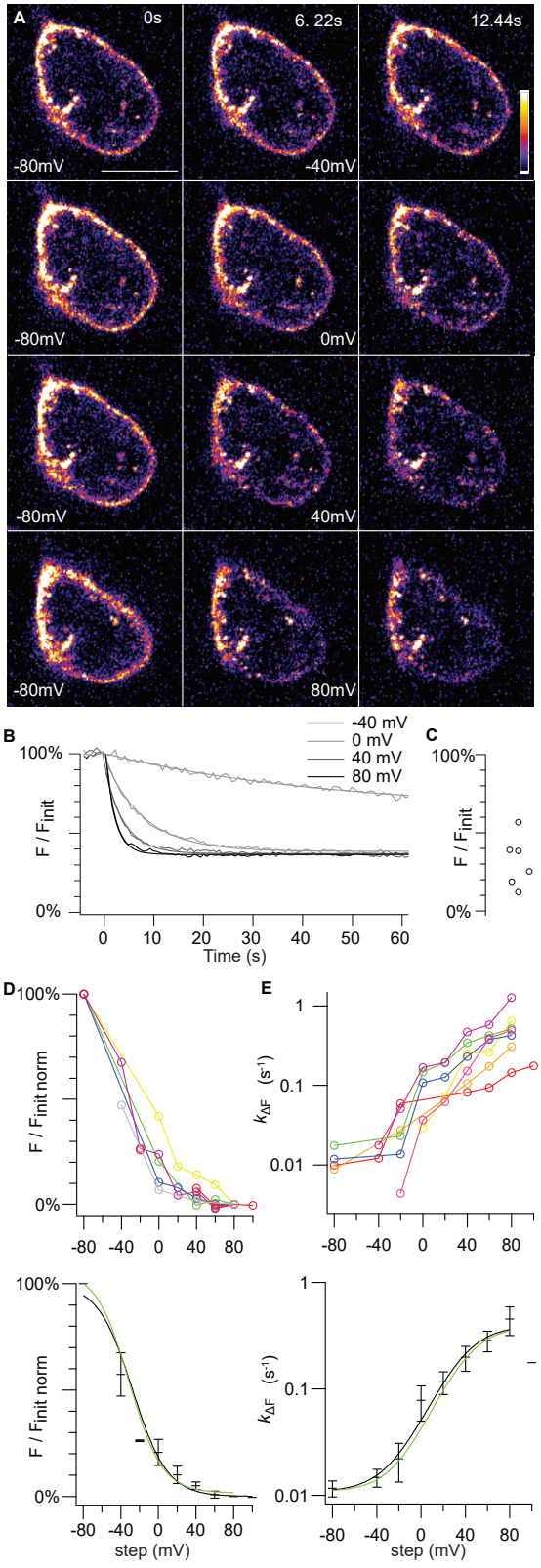
A
0s
6. 22s
12.44s
-80mV
-40mV
-80mV
0mV
-80mV
40mV
-80mV
80mV
B
-40 mV
0 mV
40 mV
80 mV
100%
F / Finit
0%
0
10
20
30
40
50
60
Time (s)
C
100%
F / Finit
0%
D
100%
F / Finit norm
0%
-80
-40
0
40
80
E
1
0.1
0.01
kΔF (s-1)
-80
-40
0
40
80
100%
F / Finit norm
0%
-80
-40
0
40
80
step (mV)
1
0.1
0.01
kΔF (s-1)
-80
-40
0
40
80
step (mV)

Figure 2.4 GxTX-594 labeling responds to transmembrane voltage

(**A**) Fluorescence from an optical section of a voltage-clamped Kv2.1-CHO cell in 9 nM GxTX–594. Color progression for pseudocoloring of fluorescence intensity is shown in vertical bar on right. Middle column in each row indicates voltage step taken from a holding potential of -80 mV. Times listed at top of each column correspond to time axis in panel B. Scale bar is 10 μm. (**B**) GxTX–594 fluorescence during steps to indicated voltages. Smooth lines are monoexponential fits: -40 mV $k_{\Delta F}$ = 2.15 x 10^{-2} ± 0.22 x 10^{-2} s^{-1}, 0 mV $k_{\Delta F}$ = 1.279 x 10^{-1} ± 0.023 x 10^{-1} s^{-1}, 40 mV $k_{\Delta F}$ = 2.492 x 10^{-1} ± 0.062 x 10^{-1} s^{-1} and 80 mV $k_{\Delta F}$ = 4.20 x 10^{-1} ± 0.11 x 10^{-1} s^{-1}. ROIs were hand-drawn around the apparent cell surface membrane based on GxTX–594 fluorescence. 0% was set by subtraction of background which was the average intensity of a region that did not contain cells over the time course of the voltage protocol. For each trace, 100% was set from the initial fluorescence intensity at -80 mV before the subsequent voltage step. Raw initial fluorescence values before normalization were within 10% of one another. (**C**) Fluorescence intensity remaining at the end of 50 s steps to +80 mV. Each circle represents one cell. Background subtraction as in panel B. (**D**) Voltage-dependence of fluorescence intensity at the end of 50 s steps. For each cell, 100% was set from the initial fluorescence intensity at -80 mV before the first step to another voltage. Cells did not always recover to initial fluorescence intensity during the -80 mV holding period between voltage steps. (Top panel) Circle coloring indicates data from the same cell and lines connect points from the same cell. Gray circles represent data shown in B. (Bottom panel) black bars represent the mean F/F_{init} at each voltage and error bars represent the standard error of the mean. Black line is fit of a first-order Boltzmann equation: $V_{1/2}$ = -27.4 ± 2.5 mV, z = 1.38 ± 0.13 e_0. Green line is prediction from the EVAP model at 9 nM GxTX. (**E**) Voltage dependence of fluorescence intensity kinetics ($k_{\Delta F}$). (Top panel) circle coloring is the same as panel D. (Bottom panel) black bars represent the average $k_{\Delta F}$ at each voltage and error bars represent the standard error of the mean. Black line is a first-order Boltzmann equation fit to the $k_{\Delta F}$–voltage relation: $V_{1/2}$ = +38 ±

15 mV, $z = 1.43 \pm 0.35\ e_0$. Green line is prediction from the EVAP model at 9 nM GxTX. Error bars are standard error of the mean.

Figure 2.5

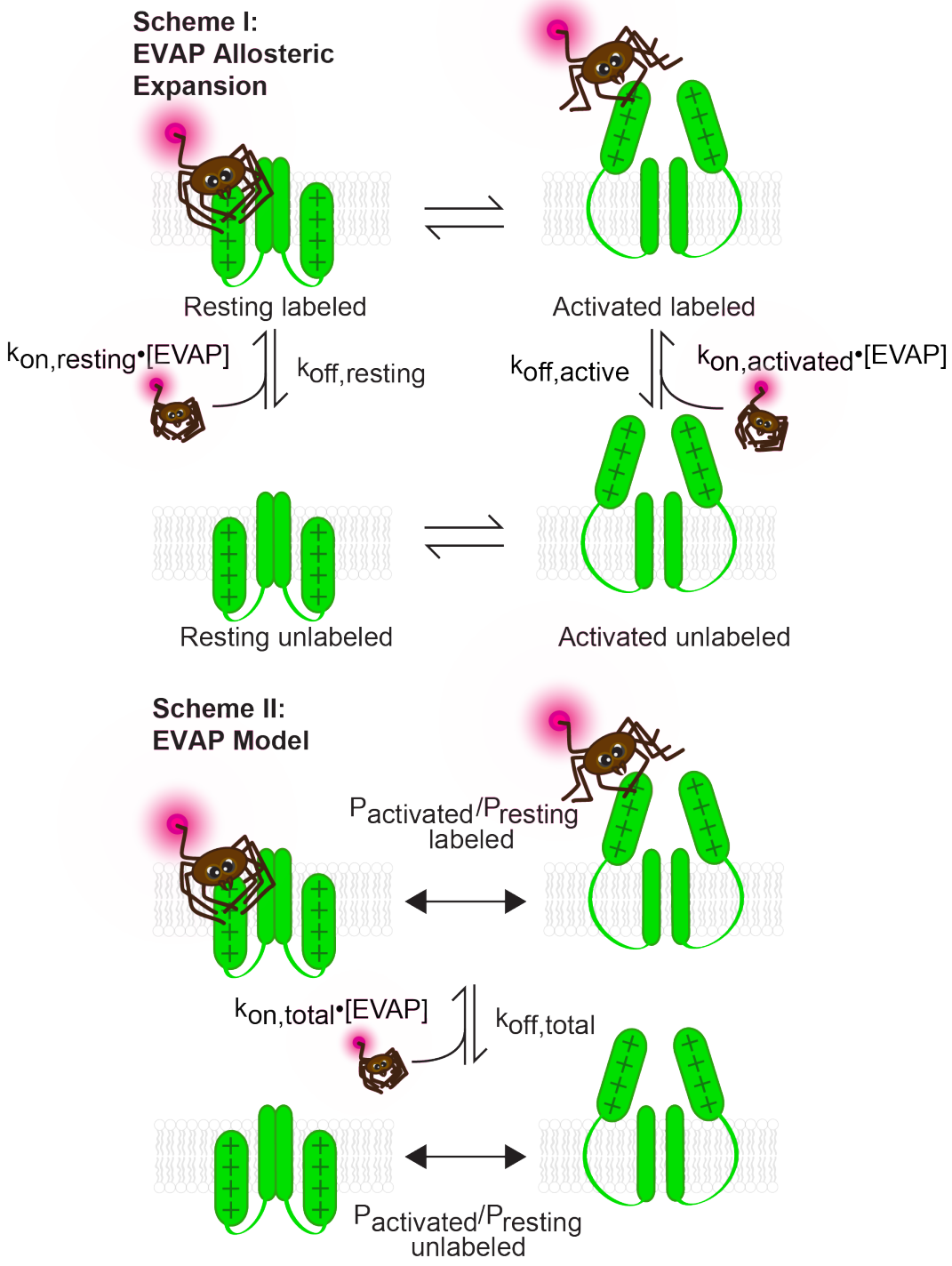

Figure 2.5 Model of the GxTX–594 mode of action

Figure 2.6

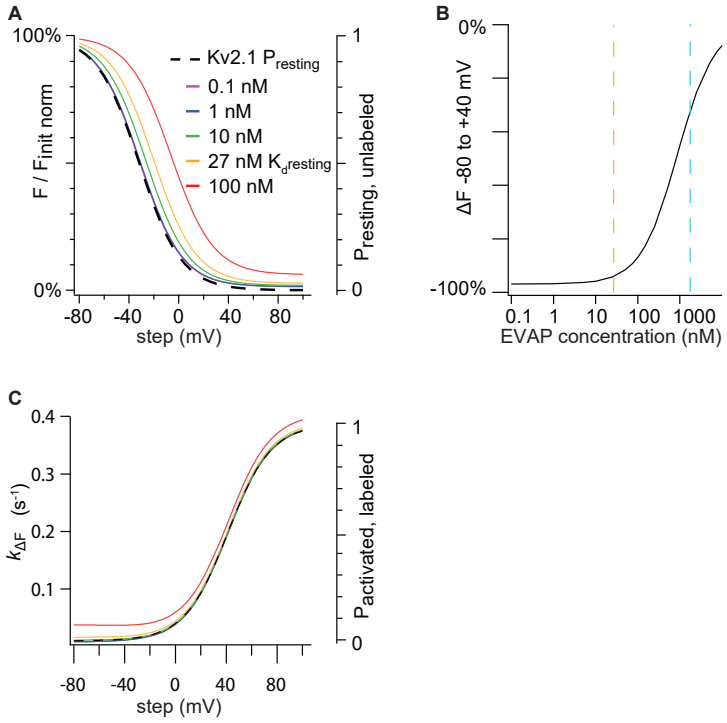

Figure 2.6 Relationship of GxTX-594 labeling to probability of Kv2 voltage sensor activation.

(**A**) EVAP model predictions of concentration- and voltage-dependence of cell surface fluorescence intensity at different concentrations of EVAP in solution. Bottom axis represents membrane voltage. The left axis represents the predicted fluorescence relative to when all voltage sensors are at rest (F_{init}) and does not include EVAP signal that is insensitive to voltage. The dashed line corresponds to the right axis and represents the probability that voltage sensors of unlabeled Kv2.1 are in their resting conformation. (**B**) EVAP model prediction of the cell surface fluorescence when cells are given a +40 mV depolarization relative to when all voltage sensors are at rest (F_{init}) at increasing concentrations of EVAP. Dashed orange line represents K_d of resting voltage sensors. Dashed blue line represents K_d of activated voltage sensors. (**C**) EVAP model predictions of concentration- and voltage-dependence of $k_{\Delta F}$. Colors correspond to panel A, except dashed line is the probability that voltage sensors bound by GxTX-594 are an activated conformation.

Figure 2.7

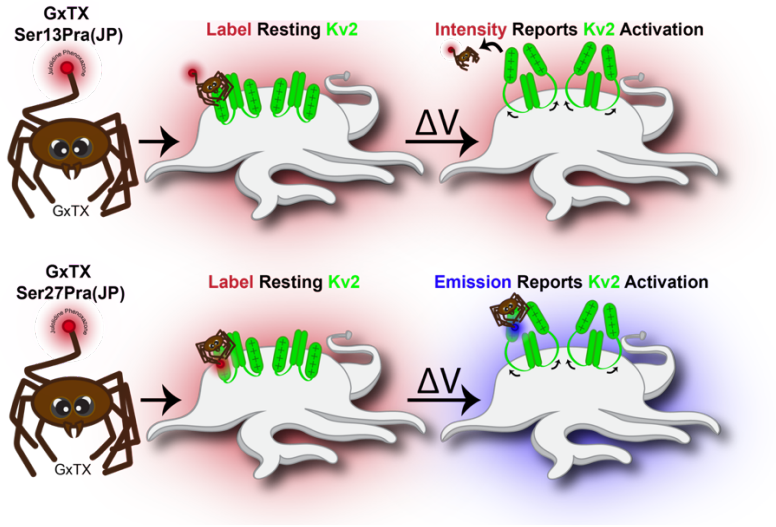

Figure 2.7 Schematic of the GxTX–JP tools

Schematic detailing the conceptual mode of action for GxTX Lys27Pra(JP) and GxTX Ser13Pra(JP). Ser13Pra(JP) is localized to a polar environment regardless of the Kv2.1 voltage sensing domain conformation. The dissociation rate of GxTX Ser13Pra(JP) is similar to that of GxTX–594 (unpublished data), such that the response of GxTX Ser13Pra(JP) emission to voltage is a complex mixture of fluorescence intensity (which increases with voltage activation) and probe occupancy (which decreases with voltage activation). Modification to GxTX at the Lsy27Pra position increases the affinity of GxTX to the resting voltage sensing domain and decreases the dissociation rate to be on a time scale significantly slower than GxTX–594 (Fletcher taylor 2020). As a result, this tool reports real-time changes to Kv2.1 voltage sensing domain-GxTX conformation. Prior to voltage stimulation, Lys27Pra(JP) is localized in a position that is largely nonpolar, such that the emission of JP is red-shifted. Following voltage stimulation, JP is exposed to a polar environment and the emission undergoes a blue-shift. Interestingly, the mid-point of the spectral transition occurs at a voltage more depolarized than what is necessary to activate Kv2.1 gating charge movement, such that this tool reports early conformational changes in the resting voltage sensing domain.

Figure 2.8

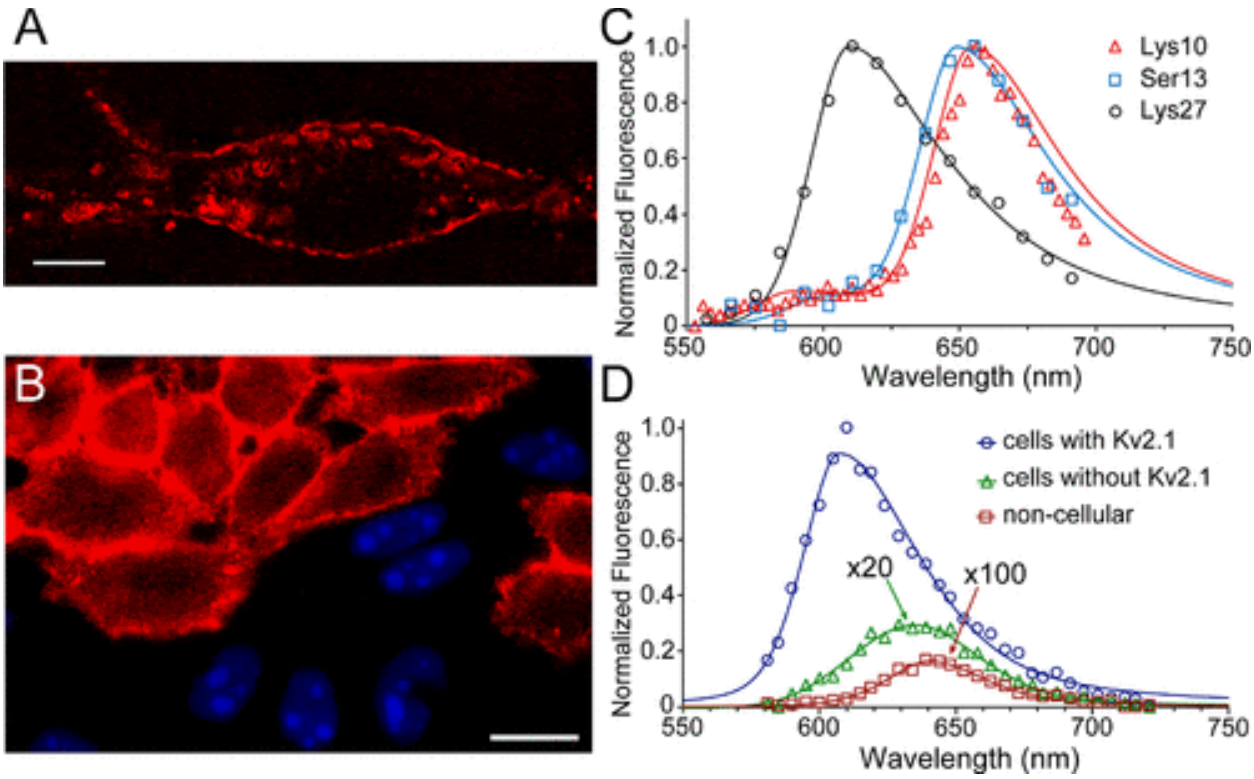

Figure 2.8 Fluorescence of JP−GxTX conjugates on live cells.

(**A**) Compressed z-stack confocal image of a live rat hippocampal neuron stained with 100 nM GxTX Lys27Pra(JP). The cell is excited at 561 nm, and its emission isolated around 625 nm. Scalebar is 10 µm. (**B**) Specificity of GxTX–JP conjugates for Kv2-expressing cells. Confocal image of co-plated CHO cells with or without Kv2.1, stained with 100 nM GxTX Lys27Pra(JP) (red membranes). Only cells without Kv2 channels express nuclear BFP. (**C**) Spectral imaging of JP−GxTX conjugates on Kv2.1 CHO cells. (**D**) Emission spectra of GxTX Lys27Pra(JP) imaged from CHO cells with (blue line) or without Kv2.1 (green line, magnified 20×) or from extracellular regions (red line, magnified 100×). Spectra are fit with 2-component split pseudo-Voigt functions.

Figure 2.9

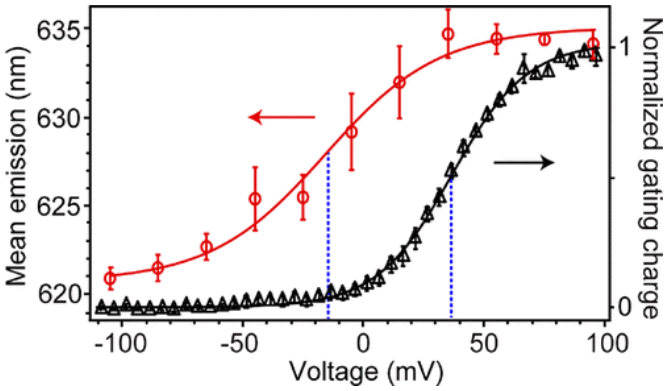

Figure 2.9 Fluorescence shifts and gating currents of Kv2.1 with Lys27Pra(JP) GxTX, recorded from Kv2.1-expressing CHO cells.

Mean fluorescence emission of Lys27Pra(JP) as a function of membrane potential (red circles), calculated from integrations of 2-component split pseudo-Voigt fittings of spectral data. Normalized Kv2.1-gating charge (black triangles), with 100 nM GxTX Lys27Pra(JP), shown as Q/Q_{Max} and measured as Q_{OFF} from −140 mV. For both plots, data are mean ± SEM and solid lines are two-state Boltzmann functions. Blue dashed lines are midpoint voltages of fluorescence shift (−15 mV) and Q_{OFF} (+37 mV).

Table 2.1

Parameters used for calculations to generate Scheme I: EVAP Allosteric Expansion.

Parameter	**Value**
$k_{on,resting}$	0.30 μM^{-1} s^{-1}
$k_{off,resting}$	0.0081 s^{-1}
$k_{on,activated}$	0.21 $\mu M^{-1} s^{-1}$
$k_{off,activated}$	0.39 s^{-1}
$V_{1/2,unlabeled}$	-32 mV
$V_{1/2,labeled}$	41 mV
z	1.5 e_0

Chapter 3: The AMIGO1 adhesion protein activates Kv2.1 voltage sensors.

Preface

This chapter details my research into the mechanistic underpinnings through which an auxiliary subunit modifies the conformational state of its voltage-gated potassium channel partner. This work has been submitted for publication to the *Biophysical Journal* as: R.J. Sepela, R.G. Stewart, L.A. Valencia, P. Thapa, Z. Wang, B.E. Cohen, J.T. Sack. The AMIGO1 adhesion protein activates Kv2.1 voltage sensors. Jon Sack and I conceived of all experiments in this chapter. For most experiments, I conducted testing and data analysis. Notably, for Fig. 3.8, the data was acquired by me and was analyzed by Luis A. Valencia and Bruce E. Cohen. Zeming Wang and Parashar Thapa provided GxTX–JP conjugates for experiments conducted in Fig. 3.8. For Supplemental Fig. 3.5 the data was acquired by Robert G. Stewart and analyzed by both Robert G. Stewart and I. Jon Sack, Karen Zito, James Trimmer, and Tsung-Yu Chen provided valuable feedback when designing experiments. Jon Sack and I wrote the manuscript that has been submitted to the Biophysical Journal and that verbiage is preserved in its entirety in this chapter.

Abstract

Kv2 voltage-gated potassium channels are modulated by AMIGO neuronal adhesion proteins. Here, we identify steps in the conductance activation pathway of Kv2.1 channels that are modulated by AMIGO1 using voltage clamp recordings and spectroscopy of heterologously expressed Kv2.1 and AMIGO1 in mammalian cell lines. AMIGO1 speeds early voltage sensor movements and shifts the gating charge–voltage relationship to more negative voltages. The gating charge–voltage relationship indicates that AMIGO1 exerts a larger energetic effect on voltage sensor movement than apparent from the midpoint of the conductance–voltage relationship. When voltage sensors are detained at rest by voltage sensor toxins, AMIGO1 has a greater impact on the conductance–voltage relationship. Fluorescence measurements from voltage sensor toxins bound to Kv2.1 indicate that with AMIGO1, the voltage sensors enter their earliest resting conformation, yet this conformation is less stable upon voltage stimulation. We conclude that AMIGO1 modulates the Kv2.1 conductance activation pathway by destabilizing the earliest resting state of the voltage sensors.

Introduction

Voltage–gated potassium (Kv) channels of the Kv2 family open following membrane depolarization and are critical regulators of neuronal electrical excitability. Mammals have two Kv2 pore-forming α subunits, Kv2.1 and Kv2.2, which function as homo- or heterotetramers (368). The molecular architecture of Kv2 channels is similar to Kv1 channels for which atomic resolution structures have been solved (296). Each α subunit monomer has six transmembrane helical segments, S1-S6. S1-S4 comprise a voltage sensor domain (VSD) while S5 and S6 together form one quarter of the central pore domain. In response to sufficiently positive intracellular voltages, gating charges within the VSD translate from an intracellular resting position to a more extracellular activated conformation. This gating charge movement powers the conformational changes of voltage sensor activation, which are coupled to subsequent pore opening and K^+ conduction (299). Kv channels progress through a landscape of conformations leading to opening, all of which define a pathway for the activation of the K^+ conductance. The activation pathway of Kv2 channels is distinct from Kv1 channels, as Kv2.1 channels have a pore opening step which is slower and more weakly voltage-dependent than the VSD movement of Kv1 channels (299, 320, 333). The unique kinetics and voltage dependence of Kv2 currents are critical to neuronal activity, as they regulate action potential duration and can either support or limit repetitive firing (6, 29, 344, 369, 370).

Kv2 channels are abundant in most mammalian central neurons (361). Genetic deletion of Kv2.1 leads to seizure susceptibility and behavioral hyperexcitability in mice (25), and human Kv2.1 mutations result in developmental epileptic encephalopathy (360, 371, 372), underscoring the importance of these channels to brain function. Homeostatic Kv2.1 regulation maintains neuronal excitability (27). Kv2.1 regulation by ischemia (17, 373), glutamate (374), phosphorylation (305) and SUMOylation (306) and AMIGO auxiliary subunits (32, 33) all shift the midpoint of the conductance–voltage relation (*G–V*).

However, it is not known which steps in the conductance activation pathway are modulated by any of these forms of regulation.

To identify steps in the Kv2.1 conduction activation pathway that are susceptible to modulation, we studied the impact of an AMIGO auxiliary subunit. The AMIGO (AMphoterin–Induced Gene and Open reading frame) family of proteins contains three paralogs in mammals: AMIGO1, AMIGO2, and AMIGO3. AMIGO proteins are single-pass transmembrane proteins with an extracellular immunoglobulin domain and several leucine-rich repeats (69). AMIGO1 has been proposed to play a role in schizophrenia biology (375). In vertebrate brain neurons, AMIGO1 is important for cell adhesion (69), neuronal tract development (124), and circuit formation (124, 375, 376). AMIGO1 colocalizes with Kv2 in neurons throughout the brains of multiple mammalian species (32, 121). Coimmunoprecipitation of AMIGO1 and Kv2.1 (32, 33, 124) and co-diffusion through cell membranes (32) indicate a robust interaction, consistent with an AMIGO1–Kv2.1 complex being sufficiently stable for intensive biophysical studies. All three AMIGO proteins activate the conductance of both Kv2 channel subtypes, shifting the conductance–voltage relation by -5 to -15 mV (32, 33). While these shifts may seem small in excitable cells that can have voltage swings of more than 100 mV, human mutations that shift the conductance–voltage relation of ion channel gating by similar magnitudes are correlated with physiological consequences (360, 377–379). However, it is difficult to determine whether the physiological consequences of mutations are caused by the gating shifts themselves.

Here we investigate which steps in the Kv2.1 conductance activation pathway are modulated by AMIGO1. In other voltage-gated ion channels, the *G–V* relation can be shifted to more negative voltages by modulating pore opening (125, 166, 168), voltage sensor movement (169, 170), or voltage sensor-pore coupling (114, 171, 172). Single-pass transmembrane auxiliary subunits modulate other voltage-gated ion channel α subunits by a variety of mechanisms (125, 171, 204, 380). However, AMIGO1 only shares a limited degree of homology with other single-pass transmembrane auxiliary subunits (123), and

divergent structural interactions have been observed among single-pass transmembrane auxiliary subunits (184, 343). As there is no consensus binding pose or mechanism of interaction for auxiliary subunits, it is difficult to predict on which step in the conductance activation pathway AMIGO1 acts. A recent study proposed that AMIGO proteins shift Kv2.1 conductance by increasing voltage sensor-pore coupling and that AMIGO-conferred changes to Kv2 voltage-sensing machinery are unlikely (33). Here we ask whether AMIGO1 alters conformational changes associated with pore opening or with voltage sensor movement using a combination of electrophysiological and imaging approaches. We find that AMIGO1 modulates voltage sensor movements which occur before pore opening. We find AMIGO1 to have a greater impact on early voltage sensor movements than the conductance–voltage relation. We conclude that AMIGO1 destabilizes the earliest resting conformation in the pathway of channel activation.

Results

AMIGO1 shifts the midpoint for activation of Kv2.1 conductance

Voltage-clamp recordings from cotransfected HEK293 cells indicate that mouse AMIGO1 shifts the *G–V* relation of mouse Kv2.1 by -5.7 ± 2.3 mV (SEM) (Supplemental Fig. 3.1). This shift was similar to the -6.1 mV ± 1.6 mV shift reported of rat Kv2.1–GFP by human AMIGO1–mRuby2 (33), and smaller than the -15.3 mV (no error listed) shift of mouse Kv2.1–GFP by mouse AMIGO1 (32). This small effect of AMIGO1 was similar to the cell-to-cell variability in our recordings. We suspected that endogenous voltage-activated conductances of HEK293 cells (381, 382) and variability inherent to transient co-transfection could increase variability. To minimize possible sources of cell-to-cell variability, further experiments were with a Chinese Hamster Ovary K1 cell line with inducible rat Kv2.1 expression (Kv2.1–CHO) transfected with a YFP-tagged mouse AMIGO1. Inducible Kv2.1 expression permits tighter control of current density (366) and fluorescence tagging of AMIGO1 permits visualization of protein expression and localization. Unlike HEK293 cells, CHO cells lack endogenous voltage-gated K^+ currents (383).

As expression systems can influence auxiliary protein interactions with ion channels (92, 99, 218, 262, 271), we assessed Kv2.1–AMIGO1 association in these CHO cells. We evaluated two hallmarks of Kv2.1 and AMIGO1 association: Kv2.1 reorganization of AMIGO1, and AMIGO1 / Kv2.1 colocalization (32, 33, 121).

In HEK293 cells, heterologously expressed AMIGO1 localization is intracellular and diffuse (33, 121). However, when co-expressed with Kv2.1, AMIGO1 reorganizes into puncta with Kv2.1, similar to the expression patterns in central neurons (33, 121). To determine whether Kv2.1 reorganizes AMIGO1 in Kv2.1–CHO cells, the degree of AMIGO1–YFP reorganization was quantified using the Coefficient of Variation (COV), which captures non–uniformity of YFP localization (243). COV was quantified following the limited 1.5 h Kv2.1 induction period used in whole-cell and single channel K^+ current

recordings and the prolonged 48 h induction period used for gating current recordings or imaging studies. COVs were compared against an uninduced control (0 h induction) and against an engineered protein, ChroME-mRuby2, which contains the Kv2.1 PRC trafficking sequence, but lacks the Kv2.1 voltage sensing and pore forming domains (12, 384). COVs were evaluated from the glass-adhered, basal membrane where evidence of reorganization is most notable (Fig. 3.1). Both $COV_{1.5h}$ and COV_{48h} were greater than the COV_{0h} or $COV_{ChroME\text{-}mRuby}$ control. This result is consistent with Kv2.1 and AMIGO1 association in CHO cells.

As an additional measure of whether Kv2.1 reorganizes AMIGO1 in Kv2.1–CHO cells, we assessed AMIGO1–YFP and Kv2.1 colocalization using the Pearson's correlation coefficient (PCC) (385). Surface-expressing Kv2.1 on live cells was labeled with GxTX Ser13Cys(Alexa594), a conjugate of a voltage sensor toxin guangxitoxin-1E derivative with a fluorophore, abbreviated as GxTX–594 (321). As auxiliary subunits can impede binding of toxins to voltage-gated ion channels (94), we tested whether AMIGO1 impacted GxTX–594 binding to Kv2.1. Under conditions where AMIGO1 modulates most, if not all, Kv2.1 voltage sensor movements (Fig. 3.6, 3.7), we found no evidence that AMIGO1 impedes GxTX–594 binding to Kv2.1 (Supplemental Fig. 3.5). Colocalization between AMIGO1–YFP and GxTX–594 was apparent as $PCC_{48h,}$ measured from the glass-adhered basal membrane, was greater than the negative control, $PCC_{ChroME\text{-}mRuby2}$ (Fig. 3.2B). With a limited 1.5 h induction, GxTX–594 was difficult to detect at the glass-adhered membrane, so we moved the confocal imaging plane further from the cover glass to image Kv2.1 on apical cell surfaces where GxTX–594 labeling was more apparent. On these apical surfaces, $PCC_{1.5h}$ and PCC_{48h} were greater than PCC_{0h} (Fig. 3.2A), consistent with some colocalization of AMIGO1–YFP and Kv2.1. The weakly significant increase of the $PCC_{1.5h}$ compared to PCC_{0h} is consistent with some colocalization. Disproportionate expression can skew PCC values (386), and the limited GxTX–594 signal is expected to depress the $PCC_{1.5h}$ value. Similarly, the lower PCC_{48h} values were associated with either minimal or exceptionally bright AMIGO1–YFP signal. Overall, we see no sign of Kv2.1 channels lacking

colocalized AMIGO1 in cells with high levels of AMIGO1 expression. Altogether, the reorganization and colocalization indicate that AMIGO1–YFP and Kv2.1 interact in the CHO cells used for K^+ current recordings and for gating current measurements.

AMIGO1 shifts the midpoint of activation of Kv2.1 conductance in CHO cells

To determine whether AMIGO1 affected the macroscopic K^+ conductance in Kv2.1–CHO cells, we conducted whole-cell voltage clamp recordings. Cells were transfected with GFP (Kv2.1–control cells) or with AMIGO1–YFP (Kv2.1 + AMIGO1 cells) and identified for whole-cell voltage clamp based on the presence of cytoplasmic GFP fluorescence or plasma membrane-associated YFP fluorescence, respectively (Fig. 3.3A). Macroscopic ionic current recordings were made in whole-cell voltage-clamp mode and K^+ conductance was measured from tail currents (Fig. 3.3B, C). In expectation of small AMIGO1 effects relative to cell-to-cell variation, recordings from control cells and AMIGO1 cells were interleaved during each day of experiments and cell identity was blinded during analysis. *G–V* relations were fit with a 4th power Boltzmann function (Eqn. C) (Fig. 3.3D, E, F) and average midpoints of half-maximal conduction ($V_{i,Mid}$) and steepness equivalents (z_i) were determined (Table 2.1). In Kv2.1–control cells, the average $V_{i,Mid}$ was -1.8 mV (Fig. 3.3H), consistent with prior reports of $V_{i,Mid}$ ranging from -3 mV to +8 mV in CHO cells (33, 333, 341, 387). Cell-to-cell variation in $V_{i,Mid}$ remained notable between Kv2.1–CHO cells, with variation in $V_{i,Mid}$ on par with other reports (see *Discussion/Limitations*). The range of $V_{i,Mid}$ values of Kv2.1 + AMIGO1 cells overlapped with Kv2.1–control cells (Fig. 3.3H), yet the average $V_{i,Mid}$ was negatively shifted by -5.7 ± 2.2 mV (SEM), similar to $\Delta V_{i,Mid}$ from mouse Kv2.1 in HEK293 cells (Table 3.1). No effect on z_i was observed. We also tested AMIGO2 and AMIGO3 on Kv2.1, and found they colocalize and induce $\Delta V_{i,Mid}$ shifts similar to those reported from HEK293 cells by Maverick and colleagues (33) (Supplemental Fig. 3.3, 3.4), indicating that the small *G–V* shifts by the AMIGO proteins are robust across different experimental preparations.

To test if AMIGO1 also alters the rate of activation of Kv2.1 conductance, we analyzed activation kinetics. The 10-90% of the rise of Kv2.1 currents following a voltage step (Fig. 3.3A, B) was fit with the power of an exponential function (Eqn. F) for sigmoidicity (σ) which quantifies delay before current rise, and activation time constant (τ_{act}). σ was not significantly altered by AMIGO1 (Fig. 3.3J, L, N), suggesting that the Kv2.1 activation pathway retains a similar structure with AMIGO1 (320). At a subset of voltages less than +70 mV, AMIGO1 expression accelerated activation, decreasing τ_{act} (Fig. 3.3I, K, M), consistent with results of Maverick and colleagues (33). Following the +10 to +120 mV activating steps, time constants of tail current decay at 0 mV were similar to τ_{act} at 0 mV (Fig. 3.3O, Eqn. G). A prior study found no impact of AMIGO1 on Kv2.1 deactivation kinetics at -40 mV (33), and deactivation is not studied further here. A model of Kv2.1 activation kinetics suggests that voltage sensor dynamics influence τ_{act} below ~+70 mV, and that at more positive voltages a slow pore opening step limits kinetics (320). This analysis suggests that AMIGO1 accelerates activation kinetics only in the voltage range which is sensitive to voltage sensor dynamics.

Effects of AMIGO1 on pore opening conformational changes were not apparent in single channel recordings

To more directly assess whether the pore opening step of the Kv2.1 activation pathway is modulated by AMIGO1, we analyzed pore openings of single Kv2.1 channels during 1 s long recordings to 0 mV (Fig. 3.4A, B). At 0 mV we expect >85% of all Kv2.1–control voltage sensors or >95% of all Kv2.1–AMIGO1 voltage sensors (Fig. 3.6T) to activate in less than 2 ms (Fig. 3.6N), such that the majority of single channel openings represent stochastic fluctuations between a closed and open conformation of the pore. Neither the single channel current amplitude (Fig. 3.4C, D, E) nor the intra–sweep open probability (Fig. 3.4F) were significantly impacted by AMIGO1. AMIGO1 did not significantly impact the single channel open or closed dwell times (Fig. 3.4G-L). These results constrain any impact of AMIGO1 on Kv2.1 pore opening to be smaller than the variability in these single channel measurements.

A voltage sensor toxin enhances modulation of AMIGO1 on the Kv2.1 conductance

To test whether AMIGO1 modulation is dependent on voltage sensor dynamics, we altered voltage sensor movement with a voltage sensor toxin. GxTX binds to the voltage sensing domain of Kv2.1 (388), such that exit from the earliest resting conformation limits opening to more positive voltages (320). If AMIGO1 modulates voltage sensors, then GxTX might be expected to amplify the AMIGO1 effect. Alternately, if AMIGO1 acts directly on pore opening, the AMIGO1 impact on the pore opening equilibrium should persist, regardless of voltage sensor modulation. To distinguish between these possibilities, we measured AMIGO1 modulation in the presence of the imaging probe GxTX–594, which modulates Kv2.1 by the same mechanism as GxTX (321) and has a similar affinity for the resting conformation of Kv2.1 with or without AMIGO1 (Supplemental Fig. 3.5). We applied 100 nM GxTX–594 to cells and activated the Kv2.1 conductance. We note that the 100-ms activating pulses are much shorter than the >2 second time constants of GxTX–594 dissociation at extreme positive voltages (321) and during these short activating pulses we saw no evidence of GxTX–594 dissociation. The AMIGO1 $\Delta V_{i,Mid}$ of -22.1 ± 4.8 (SEM) with GxTX–594 was distinct from the AMIGO1 $\Delta V_{i,Mid}$ of -5.7 ± 2.2 mV (SEM) without GxTX–594 ($p = 0.00018$, unpaired, two-tailed t-test), indicating that GxTX–594 amplifies the impact of AMIGO1 on Kv2.1 conductance. We did not observe a significant effect of AMIGO1 on τ_{act} or σ in GxTX–594 (Fig. 3.5J-N). We calculated the impact of AMIGO1 on a pore opening equilibrium constant (K_{eq}) at the midpoint of the Kv2.1 *G–V* relation and found a 3.7-fold bias towards a conducting conformation in 100 nM GxTX–594 versus a 1.4-fold bias under control conditions (ΔG_{AMIGO1} = -0.77 versus -0.28 kcal/mol respectively, Table 3.1). This result indicates that the impact AMIGO1 has on the Kv2.1 conductance is dependent on the dynamics of the activation path. Further, this result indicates that AMIGO1 opposes the action of GxTX–594, which stabilizes the earliest resting conformations of Kv2.1 voltage sensor. We also note that the more dramatic modulation by AMIGO1 with GxTX–594 verifies that most Kv2.1 channels

are modulated by AMIGO1 in this cell preparation in which only a small impact on $V_{i,Mid}$ was observed without GxTX–594 (Fig. 3.3).

AMIGO1 facilitates the activation of Kv2.1 voltage sensors

To determine if AMIGO1 affects voltage sensor movement, we measured gating currents (I_g), which correspond to movement of Kv2.1 voltage sensors across the transmembrane electric field. Kv2.1–CHO cells were patch clamped in whole–cell mode in the absence of K^+ (Fig. 3.6A) and given voltage steps to elicit gating currents (Fig. 3.6B, C). The resolvable ON gating currents ($I_{g,ON}$) represent an early component of gating charge movement, but not all of the total gating charge; the later charge movements, which include any charge associated with the pore opening, move too slowly for us to resolve accurately in ON measurements (320, 333). If AMIGO1 acts solely through the pore we would not expect to detect an impact on early components of ON gating currents which occur before pore opening.

At voltages above 50 mV, the charge density translocated over the first 3.5 ms, $Q_{ON,fast}$, was not significantly different with AMIGO1 (Fig. 3.6D, E, F), indicating that AMIGO1 did not alter the total charge translocated during early conformational transitions. However, between -10 mV and +50 mV, Kv2.1–control cells did not move as much gating charge as Kv2.1 + AMIGO1 cells, indicating a shift in gating current activation (Fig. 3.6F). The shift in voltage dependence was quantified by fitting $Q_{ON,fast}$–V with a Boltzmann (Fig. 3.6G, H, I) yielding $\Delta V_{g,Mid,ON,fast}$ of -12.8 ± 3.5 mV (SEM) (Fig. 3.6K) and a $\Delta z_{g,ON,fast}$ of 0.215 ± 0.058 e_0 (SEM) (Fig. 3.6J) (Table 3.2). This result indicates that AMIGO1 modulates the early gating charge movement which occurs before pore opening.

To determine whether AMIGO1 modulates the kinetics of early gating charge movement, we extracted a time constant (τ_{ON}) from the decay phase of $I_{g,ON}$ that occurs before 10 ms (Fig. 3.6B top, C top) (Eqn. H) as in (320). In Kv2.1 + AMIGO1 cells, the τ_{ON}–V relation shifts to more negative voltages compared to control (Fig. 3.6L, M, N). Above +30 mV, the mean τ_{ON} for Kv2.1 + AMIGO1 cells was faster than the mean τ_{ON} from Kv2.1–control cells (Fig. 3.6N). Fitting the τ_{ON}–V with rate theory equations

indicated AMIGO1 accelerates the forward rate of gating charge movement by 1.7x at neutral voltage and decreases the voltage dependence of this rate by 13% (Fig. 3.6N). This result indicates that voltage sensors activate faster in the presence of AMIGO1, consistent with destabilization of the earliest resting conformation of the voltage sensors by AMIGO1.

To measure if AMIGO1 alters the total gating charge movement, we integrated OFF gating currents ($I_{g,OFF}$) at -140 mV after 100 ms voltage steps (Fig. 3.6B bottom, C bottom, O, P, Q). The density of Q_{OFF} elicited by voltage steps above -10 mV was not significantly different between Kv2.1–control and Kv2.1 + AMIGO1 cells (Fig. 3.6Q), indicating that AMIGO1 did not alter the density of channels expressed, nor the total gating charge per channel. However, between -25 mV and -10 mV, Kv2.1–control cells did not move as much gating charge as Kv2.1 + AMIGO1 cells, indicating a shift in voltage dependence (Fig. 3.6Q). Boltzmann fits (Fig. 3.6R, S, T), yielded $\Delta V_{g,Mid,OFF}$ of -10.8 ± 2.4 mV (SEM) (Fig. 3.6V) and a $\Delta z_{g,OFF}$ of 0.43 ± 0.20 e_0 (SEM) (Fig. 3.6U) (Table 3.2), indicating that AMIGO1 shifts total gating charge movement to more negative voltages. Overall, we find that AMIGO1 affects every aspect of gating current we have analyzed to a greater degree than the K^+ conductance. As both $Q_{ON,fast}$–V and α_{0mV} measurements report the gating charge movements out of the earliest resting conformation, these results indicate that AMIGO1 destabilizes the earliest resting conformation relative to voltage sensor conformations later in the conduction activation pathway of Kv2.1.

AMIGO1 accelerates voltage-stimulated GxTX–594 dissociation

To further test the hypothesis that AMIGO1 specifically destabilizes the earliest resting conformation of Kv2.1 voltage sensors, we probed the stability of this conformation with GxTX–594 fluorescence. The earliest resting conformation is stabilized by GxTX (320) and when occupancy of this conformation is decreased by voltage activation, the rate of GxTX–594 dissociation accelerates (321). Destabilization of the earliest resting conformation by AMIGO1 is expected to increase the rate of GxTX–594 dissociation when voltage sensors are partially activated. To test this prediction, we measured the

rate of GxTX–594 dissociation at +30 mV, a potential at which about 20% of Kv2.1 gating charge is activated with GxTX bound (320). The rate of GxTX–594 dissociation from Kv2.1 ($k_{\Delta F}$) accelerated from 0.073 ± 0.010 s^{-1} (SEM) in control cells to 0.115 ± 0.015 s^{-1} (SEM) in cells positive for AMIGO1–YFP fluorescence (Fig. 3.7). As we see no evidence that AMIGO1 alters GxTX–594 affinity in cells at rest (Supplemental Fig. 3.5), this 1.6-fold acceleration of $k_{\Delta F}$ is consistent with AMIGO1 destabilizing the earliest resting conformation of voltage sensors. The thermodynamic model developed to interpret the $k_{\Delta F}$ of GxTX–594 dissociation (321) estimates that AMIGO1 decreases the stability of the earliest resting conformation of each voltage sensor by 1.9-fold or a ΔG_{AMIGO1} of -1.5 kcal/mol for Kv2.1 tetramers (Eqn. L). This result is consistent with AMIGO1 destabilizing the resting voltage sensor conformation to speed up voltage sensor activation and shift conductance to lower voltages.

An extracellular surface potential mechanism of AMIGO1 was not detected

To differentiate between mechanisms through which AMIGO1 could change voltage sensor activation we probed whether the large AMIGO1 extracellular domain is directly changing the electrostatic environment of Kv2.1's voltage sensors. Per surface charge theory, local extracellular negative charges could attract positive gating charges to activate channels (389). AMIGO1 possesses five extracellular glycosylation sites (201), each potentially decorated with negatively-charged sugar moieties (121). AMIGO1 also has a conserved negatively charged residue predicted to be near the extracellular side of the membrane (69, 201). Similar structural characteristics are found in Nav β auxiliary subunits which, like AMIGO1, are glycosylated, single transmembrane pass protein with an immunoglobulin-domain. Nav β1 has been proposed to interact with Nav1.4 α subunit through surface charge effects (273, 390, 391). We tested if AMIGO1 likewise affects Kv2.1 activation through electrostatic surface charge interactions.

To measure the electrostatics of the environment immediately surrounding the Kv2.1 voltage sensor domain complex with and without AMIGO1, we employed far-red polarity-sensitive fluorescence

(331). The polarity-sensitive fluorophore, JP, was localized to the Kv2.1 voltage sensor by conjugating GxTX to JP at either residue Ser13 or Lys27 (322). When GxTX binds to the extracellular S3b region of the Kv2.1 channel, Ser13 and Lys27 occupy positions of distinct polarity (322). At resting membrane potentials, GxTX Ser13Pra(JP) has an emission maximum of 644 nm, consistent with the homology-based prediction that Ser13 of GxTX localizes in an aqueous environment branched away from S4. Conversely, GxTX Lys27Pra(JP) has an emission maximum of 617 nm, consistent with the prediction that Lys27 sits in the polar region of the membrane adjacent to S4 (322). If AMIGO1 were to alter the electrostatic environment of the resting conformation of the Kv2.1 voltage sensor domain, we would expect either of these environmental point detectors, GxTX Ser13Pra(JP) or GxTX Lys27Pra(JP), to exhibit an altered emission maximum.

Full emission spectra of JP fluorescence from Kv2.1–CHO cells transfected with AMIGO1–YFP and treated with GxTX Ser13Pra(JP) or GxTX Lys27Pra(JP) were fitted with 2-component split pseudo-Voigt functions (Fig. 3.8C, F). Fitting shows emission peaks, 644 nm and 617 nm, respectively, are unchanged with or without AMIGO1–YFP, consistent with the local electrostatic environment surrounding the JP probes positioned on resting Kv2.1 voltage sensors not being altered by AMIGO1 expression. Previous work has shown that GxTX Lys27Pra(JP) emission peak wavelength is sensitive to conformational changes among early resting states of voltage sensors (322). The absence of any AMIGO1-induced change in environment for either of these GxTX sidechains suggests that AMIGO1 does not cause significant changes to the local environment of the GxTX binding site on the S3b segment of Kv2.1, nor the GxTX position in the membrane when bound to the channel. These results are consistent with destabilization of the GxTX binding site by AMIGO1 being indirect, as the binding site itself appears to retain the same conformation and local environment in the presence of AMIGO1. However, it remains possible that AMIGO1 acts extracellularly to modulate Kv2.1 by a mechanism that these GxTX(JP)-based sensors do not detect.

We also tested whether AMIGO1 acts by a surface charge mechanism with a classical charge screening approach. Surface charge interactions can be revealed by increasing the concentration of Mg^{2+} to screen, or minimize, the impact of fixed negative charges near the voltage sensors (389, 392). If AMIGO1 alters surface potential, we would expect elevated Mg^{2+} to shrink $\Delta V_{i,Mid}$. To determine whether surface charge screening suppresses the AMIGO1 effect, voltage clamp experiments were conducted as in Fig. 3.3, except external recording solutions contained 100 mM Mg^{2+} (Fig. 2.9A, B, C). Kv2.1 requires more positive voltage steps to activate in high Mg^{2+} solutions (Table 3.1), consistent with sensitivity to surface charge screening (393). In high Mg^{2+}, AMIGO1 effected a $\Delta V_{i,Mid}$ of -7.4 ± 2.4 mV (SEM) (Fig. 3.10H) but did not change z_i (Fig. 3.9G) (Table 3.1). When compared to low Mg^{2+} conditions by Ordinary 2-way ANOVA, $\Delta V_{i,Mid}$ was not significantly different in normal versus 100 mM Mg^{2+} (interaction of $p = 0.33$). Hence, Mg^{2+} altered Kv2.1 activation in a manner consistent with surface charge screening, yet Mg^{2+} did not detectably abrogate the AMIGO1 effect. However, we cannot rule out the possibility of a screened site that is inaccessible to Mg^{2+}. While neither extracellular fluorescence measurements nor surface charge screening detected an extracellular impact of AMIGO1, we are not able to rule out the possibility of an extracellular coupling to AMIGO1 that was not detected by these methods.

Discussion

We asked whether AMIGO1 modulates Kv2.1 conductance by modulating conformational changes of pore opening or voltage sensor activation. We found that AMIGO1 destabilizes the resting, inward conformation of Kv2.1 voltage sensors, causing channels to activate at more negative voltages. This conclusion is supported by three major results:

1) AMIGO1 destabilizes the earliest resting conformation of Kv2.1 voltage sensors.

AMIGO1 expression accelerated conductance activation only at a subset of voltages where the activation kinetics are voltage sensitive (Fig. 3.3M). When voltage sensor movements were measured directly, gating current recordings revealed an acceleration of the forward rate constant (τ_{ON}) of gating charge activation in cells with AMIGO1. Between 0 and 120 mV, pore opening is 10-30x slower than $I_{g,ON}$ decay (Fig. 3.3M, 3.6N), too slow to influence the first few ms of $I_{g,ON}$. When the change in the forward rate α_{0mV} (Fig. 3.6N), was used to estimate the amount of energy AMIGO1 contributes to modulating Kv2.1 conformational bias, we found that AMIGO1 imparted -1.3 kcal/mol per channel (Eqn. J) to $\Delta G^{\ddagger}_{AMIGO1}$. From this result we conclude that AMIGO1 speeds the rate of conformational change between the earliest resting conformation and its transition state in the activation path. Additionally, the AMIGO1 effect on GxTX–594 dissociation at +30 mV is consistent with AMIGO1 opposing the action of GxTX–594, which stabilizes resting voltage sensors. All available evidence indicates that AMIGO1 destabilizes the earliest resting conformation of Kv2.1 voltage sensors. We estimate that AMIGO1 destabilizes the fully resting conformation of Kv2.1 channels by ~3 kcal/mol, relative to the fully active open state, and that about half of this energy lowers the barrier for the initial exit of voltage sensors from their resting conformation (Fig. 3.10A).

2) AMIGO1 has a greater impact on the voltage sensors than the pore opening.

Free energy estimates indicate more AMIGO1 perturbation of the *Q–V* than the midpoint of the *G–V*. The ΔG for AMIGO1's impact on voltage sensor activation ranged from -1.9 kcal/mol to -3.1 kcal/mol depending on the calculation method (Table 3.2). Yet, the ΔG_{AMIGO1} calculated at the conductance midpoint was only -0.3 kcal/mol (Table 3.1). This lesser impact on pore opening is consistent with a direct impact of AMIGO1 on voltage sensor movements which are coupled to pore opening. Notably ΔG_{AMIGO1} calculated at the conductance midpoint widens to -0.8 kcal/mol when voltage sensor activation is limited with GxTX–594. When we looked at pore opening directly, we saw no evidence suggesting a direct effect of AMIGO1. We saw no change in the slope of the *G–V* relationship with AMIGO1 (Table 3.1), nor sigmoidicity (Fig. 3.3), nor single channel measurements (Fig. 3.4). While these negative results do not eliminate the possibility that AMIGO1 has a small direct effect on pore opening, these negative results constrain the effect size of AMIGO1 on pore opening equilibria to be smaller than the error associated with our measurements.

3) The AMIGO1 impact on conductance is malleable

In Kv2.1–CHO cells, AMIGO1 shifts the V_{Mid} of conductance by -5.7 ± 2.2 mV (SEM). With GxTX–594, the AMIGO1 *G–V* shift widens to -22.3 ± 4.8 (SEM) (Table 3.1). This remarkable result indicates that the AMIGO1 effect on conductance can change in magnitude. While we have not completely excluded the possibility that AMIGO1 has a direct interaction with GxTX–594, we think this unlikely, as we saw no sign of an AMIGO1-dependent environmental change around GxTX–JP conjugates, and GxTX–594 had a similar affinity for resting Kv2.1. We think it is more likely that AMIGO1 and GxTX–594 interact only allosterically, and favor the explanation that GxTX makes the $V_{i,Mid}$ of conductance more sensitive to the early voltage sensor transition which AMIGO1 modulates. After its fast voltage sensor movement, Kv2.1 has a slow conductance-activating step that makes the 4th power of the *Q–V* not predictive of the *G–V* (299, 320, 333, 334). GxTX stabilizes the earliest resting conformation of Kv2.1 voltage sensors such that 4th

power Boltzmann fits to the *G–V* are similar to the *Q–V* (320). This suggests the $V_{i,Mid}$ is more responsive to AMIGO1 in GxTX–594 because the *G–V* becomes limited by early voltage sensor movement.

To test the idea that AMIGO1 modulation of voltage sensors could result in different $\Delta V_{i,Mid}$ of *G–Vs*, we performed calculations with a voltage sensor shift model composed of simple gating equations. This voltage sensor shift model incorporates distinct $V_{1/2}$ values assigned to independent voltage sensor ($V_{VSD,1/2}$) and pore ($V_{Pore,1/2}$) transitions, all of which must activate to allow channel opening. Calculations incorporating a constant $\Delta V_{VSD,1/2}$ shift with no change in $V_{Pore,1/2}$ demonstrate that the $\Delta V_{i,Mid}$ of *G–V* can be malleable. In these calculations an AMIGO1 shift of $\Delta V_{VSD,1/2}$ = -22.4 mV resulted in $\Delta V_{i,Mid}$ = -5.0 mV (Fig. 3.10B), similar to the empirical measurement $\Delta V_{i,Mid}$ = -5.7 mV of Kv2.1 with AMIGO1 (Fig. 3.3). However, when $V_{VSD,1/2}$ was modified to fit GxTX–594 data, this same AMIGO1 shift of $\Delta V_{VSD,1/2}$ = -22.4 mV yielded a larger shift *G–V* shift, $\Delta V_{i,Mid}$ = -21.8 mV (Fig. 3.10B). While the gating model implied by these calculations is highly simplified and does not recapitulate all of our data, it does demonstrate a mechanism by which a fixed modulation of voltage sensors could result in varying $\Delta V_{i,Mid}$ shifts. As the voltage dependence of Kv2.1 activation is dynamically modulated by many forms of cellular regulation and can vary dramatically (17, 23, 27, 28, 305, 355, 373, 374, 394–396), the impact of AMIGO1 might also fluctuate. A malleable impact of AMIGO1 in response to Kv2.1 regulation could perhaps explain why a larger *G–V* shift was originally reported (32), than was observed here or elsewhere (33).

The voltage sensor shift mechanism we propose does not require changes in pore opening, or voltage sensor-pore coupling. Maverick and colleagues (33) suggested that the effects of AMIGO proteins on Kv2.1 conductance could be described by increasing the coupling between the voltage sensor and pore opening without a shift in the *Q–V* curve (33), similar to a mechanism by which leucine-rich-repeat-containing protein 26, LRRC26, modulates large-conductance Ca^{2+}-activated K^+ channels (114). As the precise voltage sensor-pore coupling mechanisms for Kv2.1 channels have yet to be defined, we cannot rule out the possibility that AMIGO1 also alters coupling. However, we see no reason that AMIGO1 must

do anything other than destabilize the earliest resting conformation of voltage sensors to modulate Kv2.1 conductance.

Limitations

More detailed investigation of the AMIGO1 impact on the Kv2.1 activation pathway was limited by the relatively small magnitude of AMIGO1-dependent effects versus the cell-to-cell variability, with $\Delta V_{i,Mid}$ as low as 5 mV, and standard deviations for $V_{i,Mid}$ of 4 to 9 mV (Table 3.1, excluding GxTX–594). While we compensated for the limited power of the AMIGO1 effect by increasing replicates, a decreased cell-to-cell would enable more precise biophysical investigation. This degree of cell-to-cell variability does not appear to be unique to our laboratory. Midpoints reported for rat Kv2.1 activation in HEK293 cells span a 36 mV range, from -20.2 mV to 16.4 mV (32, 33, 243, 345, 354, 388, 397–403). When we calculated V_{Mid} standard deviation values from the standard errors and n-values in these studies, standard deviations ranged from 1 to 17 mV, on par with our own. We suspect these notable V_{Mid} deviations result from the many different types of regulation to which Kv2.1 channels are susceptible (305, 306). Techniques to constrain the cell-to-cell variability in Kv2.1 function could allow more precise mechanistic studies of AMIGO1 modulation.

Our interpretations assume that the AMIGO1 effect is similar whether Kv2.1 is expressed at low density to measure K^+ currents or at high density for gating current and imaging experiments. Auxiliary subunit interactions with pore α subunits can be influenced by many factors that can alter their assembly and functional impact on channel currents (265, 404–408). However, if Kv2.1 channels in K^+ current recording were modulated less by AMIGO1, we would expect a decrease in Boltzmann slope of the fit, a bimodal *G–V* relation, or increased cell-to-cell variability with AMIGO1. We do not observe any of these with CHO cells. The similar impact of AMIGO1 on Kv2.1 conductance in two cell lines (Table 3.1) and consistency in effect magnitudes with an independent report (33), further suggest that AMIGO1 effect is saturating in our K^+ conductance measurements. Thus, while incomplete complex assembly and other

factors could in theory influence the magnitude of the AMIGO1 impact on Kv2.1 conductance, we do not see evidence that would negate our biophysical assessment of the mechanism through which AMIGO1 alters Kv2.1 conductance.

The most parsimonious explanation for the effect AMIGO1 has on the Kv2.1 conduction–voltage relation seems to be a direct interaction with Kv2.1 voltage sensors. However, it also seems possible that AMIGO1 proteins could change cellular regulation of which in turn modulates Kv2.1. Even if AMIGO1 acts by an indirect mechanism, our mechanistic conclusions remain valid, as they are not predicated on a direct protein–protein interaction between AMIGO1 and Kv2.1.

Potential physiological consequences of an AMIGO1 gating shift

The impact of AMIGO1 on Kv2.1 voltage sensors suggests that all voltage-dependent Kv2 functions are modulated by AMIGO1. How might the AMIGO1 impact on voltage sensor dynamics affect cellular physiology? As AMIGO1 is colocalized with seemingly all the Kv2 protein in mammalian brain neurons (32, 121, 409), our results suggest that AMIGO1 could cause Kv2 voltage-dependent functions to occur at more negative potentials in neurons. Consistent with this suggestion, I_K currents from hippocampal pyramidal neurons isolated from AMIGO1 knockout mice are altered compared to wild type I_K currents (375). AMIGO1 knockout mice display schizophrenia-related features (375) and AMIGO1 knockdown zebrafish have deformed neural tracts (124). However, it is unclear whether these deficits are due to effects on channel gating or other functions of AMIGO1, such as extracellular adhesion. In addition to electrical signaling, Kv2 proteins have important nonconducting functions (121, 242, 243, 349, 350, 352), which AMIGO1 could potentially impact. Currently, we can only speculate about whether physiological impacts of AMIGO1 are due to alteration of Kv2-mediated signaling.

Are the AMIGO1 effects on Kv2.1 conductance activation big enough to meaningfully impact cellular electrophysiology? To begin to address this question, we estimated the impact that AMIGO1

would have on neuronal action potentials. In mammalian neurons, Kv2 conductance can speed action potential repolarization (29, 410), dampen the fast afterdepolarization phase (410), deepen trough voltage, and extend after-hyperpolarization (29) to impact repetitive firing (3, 29, 410–412). To estimate the impact AMIGO1 might have on the action potentials, we superimposed the impact of AMIGO1 measured in Kv2.1–CHO cells onto the Kv2 conductance in rat superior cervical ganglion (SCG) neurons, which Liu and Bean (29) found to account for ~55% of outward current during an action potential. We roughly approximated an SCG action potential as a 1.5 ms period at 0 mV, during which the parameters fit by Liu and Bean predict 2.2% of the maximal Kv2 conductance will be activated. If the Kv2 parameters are modified to mimic removal of AMIGO1, SCG neuron Kv2 conductance at the end of the mock action potential decreases by 70% (Table 3.3). This large effect due to small changes in conductance activation suggests that the AMIGO1 gating shift could have a profound impact on electrical signaling. Furthermore, we think the AMIGO1 impact could be even greater. Liu and Bean found that in SCG neurons, Kv2 activation lacks the slow pore-opening step we see in Kv2.1–CHO cells, and SCG Kv2 kinetics were effectively modeled by a Hodgkin-Huxley n4 model of activation (342). This suggests that only voltage sensor activation limits conductance activation in the SCG neurons. When the impact of AMIGO1 on Kv2.1–CHO voltage sensors is applied to SCG neuron parameters, Kv2 conductance at the end of the mock action potential decreases by 89% (Table 3.3). This analysis suggests that removal of the AMIGO1 effect in neurons could be functionally equivalent to blocking the majority of the Kv2 current during an action potential, which would in turn be expected to have impacts on repetitive firing (3, 29, 410–412). However, we stress that any predicted impact of AMIGO1 on action potentials is merely speculation.

Conclusions

To shift the activation midpoint of Kv2.1 conductance to lower voltages, AMIGO1 destabilizes the earliest resting conformations of Kv2.1 voltage sensors relative to more activated conformations. While we cannot rule out a direct influence on pore dynamics, we saw no indication of such. We propose that AMIGO1 shifts the voltage–dependence of Kv2.1 conduction to more negative voltages by modulating early voltage sensor movements. We also propose that because AMIGO1 acts on early voltage sensor movements, modulation of Kv2 gating can alter the impact of AMIGO1 on K^+ conductance.

Acknowledgements

We thank Vladimir Yarov-Yarovoy, James Trimmer, Karen Zito, and Tsung-Yu Chen of University of California Davis for constructive feedback integral to design and synthesis of experimental ideas. The authors would like to thank the UC Davis statisticians Dr. Sandra Taylor and Dr. Susan Stewart and as well as Karl Brown for their consultation on statistical approaches.

This research was funded by National Institutes of Health grants T32GM007377 (RJS), F31NS108614 (RJS), R01NS096317 (JTS and BEC), and R21EY026449 (JTS). The GxTX-Ser13Cys, GxTX-Ser13Pra, and GxTX-Lys27Pra peptides were synthesized at the Molecular Foundry of the Lawrence Berkeley National Laboratory under U.S. Department of Energy contract DE-AC02-05CH11231. The authors declare no competing financial interests.

Methods and Materials

GxTX peptides

A conjugate of a cysteine–modified guangxitoxin–1E and the maleimide of fluorophore Alexa594 (GxTX Ser13Cys(Alexa594)) was used to selectively modulate Kv2.1 channel gating and to fluorescently identify surface-expressing Kv2.1 channels (321). Conjugates of propargylglycine (Pra)–modified GxTX and the fluorophore JP–N_3 (GxTX Ser13Pra(JP) and GxTX Lys27Pra(JP)) were used to monitor the chemical environment surrounding GxTX when localized to the channel (322). All modified GxTX–mutants were synthesized by solid phase peptide synthesis as described (322, 341, 413). Stock solutions were stored at -80 °C and thawed on ice on the day of experiment.

Cell culture and transfection

The HEK293 cell line subclone TS201A was a gift from Vladimir Yarov-Yarovoy and was maintained in DMEM (Gibco Cat# 11995-065) with 10% Fetal Bovine Serum (HyClone, SH30071.03HI, LotAXM55317) and 1% penicillin/streptomycin (Gibco, 15-140-122) in a humidified incubator at 37°C under 5% CO_2. Chinese Hamster Ovary (CHO) cell lines were a Tetracycline-Regulated Expression (T-REx) variant (Invitrogen, Cat# R71807), and cultured as described previously (341). The Kv2.1–CHO cell subclone (366) was stably transfected with pCDNA4/TO encoding the rat Kv2.1 (rKv2.1) channel. Cell lines were negative for mycoplasma by biochemical test (Lonza, LT07). 1 μg/ml minocycline (Enzo Life Sciences), prepared in 70% ethanol, was added to Kv2.1–CHO cells to induce rKv2.1 channel expression for 1.5 hours to minimize series resistance-induced voltage errors in K^+ current recordings or for 48 hours to produce sufficient Kv2.1 density necessary for recording gating currents. 5 minutes prior to transfection, cells were plated at 40% confluency in unsupplemented culture media free of antibiotics, selection agents, and serum and allowed to settle at room temperature. For imaging studies (except

concentration–response), cells were plated in 35 mm No. 1.5 glass–bottom dishes (MatTek, P35G-1.5-20-C). For concentration-response time–lapse imaging, cells were plated onto 22 x 22 mm No. 1.5H cover glass (Deckglaser). For electrophysiological studies, cells were plated in 35 mm tissue culture treated polystyrene dishes (Fisher Scientific, 12-556-000). Transfections were achieved with Lipofectamine 2000 (Life Technologies, 11668-027). Each transfection included 220 μL Opti–MEM (Life Technologies, 31985062), 1.1 μL Lipofectamine, and the following amount of plasmid DNA. HEK293 cell experiments: 0.1 μg of mKv2.1 DNA and either 0.1 μg of pEGFP, mAMIGO1–pIRES2–GFP DNA, or hSCN1β–pIRES2–GFP. The pIRES2–GFP vector has an encoded internal ribosome entry site which promotes continuous translation of two genes from a singular mRNA (414) so that GFP fluorescence indicates the presence of AMIGO1 or SCN1β mRNA. Kv2.1–CHO cell experiments: 1 μg of either mAMIGO1–pEYFP–N1, pEGFP, rAMIGO2–pEYFP–N1, or rAMIGO3–pEYFP–N1. CHO cell experiments: 1 μg of both pCAG–ChroME–mRuby2-ST and mAMIGO1-pEYFP-N1. Cells were incubated in the transfection cocktail and 2 mL of unsupplemented media for 6-8 hours before being returned to regular growth media, and used for experiments 40-48 hours after transfection. pEGFP, mAMIGO1–pEYFP–N1, and pCAG–ChroME-mRuby2-ST (384) plasmids were gifts from James Trimmer. mAMIGO1–pEYFP–N1 uses a VPRARDPPVAT linker to tag the internal C–terminus of wild–type mouse AMIGO1 (NM_001004293.2 or NM_146137.3) with eYFP. pCAG–ChroME–mRuby2–ST encodes an mRuby2–tagged channelrhodopsin with a Kv2.1 PRC trafficking sequence (12, 384). mKv2.1 (NM_008420) was purchased from OriGene (MG210968). hSCN1β–pIRES2–GFP was a gift from Vladimir Yarov-Yarovoy. mAMIGO1 was subcloned into pIRES2–GFP between NheI and BamHI restriction sites. rAMIGO2–pEYFP–N1 and rAMIGO3–pEYFP–N1 were generated by subcloning rat AMIGO2 (NM_182816.2) or rat AMIGO3 (NM_178144.1) in place of mAMIGO1 in the mAMIGO1–pEYFP–N1 vector.

Whole-cell K+ ionic currents

Voltage clamp was achieved with an Axopatch 200B patch clamp amplifier (Axon Instruments) run by Patchmaster (HEKA). Solutions: HEK293 internal (in mM) 160 KCl, 5 EGTA, 10 HEPES, 1 $CaCl_2$, 2 $MgCl_2$, and 10 glucose, adjusted to pH 7.3 with KOH, 345 mOsm. HEK293 external (in mM) 5 KCl, 160 NaCl, 10 HEPES, 2 $CaCl_2$, 2 $MgCl_2$, 10 glucose, pH 7.3 with NaOH, 345 mOsm, 5 μM tetrodotoxin added to recording solution: LJP 3.9 mV, E_K: -89.0 mV with HEK293 internal. Kv2.1–CHO internal (in mM) 70 KCl, 5 EGTA, 50 HEPES, 50 KF, and 35 KOH, adjusted to pH 7.4 with KOH, 310 mOsm. Kv2.1–CHO external (in mM) 3.5 KCl, 155 NaCl, 10 HEPES, 1.5 $CaCl_2$, 1 $MgCl_2$, adjusted to pH 7.4 with NaOH, 315 mOsm: LJP 8.5 mV, E_K: -97.4 mV with Kv2.1–CHO cell internal. High Mg^{2+} Kv2.1–CHO external (in mM) 3.5 KCl, 6.5 NaCl, 10 HEPES, 1.5 $CaCl_2$, 100 $MgCl_2$, adjusted to pH 7.4 with NaOH, 289 mOsm: LJP 13.1 mV, E_K: -97.4 mV with Kv2.1–CHO internal. Osmolality measured with a vapor pressure osmometer (Wescor, 5520), 5% difference between batches were tolerated. Liquid junction potential (LJP) values were tabulated using Patcher's Power Tools version 2.15 (Max-Planck), and corrected *post hoc*, during analysis. Voltage protocols list command voltages, prior to LJP correction. Kv2.1–CHO cells were harvested by scraping in Versene (Gibco, 15040066) or TrypLE (Gibco, 12563011). HEK293 cells were dislodged by scraping. Cells were washed three times in a polypropylene tube in the external solution used in the recording chamber bath by pelleting at 1,000 x *g* for 2 min, and rotated at room temperature (22-24 °C) until use. Cells were then pipetted into a 50 μL recording chamber (Warner Instruments, RC-24N) and allowed to settle for 5 or more minutes. After adhering to the bottom of the glass recording chamber, cells were rinsed with external solution using a gravity–driven perfusion system. Cells showing plasma membrane-associated YFP, or intracellular GFP of intermediate intensity, were selected for patching. Thin-wall borosilicate glass recording pipettes (BF150-110-7.5HP, Sutter) were pulled with blunt tips, coated with silicone elastomer (Sylgard 184, Dow Corning), heat cured, and tip fire-polished to

resistances less than 4 MΩ. Series resistance of 3–9 MΩ was estimated from the whole-cell parameters circuit. Series resistance compensation (of < 90%) was used as needed to constrain voltage error to less than 10 mV, lag was 10 μs. Cell capacitances were 4–15 pF. Capacitance and Ohmic leak were subtracted using a P/5 protocol. Output was low-pass filtered at 10 kHz using the amplifier's built-in Bessel and digitized at 100 kHz. Traces were filtered at 2 kHz for presentation. Intersweep interval was 2 s. HEK293 cells with less than 65 pA/pF current at +85 mV were excluded to minimize impact of endogenous K^+ currents (382).). The average current in the final 100 ms at holding potential prior to the voltage step was used to zero-subtract each recording. Mean outward current ($I_{avg,step}$) was amplitude between 90-100 ms post depolarization. Mean tail current was the current amplitude between 0.2-1.2 ms into the 0 mV step. 100 μL of 100 nM GxTX-594 was flowed over cells with membrane resistance greater than 1 GΩ, pulses to 0 mV gauged the time course of binding, and the *G–V* protocol was run. Data with predicted voltage error, $V_{error} \geq 10$ mV was excluded from analysis. V_{error} was tabulated using estimated series resistance post compensation ($R_{s,post}$)

$$V_{error} = I_{avg,step} * R_{s,post} \qquad \text{(Eqn. A)}$$

For *G–V* profiles cell membrane voltage ($V_{membrane}$) was adjusted by V_{error} and *LJP*.

$$V_{membrane} = V_{command} - V_{error} - LJP \qquad \text{(Eqn. B)}$$

Tail currents were normalized by the mean current from 50 to 80 mV. Fitting was carried out using Igor Pro software, version 7 or 8 (Wavemetrics, Lake Oswego, OR) that employs nonlinear least squares curve fitting via the Levenberg-Marquardt algorithm. To represent the four independent and identical voltage sensors that must all activate for channels to open, *G–V* relations were individually fit with a 4th power Boltzmann

$$f(V) = A\left(1 + e^{\frac{-(V-V_{1/2})zF}{RT}}\right)^{-x} \qquad \text{(Eqn. C)}$$

where f(V) is normalized conductance (G), A is maximum amplitude, x is the number of independent identical transitions required to reach full conductance (for a 4th power function, x=4), $V_{1/2}$ is activation

midpoint, z is the valence in units of elementary charge (e_0), F is the Faraday constant, R is the ideal gas constant, and T is absolute temperature. The half-maximal voltage (V_{Mid}) for 4th power functions is

$$V_{\mathrm{Mid}} = V_{\mathrm{i},1/2} + \frac{42.38}{z_{\mathrm{i}}} \qquad \text{(Eqn. D)}$$

Reconstructed Boltzmann curves use average z_i and $V_{1/2} \pm$ SD. The minimum Gibbs free energy (ΔG_{AMIGO1}) that AMIGO1 imparts to conductance, was tabulated as

$$\Delta G = -\mathrm{R} \times \mathrm{T} \times \ln\left(K_{\mathrm{eq}}\right) \qquad \text{(Eqn. E)}$$

Here R = 0.00199 kcal/(K•mol) and T = 298K. K_{eq}, or the equilibrium constant of channel opening, was approximated by $\frac{f_{\mathrm{Kv2.1+AMIGO1}}(V_{\mathrm{i,Mid,Kv2.1}})}{1-f_{\mathrm{Kv2.1+AMIGO1}}(V_{\mathrm{i,Mid,Kv2.1}})}$ where $f_{\mathrm{Kv2.1+AMIGO1}}(V_{\mathrm{i,Mid,Kv2.1}})$ is the reconstructed relative conductance of Kv2.1 + AMIGO1 at $V_{i,Mid}$ of Kv2.1–control cells (Table 2.1).

Activation time constants (τ_{act}) and sigmoidicity values (σ) (415) were derived by fitting 10-90% current rise with

$$I_K = A\left(1 - e^{-\frac{t}{\tau_{\mathrm{act}}}}\right)^{\sigma} \qquad \text{(Eqn. F)}$$

Where current at end of step, $I_{avg,step}$, was set to 100%. $t = 0$ was adjusted to 100 μs after voltage step start to correct for filter delay and cell charging. Deactivation time constants (τ_{deact}) were from fitting 1 to 100 ms of current decay during 0 mV tail step with an exponential function

$$I_K = y_0 + Ae^{-\frac{t-t_0}{\tau_{deact}}} \qquad \text{(Eqn. G)}$$

Reported τ_{deact} was the average after steps to +10 mV to +120 mV or +50 mV to +120 mV in GxTX–594. Kv2.1 deactivation kinetics became progressively slower after establishment of whole-cell mode, similar to Shaker deactivation after patch excision (312). Due to the increased variability of deactivation kinetics expected from this slowing phenomenon, deactivation kinetics were not analyzed further.

On-cell single channel K+ currents

Single channel recordings were made from on-cell patches, to avoid Kv2.1 current rundown that occurs after patch excision (416). Methods same as whole-cell K^+ ionic currents unless noted. While cells selected for recording had AMIGO1–YFP fluorescence apparent at the surface membrane, we cannot be certain each single Kv2.1 channel interacted with AMIGO1. Solutions: Kv2.1–CHO single channel internal (in mM) 155 NaCl, 50 HEPES, 20 KOH, 2 $CaCl_2$, 2 $MgCl_2$, 0.1 EDTA, adjusted to pH 7.3 with HCl, 347 mOsm. Kv2.1–CHO single channel external (in mM) 135 KCl, 50 HEPES, 20 KOH, 20 NaOH, 2 $CaCl_2$, 2 $MgCl_2$, 0.1 EDTA, adjusted to pH 7.3 with HCl, 346 mOsm: LJP -3.3 mV with Kv2.1–CHO single channel internal. Thick-wall borosilicate glass (BF150-86-7.5HP; Sutter Instruments) was pulled, Sylgard-coated and fire–polished, to resistances >10 MΩ. Analysis methods were same as prior (320) unless noted. To subtract capacitive transients, traces without openings were averaged and subtracted from each trace with single-channel openings. Peaks in single channel amplitude histograms were fit to half maximum with a Gaussian function to define single channel opening level for idealization by half-amplitude threshold. Open dwell times were well described by a single exponential component which was used to derived $\tau_{closing}$. Average open dwell times were also described as the geometric mean of all open dwell times. Closed dwell times appeared to have multiple exponential components and were solely described as the geometric mean of all closed dwell times.

Whole–cell gating current measurements

Methods same as whole-cell K^+ ionic currents unless noted. Solutions: gating current internal (in mM) 90 NMDG, 1 NMDG-Cl, 50 HEPES, 5 EGTA, 50 NMDG-F, 0.01 CsCl, adjusted to pH 7.4 with methanesulfonic acid, 303 mOsm. Gating current external (in mM) 150 TEA-Cl, 41 HEPES, 1 $MgCl_2 \cdot 6 H_2O$, 1.5 $CaCl_2$, adjusted to pH to 7.3 with NMDG, 311 mOsm: LJP -3.3 mV with gating current internal.

To avoid KCl contamination of the recording solution from the pH electrode, pH was determined in small aliquots that were discarded. Cells were resuspended in Kv2.1–CHO external and washed in the recording chamber with 10 mL gating current external. Pipettes has resistances of 6-14 MΩ. Series resistances were 14-30 MΩ and compensated 50%. Cell capacitances were 6-10 pF. V_{error} was negligible (< 1 mV). P/5.9 leak pulses from -133 mV leak holding potential. An early component ON gating charge movement was quantified by integrating ON gating currents in a 3.5 ms window ($Q_{ON,fast}$) following the end of fast capacitive artifacts created from the test voltage step (which usually concluded 0.1 ms following the voltage step). The slow tail of the ON charge movement is difficult to accurately integrate in these cells, making the cutoff point arbitrary. This 3.5 ms integration window resulted in a more positive $Q_{ON,fast}$–V midpoint than with a 10 ms window (320), and more positive midpoint than the G–V relation. Differences in gating current solutions compared to prior studies may also contribute to the different midpoints reported (320, 333, 334). Currents were baseline-subtracted from 4 to 5 ms into step. Q_{OFF} was determined by integration of OFF charge movement in a 9.95 ms window after capacitive artifacts (usually 0.1 ms). Currents were baseline-subtracted from 10 to 20 ms into the step. Gating charge density *fC/pF* was normalized by cell capacitance. Q–V curves normalized to average from 100-120 mV. Q–V relations were individually fit with a 1st power Boltzmann (Eqn. C., x=1). Time constants (τ_{ON}) were determined from a double-exponential fit function

$$I_{g,ON} = A\left(e^{\frac{-t}{\tau_{ON}}}\right) + B - A_{rise}\left(e^{\frac{-t}{\tau_{rise}}}\right) \qquad \text{(Eqn. H)}$$

τ_{rise} was not used in analyses. $I_{g,OFF}$ was not well fit by Eqn. H and τ_{OFF} was not analyzed. The voltage-dependence of the forward voltage sensor activation (α) rate was determined by fitting the average τ_{ON}–V weighted by the standard error

$$\tau_{ON} = \frac{1}{\alpha_{0mV} e^{Vz_\alpha F/RT} + \beta_{0mV} e^{Vz_\beta F/RT}} \qquad \text{(Eqn. I)}$$

Reverse rates were not analyzed. Energy of AMIGO1 impact on the activation rate of all 4 voltage sensors ($\Delta G^{\ddagger}_{AMIGO1}$) was

$$\Delta G = -4 \times R \times T \times \ln\left(\frac{k_{\text{Kv2.1 + AMIGO1}}}{k_{\text{Kv2.1}}}\right) \quad \text{(Eqn. J)}$$

where $k = \alpha_{0\text{mV}}$. Estimates of ΔG_{AMIGO1} from Q–V relations were with Eqn. E or

$$\Delta G = V_{1/2} \times Q \times F \quad \text{(Eqn. K)}$$

Here F = 23.06 kcal/V • mol • e_0. Q was either z_g from fits or 12.5 e_0 as determined from a limiting slope analysis of the Kv2.1 open probability-voltage relation (299). $V_{1/2}$ was either $V_{g,\text{Mid}}$ or a median voltage ($V_{g,\text{Med}}$) as calculated from integration above and below Q_{OFF}–V relations using a trapezoidal rule (417).

Fluorescence imaging

Images were obtained with an inverted confocal/airy disk imaging system with a diffraction grating separating 400-700 nm emission into 9.6 nm bins (Zeiss LSM 880, 410900-247-075) run by ZEN black v2.1. Laser lines were 3.2 mW 488 nm, 1.2 mW 514 nm, 0.36 mW 543 nm, 0.60 mW 594 nm. Images were acquired with a 1.4 NA 63x (Zeiss 420782-9900-799), 1.3 NA 40x (Zeiss 420462-9900-000), or 1.15 NA 63x objectives (Zeiss 421887-9970-000). Images were taken in either confocal or airy disk imaging mode. The imaging solution was Kv2.1–CHO external supplemented with 0.1% bovine serum albumin and 10 mM glucose. Temperature inside the microscope housing was 24-28 °C. Representative images had brightness and contrast adjusted linearly.

C*oncentration-effect imaging.* Cells plated on coverslips were washed 3x with imaging solution then mounted on an imaging chamber (Warner Instruments, RC-24E) with vacuum grease. 100 μL GxTX–594 dilutions were applied for 10 minutes, then washed-out by flushing 10 mL at a flow rate of ~1 mL / 10 sec. 15 minutes after wash–out, the next GxTX–594 concentration was added. Airy disk imaging, 1.4 NA 63x objective (Zeiss 420782-9900-799), 0.13 μm pixels, 0.85 μs dwell, 5 sec frame rate. YFP excitation 488 nm 2% power, emission 495-550 nm. GxTX–594 excitation 594 nm 2% power, emission 495-620 nm.

Intensities extracted using FIJI (418). ROIs drawn around groups of cells ± YFP fluorescence. Dissociation constant (K_d) fit with fluorescence intensity at 0 nM GxTX–594 set to 0 with

$$f(x) = A\,\frac{1}{(1 + {K_d}/{x})} + B \qquad \text{(Eqn. L)}$$

Voltage clamp fluorimetry was conducted as described (321). Briefly, 100 μL 100 nM GxTX–594 in imaging external was applied for 10 minutes then diluted with 1 mL Kv2.1–CHO external for imaging. Airy disk imaging, 1.15 NA 63x objective (Zeiss 421887-9970-000), 0.11 μm pixels, 0.85 μs dwell, 2x averaging, 1 sec frame rate. GxTX–594 excitation 594 nm 1% power, emission 605nm long-pass. Cells with obvious GxTX–594 labeling were whole-cell voltage-clamped. Voltage clamp fluorimetry internal (in mM) 70 mM CsCl, 50 mM CsF, 35mM NaCl, 1 mM EGTA, 10 mM HEPES, adjusted to pH 7.4 with CsOH, 310 mOsm: LJP -5.3 mV with Kv2.1–CHO external. Pipettes from thin-wall glass were less than 3.0 MΩ. Cells were held at -100 mV for 30 images and stepped to +35 mV until fluorescence change appeared complete. Intensity data was extracted using Zen Blue from ROIs drawn around apparent surface membrane excluding pipette region. For presentation, fluorescence intensity traces were normalized from minimum to maximum. Rate of GxTX–594 dissociation ($k_{\Delta F}$) was fit with a monoexponential function (Eqn. G), and K_{eq} for resting vs. activated voltage sensors was calculated as described (321). ΔG_{AMIGO1} from with Eqn. J where $k = K_{eq}$.

Environment-sensitive fluorescence imaging with GxTX Ser13Pra(JP) and GxTX Lys27Pra(JP). Cells were incubated in 100 μL of GxTX(JP) solution for 5-10 minutes then washed with imaging solution. Spectral confocal imaging, 1.4 NA 63x objective, 0.24 μm pixels, 8.24 μs dwell, 2x averaging. YFP excitation 514 nm. GxTX Ser13Pra(JP) excitation 594 nm. GxTX Lys27Pra(JP) excitation 543 nm. Fluorescence counts extracted in Zen Blue. JP emission spectra were fit with two-component split pseudo-Voigt functions (322) using the curve fitting software Fityk 1.3.1 (https://fityk.nieto.pl/), which employed a Levenberg–Marquardt algorithm. Goodness of fit was determined by root-mean-squared deviation (R^2) values, which are listed in Supplemental Table 2.2 along with the parameters of each

component function. To avoid YFP overlap, fittings for spectra from cells expressing AMIGO1–YFP include emission data points from 613-700 nm for GxTX Ser13Pra(JP) and 582-700 nm for GxTX Lys27Pra(JP). Fittings for JP spectra from cells without AMIGO1-YFP included all data from 550-700 nm.

Experimental Design and Statistical Treatment

Independent replicates (*n*) are individual cells pooled over multiple transfections. The *n* from each transfection for each figure are listed in Supplemental Tables 2.3 and 2.4. In each figure panel, control and test cells were plated side by side from the same suspensions, transfected side by side, and the data was acquired from control and test cells in an interleaved fashion. Identity of transfected constructs was blinded during analysis. ANOVA analysis of transfection- or acquisition date-dependent variance of Boltzmann fit parameters and PCC/COV did not reveal a dependence, and all *n* values were pooled. Statistical tests were conducted with Prism 9 (GraphPad Software, San Diego, CA), details in figure legends.

Figures and Tables

Figure 3.1

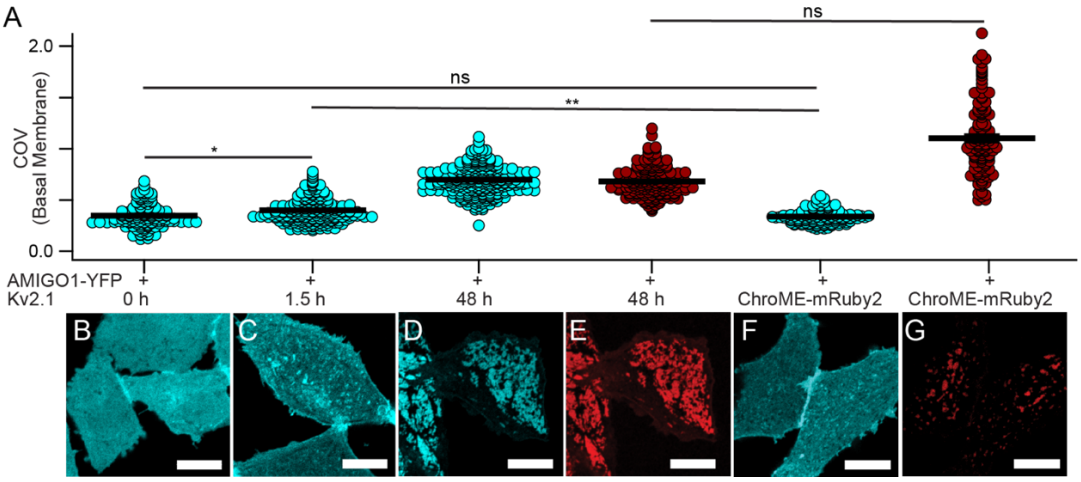

Figure 3.1. Kv2.1 reorganizes AMIGO1 in CHO cells.

(**A**) Coefficient of variation of fluorescence from AMIGO1–YFP (blue circles), GxTX–594 (red circles), or ChroME-mRuby2 (red circles). Bars are mean ± SEM. COV measurements were calculated from confocal images acquired from the glass–adhered basal membrane of the cell (exemplar confocal images in B-G). All cells were transfected with AMIGO1–YFP 48 h prior to imaging. COV from individual cells (*n*) were pooled from 4 separate transfections for each experimental condition. AMIGO1–YFP fluorescence from cells (**B**) not induced for Kv2.1 expression (COV_{0h} = 0.3492 ± 0.0098, *n* = 134), (**C**) induced 1.5 h ($COV_{1.5h}$ = 0.4013 ± 0.0077, *n* = 217), (**D**) induced 48 h (COV_{48h} = 0.6984 ± 0.0083, *n* = 277). (**E**) GxTX–594 labeling from panel D ($COV_{48h(GxTX–594)}$ = 0.6822 ± 0.010, *n* = 197). (**F**) AMIGO1–YFP fluorescence from CHO cells which lack Kv2.1 co-transfected with ChroME-mRuby2 (COV_{lack} = 0.3377 ± 0.0059, *n* = 125). (**G**) ChroME-mRuby2 fluorescence from panel F ($COV_{(ChroME-mRuby2)}$ = 1.102 ± 0.030, *n* = 128). Scale bars 10 μm.

(**Statistics**) Outliers removed using ROUT, Q = 1%. Ordinary one-way ANOVA with multiple comparisons. P-values: $COV_{0h}COV_{1.5h}$: p = 0.0467; $COV_{0h}COV_{lack}$: p = 0.9936; $COV_{1.5h}COV_{lack}$: p = 0.0081; $COV_{48h(GxTX–594)}$ $COV_{(ChroME-mRuby2)}$: p =0.9010. All other p-values ≤ 0.0001.

Figure 3.2

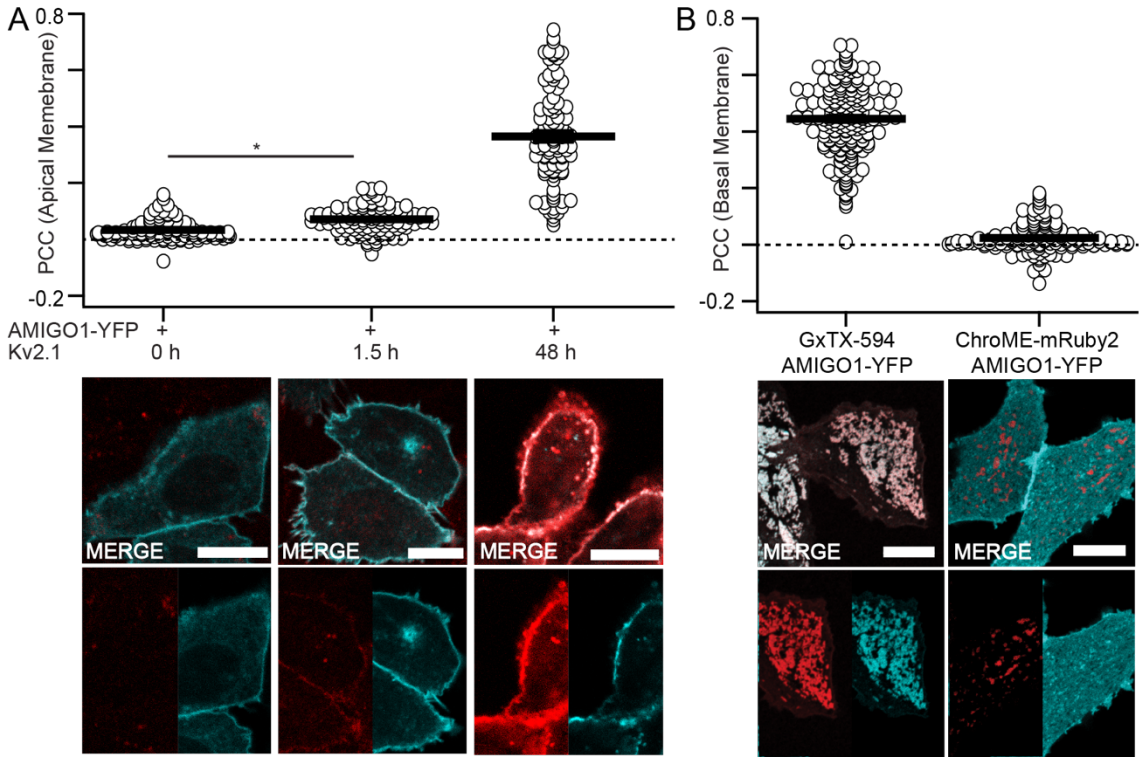

Figure 3.2. AMIGO1 colocalizes with Kv2.1 in CHO cells.

(**A**) Costes thresholded, Pearson's colocalization between AMIGO1–YFP and GxTX–594 at the cell membrane following, from left to right, 0, 1.5, or 48 h of Kv2.1 induction (exemplar confocal images in B-J below). Mean ± SEM (one-tailed ≥ 0 t-test): $PCC_{0h} = 0.0321 \pm 0.0033$, ($p < 0.0001$), $n = 101$; $PCC_{1.5h} = 0.0718 \pm 0.0042$, ($p < 0.0001$), $n = 118$; and $PCC_{48h} = 0.365 \pm 0.017$, ($p < 0.0001$), $n = 101$. (**B**) Costes thresholded, Pearson's colocalization between (left to right) AMIGO1–YFP/GxTX–594 and AMIGO1–YFP/ChroME-mRuby2 at the glass-adhered basal membrane of the cell. Exemplar images are the same as in Fig. 1 D-G. From left to right: $PCC_{GxTX–594} = 0.4449 \pm 0.0090$, ($p < 0.0001$), $n = 195$; $PCC_{ChroME\text{-}mRuby2} = 0.0242 \pm 0.0045$, ($p < 0.0001$), $n = 129$. Image panels with merge overlays (white) of GxTX–594 (red) and AMIGO1–YFP (cyan) correspond to conditions above. All scale bars are 10 μm. (**Statistics**) Outliers were removed using ROUT, Q = 1%. Ordinary one-way ANOVA with multiple comparisons. P-values: $PCC_{0h}PCC_{1.5h}$: $p = 0.346$; $PCC_{1.5h}PCC_{ChroME\text{-}mRuby2}$: $p = 0.0025$; $PCC_{0h5h}PCC_{ChroME\text{-}mRuby2}$: $p = 0.9777$. All other p-values were ≤ 0.0001.

Figure 3.3

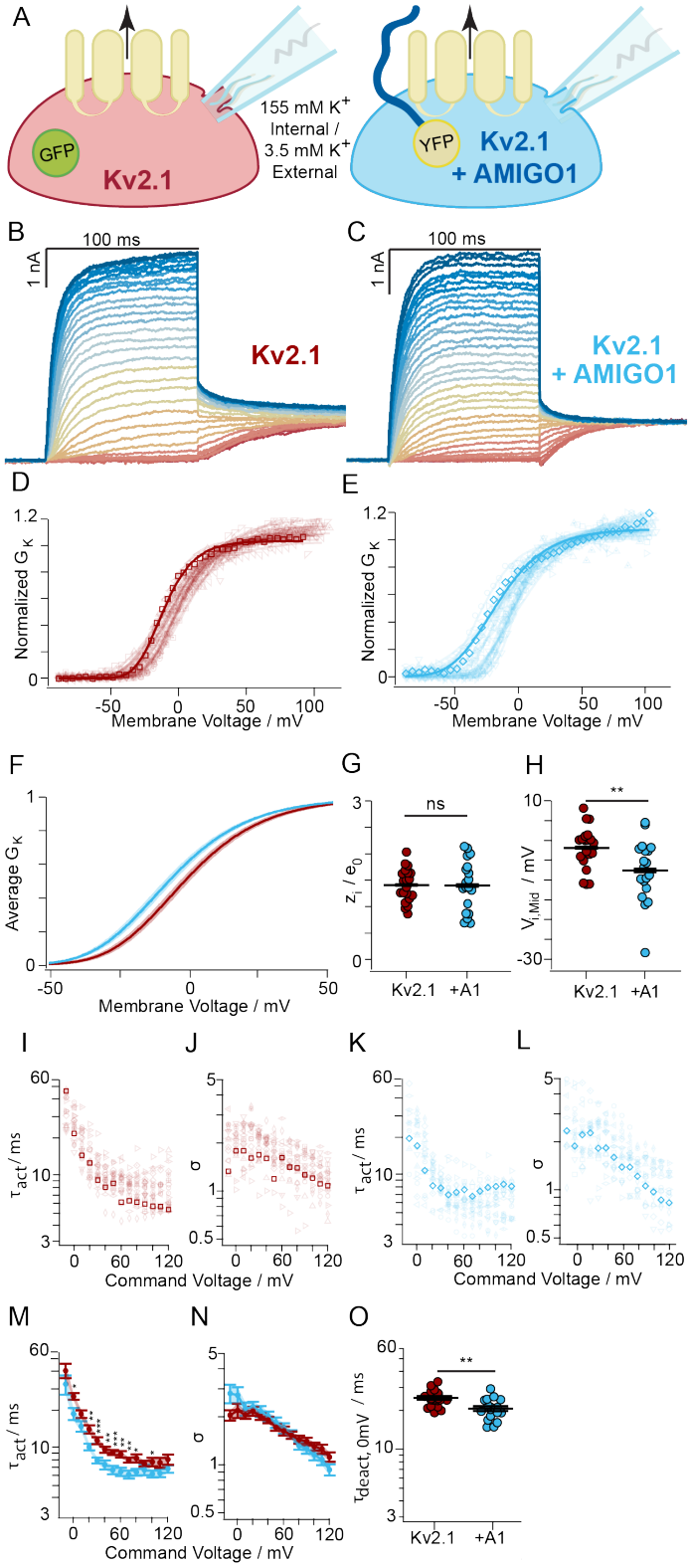
A
GFP
Kv2.1
155 mM K+
Internal /
3.5 mM K+
External
YFP
Kv2.1
+ AMIGO1
B
100 ms
1 nA
Kv2.1
C
100 ms
1 nA
Kv2.1
+ AMIGO1
D
Normalized G K
Membrane Voltage / mV
E
Normalized G K
Membrane Voltage / mV
F
Average G K
Membrane Voltage / mV
G
ns
Kv2.1 +A1
H
**
Kv2.1 +A1
I
τact / ms
J
σ
Command Voltage / mV
K
τact / ms
L
σ
Command Voltage / mV
M
τact / ms
N
σ
Command Voltage / mV
O
**
τdeact, 0mV / ms
Kv2.1 +A1

Figure 3.3. AMIGO1 shifts the midpoint and speeds activation of the Kv2.1 conductance in CHO cells.

(**A**) Experimental set up: Whole-cell K^+ currents (arrow) from Kv2.1–CHO transfected with GFP (red) or AMIGO1–YFP (blue). (**B**, **C**) Representative Kv2.1–control (6.0 pF) or Kv2.1 + AMIGO1 (14.5 pF) cell. 100 ms voltage steps ranging from -80 mV (dark red trace) to +120 mV (dark blue trace) in 5 mV increments and then to 0 mV for tail currents. Holding potential was -100 mV. Data points from representative cells are bolded in analysis panels. (**D**, **E**) Normalized tail *G–V* relationships for Kv2.1–control or Kv2.1 + AMIGO1 cells. Symbols correspond to individual cells. Lines are 4th order Boltzmann fits (Eqn. C). (**F**) Reconstructed Boltzmann fits from average $V_{i,Mid}$ and z_i (Table 2.1). Shading $V_{i,Mid}$ ± SEM. (**G**) Steepness and (**H**) midpoint of fits. (**I**, **K**) τ_{act} and (**J**, **L**) σ from fits of Eqn. F to activation (**M**) Mean τ_{act} and (**N**) σ. (**O**) τ_{deact} fits of Eqn. G to 0 mV tails: Kv2.1–control 24.9 ± 3.6 ms, Kv2.1+AMIGO1 20.6 ± 3.8 ms. Unpaired t-test $p > 0.5$ between 0 mV τ_{act} and τ_{deact} for Kv2.1–control and Kv2.1 + AMIGO1. All other statistics in Table 2.1. ***: $p = \leq 0.001$, **: $p = \leq 0.01$, *: $p = \leq 0.05$, ns: not significant. Bars are mean ± SEM.

Figure 3.4

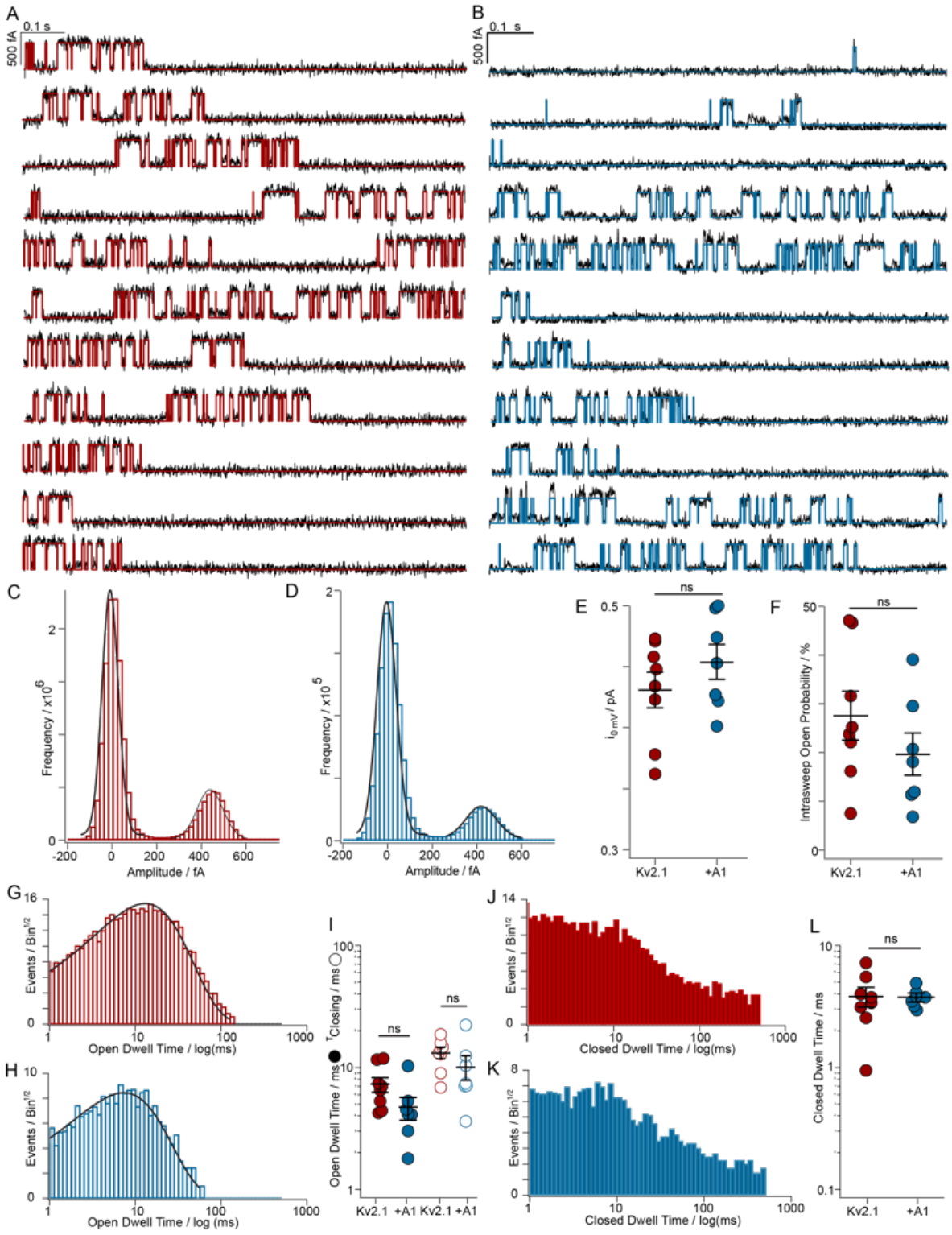
A
0.1 s
500 fA
B
0.1 s
500 fA
C
Frequency / x10^6
Amplitude / fA
D
Frequency / x10^5
Amplitude / fA
E
ns
i0 mV / pA
Kv2.1
+A1
F
ns
Intrasweep Open Probability / %
Kv2.1
+A1
G
Events / Bin^1/2
Open Dwell Time / log(ms)
H
Events / Bin^1/2
Open Dwell Time / log (ms)
I
ns
ns
τClosing / ms
Open Dwell Time / ms
Kv2.1 +A1 Kv2.1 +A1
J
Events / Bin^1/2
Closed Dwell Time / log(ms)
K
Events / Bin^1/2
Closed Dwell Time / log(ms)
L
ns
Closed Dwell Time / ms
Kv2.1
+A1

Figure 3.4. Effects of AMIGO1 on pore opening conformational changes were not apparent in single channel recordings.

(**A)** Representative single channel currents at 0 mV from Kv2.1–control and (**B**) Kv2.1 + AMIGO1. Red or blue lines are idealizations. (**C,D**) Amplitude histograms at 0 mV from the patches in A,B fit with Gaussians. (**E**) Mean single channel current amplitude: Kv2.1–control 0.43 ± 0.01 pA, Kv2.1 + AMIGO1 0.45 ± 0.02 pA. (**F**) Open probability from amplitude histograms: Kv2.1–control 28 ± 4.9%, Kv2.1 + AMIGO1 20 ± 4.2%. (**G**) Open dwell-time distributions and single exponential fits for a Kv2.1–control or (**H**) Kv2.1 + AMIGO1 patch. (**I**) Open dwell times from mean (filled circles) or exponential fit (hollow circles). Kv2.1–control: 13.0 ± 1.3 μs. Kv2.1 + AMIGO1: 9.98 ± 2.3 μs. (**J**) Closed dwell-time distributions and single exponential fit for a Kv2.1–control or (**K**) Kv2.1 + AMIGO1 patch. (**L**) Closed dwell times from mean.. Kv2.1–control: 3.80 ± 0.67 μs. Kv2.1 + AMIGO1: 3.73 ± 0.250 μs. ns = two-tailed t-test p-value > 0.05. Means ± SEM.

Figure 3.5

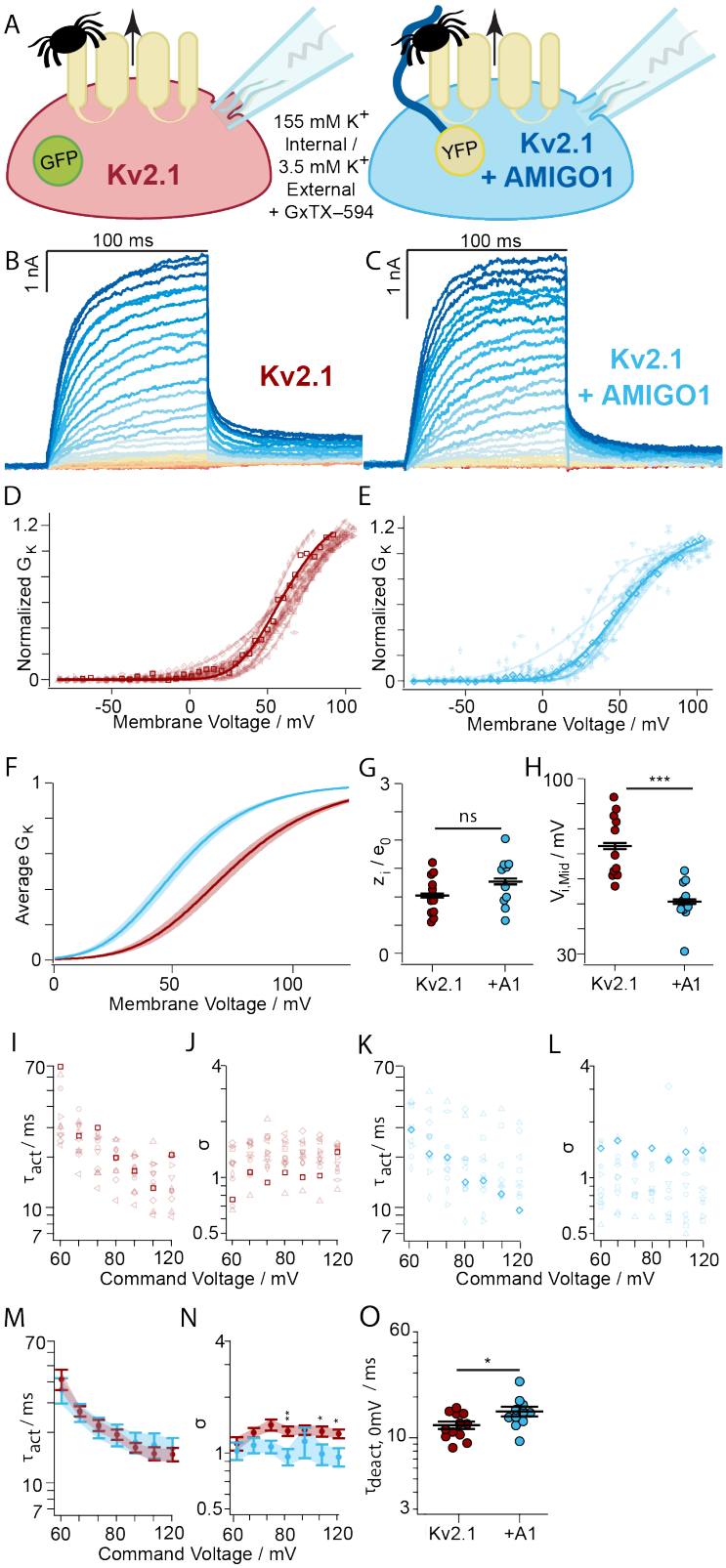
A
GFP
Kv2.1
155 mM K+
Internal /
3.5 mM K+
External
+ GxTX–594
YFP
Kv2.1
+ AMIGO1
B
100 ms
1 nA
Kv2.1
C
100 ms
1 nA
Kv2.1
+ AMIGO1
D
Normalized G K
Membrane Voltage / mV
E
Normalized G K
Membrane Voltage / mV
F
Average G K
Membrane Voltage / mV
G
z i / e0
ns
Kv2.1
+A1
H
V i,Mid / mV
***
Kv2.1
+A1
I
τact / ms
Command Voltage / mV
J
σ
Command Voltage / mV
K
τact / ms
Command Voltage / mV
L
σ
Command Voltage / mV
M
τact / ms
Command Voltage / mV
N
σ
Command Voltage / mV
O
τdeact, 0mV / ms
*
Kv2.1
+A1

Figure 3.5. The voltage sensor toxin GxTX–594 enhances AMIGO1 modulation of Kv2.1 conductance.

(**A**) Experimental set up: Whole-cell K^+ currents (arrow) from Kv2.1–CHO transfected with GFP (red) or AMIGO1–YFP (blue). Cells were treated with 100 nM GxTX–594 (tarantulas). (**B, C**) Representative Kv2.1–control (6.0 pF) or Kv2.1 + AMIGO1 (14.5 pF) cell. Same voltage protocol and representations as Fig. 2.3. (**D, E**) Normalized *G-V* relationships (**F**) Reconstructed 4th order Boltzmann fits from $V_{i,Mid}$ and z_i in Table 2.1. Shading $V_{i,Mid}$ ± SEM. (**G**) Steepness and (**H**) midpoint of fits. (**I**, **K**) τ_{act} and (**J**, **L**) σ from fits of Eqn. F to activation (**M**) Mean τ_{act} and (**N**) σ. (**O**) τ_{deact} fits of Eqn. G to 0 mV tails: Kv2.1 with GxTX–594 = 12.4 ± 2.7 ms. Kv2.1+AMIGO1 with GxTX–594 = 15.7 ± 4.2 ms. All other statistics in Table 2.1. ***: p = ≤0.001, **: p = ≤0.01, *: p = ≤0.05, ns: not significant. Bars are mean ± SEM.

Figure 3.6

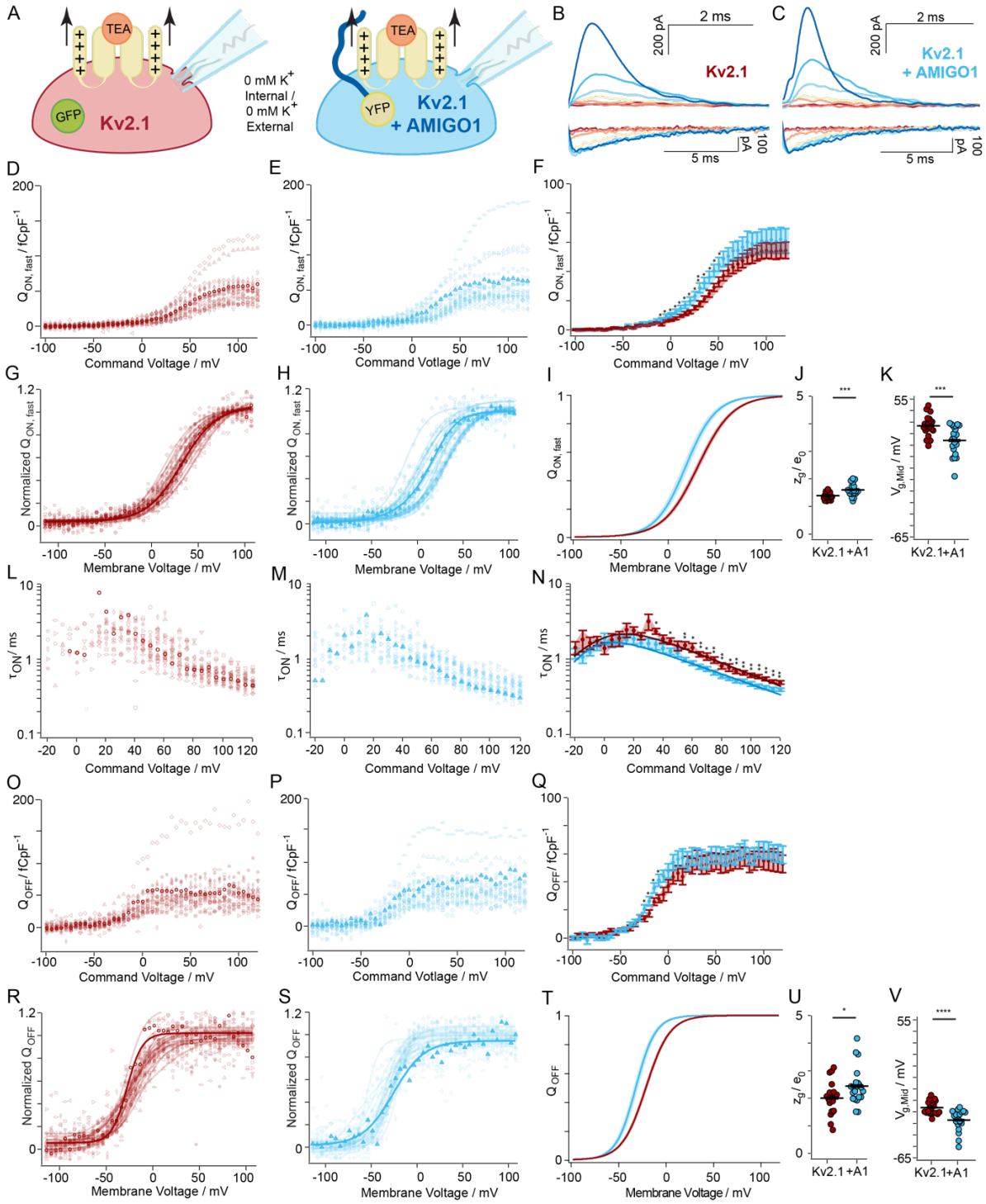
A
TEA
GFP
Kv2.1
0 mM K+ Internal / 0 mM K+ External
TEA
YFP
Kv2.1 + AMIGO1
B
200 pA
2 ms
Kv2.1
100 pA
5 ms
C
200 pA
2 ms
Kv2.1 + AMIGO1
100 pA
5 ms
D
E
F
Command Voltage / mV
G
H
I
Membrane Voltage / mV
J
K
Kv2.1+A1
L
M
N
Command Voltage / mV
O
P
Q
Command Voltage / mV
R
S
T
Membrane Voltage / mV
U
V
Kv2.1+A1

Figure 3.6. AMIGO1 facilitates the activation of Kv2.1 voltage sensors.

(**A**) Experimental set up: Gating currents (arrows) from Kv2.1–CHO transfected with GFP (red) or AMIGO1–YFP (blue). K^+ currents were eliminated removal of K^+ ions and the external tetraethylammonium, a Kv2 pore-blocker (orange). (**B, C**) Top/Bottom: Representative $I_{g,ON}/I_{g,OFF}$ from Kv2.1–control (11.9 pF) or Kv2.1 + AMIGO1 (8.2 pF). Cells were given 100 ms voltage steps ranging from -100 mV (dark red trace) to +120 mV to record $I_{g,ON}$ and then stepped to -140 mV to record $I_{g,OFF}$. The holding potential was -100 mV. Voltage pulses to -100, -50, -25, +0, +25, +50, and +100 mV are presented. Data points from representative cells are bolded in analysis panels. (**D, E**) $Q_{ON,fast}/pF$–V relation from individual cells. $Q_{ON,fast}/pF$ is gating charge integrated over the first 3.5 ms normalized to cell capacitance. (**F**) Mean $Q_{ON,fast}/pF$ (**G, H**) $Q_{ON,fast}$–V relations normalized to maximum $Q_{ON,fast}$ from +50 to +100 mV voltage steps. Solid lines represent Boltzmann fit (Eqn. C). (**I**) Reconstructed Boltzmann fits from average $V_{g,Mid,ON,fast}$ and $z_{g,ON,fast}$ (Table 2.2). Shading $V_{g,Mid,ON,fast}$ ± SEM. (**J**) Steepness and (**K**) midpoint of Boltzmann fits. (**L, M**) τ_{ON} from individual cells fit with Eqn. I. (**N**) Average τ_{ON}–V. Solid lines are Eqn. I fit. Fit values ± SD for Kv2.1–control cells: α_{0mV} = 254 ± 26 s^{-1}, z_α = 0.468 ± 0.026 e_0, β_{0mV} = 261 ± 50 s^{-1}, z_β = -1.31 ± 0.37 e_0; for Kv2.1 + AMIGO1 cells: α_{0mV} = 443 ± 26 ms^{-1}, z_α = 0.405 ± 0.019 e_0, β_{0mV} = 157 ± 52 ms^{-1}, z_β = -2.00 ± 0.55 e_0. (**O, P**) Q_{OFF}/pF relation from individual cells normalized to cell capacitance. (**Q**) Q_{OFF}/pF–V relation. (**R, S**) Q_{OFF}–V relations normalized to average Q_{OFF} from +50 to +100 mV voltage steps. Solid lines are Boltzmann fits (Eqn. C). (**T**) Reconstructed Boltzmann fits using the average $V_{g,Mid,OFF}$ and $z_{g,OFF}$ (Table 2.2). Shading $V_{g,Mid,OFF}$ ± SEM (**U**) Steepness and (**V**) midpoint of Boltzmann fits. Mean ± SEM. Statistics in Table 2.2. ****: $p = \leq 0.0001$, ***: $p = \leq 0.001$, **: $p = \leq 0.01$, *: $p = \leq 0.05$, ns: not significant. Bars are mean ± SEM.

Figure 3.7

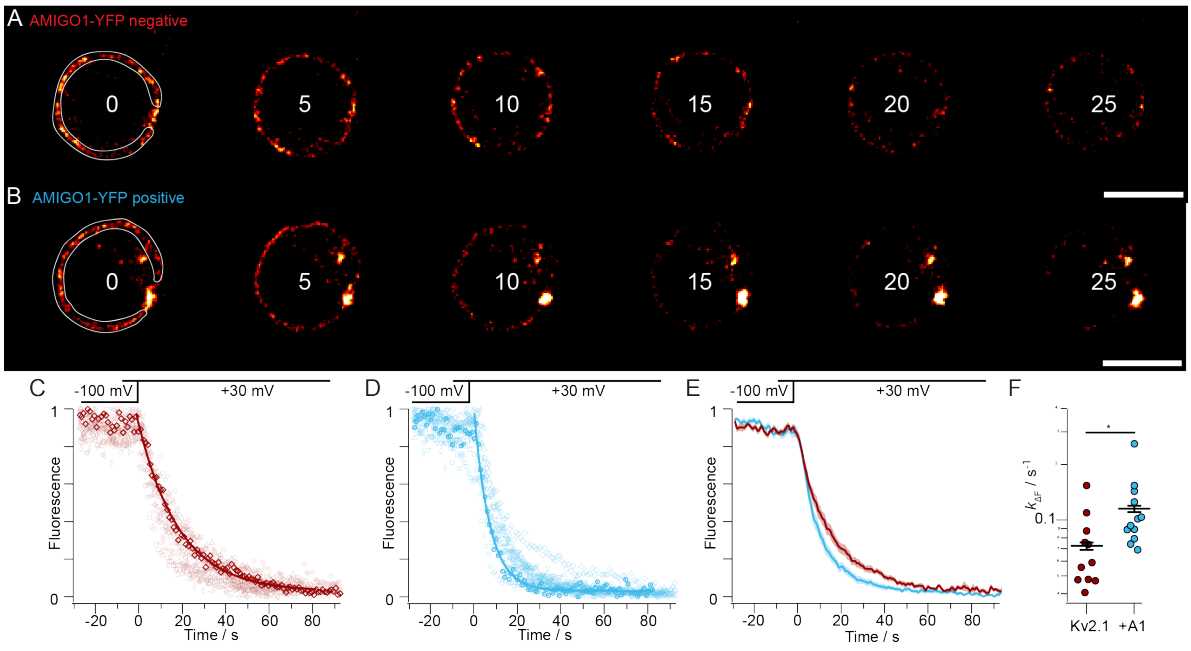

Figure 3.7. AMIGO1 accelerates voltage-stimulated GxTX–594 dissociation.

(**A, B**) Fluorescence from the solution-exposed membrane of voltage-clamped Kv2.1–CHO cells ± AMIGO1–YFP. Kv2.1 expression was achieved through a 48-hour induction period. Cells were held at -100 mV for 30 seconds before being stimulated to +30 mV (time = 0 s) to trigger GxTX–594 dissociation. The time point in seconds of each image is listed. Region of interest for analysis is shown by the white line in left panel, which excludes the point contact with pipette and intracellular regions which have voltage-insensitive fluorescence. 10 μm scale bar. (**C, D**) Normalized fluorescence intensity decay plots for Kv2.1–CHO cells without (red) and with (blue) AMIGO1–YFP fluorescence. The bolded traces correspond to exemplar cells in (A) and (B). Solid line is monoexponential fit (Eqn. G). (**E**) Averaged fluorescence intensity decay for AMIGO1–YFP negative (red), and AMIGO1–YFP positive (blue) cells. SEM is shaded. (**F**) Rates of fluorescence change (kΔF) were calculated as 1/τ from Eqn. G fits. *: p = 0.03 unpaired, two-tailed, t-test.

Figure 3.8

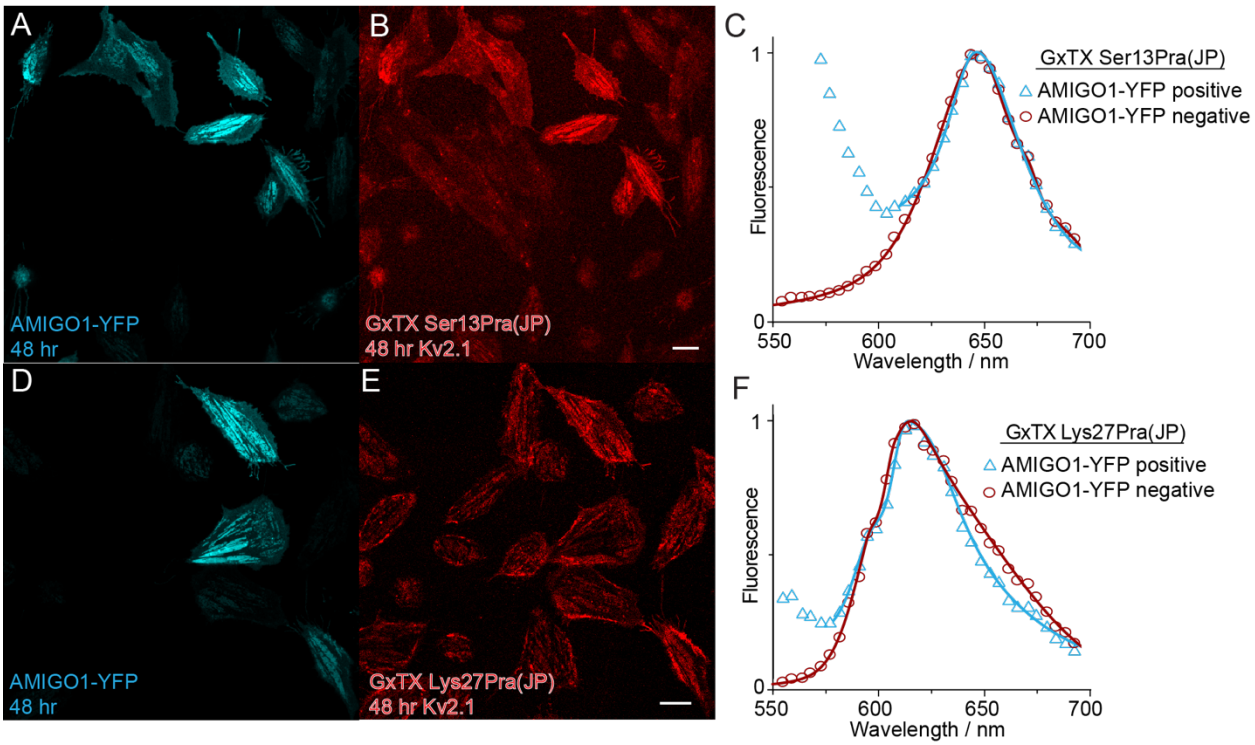

Figure 3.8. AMIGO1 does not alter the Kv2.1–GxTX interface on resting voltage sensors.

Kv2.1–CHO cells transfected with AMIGO1-YFP were treated with GxTX Ser13Pra(JP) or GxTX Lys27Pra(JP) (A, D) Confocal image of AMIGO1–YFP fluorescence (blue) and (B, E) JP fluorescence. (C, F) Fitted emission spectra of cells positive (blue) and negative (red) for AMIGO1–YFP fluorescence. Data points for all spectra are the mean of normalized emission from AMIGO1–YFP positive cells and AMIGO1–negative cells. Spectra were fit with two–component split pseudo–Voigt functions with shape parameters and root–mean–squared values found in Supplemental Table 2.1.

Figure 3.9

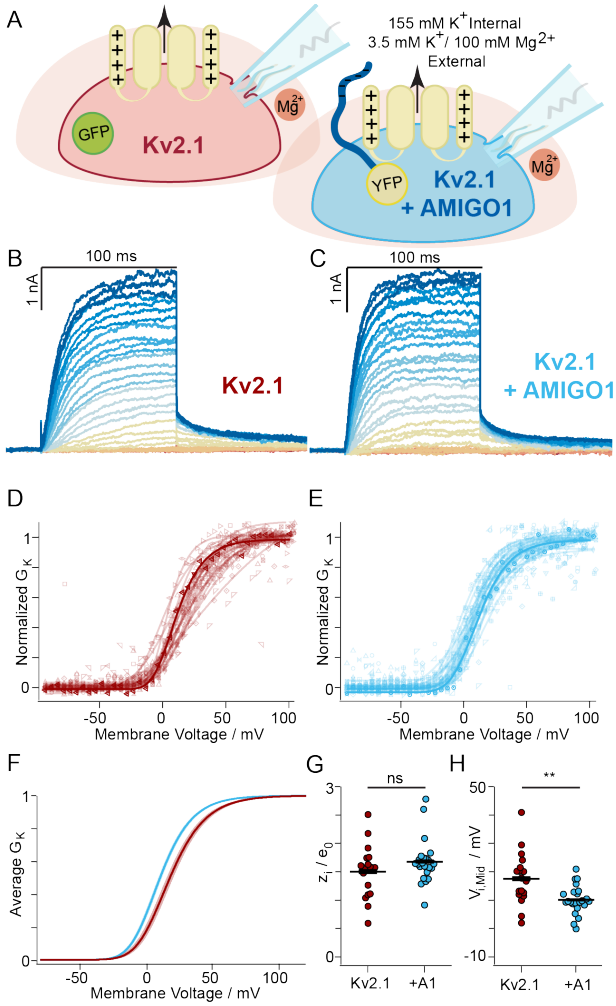

Figure 3.9. Surface charge screening does not suppress the AMIGO1 effect.

(**A**) Experimental set up: Whole-cell K^+ currents (arrow) from Kv2.1–CHO transfected with GFP (red) or AMIGO1–YFP (blue). 100 mM magnesium was used to shield surface charges (peach halo). Same voltage protocol and representations as Fig. 2.3. (**B, C**) Representative Kv2.1–control (10.0 pF) or Kv2.1 + AMIGO1 (6.3 pF) cell. (**D, E**) Normalized *G–V* relationships. (**F**) Reconstructed 4th order Boltzmann fits from average $V_{i,Mid}$ and z_i (Table 2.1). Shading $V_{i,Mid}$ ± SEM. (**G**) Steepness and (**H**) midpoint of 4th order Boltzmann fits. Mean ± SEM. Statistics in Table 2.1. **: $p = \leq 0.01$, ns: not significant.

Figure 3.10

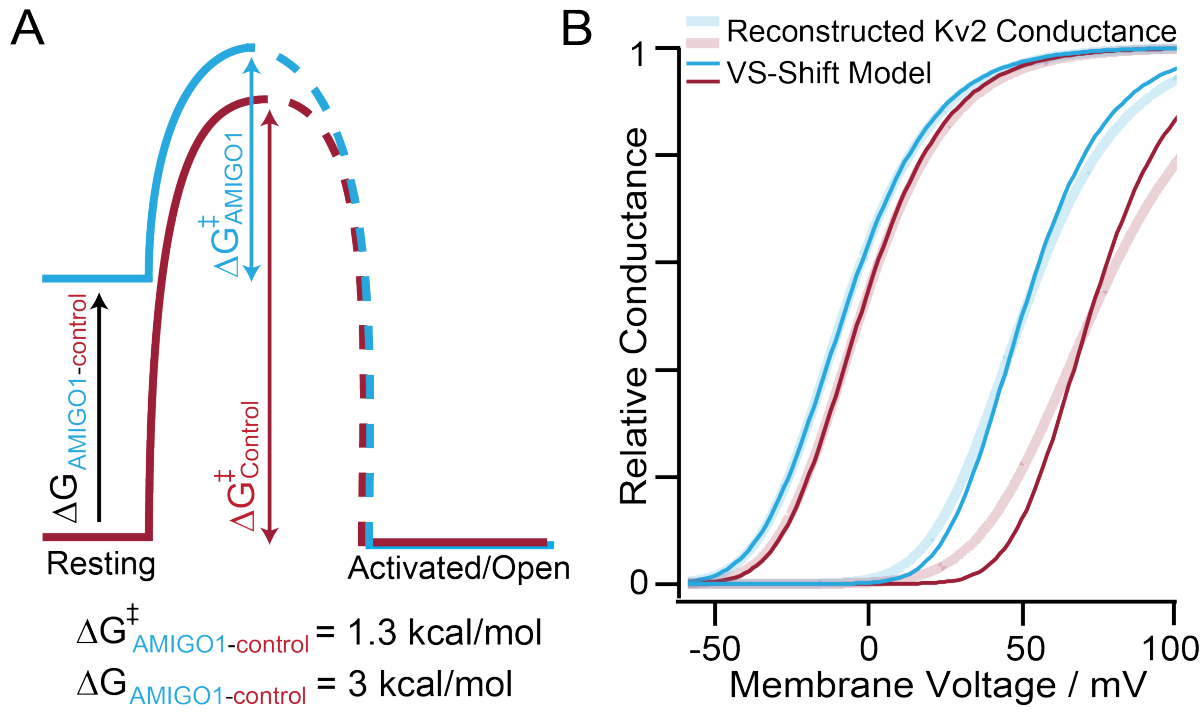

Figure 3.10. AMIGO1 destabilizes the resting conformation of Kv2.1 voltage sensors.

(**A**) AMIGO1 raises resting state energy (Δ*G*) of Kv2.1 voltage sensors and lowers the energy barrier (Δ*G*‡) of Kv2.1 activation. (**B**) Voltage sensor shift model of AMIGO1 modulation (dark lines) plotted with reconstructed *G*–*V*s from Kv2.1–CHO Table 2.1 values (pale lines). From left to right: Kv2.1+AMIGO1, Kv2.1–Control, Kv2.1+AMIGO1 with GxTX–594, Kv2.1–Control with GxTX–594. Voltage sensor shift model is $f(V) = \left(1 + e^{-(V - V_{VSD,1/2})(z/25.46)}\right)^{-4} \cdot \left(1 + e^{-(V - V_{Pore,1/2})(z/25.46)}\right)^{-1}$, where $z = 1.5\ e_0$, $V_{Pore,1/2}$ = -16 mV, and $V_{VSD,1/2}$ varies. Kv2.1–Control $V_{VSD,1/2}$ = -33 mV and Kv2.1–Control with GxTX–594 $V_{VSD,1/2}$ = 51 mV. AMIGO1 $\Delta V_{VSD,1/2}$ = -22 mV with or without GxTX–594.

Table 3.1

	G–V fit parameters				ΔG_{AMIGO1} (kcal/mol)
	$V_{i,1/2}$ *(mV)*	$V_{i,Mid}$ *(mV)*	z_i *(e_0)*	*n*	*(Eqn. E)*
HEK293 cells					
mKv2.1 + GFP	-26.8 ± 3.0	-1.7 ± 1.4 [A]	1.79 ± 0.17 [D]	7	-0.31
mKv2.1+ AMIGO1 + GFP	-30.9 ± 0.8	-7.4 ± 1.8 [B]	1.95 ± 0.16 [E]	14	
mKv2.1 + SCNβ1 + GFP	-24.8 ± 1.5	0.2 ± 1.8 [C]	1.720 ± 0.074 [F]	8	
Kv2.1–CHO cells					
rKv2.1 + GFP	-33.4 ± 1.7	-1.8 ± 1.2 [G]	1.411 ± 0.070 [I]	20	-0.28
rKv2.1+ AMIGO1–YFP	-42.0 ± 3.3	-7.6 ± 1.8 [H]	1.40 ± 0.11 [J]	19	
Kv2.1–CHO cells + Mg^{2+}					
rKv2.1 + GFP	-13.8 ± 1.8	17.6 ± 2.2 [K]	1.51 ± 0.11 [M]	18	-0.37
rKv2.1+ AMIGO1–YFP	-16.3 ± 1.5	10.2 ± 1.0 [L]	1.682 ± 0.082 [N]	23	
Kv2.1–CHO cells + GxTX–594					
rKv2.1 + GFP	26.8 ± 2.9	73.2 ± 3.8 [O]	1.03 ± 0.11 [Q]	13	-0.77
rKv2.1+ AMIGO1–YFP	12.9 ± 4.4	50.9 ± 2.8 [P]	1.27 ± 0.14 [R]	12	

Table 3.1. Fourth order Boltzmann parameters for G–V relationships.

Average $V_{i,1/2}$, $V_{i,Mid}$, and z_i values were derived from a 4th order Boltzmann fits (Eqn. C) of *n* individual cells. All values are given ± SEM. Brown-Forsythe and Welch (appropriate for differing SD) ANOVA test with a Dunnett's T3 multiple comparisons p-values: AB: 0.046. AC: 0.64. DE: 0.75. DF: 0.91. Unpaired, two-tailed t-test p-values: GH: 0.012. IJ: 0.95. KL: 0.0051. MN: 0.21. OP: 0.00018. QR: 0.19. ΔG_{AMIGO1} from Eqn. E, at $V_{i,Mid}$ for Kv2.1 + GFP.

Table 3.2

Kv2.1–CHO cells	*Q–V* fit parameters				ΔG$_{AMIGO1}$ (kcal/mol)		
$Q_{ON,fast}$	$V_{g,Mid}$ (mV)		z_g (e_0)	*n*	*Eqn. E*		
rKv2.1 + GFP	30.6 ± 2.0 [S]		1.38 ± 0.03 [U]	20	-1.92		
rKv2.1+ AMIGO1–YFP	17.8 ± 2.9 [T]		1.61 ± 0.05 [V]	20			
Q_{OFF}	$V_{g,Mid}$ (mV)	$V_{g,Med}$ (mV)	z_g (e_0)	*n*	*Eqn. E*	*Eqn. K**	*Eqn. K*°*
rKv2.1 + GFP	-22.0 ± 1.3 [W]	-19.5	2.00 ± 0.13 [Y]	20	-2.45	-3.11 ± 0.69	-2.74
rKv2.1+ AMIGO1–YFP	-32.8 ± 2.0 [X]	-29.0	2.43 ± 0.15 [Z]	20			

Table 3.2. Boltzmann parameters and ΔG calculations for gating charge movement.

Average $V_{g,Mid}$ and z_g values were derived from 1st order Boltzmann fits of *n* individual cells. Means ± SEM. $V_{g,Mid} = V_{g,1/2}$. $V_{g,Med}$ is median voltage (417). Unpaired, two-tailed t-test p-values: $Q_{ON,fast}$: ST: 0.00093. UV: 0.00084. OFF Gating currents: WX: 7.82×10^{-5}. YZ: 0.038. *z =12.5 e_0, ° $V_{g,Med}$ was used.

Table 3.3

Calculated activation of native Kv2 conductance after 1.5 ms at 0 mV			
Type of AMIGO1 impact	**τ_{0mV} (s)**	**V_{Mid} (mV)**	**Relative Conductance**
none, values from (29)	0.0029	-13.1	0.022
from conductance data	0.0040†	-7.1	0.0067
from voltage sensor data	0.0050†	-2.3	0.0024

Table 3.3. Prediction of AMIGO1 impacts on Kv2 conductance in superior cervical ganglion neurons.

Liu and Bean fit Kv2 kinetics with $\left(1 - e^{-t/\tau_{0mV}}\right)^4$ and the *G*–*V* with $\left(1 + e^{-(V - V_{Mid})/k}\right)^{-1}$, and these equations are used to calculate relative conductance here τ_{0mV} and ΔV_{Mid} adjusted for the impact of loss of AMIGO1 from Kv2.1–CHO cells. The AMIGO1 impact on conductance activation was a 1.38-fold acceleration of τ_{0mV} (Fig. 3.3M) and *G*–*V* $\Delta V_{i,Mid}$ = -5.7 mV (Table 3.1). The AMIGO1 impact on voltage sensor activation was a 1.74-fold acceleration of τ_{0mV} (change in α_{0mV} from fit in Fig. 3.6N) and Q_{OFF}–*V* $\Delta V_{g,Mid}$ = -10.8 mV (Table 3.2).

Supplemental Figure 3.1

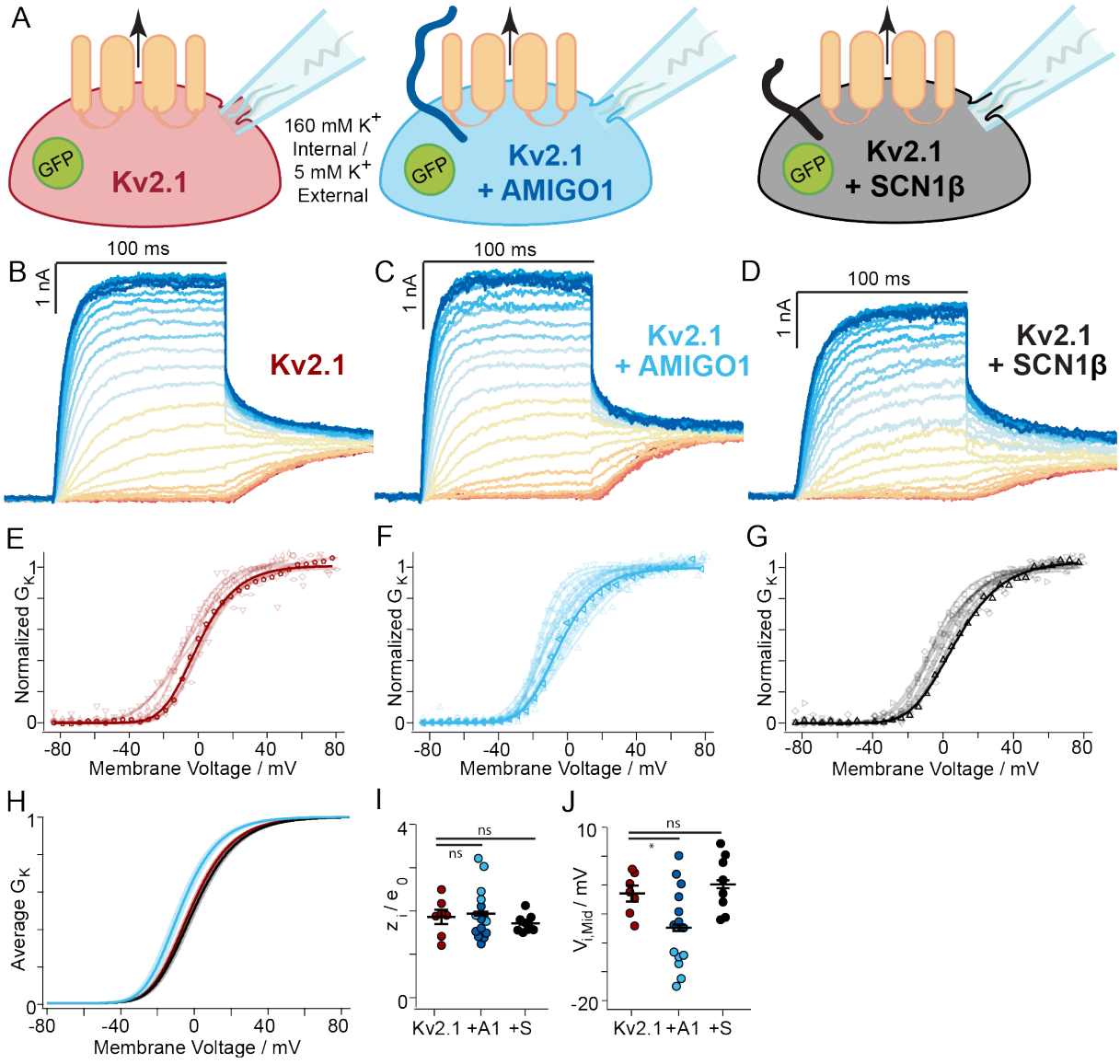

Supplemental Figure 3.1. AMIGO1, but not SCN1β, modulates Kv2.1 conductance in HEK293 cells.

(**A**) Experimental set up: Whole-cell K^+ currents from HEK293 cells co-transfected with mKv2.1 and either GFP (red), or AMIGO1–pIRES2–GFP (blue), or SCN1β–pIRES2–GFP (black). (**B**, **C, D**) Representative mKv2.1–control (14.8 pF), mKv2.1 + AMIGO1 (9.6 pF), or mKv2.1 + SCN1β (10.0 pF) HEK293 cell. Data points from representative cells are bolded in analysis panels. (**E, F, G**) Normalized *G–V* relationships for mKv2.1–control, mKv2.1 + AMIGO1, or mKv2.1 + SCN1β cells. Symbols correspond to individual cells. Lines are 4th order Boltzmann relationships (Eqn. C). (**H**) Reconstructed 4th order Boltzmann fits using the average $V_{i,Mid}$ and z_i (Table 2.1). Shaded areas represent $V_{i,Mid}$ ± SEM. (**I**) Steepness and (**J**) midpoint of 4th order Boltzmann fits. For the mKv2.1 + AMIGO1 cells, individual $V_{i,Mid}$ and z_i values are displayed in dark or light blue to highlight an increase in variability. Specifically, the standard deviation of $V_{i,Mid}$ increased from ± 3.6 mV in control cells to ± 6.9 mV in mKv2.1 + AMIGO1 cells. We note that the $V_{i,Mid}$ values for mKv2.1 + AMIGO1 cells seemed to partition into two groups: a more negatively shifted group with an average $V_{i,Mid}$ of -13.9 mV (light blue), and a group similar to mKv2.1 alone with an average $V_{i,Mid}$ of -2.5 mV (dark blue). Although all cells analyzed had GFP fluorescence indicating transfection with the AMIGO1–pIRES2–GFP vector, it is possible that some cells were not expressing sufficient AMIGO1 to have a functional effect. Statistics in in Table 2.1. *: $p = \leq 0.05$, ns: not significant. Bars are mean ± SEM.

Supplemental Figure 3.2

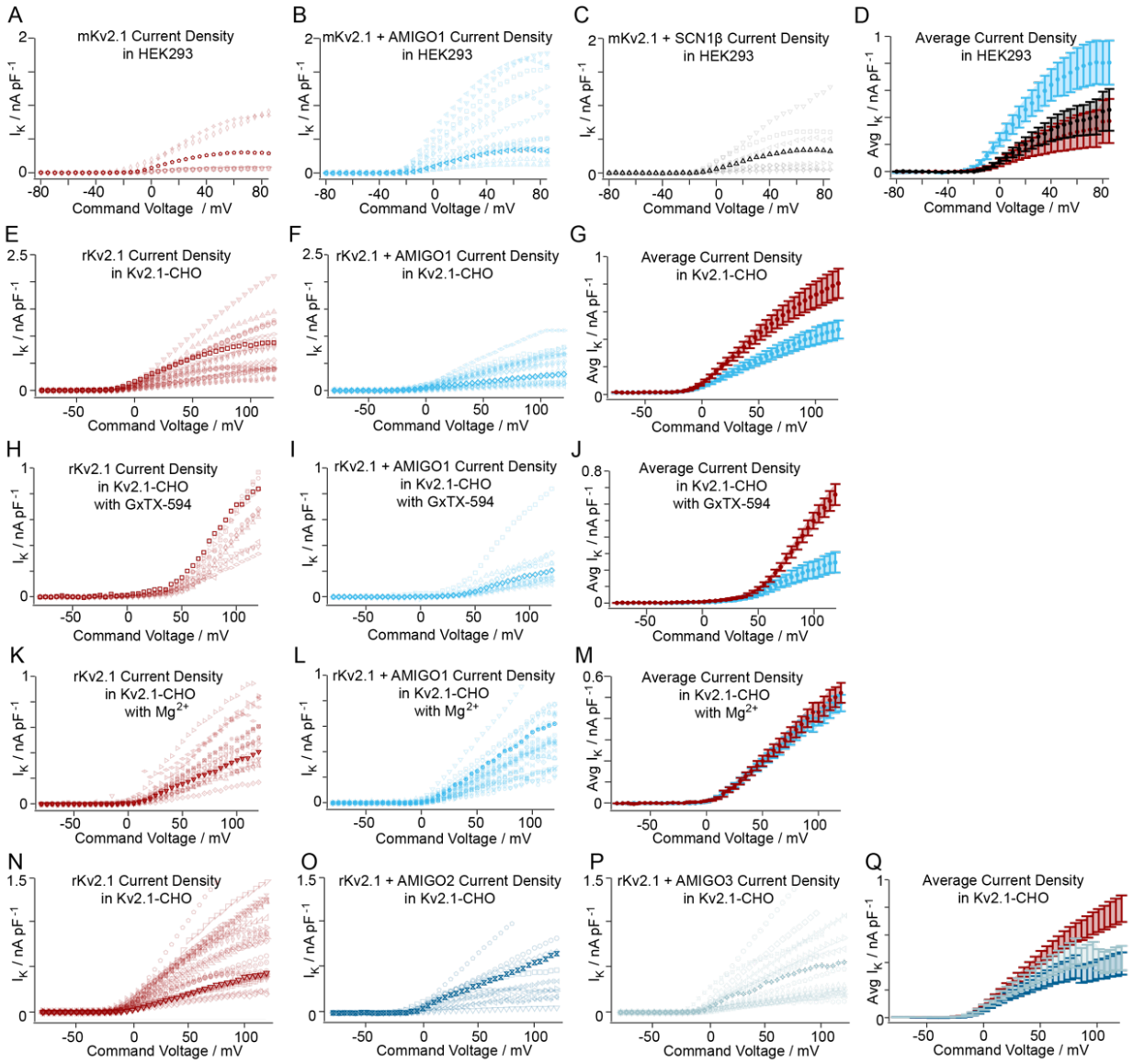

Supplemental Figure 3.2. Kv2.1 current density ± AMIGO1 in HEK293 and Kv2.1–CHO cells.

AMIGO1 has mixed effects on current density in HEK293 and Kv2.1–CHO cells. Outward current densities normalized by cell capacitance were calculated from mean of the last 10 ms of each voltage step and plotted against the command voltage. Symbols represent individual cells. (**A, B, C**) HEK293 cells co-transfected with mKv2.1 + GFP, mKv2.1 + AMIGO1–pIRES2–GFP, or mKv2.1 + SCN1B–pIRES2–GFP. To limit the proportion of currents from endogenous voltage-dependent channels (381, 382), we set a minimum outward current density as an inclusion threshold for analysis (65 pA/pF at +85 mV). Of the cells patched, 7 of 18 mKv2.1–control cells, 14 of 28 mKv2.1 + AMIGO1 cells, and 8 of 27 mKv2.1 + SCN1β cells satisfied this inclusion threshold and displayed currents consistent with a Kv2.1 delayed rectifier conductance (IK). Cells that did not meet the inclusion criteria are not plotted making the full variability of current densities is extreme than depicted here. Bolded symbols are exemplars from Supplemental Fig. 3.1B, C, or D. (**D**) Averages of A, B, and C. (**E, F**) Kv2.1–CHO ± AMIGO1–YFP. Bolded symbols are exemplars from Fig. 3.3B or 3.3C. (**G**) Averages of E and F. (**H, I**) Kv2.1–CHO ± AMIGO1–YFP in 100 nM GxTX–594. Bolded symbols are exemplars from Fig. 3.5B or 3.5C. Cell symbols matched between E/H and F/I before and after GxTX–594 addition. (**J**) Averages of H and I. (**K, L**) Kv2.1–CHO ± AMIGO1–YFP in 3.5 mM K+/100 mM Mg2+ external. Bolded symbols are exemplars from Fig. 3.9B or 3.9C. (**M**) Averages of E and F. Averaged data are means ± SEM.

Supplemental Figure 3.3

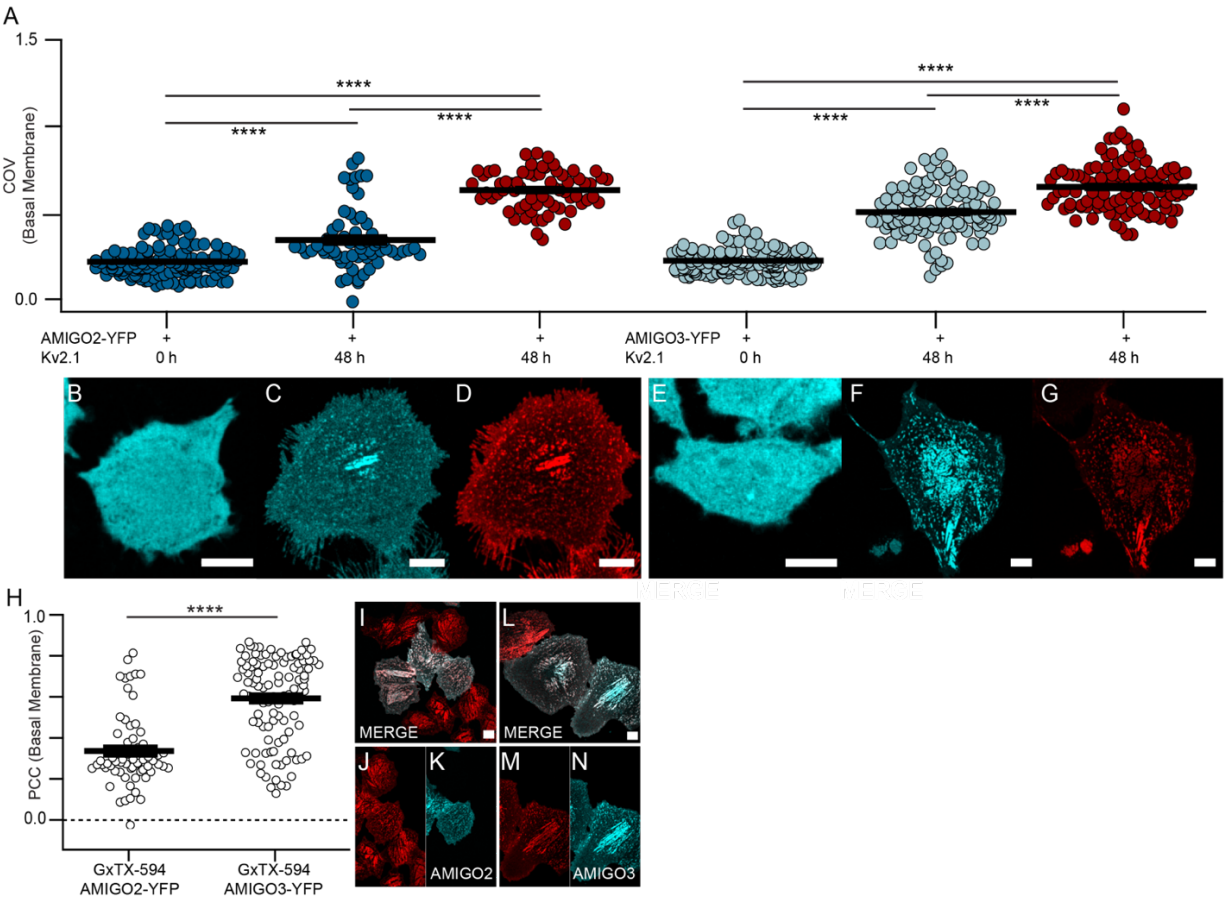

Supplemental Figure 3.3. Kv2.1 reorganizes and colocalizes with AMIGO homologs in CHO cells.

(**A**) Coefficient of variation of fluorescence from AMIGO2–YFP (dark blue circles), AMIGO3–YFP (light blue circles), or GxTX–594 (red circles). COV from confocal images of glass–adhered membranes (exemplar images in B-G). AMIGO2–YFP fluorescence from cells (**B**) not induced for Kv2.1 expression ($COV_{A2,0h}$ = 0.2090 ± 0.0062, n = 144), (**C**) induced 48 h for Kv2.1 expression ($COV_{A2,48h}$ = 0.342 ± 0.022, n = 65). (**D**) GxTX–594 labeling of the cells in C ($COV_{A2,48h(GxTX–594)}$ = 0.631 ± 0.013, n = 65 cells). AMIGO3–YFP fluorescence from cells (**E**) not induced for Kv2.1 expression ($COV_{A3,0h}$ = 0.2186 ± 0.0052, n = 160), (**F**) induced 48 h for Kv2.1 expression ($COV_{A3,48h}$ = 0.503 ± 0.014, n = 109). (**G**) GxTX–594 labeling of the cells in panel F ($COV_{A3,48h(GxTX–594)}$ = 0.650 ± 0.013, n = 109 cells). (**H**) Costes thresholded, Pearson's colocalization coefficients from cells induced for Kv2.1 expression 48 h prior to imaging.. From left to right: $PCC_{A2,GxTX–594}$ = 0.342 ± 0.022, ≥ 0 ($p < 0.0001$, one–tailed, t-test), n = 65; $PCC_{A3,GxTX–594}$ = 0.597 ± 0.020, ≥ 0 ($p < 0.0001$, one–tailed, t-test), n = 108. (**I, J, K)** Exemplar images where merge overlay (white) shows colocalization between GxTX–594 (red) and AMIGO2–YFP (cyan) or **(L, M, N**) AMIGO2–YFP (cyan) Arithmetic means and standard errors are plotted. (**Statistics**) Outliers were removed using ROUT, Q = 1%. An ordinary one-way ANOVA with multiple comparisons was used to evaluate the differences between groups in COV analysis, while a t-test was used to evaluate the PCC data. ****: p = ≤0.0001. Bars are mean ± SEM. All scale bars are 10 μm.

Supplemental Figure 3.4

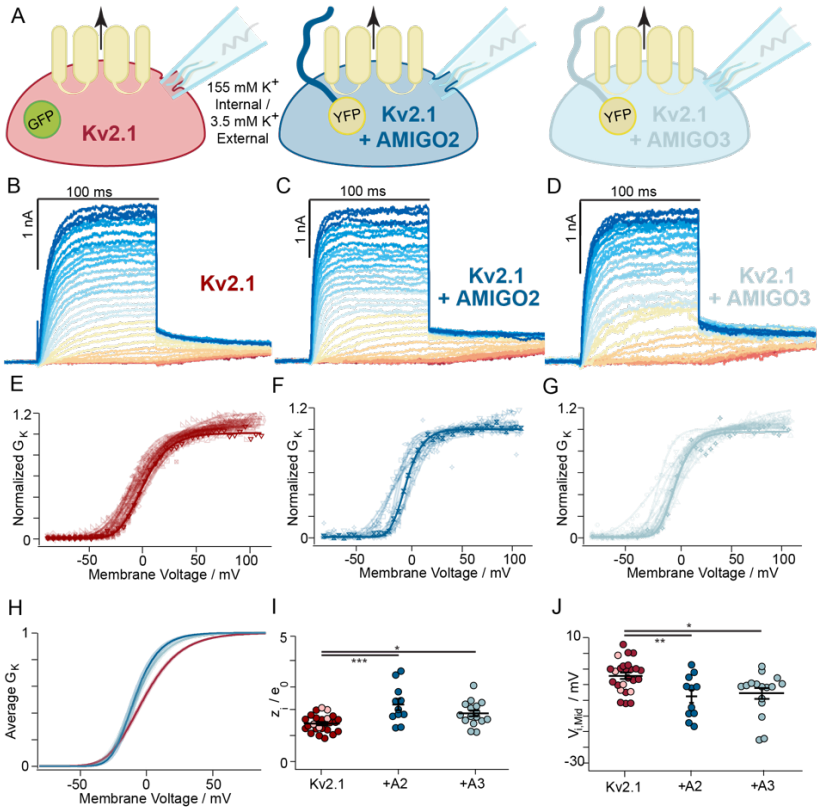

Supplemental Figure 3.4. AMIGO2 and AMIGO3 modulate Kv2.1 conductance in CHO cells.

(**A**) Experimental set up: Whole-cell K^+ currents (arrow) from Kv2.1–CHO transfected with GFP (red), rAMIGO2–YFP (dark blue), or rAMIGO3–YFP (light blue). Same voltage protocols and representation as Fig. 2.3. (**B**, **C, D**) Representative Kv2.1–control (5.1 pF), Kv2.1 + AMIGO2 (6.6 pF) or Kv2.1 + AMIGO3 (2.4 pF) cells. (**E**, **F, G**) Normalized *G-V* relationships. 5 of the Kv2.1–control cells were recorded from side by side with the Kv2.1 + AMIGO2 cells and Kv2.1 + AMIGO3 cells (light red). There was no statistical difference between these 5 cells and the data previously acquired during Kv2.1 + AMIGO1 recordings for Fig. 2.3 (assessed by t-test), and data was pooled. Solid lines a 4th order Boltzmann fits (Eqn. C). (**H**) Reconstructed 4th order Boltzmann fits from average $V_{i,Mid}$ and z_i (Supplemental Table 2.1). Shading $V_{i,Mid}$ ± SEM. (**I**) Steepness and (**J**) midpoint of fits. Statistics in Supplemental Table 2.1. ***: $p = \leq 0.001$, **: $p = \leq 0.01$, *: $p = \leq 0.05$. Bars are mean ± SEM.

Supplemental Figure 3.5

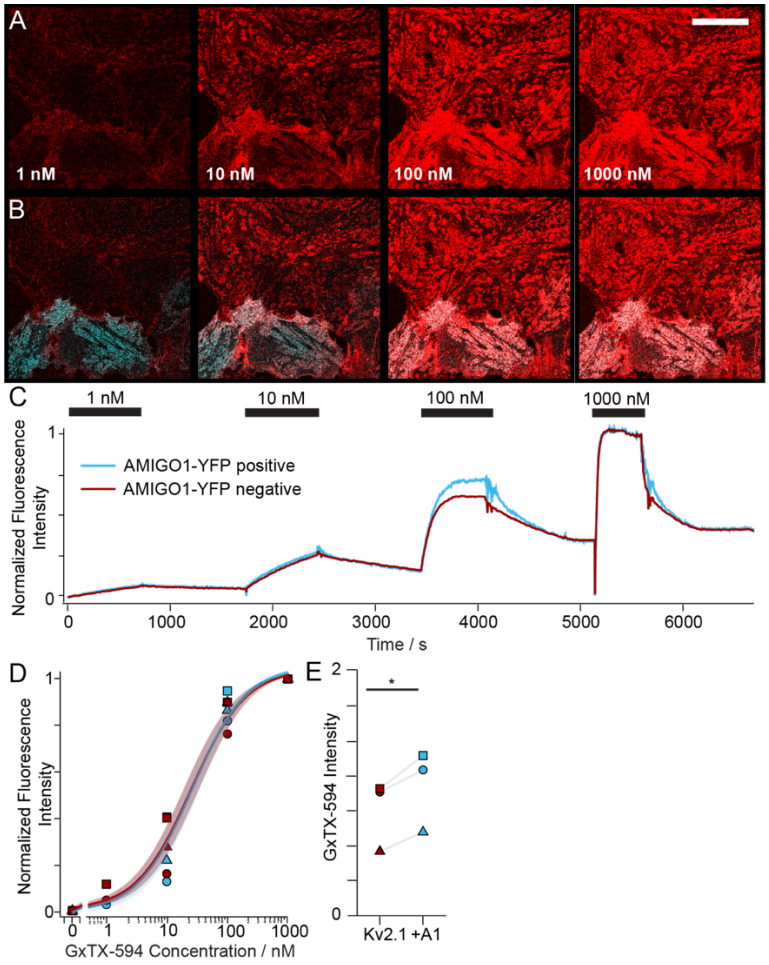

Supplemental Figure 3.5. AMIGO1 does not impede GxTX–594 binding to Kv2.1.

(**A**) Fluorescence from Kv2.1–CHO cells transfected with AMIGO1–YFP, induced for Kv2.1 expression for 48 hours and labeled with indicated concentrations of GxTX–594 (red). Scale bar 20 μm. (**B**) Overlap (white) between AMIGO1–YFP (cyan) and GxTX–594 fluorescence. (**C**) Mean fluorescence intensities from ROIs encompassing AMIGO1–YFP positive or negative cells from the concentration-response experiment shown in A. (**D**) Normalized fluorescence intensity after 500 s at each concentration as in panel C. Symbol shapes represent data from each of 3 experiments. Curves and shaded regions represent the mean ± SEM of a Langmuir binding isotherm (Eqn. L) fit to individual experiments. K_d = 27.5 ± 8.3 nM without and 27.9 ± 7.2 nM with AMIGO1–YFP. K_d likely is overestimated due to incomplete equilibration

at 1 and 10 nM. (**E**) Cells expressing AMIGO1–YFP had brighter GxTX–594 fluorescence with 1000 nM GxTX–594. Symbols correspond with D.

Supplemental Table 3.1

	G–V fit parameters				ΔG_{AMIGOX} (kcal/mol)
	$V_{i,1/2}$ *(mV)*	$V_{i,Mid}$ *(mV)*	z_i *(e_0)*	*n*	*(Eqn. E)*
Kv2.1–CHO cells					
rKv2.1 + GFP	-32.5 ± 1.5	-2.0 ± 1.0 [A]	1.471 ± 0.067 [D]	25	
rKv2.1+ AMIGO2–YFP	-29.7 ± 3.4	-8.7 ± 2.1 [B]	2.25 ± 0.23 [E]	11	-0.39
rKv2.1+ AMIGO3–YFP	-31.8 ± 2.4	-7.8 ± 1.7 [C]	1.88± 0.12 [F]	16	-0.31

Supplemental Table 3.1. Fourth order Boltzmann parameters for G–V relationships of AMIGO homologs.

Average $V_{i,1/2}$, $V_{i,Mid}$, and z_i values were derived from a 4th order Boltzmann fits (Eqn. C) of *n* individual cells. All values are given ± SEM. Ordinary one-way ANOVA test with Dunnett's multiple comparisons p-values: AB: 0.0082. AC: 0.010. DE: 0.0002. DF: 0.026. ΔG_{AMIGO1} from Eqn. E, at $V_{i,Mid}$ for Kv2.1 + GFP.

Supplemental Table 3.2

GxTX(JP) conjugate	AMIGO1–YFP Expression	fitting component	a0	a1	a2	a3	a4	a5	R^2
GxTX Ser13Pra(JP)	- AMIGO	1	0.229	670.4	47.88	11.41	1.075	2.323	0.999
		2	0.813	647.0	25.73	21.77	0.631	1.685	
	+ AMIGO	1	0.893	646.7	23.30	25.63	1.822	0.721	0.997
		2	0.006	-1610	-15206	-1877	4967	461.2	
GxTX Lys27Pra(JP)	- AMIGO	1	0.352	594.3	12.11	-11.53	0.568	5.364	0.998
		2	0.719	608.2	9.71	59.05	0.359	-0.264	
	+ AMIGO	1	0.715	597.8	16.07	18.08	1.578	2.912	0.997
		2	0.632	616.3	9.05	26.28	-1.657	1.488	

Supplemental Table 3.2. Split Pseudo–Voigt fitting parameters.

Fluorescence emission spectra split pseudo–Voigt fitting parameters and root-mean squared values.

Supplemental Table 3.3

Figure	# Transfections	*n* per transfection		
Fig. 3.3	7	peGFP: 5, 2, 2, 4, 1, 2, 4	+AMIGO1: 3, 3, 3, 4, 3, 2, 1	
Fig. 3.4	6	peGFP: 2, 1, 1, 1, 1, 2	+AMIGO1: 1, 2, 1, 3, 0, 0	
Fig. 3.5	5	peGFP: 4, 2, 2, 3, 2	+AMIGO1: 3, 3, 1, 3, 2	
Fig. 3.6	6	peGFP: 5, 4, 4, 2, 1, 4	+ AMIGO1: 2, 3, 4, 1, 4, 6	
Fig. 3.7	2	AMIGO1 (-): 6, 5	AMIGO1 (+): 5, 6	
Fig. 3.9	4	peGFP: 1, 3, 4, 10	+AMIGO1: 5, 5, 7, 6	
Sup. Fig. 3.1	4	peGFP: 3, 3, 1, 0	+AMIGO1: 4, 4, 6, 0	+SCNB1: 1, 1, 2, 4
Sup. Fig. 3.4	5	peGFP: 5, 0, 0, 0, 0 (+peGFP n-values from Fig. 2.3)	+AMIGO2: 1, 2, 0, 1, 7	+AMIGO3: 1, 7, 5, 0, 3

Supplemental Table 3.3. N-values for electrophysiology experiments.

Supplemental Table 3.4

Figure	# Transfections	# *n* values per transfection					
Fig. 3.1	4	YFP (0 hr): 28, 48, 0, 58	YFP (1.5 hr): 25, 55, 42, 95	YFP (48 hr): 82, 54, 74, 67	YFP (ChR): 11, 21, 32, 61	GxTX-594 (48 hr, AMIGO1): 84, 44, 69, 0	mRuby-ChR (AMIGO1): 20, 16, 32, 60
Fig. 3.2.	4	AMIGO1-YFP +GxTX-594 (48 hr): 85, 41, 69, 0			AMIGO1-YFP +ChR-mRuby: 18, 22, 28, 61		
Fig. 3.2	3	0 hr: 41, 35, 25		1.5 hr: 38, 39, 41		48 hr: 28, 17, 56	
Fig. 3.8	3	AMIGO1(-) (GxTX Ser27Pra-JP): 20, 12, 8			AMIGO1(+) (GxTX Ser27Pra-JP): 39, 20, 13		
	2	AMIGO1(-) (GxTX Ser13Pra-JP): 15, 55			AMIGO1(+) (GxTX Ser13Pra-JP): 7, 62		
Sup. Fig. 3.3	2	AMIGO2-YFP (0 hr): 28, 116	AMIGO2-YFP (48 hr): 59, 6	GxTX-594 (48 hr, AMIGO2): 59, 6	AMIGO3-YFP (0 hr): 117, 43	AMIGO3-YFP (48 hr): 109, 0	GxTX-594 (48 hr, AMIGO3): 109, 0
Sup. Fig. 3.3	2	AMIGO2-YFP +GxTX-594: 64, 1			AMIGO3-YFP +GxTX-594: 108,0		
Sup. Fig. 3.5	3	AMIGO1(-): 1, 1, 1			AMIGO1(+): 1, 1, 1		

Supplemental Table 3.4. N-values for imaging experiments.

Chapter 4: Conclusion and potential directions for future study of AMIGO1-Kv2 interactions.

Preface

This concluding chapter describes the main conclusions of my thesis and highlights potential future directions for the study of AMIGO1-Kv2 interactions. I drafted and conceptualized this chapter. Jon Sack and James Trimmer provided editorial feedback.

Conclusions

Over the course of this thesis I set out to **(1) develop technologies for live, cellular and subcellular resolution of subtype-specific ion channel activation in native systems, and (2) describe the biophysical mechanism through which Kv2 channels shift their voltage-dependence.**

In Chapter 2, I presented GxTX–594, which is the only method we are aware of for measuring voltage-sensitive conformational changes of a specific, endogenous protein. As GxTX binding selectively stabilized the fully resting conformation of Kv2.1 voltage sensors (320), reversible GxTX–594 labeling is expected to bind with highest affinity specifically to the fully resting conformation of the Kv2 voltage sensor in which the first gating charge of the Kv2 S4 segment is in the gating charge transfer center (302). Images of GxTX–594 fluorescence reveal this conformation's occurrence with subcellular spatial resolution. Importantly the statistical model we developed allows deconvolution of the behavior of unlabeled proteins. This enables the subcellular locations where Kv2 voltage sensing occurs to be seen for the first time. Similarly, the novel far-red environment-sensitive GxTX–JP tools report voltage-dependent conformational changes of Kv2.1 channels in the cell membrane. Fluorescence of these tools is both position- and state-specific for GXTX conjugates bound to Kv2.1 channels, which enables us to use fluorescence shifts to characterize channel allostery. For GxTX Lys27Pra(JP), a conjugate in which JP interacts directly with the channel, we saw that emission shifts occurred at voltages almost 50 mV more negative than those measured for Kv2.1-channel opening or gating currents. This suggests that there are substantial conformational changes at the toxin-channel interface associated with early gating charge transitions distinct from VSD motions at more depolarized potentials. These GxTX–JP tools place channel structures and models into the context of cell membranes and physiological states for detailed study of channel allostery.

Then in Chapter 3 and Appendix B, I dissect the biophysical mechanism through which AMIGO1 shifts the voltage-dependence of Kv2.1 channels. We found that to shift the activation midpoint of Kv2.1

conductance to lower voltages, AMIGO1 destabilizes the earliest resting conformations of Kv2.1 voltage sensors relative to more activated conformations. While we cannot rule out a direct influence on pore dynamics, we saw no indication of such. We propose that AMIGO1 shifts the voltage–dependence of Kv2.1 conduction to more negative voltages by modulating early voltage sensor movements. Studies executed with Kv2.1 truncation mutants suggest that the residues retained in the C-terminus of Δ333C, but not Δ376C, are necessary for detaining Kv2.1 voltage sensors in their earliest resting conformation. Further, without these residues, the effect of AMIGO1 on destabilizing Kv2.1 voltage sensors disappears. Together these experiments provide a method to interrogate how Kv2 conductances integrate in endogenous signaling cascades and further a biophysical method that can be targeted in order to tune how Kv2 channels participate within these signaling events.

Discussion

There are still many open questions regarding the AMIGO1-Kv2.1 interaction: what are the molecular determinants of AMIGO1-Kv2.1 association? What is the structural mechanism through which AMIGO1 modulates Kv2.1 conformational change? More broadly, what is the structural mechanism through which Kv2.1 voltage-dependence is susceptible to modulation? I explore possibilities on these topics in this final chapter.

Potential technique improvements for future studies

As noted in Chapter 3, interrogating the mechanism by which AMIGO1 modulates Kv2.1 conformational change is hampered by the effect size and the cell-to-cell variation exhibited with Kv2.1 current recordings. I would advise interested researchers to consider the practical signal-to-noise limitations associated with electrophysiological recording techniques before undertaking further voltage-

clamp studies with AMIGO1-Kv2.1. I utilized an approach optimized for biophysical characterization which included patching detached cells with nonphysiological solutions. Some approaches that could be explored to further control cell-to-cell variability including: waiting for current recordings to stabilize after break-in (419), intracellular inclusion of phosphorylating/dephosphorylating enzymes (354), inclusion of enzymes that affect glycosylation (420), intracellular application of the phospholipid PIP_2 (398), working with Kv2.2 which is less regulated by phosphorylation (421), working with adhered cells , or utilizing more physiological internal and external patching solutions, or utilizing a concatenated Kv2-AMIGO1 construct to regulate 1:1 transfection efficiency (113).

Determining the Region of AMIGO1-Kv2.1 Interaction

In Chapter 3, I found that AMIGO1 destabilized the earliest resting conformation of the Kv2.1 voltage sensing domains. AMIGO1 did not significantly change the amount of gating charge expressed within the cell (Fig. 3.6.F), and it did not localize near enough to the Kv2.1 S3-S4 linker to be resolved with GxTX–JP tools (Fig. 3.8), consistent with AMIGO1 modulating Kv2.1 voltage-sensing allosterically. What are the molecular determinants through which AMIGO1 interacts with Kv2 channels? Determining the region of interaction between AMIGO1 and Kv2.1 will shed light on the molecular determinants that control ion channel conformational change. In the following sections, I propose additional experiments designed to determine the molecular region and mechanism of AMIGO1-Kv2.1 interaction.

Does AMIGO1 associate with Kv2.1 channels via the transmembrane, extracellular, or intracellular region?

One way to determine the molecular regions necessary for an interaction is to create truncation mutants that are missing the region of interest. Under this paradigm, to investigate if AMIGO1 associates with Kv2.1 channels through a particular region, each region would need to be systematically removed

from the protein and then interactions could be assessed either visually (as an assay for colocalization) or electrophysiologically (as an assay for AMIGO1-dependent modulation). A group interested in testing a similar question about the molecular region(s) necessary for the AMIGO1-Kv2.1 interaction created a series of AMIGO1-NCAM chimeras, where NCAM is the non-related neuronal cell adhesion molecule that has similar Type I topology and extracellular domains as AMIGO1 (32). Since NCAM had no electrophysiological effect on Kv2.1 voltage-dependence on its own, this approach could isolate different regions of AMIGO1 that were sufficient to reconstitute a Kv2.1 gating shift. From this study, the researchers revealed that the AMIGO1 transmembrane domain was absolutely necessary to confer a Kv2.1 gating shift. However, the presence of the AMIGO1 intracellular domain and extracellular domain were necessary for conferring the *full* Kv2.1 gating shift (32). Because this study was not paired with imaging approaches, we do not know if constructs lacking the AMIGO1 transmembrane domain had no effect on Kv2.1 gating because (1) the necessary molecular interactors were not present or because (2) the NCAM transmembrane chimera was unable to localize with the channel and therefore molecular interactors were physically unable to confer a functional effect. Further, the small effects seen with chimeras that had the AMIGO1 transmembrane domain but lacked the AMIGO1 intracellular or extracellular domain could have been a result of non-specific interactions resulting from localizing a protein near Kv2 voltage sensing machinery.

To complement these prior studies and investigate the region for AMIGO1-Kv2.1 interaction a competition assay could be employed. In a competition experiment, a solution containing an exogenously prepared peptide fragment composed of the AMIGO1 intracellular (99 amino acids), transmembrane (20 amino acids), or extracellular domain (344 amino acids)[48] could be flooded into an imaging or

[48] Producing purified protein fragments of this size is significant task itself. Structural elucidation of the AMIGO1-Kv2.1 interaction could narrow down small regions of interest that could be competitively targeted with smaller peptide fragments that are able to be produced synthetically. Cell-penetrating TAT peptides could be an additional approach for localizing the peptide fragment on the appropriate side of the cell membrane.

electrophysiology experiment. In theory, application of a saturating amount of transactivator of transcription (TAT) peptides[49] or the AMIGO1 intracellular domain, would out compete endogenous AMIGO and Kv2.1 interactions. If the effects of AMIGO1 on Kv2.1 voltage sensor movement were abolished, then this experiment would provide evidence that the targeted molecular region participates in AMIGO1-Kv2.1 interactions.

An alternate approach would be to progressively mutate residues thought to be important in facilitating interacting regions. If the addition of one repulsive residue into an interacting face abrogates a functional output and a complementary, attractive mutation on the opposite face rescues it, those two residues are likely form an interacting pair, which could constitute all or some of an interacting face. This type of approach is work intensive and would be best executed with a corresponding atomistic structure. However, there are still caveats as exemplified by a recent study that used this approach to investigate the molecular determinants of the DPP6-Kv4.2 interaction. Functional experiments identified the single transmembrane helices and short intracellular segments of DPP6 as regions responsible for shifting the voltage-dependence of Kv4 channel activation and inactivation to more negative potentials (152, 176). To validate these molecular determinants with single residue resolution, researchers used an atomistic structure of DPP6 with Kv4.2, which revealed that the single transmembrane pass portion of DPP6 forms hydrophobic interactions between S1 and S2 of the Kv4.2 voltage sensor (160). The researchers created a series of single point mutants in the DPP6-S1/S2 interface of Kv4.2 and then measured the voltage-dependence of activation, inactivation, and recovery as it compared to the voltage-dependences of wild type Kv4.2 with and without DPP6. Interestingly, *G–V* measurements made from these single-point mutants revealed that the interface had some effect on influencing the voltage-dependence of activation. However, no single mutation was able to completely abrogate the effect of DPP6 on Kv4.2 voltage-dependence. This intermediate result could mean that either no one residue is fully responsible for

[49] TAT peptides are derived from the human immunodeficiency virus and are cell-penetrating peptides.

conferring the interaction, and possibly the residues identified were just a small part of a bigger interacting face, or rather, the wrong interacting face was probed[50].

My favored hypothesis regarding the molecular determinants of the AMIGO1-Kv2.1 interaction is that the transmembrane region of AMIGO1 is responsible for localizing AMIGO1 to the Kv2 channel. Based on the DPP6-Kv4.2 (160) and Nav β1/β2-Nav1.7 (159) structures, I would predict that AMIGO1 similarly localizes between the S1 and S2 of the Kv2.1 voltage sensing domain. To test the idea that the AMIGO1 transmembrane domain is responsible for localizing AMIGO1 with the Kv2.1 channel, one could create recreate the chimeras employed by Peltola et al.,2011 but with fluorescent tags to follow protein localization visually (32). If constructs lacking the AMIGO1 transmembrane still trafficked to the surface but were unable to colocalize with Kv2.1 channels, then the transmembrane segment would be necessary for interaction. To troubleshoot trafficking issues that might be associated with this chimeric construct, one could create an N-Kv2.1-AMIGO1-C "concatemer". When arranged in this order, the two proteins would be translated as part of the same peptide, but because of AMIGO1's signal sequence, I would expect the two proteins to be cleaved post-translationally, similar to a technique used in (113). The inverse experiment could also be conducted using a chimera made from the transmembrane regions of the Kv2.1 S1-S2 helices along with the N-terminal, S3-S6 helices, and C-terminal from a different channel (e.g., Kv1.5). If AMIGO1-YFP were to colocalize with the chimeric construct and not the wild-type unrelated channel, then together these results could support the hypothesis that the transmembrane regions of AMIGO1 are needed for interacting with Kv2.1. However, I predict that new structures determined from cryo-EM and advances in computational biology such as paired application of

[50] In contrast, these mutations had drastic effects on steady-state inactivation and recovery, suggesting that the DPP6-S1/S2 interface is important for regulating the speed and stability of voltage sensor movement but does not entirely define the mechanism for modulating voltage-dependence of activation. Most of the intracellular segment of DPP6 was not resolved, so similar structure-guided studies were not implemented to interrogate cytosolic interactions (160).

AlphaFold and RoseTTAFold molecular docking (422) will be transformative approaches in uncovering the molecular determinants of interacting protein pairs going forward.

Which AMIGO1 domain(s) are responsible for modulating Kv2.1 conformational change?

In Appendix B, I found that cotransfection of AMIGO1 with Kv2.1 Δ376C produced a *Q–V* curve statistically indistinguishable from the *Q–V* curve of Kv2.1 Δ376C alone, yet the preliminary trafficking and colocalization data was consistent with AMIGO1 still associating with Kv2.1 Δ376C. Because of this preliminary result, I hypothesize that the AMIGO1 intracellular terminus interacts with the Kv2.1 C-terminus to alter the stability of the earliest resting conformation. Interestingly, the preliminary results presented in Appendix B suggest that AMIGO1 gating modulation and Kv2.1 association are separable properties of the AMIGO1 protein. Because of this observation, my preferred hypothesis surrounding the AMIGO1-Kv2.1 interaction is that specific interactions between the AMIGO1 transmembrane and Kv2.1 transmembrane regions are responsible for conferring colocalization, while localization of an intracellular domain near the cytoplasmic face of the channel is sufficient to modulate Kv2.1 conformational change. The experiments presented in the following paragraphs are designed to test this hypothesis. However, it is worth noting that AMIGO1 could, alternatively, influence Kv2.1 voltage sensing by interacting extracellularly[51] with its Ig/LRR domains or intramembraneously[52] with its transmembrane domain to destabilize the resting conformation of the Kv2.1 voltage-sensing helix.

[51] Extracellular effects are expected for α2δ subunits. A recent structure demonstrated that the VWA domain of α2δ-1 makes contacts with Cav1.1 through the extracellular S5 and P1 helices in the 2nd and 3rd domains (161) and further, α2δ-2 enhancement of Cav2.2 expression requires an intact VWA domain (140).

[52] Weak effects on Kv4.2 gating are seen with mutations of transmembrane regions of DPP6 (160).

Prior to testing the hypothesis that the intracellular domains are responsible for gating modulation, additional replication and further analyses of experiments presented in Appendix B are advised, first and foremost. ON gating current measurements could be analyzed to assess the effects of AMIGO1 on early gating charge movements, the charge movement previously determined to be the primary target of AMIGO1's biophysical effect (177). Gating charge density could to be measured to assess if channel expression is altered between WT Kv2.1, Kv2.1 Δ333C, and Kv2.1 Δ376C. Additionally, a negative control could be done to assess colocalization between two non-interacting membrane proteins with diffuse surface expression; I expect that AMIGO1–YFP coexpression with Kv4.2–RFP or Kv2.1 coexpression with a YFP-labeled single-pass transmembrane protein (any of the proteins listed in Fig. 1.1) could serve as negative controls as long as they are verified to not independently associate with Kv2.1 channels. A complementary positive control to supplement these experiments would be simultaneous imaging of GxTX594 labeled Kv2.1 Δ333C and AMIGO1-YFP, while this channel is still predicted to express in a diffuse manner, the presence of an AMIGO1–dependent shift in the *Q–V* suggests that these two proteins might still be interacting. Finally, images demonstrating deferential AMIGO1 trafficking need to be quantitatively assessed. One method to assess trafficking would be to quantitate the total fluorescence intensity within an entire cell ($AMIGO1_{Total}$) and then to quantitate the amount of fluorescence associated with the cell surface membrane, a region that could be labeled with WGA-405 ($AMIGO1_{Surface}$) or identified systematically in analysis. The ratio of ($AMIGO1_{Surface}$)/($AMIGO1_{Total}$) would approximate how much AMIGO1 is trafficked to the cell surface under the different expression conditions. Such a method was previously employed to study how Kv2 expression modulates AMIGO trafficking (33). To automate this assessment, new images with better signal to noise ratios or lower plating densities might be warranted.

Do intracellular domains interact sterically?

The aforementioned analyses could make a convincing, but incomplete case that the most distal 376 amino acids of the Kv2.1 C-terminus are necessary for AMIGO1 to confer gating modulation. The hypothesis that these domains interact sterically could additionally be tested by a reconstitution assay in which patches containing AMIGO1 and Δ376C Kv2.1 are exposed to a solution containing an exogenously prepared peptide fragment composed of the most distal 376 amino acids. If a gating modulation of AMIGO1's approximate magnitude were to be recovered, then this experiment could provide strong evidence that the distal Kv2.1 C-terminus is needed for gating modulation. Alternately, the Kv2.1 C-terminus could be tested by first identifying the minimum fragment necessary to confer a gating shift, something that could be assessed by making gating current measurements from serial truncation mutants that successively narrow down the region of interaction. Once this region is identified, one could carry out a competitive binding assay targeted at this region using cell penetrating TAT-peptides (423). Alternatively, competition experiments could be carried out with a solution containing an exogenously prepared peptide fragment composed of the AMIGO1 intracellular domain. In theory, application of a saturating amount of TAT peptides or the AMIGO1 intracellular domain, would out compete endogenous AMIGO and Kv2.1 interactions. If the effects of AMIGO1 on Kv2.1 voltage sensor movement were abolished, then this experiment would provide evidence that the targeted molecular region participates in AMIGO1-Kv2.1 interactions.

Does AMIGO1 expression alter the phosphorylation status of Kv2.1 intracellular domains?

Alternative to AMIGO1 and Kv2.1 intracellular domains interacting sterically, it is also possible that AMIGO1 alters the Kv2.1 C-terminal domain in a manner that cannot affect the Δ376C truncation mutant, but does affect the Δ333C truncation mutant. One key difference between these two Kv2.1 mutants is the inclusion of S563 in Δ333C, a residue that is important for phosphorylation-dependent

modulation of Kv2.1 activation (354)[53]. Further, there are at least five other residues present in Δ333, but not in Δ376C, that are predicted by sequence or determined by mass spectrometry to be sites for phosphorylation (Fig. B.4). Kv2.1 channels are known to regulate their voltage-dependence based on their phosphorylation status; does AMIGO1 modulate Kv2.1 voltage sensing by changing the phosphorylation status of the C-terminal?

To test this hypothesis, one could carry out immunohistochemical experiments with phosphospecific antibodies raised against the S563 site. If S563 site was differentially phosphorylated in cells that lack AMIGO1 compared to cells that coexpress AMIGO1, this would suggest that AMIGO1 influences channel post-translational modifications, an effect similarly seen between DPP6 and Kv4.2 (259). These results could be complemented with an electrophysiological study of AMIGO1 coexpressed with Kv2.1 S563A mutant and wild-type Kv2.1. If both constructs gave similar AMIGO1-dependent shifts in the *G–V* or *Q–V*, then these two results would be consistent with the presence of AMIGO1 changing Kv2.1 phosphorylation patterns at S563 to confer a hyperpolarizing shift in the voltage-dependence of activation, much like what is seen with dephosphorylation of other sites on the Kv2.1 C-terminus (354).

If the intracellular regions appear to be important for facilitating AMIGO1-Kv2.1 interactions, the ramifications for voltage-dependent modulation of gating could be tested by carrying out voltage-clamp FRET experiments. The Kv2.1 C-terminals and N-terminals of a doubly-tagged CFP-Kv2.1-YFP construct undergo voltage-dependent rearrangements that can be resolved through FRET (424). To assess if AMIGO1 disrupts this intracellular conformational change, AMIGO1-pIRES-mplum could be expressed in the presence of CFP-Kv2.1-YFP, and CFP-YFP FRET would be assessed while under voltage-control. If voltage steps that do not activate gating charge movement alter CFP-YFP FRET in cells that express

[53] S563A (a non-phosphorylate-able mutant) and S563D (a phosphomimetic mutant) exhibit a $\Delta V_{1/2}$ of -15.6 mV, with the voltage-dependence of S563D being more depolarized than S563A (354).

AMIGO1, but not in control cells, this would provide evidence that C-terminal rearrangements precede voltage-dependent activation and that AMIGO1 alters these arrangements.

Determining the structural mechanism through which the voltage-dependence of Kv2.1 can be modulated

While more experiments are required to determine the structural mechanism through which AMIGO1 alters Kv2.1 conformational change, a second interesting result from Appendix B raises a larger question about the overall structural mechanism that underlies the voltage-dependence of Kv2.1 conformational change. In these experiments, I observed that the *Q–V* relationship for Δ376C was shifted to hyperpolarized voltages, which suggests that the distal 376 amino acids of the C-terminal domain detain Kv2.1 voltage sensors in an early resting conformation. Why would this be? From FRET experiments, it is clear that Kv2.1 intracellular domains undergo voltage-dependent rearrangements (425). Further, electrophysiology experiments, demonstrate that the phosphorylation status of the C-terminus affects the voltage-dependence of activation (354), suggesting that C-terminal and voltage sensor conformations are coupled. What are the structural underpinnings of this coupling? Does the C-terminus directly interact with the resting conformation of the voltage sensor or is there an allosteric interaction?

To being to answer these questions, we can first turn to the atomistic structures of other voltage-gated ion channels. Intracellular C-terminal interactions were characterized in the cockroach NavPaS structure (185), which depict the globular C-terminus interacting with the 3rd and 4th domain linker (reminiscent of the Cav1.1 structure (161)), the 4th domain voltage sensor, the 4th domain S4-S5 linker, the 4th domain S6 helix, and the 3rd domain S6 helix. While these interactions were nearly the same as those seen in the crystal structure of the Nav1.5 C-terminal domain (426), Nav channels have a considerably

smaller intracellular domain than Kv2.1 channels. Might disrupting intracellular C-terminal interactions be an additional mechanism to alter voltage sensor movement? My preferred hypothesis is that cytoplasmic interactions between the C-terminus form an intracellular gate that must be unlocked by sufficient S4 activation in order for the channel pore to open.

To test this hypothesis, one could carry out a competitive binding experiment designed to abrogate the intracellular face between the globular C-terminal domain and the intracellular faces of the voltage sensor. Alternatively, Kv2.1 constructs could be engineered by tandem protein splicing to contain non-natural amino acids near the hypothesized sites of interaction (30), the fluorescence of which could be monitored while simultaneously carrying out voltage clamp experiments to provide functional insight into intracellular conformational changes.

Open Questions

Potential roles of AMIGO1 as a part of the Kv2.1 channel complex

Because of the ubiquity of AMIGO1 and Kv2.1 coexpression and codiffusion (32, 121), I conclude that the extracellular adhesion protein, AMIGO1, forms a functional part of the Kv2.1 voltage sensing domain. Further research is warranted to understand the physiological role of such a coupling and what the pathophysiological implications of decoupling would be. Several outstanding questions about Kv2–AMIGO1 interactions could be worth investigating:

Is the AMIGO1 gating shift physiologically important?

We have previously outlined the impact of Kv2.1 conductance on macroscopic neuronal signaling (29, 427) and even though the effect of AMIGO1 on Kv2.1 voltage dependence is only ~ -7 mV a study from AMIGO1 knockout mice does reveal modified I_K currents. Without AMIGO1 present, I_K currents from

CA1 pyramidal neurons require ~5-10 mV of additional voltage to activate (375), consistent with the lack of an AMIGO1–dependent leftward shift in voltage dependence that we note here. Interestingly, AMIGO1 knockout mice also display schizophrenia-related features (375), suggesting that the physiological role of AMIGO1 is important. Similarly, our assessment that the AMIGO1-induced shift is small, stems from a comparative frame of reference. Other auxiliary subunits have much larger effects on their partner ion channels (113, 114, 125, 171, 401, 428)(Table 1.3) and hippocampal neurons, a cell type where Kv2 channel are populous, experience ~90 mV voltage swings during the course of an action potential (429). Both reference points suggest that a ~7 mV voltage shift might be inconsequential. However, are these metrics the correct reference points? Might conceptualization of AMIGO1's effect size be more comprehensible if compared to the physiological and pathophysiological bounds to which Kv2 channel voltage-dependence can be modulated. Under a hypoxic, pathophysiological-like insult, Kv2 channels experience a ~-20mV depolarizing shift in the conductance–voltage relationship of Kv2.1 (17, 23), and compared with this scale, a ~-7 mV voltage shift would be significant. The extent to which AMIGO1 is physiologically important is further supported by data from ~125,000 aggregated genome data sets, which suggest that loss of function mutations within AMIGO1 are more rare than expected by a depth corrected probability of mutation for each gene; 12.6 loss of function mutations are expected, yet none are observed (430)[54].

[54] Similar analyses on other auxiliary subunits report (X observed loss of function mutations/ Y expected loss of function mutations): Nav β1: (2/4.9). Nav β2: (5/7.4). Nav β3: (4/11.4). Nav β4: (9/8.2). AMIGO2: (2/11.4). AMIGO3: (7/10.5). LINGO1: (0/15.3). HEPACAM(1): (2/15.4). HEPACAM2: (17/20.3). LRRC26: (3/4.2). LRRC52: (8/8.4). LRRC55: (4/10.6). LRRC38: (2/5.8). DPP6: (11/48.3). DPP10: (4/51.4). α2δ -1: (17/119.1). α2δ -2: (10/74). α2δ -3: (15/68.5). α2δ -4: (60/73.6). For Kv2.1 there are 24 predicted loss of function mutations, yet none are observed. For reference, the gnomAD exome project found a median of 17.9 expected loss of function variants per gene and that 72.1% of genes had more than 10 loss of function variants observed (430).

Could AMIGO1 modulate nonconducting functions of Kv2 channels?

Nearly twice the size of AMIGO1's impact on Kv2.1 conductance is AMIGO1's impact on Kv2.1 voltage sensor movement (Table 3.1, Table 3.2). Due to a striking finding that Kv2.1 conductance is tied to the density of surface expression (352, 431), it has been proposed that the vast majority of Kv2.1 channels exist in a nonconducting, but still voltage–sensitive, state (432). Identification of Kv2.1 nonconducting roles is an area of active study (243, 350), and while the stoichiometry between AMGIO1 and Kv2.1 in these large clusters is unknown, we expect AMIGO1 to alter any and all of voltage-sensitive, nonconducting functions of Kv2.1 that may exist.

Does Kv2.1 conformational change affect AMIGO1 function?

The principle of microscopic reversibility and coupled equilibria dictates that because AMIGO1 destabilizes the conformation of Kv2.1 voltage sensors, then the resting conformation of Kv2.1 voltage sensors must destabilize an AMIGO1 conformation. In theory this could confer a voltage sensitivity to AMIGO1 function. Could Kv2.1 voltage sensing modulate AMIGO1 actions as an extracellular adhesion protein? Could AMIGO1 actions as an extracellular adhesion protein modulate Kv2.1 voltage sensing? While it is unclear whether there are functionally important allosteric interactions between AMIGO1 conformational change and AMIGO1 conformational change, but it could be an interesting avenue for future studies.

Does AMIGO1 facilitate Kv2 electrical signaling between cells?

Using its leucine rich repeat domain, AMIGO1 homo- and heterotetramerizes with other AMIGO proteins in *vitro* (201). It would be interesting to test if AMIGO1 participates in cell-cell *trans* interactions. Based on the Kv4.2-DPP6 structure, it is reasonable to speculate that four AMIGO1 subunits might

associate with the Kv2.1 channel, forming two dimers that interact in *cis* above the pore of the channel (160). This *cis* interaction could create an interface suited to facilitate additional *trans* interactions. To test if AMIGO1 formed *trans* interactions in culture, individual stocks of cells could be transfected with either AMIGO1 extracellularly tagged with a donor molecule or AMIGO1 extracellular tagged with an acceptor molecule, the presence of FRET or BRET at cell-to-cell junctions would suggest that AMIGO1 localizes within a distance suitable for making *trans* interactions. Exogenous application of the AMIGO1 ectodomain could be applied to abrogate these interactions. If the *trans* interactions are present, one cell could be identified for current clamp while the opposing cell could be monitored for changed in the membrane potential. If application of exogenously prepared AMIGO1 ectodomain alters the electrical coupling between cells, this could be grounds for further investigation into whether AMIGO1 promotes epiphatic electrical coupling between cells. Such intercellular electrophysiological communication is facilitated by HEPACAM at tripartite synapses, which are the junctions between the presynaptic, postsynaptic, and glial cell membranes (433).

Could AMIGO facilitate communication between the extracellular matrix and endoplasmic reticulum?

AMIGO1 *cis*-intracellular interactions could further reinforce Kv2.l's proclivity to cluster, or even packing channel proteins in tighter than what is seen in the absence of AMIGO1, creating Kv2.1 channel dimers, such as seen for Nav channels (245). In HEK293T cells and cultured hippocampal neurons, Kv2.1 interaction with ER-resident VAMP-associated proteins creates ER-plasma membrane junctions (349) that are densely populated with Kv2.1 channels and are platforms for ion channel insertion and endocytosis (241). Here, Kv2.1 clustering promotes local and global Ca^{2+} signaling by bringing plasma membrane L-type Ca^{2+} channels and ER-localized ryanodine receptors into a range sufficient to foster Ca^{2+} induced Ca^{2+} release (350). These Kv2.1 clusters and ER-plasma membrane junctions are found both on neuronal cell membranes directly opposed to astrocytic end feet (16) and on rat alpha motor neuron membranes

apposed to cholinergic c-type synaptic terminals (434), as such, any changes in surface potential experienced by or created by Kv2.1 voltage sensors/channel complexes in these microdomains could be propagated intercellularly. How these intracellular communication hubs are created is unknown. Does AMIGO1 localize Kv2.1 to these tightly apposed intercellular membrane junctions? To test this, one could potentially use single particle TIRF imaging with GxTX-Qdot technology, Kv2.1-GFP, or immunohistochemistry and image the distribution or density of channel clusters with and without AMIGO1. This could be assessed in closely apposed cells expressing nonclustering Kv2.1(S586A) or with a limited induction time using the Kv2.1–CHO cell line. Alternatively, this could be assessed in co-culture of transduced or transfected astrocytes and neurons.

Concluding Remarks

To fully integrate and assess potential of AMIGO1-Kv2.1 physiology, studies designed to dissect how the adhesive properties of AMIGO1 contribute to and intermingle with Kv2.1 voltage-sensitivity physiology are needed. Ultimately, the importance of any of these *in vitro* results would be difficult to interpret without a glimpse of physiological relevance. To probe this, cell types that localize in proximity (such as at astrocytic end feet) would need to be genetically engineered or transduced so that the effects of cell-type specific knockdown of AMIGO1 could be assessed. Cell-to-cell junction morphology, Kv2.1 localization, and electrical activity could be assessed to determine if AMIGO1 is key in forming these cell-to-cell interactions. Alternatively, similar parameters could be assessed a mouse line with genetically altered Kv2.1 voltage sensing to determine if the formation of these junctions have a voltage dependence. Understanding the interdependence of adhesion proteins and ion channels will provide insight into potentially unique aspects of the molecular machines that drive electrical systems.

APPENDIX A: Efforts towards developing a photoacoustic tracer to detect Kv2 ion channel conformational change in deep tissue

Preface

This appendix details my efforts towards developing a tracker for Kv2.1 conformational change that is compatible with photoacoustic imaging. This work has not been previously published, and some preliminary results were presented as an abstract at the 2016 3rd annual NIH BRAIN Investigators meeting in Rockville, MD and at the 2017 SPIE Biophotonics West Conference in San Francisco, CA. I wrote this chapter with editorial feedback from Jon Sack. I acquired and analyzed most of the data included within this chapter. Notable exceptions include the following. The absorbance data was collected by Lindsay Fague (Fig. A.2B). The fluorescence emission data was collected by Sebastian Fletcher-Taylor (Fig. A.2C). The voltage clamp data was acquired with technical assistance from Parashar Thapa (Fig. A.4). Diego Yankelevich, Ben Sherlock, and Clay Sheaff were instrumental in helping to assemble the photoacoustic microscope for image acquisition (Fig. A.5A). Ben Sherlock also wrote the MatLab code for photoacoustic image processing.

Abstract

A three-dimensional understanding of electrophysiological dynamics in the brain requires a technique that spatially and temporally resolves neuronal activity deep in the brain. Photon scattering in brain tissue limits most light microscopy to superficial depths. When photons propagate longer than one mean free path, about 1 mm in turbid tissue, they lose coherence and are not resolved with integrity by ballistic imaging methods. Photoacoustic imaging, an emerging technology, combines a photonic stimulus with deep-tissue ultrasonic detection to create an absorbance-based imaging modality capable of imaging cm depths in tissue. To take advantage of the tissue-penetrative capacity of this imaging modality, I conjugated a tracker of Kv2 conformational change, GxTX, to a photoacoustic contrast agent with the goal of creating a tracer for neuronal ionic activity in the deep brain. GxTX affords molecular selectivity and conformational specificity to the molecular tracer by binding to resting state Kv2 ion channels. In response to depolarizing membrane voltages, Kv2 channels change conformational states which alters the Kv2.1–GxTX complex. Different activity-dependent conformations of the Kv2.1–GxTX complex expose the 27th GxTX residue to different environments and garner a contrast agent with different spectroscopic properties. So far, we have confirmed that different spectroscopic properties coincide with different photoacoustic properties, suggesting that this approach may be compatible for photoacoustic imaging Kv2.1 conformational changes in deep tissue. While we were able to collect data suggesting that there is a robust photoacoustic signal intensity change when the tracer moves between chemical environments that mimic those experienced by resting and activated Kv2.1 voltage sensing domains. However, I was unable to see similar photoacoustic intensity shifts in response to modulated ion channel dynamics in live cells, suggesting a new approach is warranted. Deep tissue imaging of electrophysiological channel dynamics will identify key regions and temporal patterns involved in physiological and pathophysiological neural activity.

Introduction

Neuronal signaling is governed by diverse ion channels that gate the flow of electrical currents within a cell. There are over 80 voltage gated ion channel proteins encoded in the human genome (331, 435) that work in concert to gate this current and produce cohesive electrical signals. The voltage-gated potassium channel family (Kv) is the largest and most genetically varied subset of neuronal ion channels (436); these channels respond to cellular depolarization, and regulate the efflux of potassium current in order to both facilitate repolarization and control action potential firing frequency (4). Kv channels are crucial in regulating neural electrical excitability (5–7). Within the potassium channel family, Kv2 channels are the most ubiquitously expressed subtype in the mammalian brain (2). Kv2's electrical properties are dynamically regulated by its expression level (9), phosphorylation state (10), expression morphology (11–15), and subcellular expression patterns (16). Due to this dynamism, identifying the precise role Kv2 plays in regulating excitability, especially neuronal hyperexcitability, has proven to be difficult.

Our ability to directly assay Kv2 activity is largely limited by available technologies. This is especially true when studying pathophysiologically vulnerable and therapeutically relevant areas of the brain, like the hippocampus. Evaluation of native hippocampal Kv2 activity is currently out of reach. Buried deep within the brain, live hippocampus activity is typically studied with invasive and low molecular/spatial resolution and nonspecific electrical recording techniques. Assessment via noninvasive, optical imaging techniques is limited by light scattering in turbid brain tissue. Photoacoustic imaging (PAI) is a noninvasive, absorbance-based imaging technique. In PAI, electromagnetic energy, delivered from a laser pulse, is absorbed by a contrast agent. Electrical excitation and subsequent relaxation creates a small increase in temperature that is transformed into an acoustic wave via thermoelastic expansion (437, 438). Acoustic waves propagate through turbid issue 2-3 orders of magnitude better than light (439) and as a result this technique breaks the 1 mm depth limit of conventional light microscopy techniques

(440). Fully optimized PAI systems can achieve 5-100 μm spatial resolution at 1-20 mm depths with 100 KHz temporal resolution (441). PAI can monitor endogenous contrast agents and track hemodynamics (441). By multiplexing detection of endogenous contrast agents and exogenous tracers for Kv2 conformational change, PAI could provide a wealth of information about how, when, and where Kv2 channels respond most to different pathophysiological insults.

Compared to competing methodologies that probe neural activity, PAI provides unmatched spatial: depth resolution (1:200). fMRI has superior depth penetration, however only able to probe hemodynamics, a correlative output of neuronal activity, on the spatial scale of large neuronal ensembles. Conventional fluorescence imaging of molecular neural activity tracers offers high, sub-micron, spatial resolution but is restricted to superficial imaging depths less than 1 mm. This mesoscale system utilizes tissue-penetrating near infrared light (NIR) and can achieve 100 μm resolution at 2 mm depths, with 20 Hz temporal resolution (442).

To evaluate endogenous Kv2 activity with high spatial and temporal resolution during neuronal hyperexcitability, I aimed to create a molecular tracker of Kv2 conformational change that was compatible with deep-tissue photoacoustic imaging. I combined the tarantula toxin based backbone, guangxitoxin 1-E (GxTX) (321, 443) with a poorly fluorescent contrast agent, aminophenoxazone (AP) (331), with spectroscopic potential for photoacoustic imaging. AP is a small molecule fluorophore with electron donating and accepting groups that are separated by an aromatic ring system. AP is zwitterionic and thus exhibits polarity-dependent spectral changes shifts of about ~30 nm (331). In polar solvents like water and methanol, AP exhibits a red-shifted excitation maxima, a poor absorption coefficient, and a poor quantum yield. In nonpolar solvents like acetonitrile, AP has a blue-shifted excitation maxima, a large absorption coefficient, and a high quantum yield (331). Thus, changes in the environment surrounding AP can be detected either by changes in fluorescence intensity or by a shift in the absorption and emission spectra. A photoacoustic signal is determined by the amount of photonic relaxation that

occurs by non-radiative (heat-producing) decay and any relaxation that proceeds through photochemical decay (or a fluorescence-producing route), directly detracts from the total photoacoustic signal. Accordingly, molecules that are efficient fluorophores are predicted to make weak photoacoustic contrast agents and vice versa.

In the following section, I discuss my attempt to create a photoacoustic tracer of Kv2 channel conformational change. I present fluorescence data supporting that AP and GxTX K27Pra(AP) exhibit environment sensitive signals and compelling data suggesting that these environmentally dependent signals could be detected by photoacoustic imaging at certain concentrations. However, I was unable to successfully detect GxTX K27Pra(AP) bound to cells with a large enough signal to noise ratio for this method to be viable in tissues. As such, I detail a list of pitfalls and challenges associated with the project and comment on what could be done next to further this line of research.

Results

Approach

The photoacoustic tracers tested here consist of an activity-responsive, Kv2 channel-selective ligand conjugated to a fluorophore. The guangxitoxin-1E (GxTX) ligand confers both channel activity detection and channel-selectivity to the tracer. Mutation of key GxTX residues, such as K27, or truncation of the toxin terminal tails, ΔC1N3, results in a ligand with altered state-dependent binding preferences and significantly decreased dissociation rates in response to voltage activation of the voltage sensing domains. We hypothesized that conjugation of GxTX K27 or GxTX ΔC1N3 to a dye with optical properties that are environmentally sensitive, will create a non-dissociating, photoacoustic tracer that changes its photoacoustic properties with respect to Kv2.1 conformational status (Fig. A.1).

GxTX–AP is environmentally sensitive and responds to Kv2.1 conformational change

Aminophenoxazone (AP) is a fluorescent molecule (Fig. A.2.A) that undergoes a large polarity-dependent bathochromic (or red) shift in its excitation and emission spectra when in a more polar environment (331). To predict how this shift in optical properties might translate to a photoacoustic output, we first assessed the absorption (extinction) coefficient of AP in two solvents of varying polarity. We found that in a less polar solvent, acetonitrile, AP has a seven-fold greater absorption coefficient than it does in a more polar solvent, neuronal buffer (Fig. A.2.B). Interestingly, when GxTX Lys27Pra(AP) is bound to channels with resting voltage sensors, its fluorescent emission spectrum mimics that of AP dye dissolved in acetonitrile (Fig. A.2.C). When GxTX Lys27Pra(AP) is dissolved in neuronal buffer, its fluorescent emission spectrum mimics that of AP dye dissolved in neuronal buffer (Fig. A.2.C). Work with a chemically related fluorophore has demonstrated that phenoxazone derivatives conjugated to GxTX at the 27th position are exposed to a polar environment upon voltage sensor activation (322). Based

on this, we would expect GxTX Lys27Pra(AP) to exhibit two distinct absorption and emission profiles when bound to the resting (nonpolar-exposed) and activated (polar-exposed) states of the Kv2 voltage sensor. Further, fluorescent images of a coculture of Kv2.1 expressing CHO cells with BFP CHO cells that lack Kv2.1 expression demonstrates that GxTX Lys27Pra(AP) has selectivity for cells that express channels (Fig. A.2.D), suggesting that this tool could be used to photoacoustically track where Kv2 channels are localized in their active state.

Prior to testing this hypothesis, I wanted to validate that an experimental preparation compatible with the constraints of photoacoustic imaging did not abrogate the ability of GxTX Lys27Pra(AP) to preferentially bind to samples expressing Kv2 channels. Since photoacoustic imaging tracks sound waves, a conducive medium like water or ultrasound gel must be used to couple the sample to the ultrasound transducer. Since salts present in neuronal buffers and cell media could harm the ultrasound transducer over time, we decided that cells must be separated with a physical barrier from the transducer. Initial attempts to couple the sample and the transducer employed a plastic wrap seal over wells loaded with cells and media, so that the transducer, coated in ultrasound gel, could raster scan over the sample atop of this barrier. While this approach had the benefit of a simple sample preparation, any air bubbles that were trapped between the liquid surface of the sample and the plastic wrap created large artifacts that were detrimental to image reconstruction. To overcome this obstacle, we switched approaches and instead loaded a suspension of cells into capillary tubes that could be suspended in water (Fig. A.5.A). This approached allowed us to couple the sample to the transducer by water and had the added benefit of exponentially increasing the number of channels present in an imaging voxel over what we could achieve in a monolayer of cell culture. To achieve the maximum density of cells possible for imaging, cells were cultured in T-175 flasks, harvested with trypsin prior to imaging, treated with GxTX Lys27Pra(AP) while in suspension, washed multiple times, and then dissolved in a minimum amount of neuronal buffer before being loaded into the capillary and sealed-in with glue. CHO cells were either

induced to express Kv2.1 channels for 48 hours or left uninduced, such that when labeled with GxTX Lys27Pra(AP), only the cells expressing Kv2.1 channels were expected to retain the GxTX–AP signal throughout the multiple wash steps. To test this hypothesis, both groups of CHO cells were loaded into capillaries and imaged with a confocal microscope (Fig A.2.E). While we did see AP aggregates in both capillaries, the average AP emission was 3-fold greater in the capillary loaded with cells that expressed Kv2.1 channels compared to the control (Fig. A.2.F). Spectral imaging of these samples revealed that the AP emission from the cells expressing Kv2.1 was largely left-shifted while the AP emission from control cells was largely right-shifted (Fig. A.2.GH). This result is consistent with GxTX Lys27Pra(AP) specifically labeling resting Kv2.1 channels in CHO cells that express Kv2.1 and nonspecifically aggregating with CHO cells that lack Kv2.1 channels in the preparation necessary for photoacoustic imaging. Similar results were obtained from GxTX ΔC1N3 Ser13Pra(AP) (Fig. A.3.A-C).

To test if GxTX Lys27Pra(AP) responds to changes the conformation of the Kv2.1 voltage sensor, we voltage clamped CHO cells induced to express Kv2.1 channels. Cells were treated with GxTX Lys27Pra(AP) and progressively stepped to depolarized potentials. Spectral imaging of AP fluorescence revealed that similar to GxTX Lys27Pra(JP) (322), GxTX Lys27Pra(AP) exhibited a small spectral shift in emission with voltage (Fig. A.4).

AP environmental sensitivity can be resolved with photoacoustic imaging

To test if we could detect the environmentally-dependent signals of AP using photoacoustic imaging and determine a rough approximation of the noise limit of the photoacoustic imaging system, we first measured the photoacoustic signal of different concentrations of AP dissolved in either neuronal buffer and acetonitrile (Fig. A.5.B). Similar to our hypotheses, AP exhibited a greater photoacoustic signal when it was exposed to the polar, neuronal buffer compared to when it was dissolved in acetonitrile (Fig. A.5.C). AP concentrations of 10 μM and higher, could be discernably distinguished from the background.

To test if the photoacoustic profile of AP retained the same sensitivities to polarity as the fluorescence emission profile, we also assessed the photoacoustic signal of AP dissolved in a battery of solvents (Fig. A.5.D). Since the polarity of the solvent dictates the stability of the zwitterionic molecule when in its excited state, the ε, absorption coefficient, and QF, quantum yield, of AP vary based on solvent. PA intensities of AP when dissolved in ethyl acetate (ε = 47,000 $M^{-1} \bullet cm^{-1}$; Q_F = 0.49), acetone (ε = 51,000 $M^{-1} \bullet cm^{-1}$; Q_F = 0.91), acetonitrile (ε = 47,000 $M^{-1} \bullet cm^{-1}$; Q_F = 0.78), DMSO (ε = 48,000 $M^{-1} \bullet cm^{-1}$; Q_F = 0.45), methanol (Q_F = 0.34), and neuronal buffer (Q_F = 0.05) were all consistent with signals predicted from the approximation of photoacoustic intensity based on ε and Q_F (Fig. A.5.D) (ε and Q_F values from (331)).

When the photoacoustic signal was assessed for cells in capillaries, we were able to detect a slight increase in signal for Kv2.1-expressing cells that had been treated with GxTX ΔC1N3 Ser13Pra(AP) compared to those that had been treated with a vehicle (Fig. A.5.F), however a similar increase with GxTX ΔC1N3 Ser13Pra(AP) was also seen in CHO cells that were not expressing Kv2.1 channels. While we expect GxTX ΔC1N3 Ser13Pra(AP) to be photoacoustically "quiet" when bound to resting Kv2.1 voltage sensors, the inability to distinguish the GxTX ΔC1N3 Ser13Pra(AP) signal in CHO cells lacking channels from the signal from CHO cells expressing Kv2.1 channels indicates that some GxTX ΔC1N3 Ser13Pra(AP) might be nonspecifically associating in cell membranes or accumulating as aggregates.

Discussion

While we were able to conjugate a slow-dissociating GxTX variant to an environmentally-sensitive dual-modality contrast agent (AP) that exhibited environmentally-sensitive photoacoustic signals (Fig. A.5), we were unable to demonstrate with photoacoustic images that this probe was selective for Kv2.1 channels (Fig. A.5.F) or that it responded to conformational changes within the Kv2.1 voltage sensor. Fluorescently, these GxTX–AP tools showed environmental-sensitivity (Fig. A.2), activity-responsiveness (Fig. A.4), and Kv2 channel specificity (Fig. A.2-3). However, several limitations prevented us from detecting these same qualities by this complementary, photoacoustic imaging modality.

Limitations

The first limitation that prevented us from assessing the specificity of GxTX–AP by photoacoustic imaging was the signal to noise ratio of the imaging system and sample preparation. In order to achieve a 2-3:1 SNR ratio with our photoacoustic system, a concentration of > 10 μM AP was necessary (Fig. A.5.C). Based on estimates (Table A.1), to even approach the number of channels necessary to accumulate these levels of AP within the imaging voxel, it was necessary to localize > 50000 cells with resting Kv2 voltage sensors within a 50 μm^2 region. This is not practical for monolayer cell culture of CHO cells which are 10 μm in diameter and have a footprint area of ~30 μm^2. We attempted to overcome this barrier by imaging the cells while loaded in 3D suspension in a capillary tube. With our PA setup, we were able to image through several mm of sample while achieving depth resolution of ~70 μm (444). Through summation of the time-resolved depth signal, we were able to integrate PA signal from cells suspended in 3D that were localized in the same voxel. This approach helped us decrease our threshold for signal detection but required large volumes of cell culture and high concentrations of GxTX–AP (> 3 μM).

The aforementioned requirements for dense cell culture likely contributed to the second limitation that we faced: GxTX–AP aggregation (Fig. A.2-3) and non-specific accumulation of GxTX–AP within the membranes of cells not expressing Kv2.1 channels (Fig. A.5.F). When binding Kv2 channels, GxTX first partitions into the outer leaflet of the plasma membrane and then localizes on the extracellular edge of the channel's voltage sensing domains (445–449). When treating with such high concentrations of GxTX–AP we expect that some of the toxin might remain non-selectively partitioned within the membrane even during the aggressive wash steps. This nonspecific signal is expected to be polar-exposed and thus would have greater photoacoustic properties than what we would expect to see from GxTX–AP specifically bound to resting Kv2 channels. Additionally, the for the PA imaging cell preparation protocol, cells were subjected to long periods in suspension in minimal media (> 45 min). These nonoptimal conditions could have led to channel internalization, which would decrease the number of GxTX–AP binding sites available, or cell death, which could lead to GxTX–AP internalization and an artificial increase in GxTX–AP signal. While all samples were treated in series, Kv2.1 expression is known to alter cell health (21), so it is possible for the control and test groups of cells to respond differently to the extensive cell preparation protocol.

We concluded that this specific contrast agent was too "quiet" for viable use in deep tissue imaging. While activation of Kv2.1 channels in CHO cells could have preferentially increased the signal of GxTX Lys27Pra(AP) by shifting the environment proximal to AP, the technical and physical limitations of this project prevented us from assessing this hypothesis.

Future Directions

Due to the limitations encountered and technical difficulties with photoacoustic instrumentation, I chose to not pursue this project further. However, one could continue this work by testing if a high potassium external solution to momentarily activates the Kv2.1 voltage sensors to increase the PA signal.

While we have had success using this stimulus to track Kv2.1 activation with fluorescent imaging approaches (443), the time-intensive requirements for PAI sample preparation would likely result in all effects of this stimulus disappearing before we are able to image. Kv2.1 channels deactivate on the timescale of ms (320) and inactivate on the timescale of s (450). While we do not expect GxTX Lys27Pra(AP) to dissociate from inactivated channels, we have not measured the optical properties of GxTX Lys27Pra(AP) when bound to inactivated channels, and do not know if this would increase or decrease the AP signal. As such, a new sample preparation protocol would likely need to be implemented.

Conclusions

Combining GxTX peptides that track conformational changes of Kv2.1 channels with contrast agents suited for photoacoustic imaging remains a viable approach for monitoring Kv2 conformational change in deep tissue. However, for this approach to be practical, GxTX must be paired with a high intensity, PA contrast agent.

Acknowledgements

Ben Sherlock, Clay Sheaff, Diego Yankelevich, Sebastian Fletcher-Taylor, Bruce Cohen, and Laura Marcu were all instrumental in the acquisition of this data. Their guidance, technical support, patience, feedback, and time are all greatly appreciated.

Methods and Materials

GxTX peptides

GxTX K27Pra was synthesized as described in Appendix B.

Conjugation and purification

GxTX K27Pra was conjugated with aminophenoxazone (AP) using 1M Tris pH 6.8 (2 uL 10 mM $CuSo_4$ (1.5 uL), 20 mM BTTAA (4.5 uL), 10 mM AP azide in DMSO (2 uL), 100% DMSO (2 uL), 2 mM GxTX K27Pra in H_2O (2 uL) and fresh 150 mM sodium ascorbate (5 uL). Reagents were mixed in a Lo Bind Eppendorf tube and allowed to react for 5-24 hours on the Thermomixer at 1000 RPM at 20 °C temperature. The reaction was quenched with an equal volume of 20 mM EDTA pH 5. If precipitate was found, the supernatant was removed, centrifuged at 10,000 RMP for 10 min and was checked again for a pellet. Soluble conjugated product was purified using a Biobasic-18 4.6 mm RP-C18 (5 μm) column using a gradient from 5-50% ACN over approximated 50 min. Fractions of unconjugated AP, conjugated AP and GxTX, and unconjugated GxTX were collected and saved. Before running the samples on the HPLC. 2 uL of a test peptide were injected with 100 uL of 95% A and 5% B to test that GxTX could be detected by 280 nm excitation and 350 nm emission. The approximated molar extinction coefficient of GxTX (18,900 AU mol^{-1} cm^{-1}) was used to calculate the concentration of the conjugated product.

Cell culture

A CHO cell line stably expressing nuclear BFP and the Kv2.1–CHO cell subclone were cultured as described in Chapter 2.

Capillary sample prep

For capillary imaging experiments, cells were grown up in T-275 flasks and harvested with 0.05% trypsin and counted using a hemocytometer. 10^7 harvested cells were resuspended in minimal volumes of neuronal external solution and treated with 3 μmoles GxTX K27Pra(AP) or ΔC1N3 Ser13Pra(AP) for 5 min in an Eppendorf tube. Cells were then spun at 500 rcf and washed with 1 mL NE to remove the unbound fraction. Spinning and washing was repeated 3 times.

Fluorescence capillary imaging

5-10 uL of the cell slurry labeled with GxTX K27Pra(AP) or ΔC1N3 Ser13Pra(AP) was loaded into quartz capillaries (ID: 0.5 mm, OD: 1.0 mm) by pipetting. A 10x objective was used to visualize both capillaries in the same field of view. Fluorescence images were taken with the 543 or 594 nm laser. Fluorescence intensity was quantitated from regions of the capillary devoid of cellular debris. Spectral images of the same capillaries were acquired with the 543 or 594 nm laser. AP emission spectra were normalized with the maximum value and background subtracted. A ration of the average emission intensity between 590-611 nm and 623-644 nm was computed to assess the nonpolar characteristic of AP emission.

Photoacoustic capillary imaging

5-10 uL of the cell slurry labeled with GxTX K27Pra(AP) or ΔC1N3 Ser13Pra(AP) was loaded into quartz capillaries (ID: 0.5 mm, OD: 1.0 mm) by pipetting. Careful attention was paid to prevent the inclusion of bubbles. Capillaries were sealed shut with hot glue and then loaded onto the imaging apparatus. A singular piece of graphite lead or an india ink loaded capillary was also loaded into the imaging apparatus to be used as an internal standard to calibrate image intensity between imaging sessions and to

denote the identities of the different samples. Capillaries were locked in place with tape or a weight and suspended in water. The UBM/laser fiber head was placed 1.5 mm above the samples, so that the entire head of the photoacoustic transducer was submerged in the water. The transducer raster scanned above the samples.

The photoacoustic imaging set up was powered by an Nd:Yag laser (1.56 V), pulsed through an OPO to tune the laser to 800 nm. The laser was triggered by a function generator powered by the computer. The laser was focused into a NA 0.22 fiber that was threaded through a donut-shaped ultrasound transducer so that 3 mm of the fiber was protruding from the face of the transducer. The output power of the laser was 300-600 μJ, for a fluence of 100 mJ/cm^2, as measured by a Thor power meter. The ultrasound waves generated by the pulse laser light were amplified and digitized by a GaGe card. In the second iteration of the photoacoustic setup, a polarizer was integrated into the light path and a beam splitter was used to divert ~30% of the energy directly to a power meter so the stability of the input laser light could be monitored in conjunction with the output sample intensity. Photoacoustic images were reconstructed using MatLab.

Figures and Tables

Figure A.1

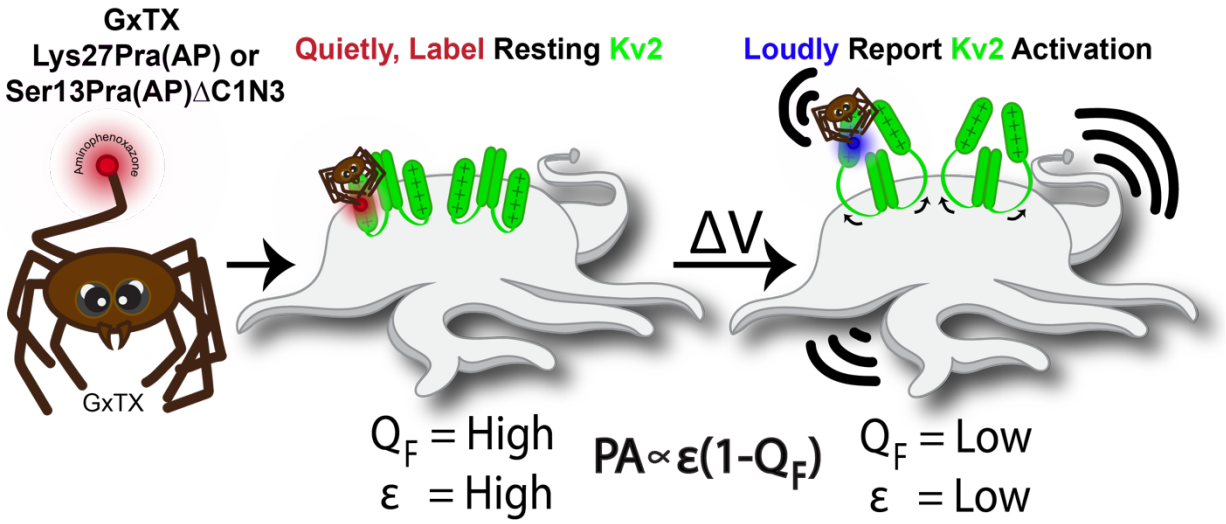

Figure A.1

A schematic detailing the relationship between absorbance and fluorescence properties with predicted photoacoustic signal generation. We hypothesize that when AP fluorescence is dim, such as when bound to activated Kv2.1 voltage sensors, that the corresponding photoacoustic signal will be loud.

Figure A.2

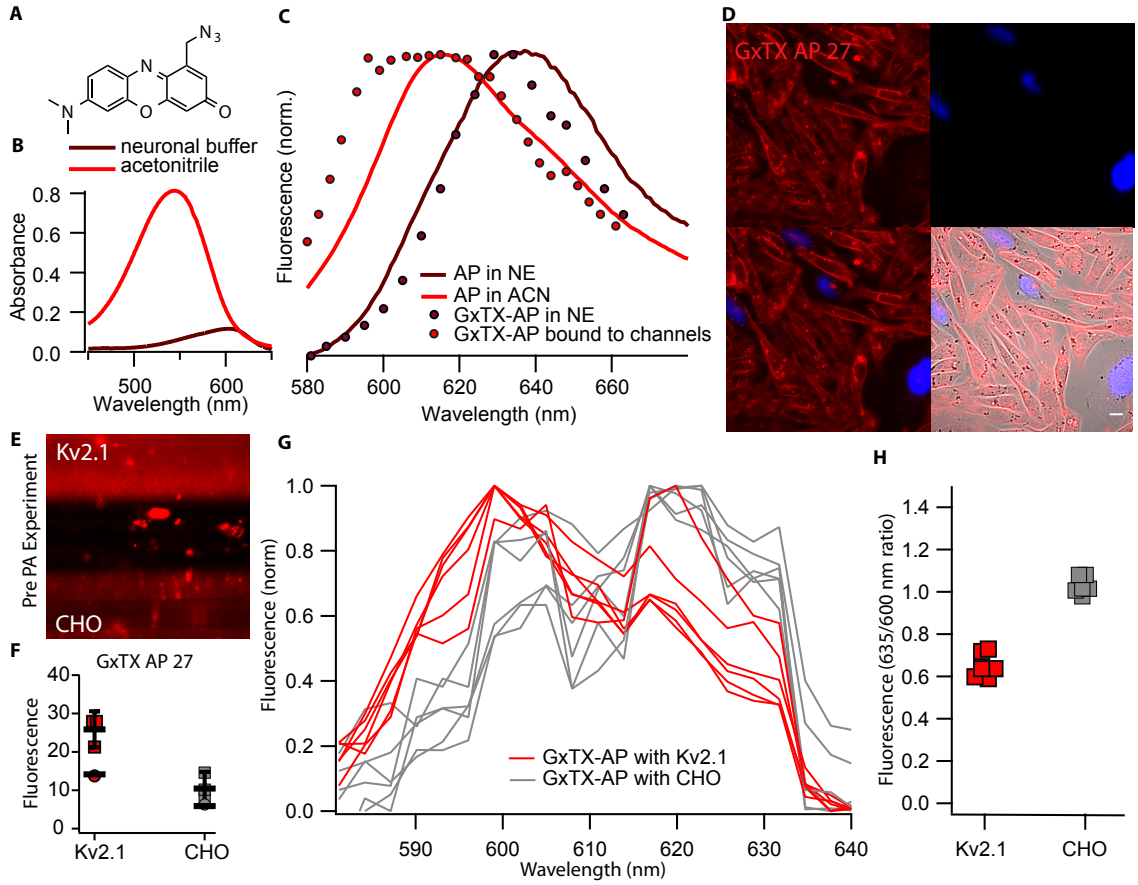

Figure A.2

(**A**) Structure of aminophenoxazone (AP). (**B**) The absorption maxima of AP shifts in neuronal external (burgundy) and acetonitrile (red). (**C**) Fluorescence emission spectra of AP dye in solution (solid lines) and of GxTX K27Pra(AP) bound to cells (dots). (**D**) Fluorescence image of a co-culture of CHO-K1 cell lines stably expressing either Kv2.1 or nuclear BFP (blue) labeled with 100 nM of GxTX K27Pra(AP). (**E**) Representative fluorescence image at 10x magnification of two quartz capillaries each loaded with 10^7 CHO cells that had been treated with 100 nM GxTX K27Pra(AP). Cells in the top capillary were induced to express Kv2.1 channels while cells in the bottom capillary were not. (**F**) Quantification of the fluorescence intensity for capillaries in (E).

Figure A.3

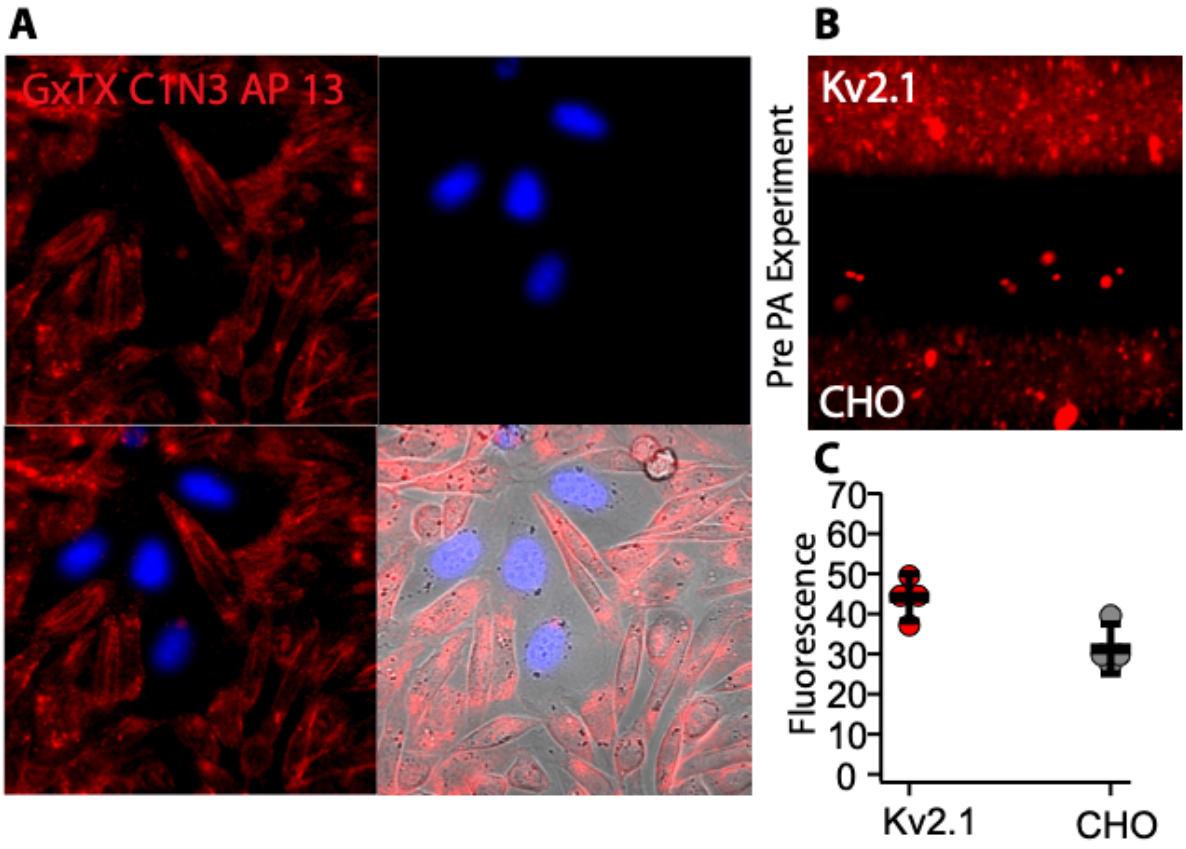

Figure A.3

(**A**) In a co-culture of CHO-K1 stable cell lines expressing either Kv2.1 or nuclear BFP, 1 μM GxTX ΔC1N3 Ser13Pra(AP) (red) selectively labels cells expressing Kv2.1 channels. (**B**) 10x image of two quartz capillaries (ID: 0.5 mm, OD: 1.0 mm) each loaded with $10*10^6$ CHO cells either induced to express Kv2.1 channels (top) or not (bottom). Before capillaries were loaded, cells were treated with 1 μM GxTX ΔC1N3 Ser13Pra(AP) for 5 min and spun at 500 rcf. The supernatant was aspirated. Cells were washed and spin 3 times more and then loaded for imaging. (**C**) Quantitation of fluorescence intensity for the two capillaries. Values were measured from images of 4 different regions of the same capillary preparation (biological rep = 1).

Figure A.4

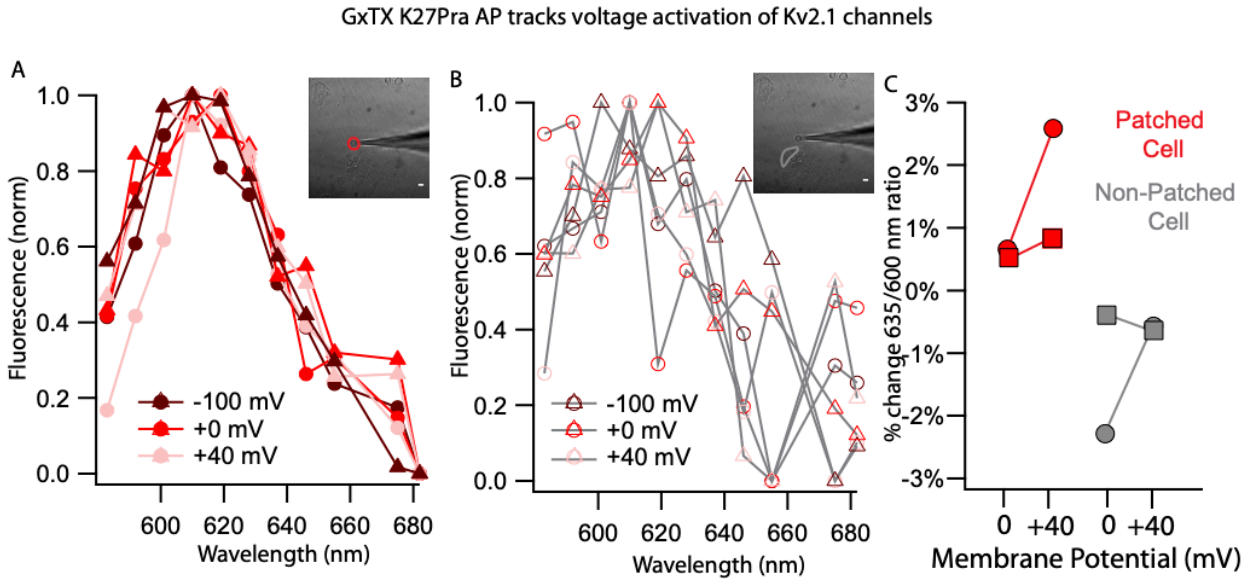

Figure A.4

(**A**) Normalized fluorescence emission spectra of a voltage-clamped CHO-K1 cell overexpressing Kv2.1 channels. The cell was treated with 100 nM GxTX K27Pra(AP) for 5 minutes and then stepped from a membrane potential of -100 mV to +0 mV and +40 mV while simultaneous lambda scan images were taken. (**B**) Normalized fluorescence emission spectra of a non-voltage clamped cell from the same field of view as (A). (**C**) Ratio of the background subtracted and normalized fluorescence intensity from spectral imaging with scan bins between 590-611 nm and 623-644 nm. The patched cell (red) sees a positive change with voltage steps to either 0 mV (circles) or +40 mV (squares) while the non-patched cell (grey) sees a negative percent change in this ratio.

Figure A.5

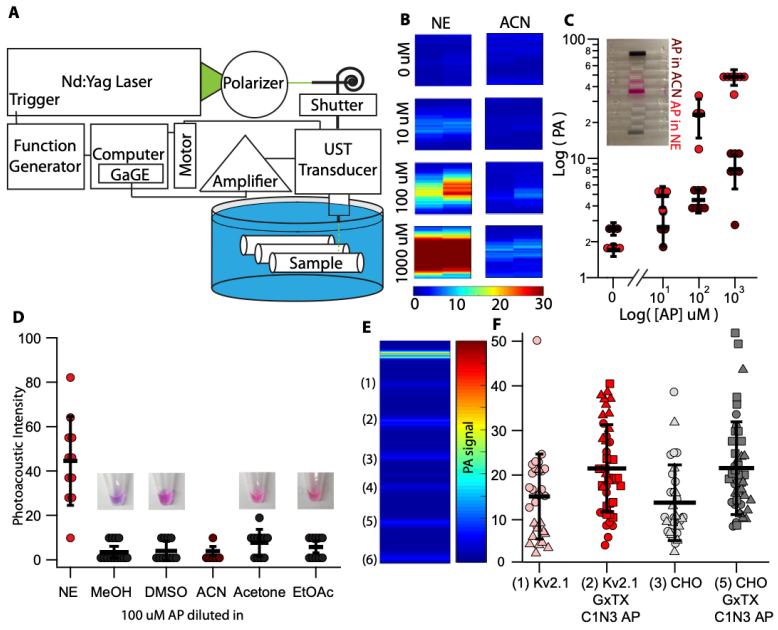

Figure A.5

(**A**) Scheme describing the photoacoustic setup. (**B**) Photoacoustic images of glass capillaries containing AP-azide dye dissolved to different concentrations in either neuronal buffer (left column) or acetonitrile (right column). (**C**) Quantitation of the average photoacoustic intensity from the images in (B). Four technical replicates were acquired from one preparation were acquired by taking imagines while translating down the length of the capillaries. (**D**) AP-azide dye was dissolved in solvents with varying dielectric constants (polarities) to a concentration of 100 μM. Multiple technical replicates were acquired from one preparation. (**E**) Photoacoustic image of quartz capillaries loaded with (1) CHO-K1 cells overexpressing Kv2.1 channels (2) CHO-K1 cells overexpressing Kv2.1 channels treated with 3 μM GxTX K27Pra(AP), (3) the saved supernatant from the first was of these cells, (4) CHO-K1 cells not expressing Kv2.1 channels, (5) CHO-K1 cells lacking channels by treated with GxTX K27Pra(AP), (6) the saved supernatant from the first wash. (**F**) Quantification of PA image intensities. Multiple technical replicates were taken from 2-3 biological replicates (triangles, circles, or squares).

Table A.1

GxTX intensity at 1.5 hrs	1 (Fig. 3.2)
GxTX intensity at 48 hrs	28 (Fig. 3.2)
Scale factor to determine channel # at 48 hrs	28
$I_{Kv2.1}$ at 1.5 hrs	1 nA (Supplemental Fig. 3.2)
Calculated $I_{Kv2.1}$ at 48 hrs	28 nA
$i_{Kv2.1}$	500 fA (Fig. 3.4)
Open Probability	0.5 (approximated)
Channels/cell at 48 hours of induction (I=iPN)	112000 channels
GxTX molecules/cell (4 molecules/channel)	448000 GxTX molecules
Cell size: 10D x 0.5H μm	5 μm^2
Voxel size: 50 axial x 70 lateral μm (442)	2500 μm^2 or $2.5x10^{-5}$ cm^2 (lateral dimension is resolved by time)
Cells/Voxel	500
Obtained GxTX molecules/Voxel	**$2.24x10^8$ GxTX molecules**
AP detection limit (10 μM in NE, 100 μM in ACN) (1 mol/L = $6.02*10^{20}$ molecules/ cm^3)	$6.02x10^{15}$ molecules/cm^3 in NE $6.02x10^{16}$ molecules/cm^3 in ACN
Approximate AP requirement for a 2D volume	$1.82x10^5$ molecules/cm^2 in NE $3.92x10^5$ molecules/cm^2 in ACN
Approximate AP requirement/voxel	**$5.2x10^9$ molecules/cm^2 in NE** **$1.12x10^{10}$ molecules/cm^2 in ACN**

Table A.1. Estimation of the concentration limit for AP detection by photoacoustic imaging

In order to achieve a SNR of 2-3:1 for AP detection over background noise with our current photoacoustic setup, an AP concentration of at least 10 μM (if in neuronal buffer) or 100 μM (if in acetonitrile) must be achieved within the imaging voxel.

APPENDIX B: The C-terminus influences Kv2.1 ion channel conformational change.

Preface

This appendix details preliminary experiments testing the role of the Kv2.1 C-terminus in Kv2 conformational change and AMIGO1 association. I conceived of, conducted, and analyzed the experiments presented in this chapter. Jon Sack provided editorial feedback.

Abstract

In Chapter 3 I identified that AMIGO1 modulates Kv2.1 voltage sensor movement. In this Appendix, I report that a truncation of Kv2.1's intracellular C-terminal domain prevents AMIGO1 from modulating voltage sensor movement. Based on gating current recordings from Kv2.1 channels with two different C-terminal truncations, I suggest that the AMIGO1-effect requires a portion of the Kv2.1 intracellular C-terminal domain. The voltage-dependence of OFF gating current movement measured from Kv2.1 channels lacking the 376 amino acids distal from the C-terminus showed no sign of AMIGO1-dependent modulation. Preliminary data suggest that AMIGO1 is still trafficked to the cell surface by this Kv2.1 truncation mutant, consistent with a preserved molecular association. If confirmed, this result would suggest that channel association and gating modification are separable properties of the AMIGO1 protein.

Introduction

As described in the Chapter 3 of this thesis, the single transmembrane pass auxiliary subunit, AMIGO1, readily associates with and modifies voltage activation of Kv2 channel conductance (121). Behavioral and developmental studies have characterized the physiological impacts associated with aberrant AMIGO1 expression (124, 375) and electrophysiological reports have characterized the biophysical mechanisms underlying AMIGO1-inducted gating modulation (33, 177), however the full spectrum of physiological ramifications of the AMIGO1-Kv2.1 association is unknown.

AMIGO1 is both a Kv2 auxiliary subunit and an adhesion protein (Chapter 1). Untangling the physiological roles and pathophysiological complications associated with these two disparate functionalities is difficult due to their linked nature. Immunoblots of membrane protein samples from brains of AMIGO1 knockout mice and western blots of extracts from AMIGO1-knockdown zebrafish larvae exhibit reduced Kv2.1 protein content (124, 375), suggesting that AMIGO1 might increase the stability of Kv2 protein expression. Are the pathophysiological phenotypes seen in the AMIGO1 knockout mouse and knockdown zebrafish a result of the decreased Kv2 expression? Similarly, electrophysiological recordings from heterologous and native samples demonstrate that AMIGO1 coexpression alters the voltage dependence of Kv2 channel activation (32, 33, 177, 375). Since the voltage dependence of channel conduction determines the extent to which that conductance can impact electrical signaling events, we theorized in Chapter 3 that even a small shift in the voltage-dependence of activation, as seen with AMIGO1, could significantly skew Kv2.1 participation in a signaling event. Are the pathophysiological phenotypes seen in the AMIGO1 knockout mouse and knockdown zebrafish a result of the abrogated Kv2 voltage sensing? Conversely, AMIGO1 has the capacity to participate in cell-to-cell adhesions (69, 201). Are the pathophysiological phenotypes in the AMIGO1 knockout mouse and knockdown zebrafish solely related to the roles of AMIGO1 as an adhesion protein? One method to interrogate such questions, would be to decouple the adhesive and auxiliary properties of AMIGO1 and

interrogate the resulting physiological consequences of abrogated adhesion or abrogated Kv2 conductance. In order to carry out such experiments, it is first necessary to understand the molecular regions that define the AMIGO1-Kv2.1 interaction.

The Kv2.1 C-terminus is known to be involved in protein-protein interactions (Fig. B.4), undergoes voltage-dependent molecular rearrangements (425), and the phosphorylation status of the C-terminus influences the voltage-dependence of channel conduction (354). In this Appendix, I test the hypothesis that the Kv2.1 C-terminus is similarly important in conferring AMIGO1-dependent shifts in the voltage-dependence of gating charge movement. Here, I assess the necessity of the Kv2.1 C-terminus for AMIGO1-dependent gating modulation by assessing if two different Kv2.1 C-terminal truncation mutants are receptive to AMIGO1 gating modulation. The preliminary results presented here suggest that a portion of the Kv2.1 C-terminus is necessary for AMIGO1-induced gating modulation but is not crucial for AMIGO1 association. If validated further, this result would be consistent with voltage sensor modulation as a non-obligatory yet conserved function of AMIGO proteins.

Results

AMIGO1 modulation of Kv2.1 gating charge movement is abolished by truncation of the distal 376 amino acids of the Kv2.1 C-terminus

To determine if AMIGO1 affects voltage sensor movement, I measured gating currents (I_g), which correspond to movement of Kv2.1 voltage sensors across the transmembrane electric field. Kv2.1–CHO cells were patch clamped in whole–cell mode in the absence of K^+ (Fig. B.1A) and given voltage steps to elicit gating currents. Cells were cotransfected with different Kv2.1 channel mutants possessing progressively shorter intracellular C-termini and either peGFP or AMIGO1–YFP. We chose to compare the effect of AMIGO1 on wild-type (WT) Kv2.1, Kv2.1 Δ376C, and Kv2.1 Δ333C. Of a list of characterized Kv2.1 channel constructs, Kv2.1 Δ376C is the most aggressive truncation mutation that still exhibits cell-surface expression (451) and the slightly less aggressive Kv2.1 Δ333C truncation includes a region known to be important for facilitating protein-protein interactions (Fig. B.4)(21, 248).

To measure if AMIGO1 alters gating charge movement, I integrated OFF gating currents ($I_{g,OFF}$) at -140 mV after 100 ms voltage steps. Between -25 mV and -10 mV, WT Kv2.1–control cells did not move as much gating charge as WT Kv2.1 + AMIGO1 cells (Fig. B.1B,C), a result similar to previous OFF gating currents measured with a cell line with inducible Kv2.1 expression (177). Boltzmann fits yielded $\Delta V_{g,Mid,OFF}$ of -11.9 ± 3.5 mV (SEM) and a $\Delta z_{g,OFF}$ of 0.36 ± 0.27 e_0 (Table B.1), which was similar to a previously reported $\Delta V_{g,Mid,OFF}$ -10.8 ± 2.4 mV (SEM)(Fig. 3.6V) and a $\Delta z_{g,OFF}$ of 0.43 ± 0.20 e_0 (SEM) (Fig. 3.6U)(Table 3.2), indicating that AMIGO1 shifts total gating charge movement to more negative voltages. Control and AMIGO1 OFF gating currents measured from cells expressing Kv2.1 Δ333C produced *Q–V* relationships similar to those recorded from WT Kv2.1 cells and WT Kv2.1+AMIGO1 cells respectively (Fig. B.1D,E,H); $\Delta V_{g,Mid,OFF}$ and $\Delta z_{g,OFF}$ were not statistically distinct from corresponding measures made

from WT Kv2.1 currents as assessed by an Ordinary 2-way ANOVA (Table B.1). *Q–V* relationship for control and AMIGO1 OFF gating currents measured from cells expressing Kv2.1 Δ376C were distinct from all previous measures. Kv2.1 Δ376C *Q–V* relationships exhibited a pronounced left-shift in the threshold for activation compared to all other OFF gating currents (Fig. B.1F,H). Additionally, the left-shift of AMIGO1 was completely absent (Fig. B.1 G,H). Boltzmann fits yielded $\Delta V_{g,Mid,OFF}$ of 1.9 ± 3.6 mV (SEM) and a $\Delta z_{g,OFF}$ of 0.01 ± 0.27 e_0 (Table B.1). Both $\Delta V_{g,Mid,OFF}$ and $\Delta z_{g,OFF}$ from Kv2.1 Δ376C currents were distinct from corresponding measures from Δ333C and WT Kv2.1 OFF currents as assessed by Ordinary two-way ANOVA. This result suggests that most distal 376 amino acids of the Kv2.1 C-terminus, but not the most distal 333, are necessary for AMIGO1 to confer an effect on Kv2.1 voltage sensor movement.

AMIGO1–YFP colocalizes with GxTX–594 labeled Kv2.1 Δ376C

If the Kv2.1 Δ376C truncation abolished AMIGO1 association, then I would expect a lack of an AMIGO1 dependent effect on OFF gating current measurements. To test if AMIGO1 associates with Kv2.1 Δ376C, I assessed AMIGO1–YFP and Kv2.1 Δ376C colocalization using the Pearson's correlation coefficient (PCC) (385). Surface-expressing Kv2.1 on live cells was labeled with GxTX Ser13Cys(Alexa594), a conjugate of a voltage sensor toxin guangxitoxin-1E derivative with a fluorophore, abbreviated as GxTX–594 (321). Notably, the Δ376C truncation removes the proximal clustering domain from the Kv2.1 C-terminus and though this does not negatively impact cell-surface trafficking, this modification abolishes the stereotypic punctate expression patterns seen with WT Kv2.1 (451). Colocalization between AMIGO1–YFP and GxTX–594 was apparent as the PCC, measured from the glass-adhered, basal membrane was greater than the staining control (Fig. B.2A). The PCC value was also

similar to PCC measurements made from AMIGO1–YFP and GxTX–594 labeling of WT Kv2.1 channels (Fig. 3.2B). Even though the PCC for AMIGO1–YFP and GxTX–594 was near 1, a standard for perfect signal colocalization, I did not conduct negative controls to assess whether this apparent colocalization was merely the product of two diffuse signals overlapping. Further experiments comparing colocalization between unrelated, single-transmembrane pass, surface expressing proteins are needed to fully interpret this result.

AMIGO1–YFP is trafficked to the cell periphery when coexpressed with Kv2.1 Δ376C

To supplement the previous experiment, I also assessed AMIGO1–YFP localization following Kv2.1 coexpression. In HEK293 and CHO cells, the localization of heterologously expressed AMIGO1 is intracellular and diffuse (33, 121, 177). However, when co-expressed with Kv2.1, AMIGO1 reorganizes into puncta with Kv2.1, similar to the expression patterns in central neurons (33, 121, 177). To determine whether Kv2.1 Δ376C is sufficient to reorganize AMIGO1 in CHO cells, a hallmark of an interaction, I imaged AMIGO1–YFP signal at a transverse plane that was apical to the basal membrane. In cells transfected with AMIGO1–YFP alone, optically sectioned images revealed that AMIGO1–YFP signal was diffuse throughout the cytosolic region of the cell. (Fig. B.3A). However, when AMIGO1–YFP was cotransfected with either Kv2.1 Δ376C (Fig. B.3B) or WT Kv2.1 (Fig. B.3C), AMIGO1–YFP trafficked to the cell periphery and formed distinctive rings at the cell surface devoid of intracellular signal. Further confirmatory experiments to substantiate observations are needed. When combined with the colocalization analysis, these preliminary data provide evidence that Kv2.1 Δ376C can facilitate a molecular interaction with AMIGO1, despite being unable to support AMIGO1 gating modification.

Discussion

In Chapter 3, I discussed AMIGO1 and the mechanism through which it alters Kv2.1 conformational change. However, Kv2.1 is receptive to many other modulators of conformational change including biochemical modifications that occur on the C-terminal domain, such as phosphorylation (354) and SUMOylation (306). The C-terminal domain is also known to interact with the N-terminal domains and undergo voltage-dependent changes in conformation (424). Further, the C-terminal domain is also a hotspot for protein-protein interactions (Fig. B.4). With these experiments I found that the C-terminal domain of Kv2.1 was similarly important for AMIGO1 modulation of Kv2.1 conformational change. Independent of AMIGO1, these experiments also revealed that the C-terminal domain was important for conferring a depolarizing shift in the threshold for voltage sensor activation, suggesting that the residues retained in the C-terminus of Δ333C, but not Δ376C, detain Kv2.1 voltage sensors in their earliest resting conformation.

Why does the C-terminus matter for modulation of voltage sensor movement?

To date, there are no atomistic structures of the intracellular domains of Kv2 channels. Because of this void, we turn to atomistic structures of other ion channels to understand available mechanisms for allosteric coupling that could similarly modulate to Kv2 voltage sensor movement. One of these comparators is the TRP channel family; nearly 50 cryo-EM structures have revealed that transient receptor potential channels (TRPs) have an architecture similar to Kv channels (452). These channels contain extended cytoplasmic N- and C-termini that are involved in the regulation of function and trafficking. While most TRP channels are not clearly voltage-dependent, nearly all TRPs have two shared features that are relevant to gating: a long S4-S5 linker connecting the VSD-like domain and the S5-pore-S6 segment, and then a TRP domain that forms extensive interactions with the S4-S5 linker and the pre-S1

region (453). This structural arrangement suggests that different cytoplasmic regions, including the N- and C-terminus contribute to a TRP channel coupling mechanism that communicates between the pore gate and voltage sensors (453)[55]. A different coupling mechanism has been described for Kv7.1 channels. Here it is thought that the S4-S5 linker binds to the base of the S6 helix, locking channels in a closed conformation that is distinct from the canonical electromechanical, S4 locking mechanism employed by other Kv channels (454, 455). In this coupling interaction, membrane depolarization drags the S4-S5 linker away from its S6 binding site, permitting the dilatation of the S6 helices bundle that constitutes the cytoplasmic gate (455)[56][57]. Additionally, in Kv1.1 and Kv1.2 channels, the N-terminal cytoplasmic T1 domain is thought to similarly play an allosteric role in defining channel gating (453). This example is relevant to Kv2.1 gating since Kv2.1 N- and C-terminal are suspected to interact with each other (456). Based on these examples, my favored hypothesis for why the Kv2.1 C-terminal domain influences gating is that intracellular interactions detain Kv2.1 voltage sensors in their resting conformation. Any attractive

[55] The atomistic structure of the NavPaS channel, resolved at 3.8 A (185), similarly reveals structural mechanisms through which the channel C-terminal domain could influence gating charge movement. The NavPaS channel is the putative Nav channel from the American cockroach. While it exhibits most of the same structural hallmarks as a voltage-gated sodium channel it is distinct from Kv channels in that it is composed of single polypeptide chain that folds to four homologous repeats (domains I to IV). Each domain of the channel contains six transmembrane segments, S1-S6, where S1-S4 comprise a voltage-sensing domain and S5-S6 comprise the central pore. Similar to Kv channels, the S4 of Nav channels carries the positively charged residues that are essential for voltage-sensing and underly gating charge movement (185). In the closed structure of NavPaS, the C-terminal domain interacts with the 4th domain voltage sensor, the 4th domain S4-S5 linker, 4th domain S6 helix, and the 3rd domain S6 helix. The cytoplasmic interactions captured in NavPaS are predicted to provide a molecular foundation for the involvement of the 4th domain voltage sensor and the C-terminal domain in inactivation (185), and could similarly influence voltage sensor activation. The structure of the NavPaS C-terminal domain is nearly identical to the resolved Nav1.5 C-terminal domain (426), suggestive that the cytoplasmic interfaces are preserved in human Nav channels.

[56] This allosteric coupling mechanism has also been proposed for Kv7.2 and Kv7.3 channels (497)

[57] Another example of channels with an allosteric gating mechanism are Kv1.1 and Kv1.2 channels; the N-terminal cytoplasmic T1 domain is thought to allosterically define channel gating (453). This example is relevant to Kv2.1 gating since Kv2.1 N- and C-terminal are suspected to interact with each other (456). While I have chosen to focus on C-terminal interactions in this Appendix due to the experimental setup, in practice abrogation of C- and N-terminal interactions could similarly facilitate modified voltage sensor movement.

interactions with the C-terminal domain must be energetically overcome before the gating charges can translocate in response to changes in membrane potential. Paired electrophysiological studies and an atomistic structure[58] detailing the faces for Kv2.1 cytoplasmic interactions could help test this hypothesis.

Through what structural regions does AMIGO1 interact with Kv2.1?

While more research is needed to characterize the full suite of conformational change that VGICs undergo in response to changes in membrane potential, using atomistic structures, we can similarly formulate hypotheses surrounding the structural determinants of the Kv2.1 and AMIGO1 interaction. The recent atomistic structure of Kv4.2 was captured in the presence of DPP6 (160). While DPP6 lacks sequence and structural homology with AMIGO1, it is similarly a single-pass transmembrane auxiliary subunit that possesses an adhesion-like extracellular domain and alters the rate and voltage dependence of Kv4.2 voltage sensor movement. The structure of DPP6 and Kv4.2 revealed that DPP6 binds to Kv4.2 and interacts with the voltage sensing domain through its transmembrane domain, hydrophobically interacting with the lower half of S1 and the upper half of S2 (160). This structure is consistent with experimental results that suggest that DPP6 confers its effects on Kv4.2 gating through the transmembrane helices and short intracellular segments (152, 176). Notably, this structural arrangement was distinct from previous structures of with other Kv channels in complex with their auxiliary subunits including Kv7.1 with KCNE (343), which is a single-pass transmembrane auxiliary subunit, and Slo1 with β1 (164), which is a two-pass transmembrane auxiliary subunit. However. the DPP6-Kv4.2 structure, in some respects resembles that of Nav1.4 and β1 (183) and Nav1.7 and β1/β2 (184); both Nav auxiliary subunits are single-pass transmembrane auxiliary subunits that possess an adhesion-like extracellular

[58] Notably, the large intracellular C-terminal domain of Kv2.1 could be difficult to resolve in a structure; a recent structure of Kv4.2, a close Kv2 homolog (498), was unable to resolve most of the C-terminal domain due to the lack of secondary structure (160).

domain, similar to DPP6 and AMIGO1. The Nav1.4, Nav1.7, and Kv4.2 structures all indicated that the transmembrane region of the single-pass auxiliary subunit localized closely to the voltage sensing domain of the channel. Based on these structures, I hypothesize that AMIGO1 would similarly localize near the voltage-sensing domain. To conclude this discussion, I will raise some mechanistic hypotheses that could be tested to further investigate how AMIGO1 modulates Kv2.1 gating.

Possible interaction of intracellular domains?

Based on this hypothesized localization of AMIGO1, where the AMIGO1 transmembrane localizes near the Kv2 voltage sensing domain, my favored mechanistic hypothesis is that the ~99 amino acid long, intracellular domain of hAMIGO1 disrupts C-terminal interactions that detain Kv2.1 voltage sensors in their earliest resting conformation. Previous electrophysiology studies attempted to identify the structural regions of AMIGO1 important for conferring an effect on the voltage-dependence of Kv2.1 conductance (32). Using whole cell recordings, the *G–V* relation for Kv2.1 conductance was measured from cells coexpressing different AMIGO1-chimera constructs. Chimeras were made by systematically substituting one or two regions of the AMIGO1 protein with the unrelated NCAM (neural cell adhesion molecule) protein. From these experiments, it was clear that the AMIGO1 transmembrane domain was necessary for conferring any *G–V* shift, while both the extracellular domain and the intracellular domains were needed to confer the full effect as seen with full-length AMIGO1. While this experiment highlights the importance of AMIGO1's transmembrane region, the results do not distinguish if the transmembrane region is responsible for associating with the channel or if it is also responsible for conferring a biophysical effect unto Kv2.1 activation. Interestingly, a chimera that only possessed the AMIGO1 transmembrane domain (along with the NCAM intracellular domain) had a small effect on the Kv2.1 *G–V* (32). This result would be expected if (1) the AMIGO1 transmembrane itself mediates the gating shift or (2) the AMIGO1 transmembrane segment localizes the single transmembrane chimera in a region where

even nonspecific intracellular interactions could facilitate a gating shift. While I speculate that the AMIGO1 transmembrane domain is responsible for colocalization with Kv2 and intracellular interactions are responsible for the AMIGO1-dependent gating shift, this model fails to address the necessity of the extracellular domain for conferring the entirety of the voltage-dependent shift in activation. I suspect that the actual nature of these interactions might not be quite as domain-separable as postulated here.

Could AMIGO1 influence Kv2.1 phosphorylation?

Alternatively, AMIGO1 localization with Kv2.1 channels could alter Kv2.1 gating through an indirect mechanism. Auxiliary subunit coexpression can alter the post-translational modification status of the ion channel partner (259). The hyperpolarizing gating shifts we see from AMIGO1 and the truncated Kv2.1 constructs could similarly be explained if AMIGO1's presence was correlated with dephosphorylation of some of the Kv2.1 C-terminal residues responsible for determining the voltage-dependence of channel activation (354). Kv2.1 Δ333C has at least five more sites for phosphorylation than Kv2.1 Δ376C (Fig. B.4) and also contains S563, a site implicated in graded regulation of the voltage-dependence of Kv2.1 conductance (354). If AMIGO1 coexpression influenced any of these residues, removal of the distal 376 amino acids would eliminate the region AMIGO1 acts upon, resulting in the lack of an AMIGO1 dependent effect on Kv2.1 gating. This hypothesis could be tested through immunohistochemical approaches that take advantage of phosphospecific antibodies, such as fractionating cell lysates with SDS-PAGE and then characterizing the presence of phosphorylation at specific Kv2.1 residues by bands that demonstrate immunoreactivity to the phospho-specific antibody as visualized by an immunoblot (355). Notably, if AMIGO1 were to influence Kv2.1 phosphorylation, abrogation of this phosphorylation event could further test if AMIGO1 acts solely through a phosphorylation-dependent mechanism to modulate the voltage-dependence of Kv2.1 activation. If this

were the case, these results would highlight an additional motivation for investigating the biophysical mechanism through which Kv2.1 C-terminal phosphorylation allosterically influences gating, a long-standing question in the Kv2.1 field (17, 23, 27, 354, 374, 421, 457, 458) .

Acknowledgements

I would like to thank Dr. Nick Vierra for outstanding intellectual discussions and feedback. Key research materials were kindly provided by Dr. James Trimmer. I would also like to thank Dr. Jon Sack, Dr. Karen Zito, and Dr. James Trimmer for their great feedback on the controls needed for these experiments. Dr. Parashar Thapa, Dr. Nick Vierra, Robert Stewart, and Matt Marquis helped discuss methods for image analysis and I am similarly thankful for these conversations.

Materials and Methods

GxTX peptides

A conjugate of a cysteine–modified guangxitoxin–1E and the maleimide of fluorophore Alexa594 (GxTX Ser13Cys(Alexa594)) was used to fluorescently identify surface-expressing Kv2.1 channels (321), as in Chapter 3.

Cell culture and transfection

Chinese Hamster Ovary (CHO) cells were cultured as described in Chapter 3. 48 hours prior to experiments cells were transfected as described in Chapter 3. Kv2.1 plasmids including rKv2.1 rgb4, rKv2.1ΔC333-HA, and rKv2.1ΔC376-HA were gifts from James Trimmer (451).

Whole–cell gating current measurements

Gating current measurement methods and OFF gating current analyses are listed in Chapter 3.

Fluorescence imaging

Images were acquired using the same instruments and settings described in Chapter 3. For PCC analysis, cells were transfected and/or induced and plated as described in the "*Transfection*" methods section and washed as described in the "*GxTX–594 dose response time–lapse imaging*" section in Chapter 3. ~5 min prior to imaging, cell culture media was exchanged with an "imaging solution". In instances where Kv2.1 was labeled with GxTX–594, cells were then incubated in 100 μL of 100 nM GxTX–594 as described in "*Environment–sensitive fluorescence and imaging".* Cells were incubated in the labeling solutions for 5-10 minutes before 1 mL of the imaging solution was used to wash out fluorescent dyes. All cells were imaged in 1 mL of fresh imaging solution. Temperature inside the microscope housing was 24-28 °C. For analysis, ROIs were drawn around the inner perimeter of each individual cell. Prior to Pearson's colocalization coefficient (PCC) analysis, images were Gaussian filtered with a σ=1. After

automatic Costes thresholding, PCC values were calculated using the colocalization function in Zen Blue software. Costes thresholding uses an algorithm to distinguish labeled structures from background and then removes low-intensity values from analysis (386, 459). Although Costes thresholding decreases the empirical value of a PCC measurement, it is an unbiased form of thresholding designed to account for nonuniformities in background fluorescence both within a singular image and between images (386). High PCC values are only obtained when two fluorescent signals overlap spatially and have linked fluorescent intensities (bright with bright and dim with dim). Perfect colocalization is represented by a value of +1, while a value of -1 represents fluorophores with mutually exclusive compartmentalization. A value of 0 indicates no colocalization, and intermediate positive values indicate some extent of colocalization (460).

Figures and Tables

Figure B.1

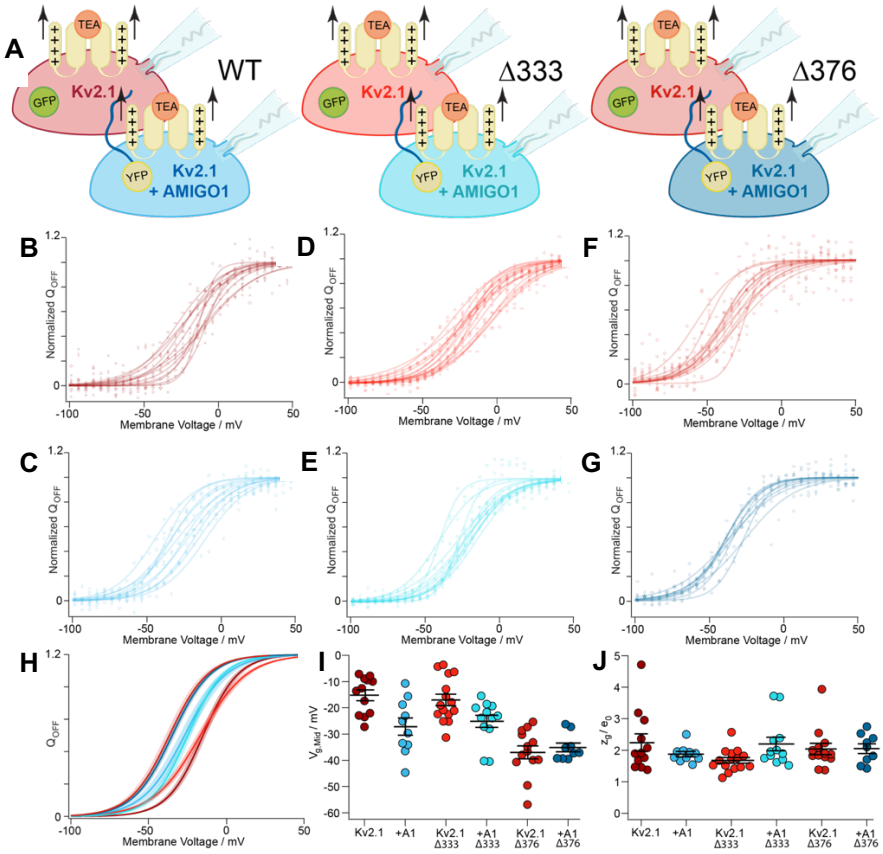

Figure B.1. AMIGO1 modulation of Kv2.1 gating charge movement requires distal 376 amino acids of the C-terminus

(**A**) Experimental set up: Gating currents (arrows) from Kv2.1–CHO transfected with GFP (red) or AMIGO1–YFP (blue). K^+ currents were eliminated removal of K^+ ions and the external tetraethylammonium, a Kv2 pore-blocker (orange). (**B-G**) Q_{OFF}–V relations normalized to average Q_{OFF} from +50 to +100 mV voltage steps. Solid lines are Boltzmann fits (Chpt. 3, Eqn. C). (**H**) Reconstructed Boltzmann fits using the average $V_{g,Mid,OFF}$ and $z_{g,OFF}$ (Table B.1). Shading $V_{g,Mid,OFF}$ ± SEM. (**I**) Steepness and (**J**) midpoint of Boltzmann fits. Mean ± SEM. Statistics in Table B.1.

Figure B.2

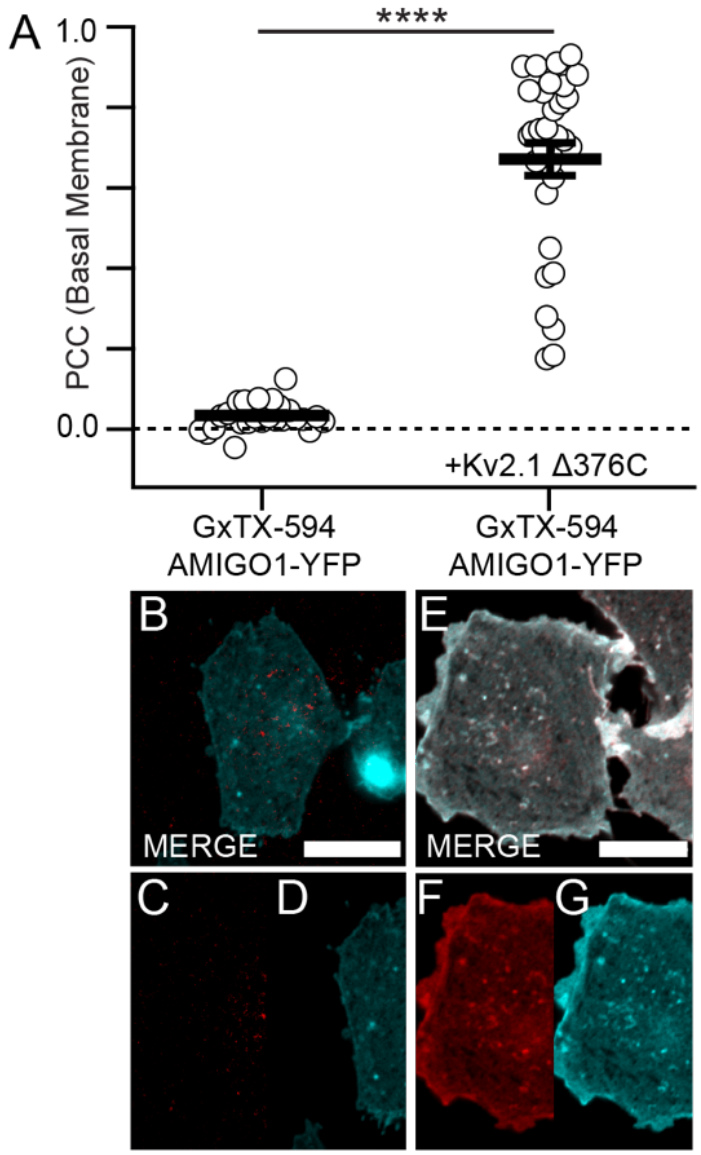

Figure B.2. AMIGO1–YFP colocalizes with GxTX–594 labeled Kv2.1 Δ376C

(**A**) Costes thresholded, Pearson's colocalization between AMIGO1–YFP and GxTX–594 at the cell membrane following transfection with AMIGO1–YFP only (**B, C, D**) or AMIGO1–YFP with Kv2.1 Δ376C (**E, F, G**).

Figure B.3

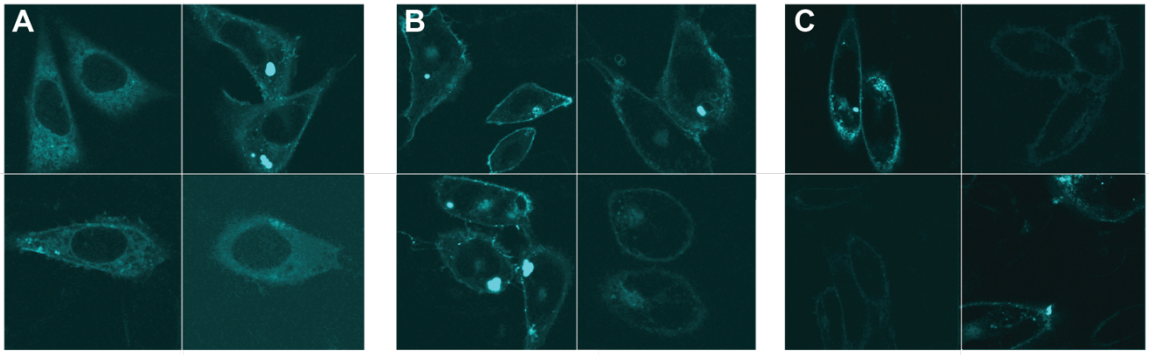

Figure B.3. AMIGO1YFP is trafficked to the cell periphery when coexpressed with Kv2.1 Δ376C

Exemplar images of CHO cells transfected with AMIGO1–YFP only (**A**), AMIGO1–YFP + Kv2.1 Δ376C (**B**), or AMIGO1–YFP + Kv2.1 (**C**). Images were acquired 20 nm above the basal membrane of the cell.

Figure B.4

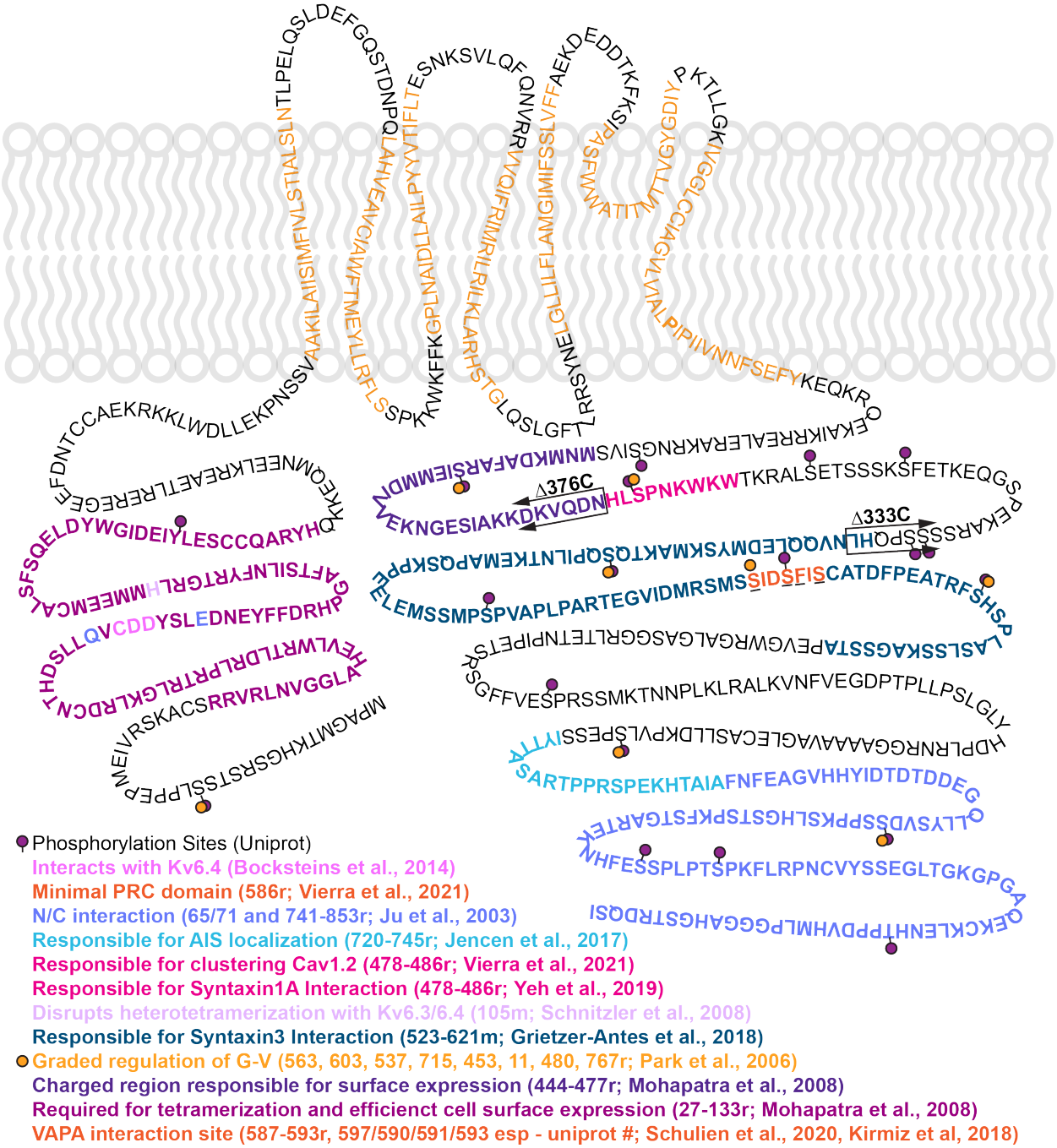

Figure B.4. The Kv2.1 C-terminal is a hot-spot for protein interactions and channel modulation

Table B.1

Kv2.1–CHO cells	Q–V fit parameters			
Q_{OFF}	$V_{g,Mid}$ (mV)	$\Delta V_{g,Mid}$	z_g (e_0)	n
rKv2.1 + GFP	-15.2 ± 2.1	-11.9 ± 3.5 [A]	2.24 ± 0.28 [Y]	12
rKv2.1+ AMIGO1–YFP	-27.1 ± 3.3		1.879 ± 0.083 [Z]	10
rKv2.1Δ333 + GFP	-17.0 ± 2.2	-8.1 ± 3.1 [B]	1.683 ± 0.090 [Y]	15
rKv2.1Δ333 + AMIGO1–YFP	-25.1 ± 2.3		2.20 ± 0.22 [Y]	12
rKv2.1Δ376 + GFP	-36.9 ± 2.5	1.9 ± 3.6[C]	2.04 ± 0.18 [Y]	13
rKv2.1Δ376 + AMIGO1–YFP	-35.1 ± 1.7		2.05 ± 0.16 [Y]	9

Table B.1. Boltzmann parameters for gating charge movement.

Average $V_{g,Mid}$ and z_g values were derived from 1st order Boltzmann fits of n individual cells. Means ± SEM. $V_{g,Mid} = V_{g,1/2}$. 2-way ANOVA test with multiple comparisons p-values: AB: >0.999. AC: <0.0001. BC: <0.0001.

References

1. Benjamin, E.J., M.J. Blaha, S.E. Chiuve, M. Cushman, S.R. Das, R. Deo, S.D. De Ferranti, J. Floyd, M. Fornage, C. Gillespie, C.R. Isasi, M.C. Jim'nez, L.C. Jordan, S.E. Judd, D. Lackland, J.H. Lichtman, L. Lisabeth, S. Liu, C.T. Longenecker, R.H. MacKey, K. Matsushita, D. Mozaffarian, M.E. Mussolino, K. Nasir, R.W. Neumar, L. Palaniappan, D.K. Pandey, R.R. Thiagarajan, M.J. Reeves, M. Ritchey, C.J. Rodriguez, G.A. Roth, W.D. Rosamond, C. Sasson, A. Towfghi, C.W. Tsao, M.B. Turner, S.S. Virani, J.H. Voeks, J.Z. Willey, J.T. Wilkins, J.H.Y. Wu, H.M. Alger, S.S. Wong, and P. Muntner. 2017. Heart Disease and Stroke Statistics'2017 Update: A Report from the American Heart Association. .
2. Frech, G.C., A.M. VanDongen, A.M. Brown, and R.H. Joho. 1989. A novel potassium channel with delayed rectifier properties isolated from rat brain by expression cloning. *Nature*. 340:642–645.
3. Murakoshi, H., and J.S. Trimmer. 1999. Identification of the Kv2.1 K+ channel as a major component of the delayed rectifier K+ current in rat hippocampal neurons. *J. Neurosci.* 19:1728–1735.
4. MacKinnon, R. 2003. Potassium channels. *FEBS Lett.* 555:62–65.
5. Bekkers, J.M. 2000. Distribution and activation of voltage-gated potassium channels in cell-attached and outside-out patches from large layer 5 cortical pyramidal neurons of the rat. *J. Physiol.* 525 Pt 3:611–20.
6. Du, J., L.L. Haak, E. Phillips-Tansey, J.T. Russell, and C.J. McBain. 2000. Frequency-dependent regulation of rat hippocampal somato-dendritic excitability by the K+ channel subunit Kv2.1. *J. Physiol.* 522 Pt 1:19–31.
7. Korngreen, A., and B. Sakmann. 2000. Voltage-gated K+ channels in layer 5 neocortical pyramidal neurones from young rats: subtypes and gradients. *J. Physiol.* 525 Pt 3:621–639.
8. Hille, B. 2001. Ion Channel Excitable Membranes. *Sunderl. Massachusetts USA*. 646–659.
9. Redman, P.T., K. He, K.A. Hartnett, B.S. Jefferson, L. Hu, P.A. Rosenberg, E.S. Levitan, and E. Aizenman. 2007. Apoptotic surge of potassium currents is mediated by p38 phosphorylation of Kv2.1. *Proc. Natl. Acad. Sci. U. S. A.* 104:3568–73.
10. Mohapatra, D.P., K.-S. Park, and J.S. Trimmer. 2007. Dynamic regulation of the voltage-gated Kv2.1 potassium channel by multisite phosphorylation. *Biochem. Soc. Trans.* 35:1064–1068.
11. Hwang, P.M., D.S. Bredt, A.M. Cunningham, and H. Snyder. 1993. Contrasting immunohistochemical localizations novel K+ channels of the shah subfamily. *J. Neurosci.* 13:0–7.
12. Lim, S.T., D.E. Antonucci, R.H. Scannevin, and J.S. Trimmer. 2000. A novel targeting signal for proximal clustering of the Kv2.1 K+ channel in hippocampal neurons. *Neuron*. 25:385–397.
13. Maletic-Savatic, M., N.J. Lenn, and J.S. Trimmer. 1995. Differential spatiotemporal expression of K+ channel polypeptides in rat hippocampal neurons developing in situ and in vitro. *J. Neurosci.* 15:3840–3851.
14. Scannevin, R.H., H. Murakoshi, K.J. Rhodes, and J.S. Trimmer. 1996. Identification of a Cytoplasmic Domain Important in the Polarized Expression and Clustering of the Kv2.1 K + Channel. *J. Cell Biol.* 135:1619–1632.
15. Trimmer, J.S. 1991. Immunological identification and characterization of a delayed rectifier K+ channel polypeptide in rat brain. *Proc. Natl. Acad. Sci. U. S. A.* 88:10764–8.
16. Du, J., J.H. Tao-Cheng, P. Zerfas, and C.J. McBain. 1998. The K+ channel, Kv2.1, is apposed to astrocytic processes and is associated with inhibitory postsynaptic membranes in hippocampal and cortical principal neurons and inhibitory interneurons. *Neuroscience*. 84:37–48.

17. Misonou, H., D.P. Mohapatra, M. Menegola, and J.S. Trimmer. 2005. Calcium- and metabolic state-dependent modulation of the voltage-dependent Kv2.1 channel regulates neuronal excitability in response to ischemia. *J. Neurosci.* 25:11184–11193.
18. Hansen, A.J., and M. Nedergaard. 1988. Brain ion homeostasis in cerebral ischemia. *Neurochem. Pathol.* 9:195–209.
19. Lee, J.M., G.J. Zipfel, and D.W. Choi. 1999. The changing landscape of ischaemic brain injury mechanisms. *Nature*. 399:A7–A14.
20. Pal, S.K., K. Takimoto, E. Aizenman, and E.S. Levitan. 2006. Apoptotic surface delivery of K+ channels. *Cell Death Differ.* 13:661–7.
21. Yeh, C.-Y., A.M. Bulas, A. Moutal, J.L. Saloman, K.A. Hartnett, C.T. Anderson, T. Tzounopoulos, D. Sun, R. Khanna, and E. Aizenman. 2017. Targeting a Potassium Channel/Syntaxin Interaction Ameliorates Cell Death in Ischemic Stroke. *J. Neurosci.* 37:5648–5658.
22. Pal, S., K.A. Hartnett, J.M. Nerbonne, E.S. Levitan, and E. Aizenman. 2003. Mediation of neuronal apoptosis by Kv2.1-encoded potassium channels. *J. Neurosci.* 23:4798–802.
23. Misonou, H., D.P. Mohapatra, E.W. Park, V. Leung, D. Zhen, K. Misonou, A.E. Anderson, and J.S. Trimmer. 2004. Regulation of ion channel localization and phosphorylation by neuronal activity. *Nat. Neurosci.* 7:711–718.
24. Bean, B.P. 2007. The action potential in mammalian central neurons. *Nat. Rev. Neurosci.* 8:451–465.
25. Speca, D.J., G. Ogata, D. Mandikian, H.I. Bishop, S.W. Wiler, K. Eum, H.J. Wenzel, E.T. Doisy, L. Matt, K.L. Campi, M.S. Golub, J.M. Nerbonne, J.W. Hell, B.C. Trainor, J.T. Sack, P.A. Schwartzkroin, and J.S. Trimmer. 2014. Deletion of the Kv2.1 delayed rectifier potassium channel leads to neuronal and behavioral hyperexcitability. *Genes, Brain Behav.* 13:394–408.
26. Misonou, H., D.P. Mohapatra, and J.S. Trimmer. 2005. Kv2.1: A voltage-gated K+ channel critical to dynamic control of neuronal excitability. *Neurotoxicology*. 26:743–752.
27. Misonou, H., M. Menegola, D.P. Mohapatra, L.K. Guy, K.-S. Park, and J.S. Trimmer. 2006. Bidirectional activity-dependent regulation of neuronal ion channel phosphorylation. *J. Neurosci.* 26:13505–13514.
28. Mulholland, P.J., E.P. Carpenter-Hyland, M.C. Hearing, H.C. Becker, J.J. Woodward, and L.J. Chandler. 2008. Glutamate transporters regulate extrasynaptic NMDA receptor modulation of Kv2.1 potassium channels. *J. Neurosci.* 28:8801–8809.
29. Liu, P.W., and B.P. Bean. 2014. Kv2 channel regulation of action potential repolarization and firing patterns in superior cervical ganglion neurons and hippocampal CA1 pyramidal neurons. *J. Neurosci.* 34:4991–5002.
30. Khoo, K.K., I. Galleano, F. Gasparri, R. Wieneke, H. Harms, M.H. Poulsen, H.C. Chua, M. Wulf, R. Tampé, and S.A. Pless. 2020. Chemical modification of proteins by insertion of synthetic peptides using tandem protein trans-splicing. *Nat. Commun.* 11:2284.
31. Galleano, I., H. Harms, K. Choudhury, K. Khoo, L. Delemotte, and S.A. Pless. 2021. Functional cross-talk between phosphorylation and disease-causing mutations in the cardiac sodium channel Na_v1.5. *Proc. Natl. Acad. Sci.* 118:e2025320118.
32. Peltola, M.A., J. Kuja-Panula, S.E. Lauri, T. Taira, and H. Rauvala. 2011. AMIGO is an auxiliary subunit of the Kv2.1 potassium channel. *EMBO Rep.* 12:1293–1299.
33. Maverick, E.E., A.N. Leek, and M.M. Tamkun. 2021. Kv2 channel/AMIGO β-subunit assembly modulates both channel function and cell adhesion molecule surface trafficking. *J. Cell Sci.*
34. González, C., D. Baez-Nieto, I. Valencia, I. Oyarzún, P. Rojas, D. Naranjo, and R. Latorre. 2012. K+ channels: function-structural overview. *Compr. Physiol.* 2087–2149.

35. Catterall, W.A. 2011. Voltage-gated calcium channels. *Cold Spring Harb Perspect Biol*. 3:1–23.
36. Wang, J., S. Ou, and Y. Wang. 2017. Distribution and function of voltage-gated sodium channels in the nervous system. *Channels*. 11:534–554.
37. Jentsch, T.J.J., V. Stein, F. Weinreich, and A.A. Zdebik. 2002. Molecular structure and physiological function of chloride channels. *Physiol. Rev.* 82:503.
38. Kim, D.M., and C.M. Nimigean. 2016. Voltage-gated potassium channels: A structural examination of selectivity and gating. *cold spring harb perspect biol*. 8:1–19.
39. Swartz, K.J. 2004. Towards a structural view of gating in potassium channels. *Nat. Neurosci.* 5:905–916.
40. Catterall, W.A. 2012. Voltage-gated sodium channels at 60: structure, function and pathophysiology. *J Physiol*. 590:2577–2589.
41. Yang, H., G. Zhang, and J. Cui. 2015. BK channels: multiple sensors, one activation gate. *Front. Physiol.* 6:1–16.
42. Cui, J., H. Yang, and U. Lee. 2009. Molecular mechanisms of BK channel activation. *Cell Mol Life Sci*. 66:852–875.
43. Hering, S., S. Beyl, A. Hohaus, S. Andranovits, and E.N. Timin. 2018. Calcium channel gating. *Eur. J. Physiol.* 470:1291–1309.
44. Lee, A., B. Fakler, L.K. Kaczmarek, and L.L. Isom. 2014. More than a pore: Ion channel signaling complexes. *J. Neurosci.* 34:15159–15169.
45. Bett, G.C.L., and R.L. Rasmusson. 2008. Modification of K+ channel-drug interactions by ancillary subunits. *J. Physiol.* 586:929–950.
46. Jerng, H.H., and P.J. Pfaffinger. 2014. Modulatory mechanisms and multiple functions of somatodendritic A-type K+ channel auxiliary subunits. *Front. Cell. Neurosci.* 8:1–20.
47. Malhotra, J.D., C. Chen, I. Rivolta, H. Abriel, R. Malhotra, L.N. Mattei, F.C. Brosius, R.S. Kass, and L.L. Isom. 2001. Characterization of sodium channel a- and B-subunits in rat and mouse cardiac myocytes. *Circulation*. 1303–1310.
48. Isom, L.L., T. Scheuer, A.B. Brownstein, D.S. Ragsdale, B.J. Murphy, and W.A. Catterall. 1995. Functional co-expression of the beta 1 and type IIA alpha subunits of sodium channels in a mammalian cell line. *J. Biol. Chem.* 270:3306–3312.
49. Capera, J., C. Serrano-novillo, S. Cassinelli, and A. Felipe. 2019. The potassium channel odyssey: mechanisms of traffic and membrane arrangement. *Int. J. Mol. Sci.* 20:1–20.
50. Gurnett, C.A., and K.P. Campbell. 1996. Transmembrane subunits of voltage-dependent ion channels. *J. Biol. Chem.* 271:27975–27978.
51. Cavallaro, U., and E. Dejana. 2011. Adhesion molecule signalling: not always a sticky business. *Nature*. 12:189–197.
52. Torres, Y.P., F.J. Morera, I. Carvacho, and R. Latorre. 2007. A marriage of convenience: β-subunits and voltage-dependent K + channels. *J. Biol. Chem.* 282:24485–24489.
53. Bouza, A.A., and L.L. Isom. 2018. Voltage-gated sodium channel β subunits and their related diseases. *Handb. Exp. Pharmacol.* 246:423–450.
54. Dolphin, A.C. 2016. Voltage-gated calcium channels and their auxiliary subunits: physiology and pathophysiology and pharmacology. *J. Physiol.* 594:5369–5390.
55. Black, J.L. 3rd. 2003. The voltage-gated calcium channel gamma subunits: a review of the literature. *J. Bioenerg. Biomembr.* 35:649–660.
56. Barrallo-Gimeno, A., A. Gradogna, I. Zanardi, M. Pusch, and R. Estévez. 2015. Regulatory-

auxiliary subunits of CLC chloride channel-transport proteins. *J. Physiol.* 593:4111–4127.

57. Campiglio, M., and B.E. Flucher. 2015. The role of auxiliary subunits for the functional diversity of voltage-gated calcium channels. *J. Cell. Physiol.* 230:2019–2031.
58. Patel, R., and A.H. Dickenson. 2016. Mechanisms of the gabapentinoids and α 2 δ-1 calcium channel subunit in neuropathic pain. *Pharmacol. Res. Perspect.* 4:e00205–e00205.
59. Isom, L.L., K.S. De Jongh, and W.A. Catterall. 1994. Auxiliary subunits of voltage-gated ion channels. *Neuron*. 12:1183–94.
60. Jepps, T.A. 2017. Unravelling the complexities of vascular smooth muscle ion channels: Fine tuning of activity by ancillary subunits. *Pharmacol. Ther.* 178:57–66.
61. Xu, J., and M. Li. 1998. Auxiliary subunits of shaker-type potassium channels. *Trends Cardiovasc. Med.* 8:229–234.
62. Martens, J.R., Y.G. Kwak, and M.M. Tamkun. 1999. Modulation of Kv channel alpha/beta subunit interactions. *Trends Cardiovasc. Med.* 9:253–8.
63. Pongs, O., and J.R. Schwarz. 2010. Ancillary subunits associated with voltage-dependent K+ channels. *Physiol. Rev.* 90:755–796.
64. Vacher, H., and J.S. Trimmer. 2011. Diverse roles for auxiliary subunits in phosphorylation-dependent regulation of mammalian brain voltage-gated potassium channels. *Pflugers Arch. Eur. J. Physiol.* 462:631–643.
65. Sun, X., M.A. Zaydman, and J. Cui. 2012. Regulation of voltage-activated K+ channel gating by transmembrane β subunits. *Front. Pharmacol.* 3:1–10.
66. O'Malley, H.A., and L.L. Isom. 2016. Sodium channel B subunits: emerging targets in channelopathies. *Annu. Rev. Physiol.* 77:481–504.
67. Hull, J.M., and L.L. Isom. 2018. Voltage-gated sodium channel B subunits: the power outside of the pore in brain development and disease. *Neuropharmacology*. 132:43–57.
68. Li, Q., and J. Yan. 2016. Chapter two - modulation of BK channel function by auxiliary beta and gamma subunits. In: Contet CBT-IR of N, editor. Big on Bk. Academic Press. pp. 51–90.
69. Kuja-Panula, J., M. Kiiltomäki, T. Yamashiro, A. Rouhiainen, and H. Rauvala. 2003. AMIGO, a transmembrane protein implicated in axon tract development, defines a novel protein family with leucine-rich repeats. *J. Cell Biol.* 160:963–973.
70. Favre-kontula, L., A. Rolland, L. Bernasconi, M. Karmirantzou, C. Power, B. Antonsson, and U. Boschert. 2008. GlialCAM , an immunoglobulin-like cell adhesion molecule is expressed in glial cells of the central nervous system. *Glia*. 645:633–645.
71. Chioni, A., W.J. Brackenbury, J.D. Calhoun, L.L. Isom, and M.B.A. Djamgoz. 2009. A novel adhesion molecule in human breast cancer cells: Voltage-gated Na+ channel B1 subunit. *Int. J. Biochem. Cell Biol.* 41:1216–1227.
72. Patino, G.A., W.J. Brackenbury, Y. Bao, L.F. Lopez-santiago, H.A.O. Malley, C. Chen, J.D. Calhoun, R.G. Lafrenie, P. Cossette, G.A. Rouleau, and L.L. Isom. 2011. Voltage-gated Na+ channel B1B: a secreted cell adhesion molecule involved in human epilepsy. *J. Neurosci.* 31:14577–14591.
73. Haworth, A.S., and W.J. Brackenbury. 2019. Emerging roles for multifunctional ion channel auxiliary subunits in cancer. *Cell Calcium*. 80:125–140.
74. Zhang, Y., T. Poobalasingam, L.L. Yates, S.A. Walker, M.S. Taylor, L. Chessum, J. Harrison, L. Tsaprouni, I.M. Adcock, C.M. Lloyd, W.O. Cookson, M.F. Moffatt, and C.H. Dean. 2018. Manipulation of dipeptidylpeptidase 10 in mouse and human in vivo and in vitro models indicates a protective role in asthma. *Dis. Model. Mech.* 11:dmm031369.
75. Wycisk, K.A., C. Zeitz, S. Feil, M. Wittmer, U. Forster, J. Neidhardt, B. Wissinger, E. Zrenner, R.

Wilke, S. Kohl, and W. Berger. 2006. Mutation in the auxiliary calcium-channel subunit CACNA2D4 causes autosomal recessive cone dystrophy. *Am. J. Hum. Genet.* 79:973–977.

76. Edokobi, N., and L.L. Isom. 2018. Voltage-gated sodium channel β1/β1B subunits regulate cardiac physiology and pathophysiology. *Front. Physiol.* 9:1–11.
77. Baroni, D., C. Picco, and O. Moran. 2017. Mutation E87Q of the β1-subunit impairs the maturation of the cardiac voltage-dependent sodium channel. *Sci. Rep.* 7:10683.
78. Alsaloum, M., M. Estacion, R. Almomani, M.M. Gerrits, G.J. Bönhof, D. Ziegler, R. Malik, M. Ferdousi, G. Lauria, I.S.J. Merkies, C.G. Faber, S. Dib-Hajj, and S.G. Waxman. 2019. A gain-of-function sodium channel β2-subunit mutation in painful diabetic neuropathy. *Mol. Pain*. 15:1744806919849802.
79. Fontanals-Cirera, B., D. Hasson, C. Vardabasso, R. Di Micco, P. Agrawal, A. Chowdhury, M. Gantz, A. de Pablos-Aragoneses, A. Morgenstern, P. Wu, D. Filipescu, D. Valle-Garcia, F. Darvishian, J.-S. Roe, M.A. Davies, C.R. Vakoc, E. Hernando, and E. Bernstein. 2017. Harnessing BET Inhibitor Sensitivity Reveals AMIGO2 as a Melanoma Survival Gene. *Mol. Cell*. 68:731-744.e9.
80. Ansar, M., S. Riazuddin, M.T. Sarwar, P. Makrythanasis, S.A. Paracha, Z. Iqbal, J. Khan, M.Z. Assir, M. Hussain, A. Razzaq, D.L. Polla, A.S. Taj, A. Holmgren, N. Batool, D. Misceo, J. Iwaszkiewicz, A.P.M. De Brouwer, M. Guipponi, S. Hanquinet, V. Zoete, F.A. Santoni, E. Frengen, J. Ahmed, S. Riazuddin, H. Van Bokhoven, and S.E. Antonarakis. 2018. Biallelic variants in LINGO1 are associated with autosomal recessive intellectual disability, microcephaly, speech and motor delay. *Genet. Med.* 20:778–784.
81. Miyagawa, Y., Y. Matsushita, H. Suzuki, M. Komatsu, T. Yoshimaru, R. Kimura, A. Yanai, J. Honda, A. Tangoku, M. Sasa, Y. Miyoshi, and T. Katagiri. 2018. Frequent downregulation of LRRC26 by epigenetic alterations is involved in the malignant progression of triple-negative breast cancer. *Int J Oncol*. 52:1539–1558.
82. Postema, P.G., I. Christiaans, N. Hofman, M. Alders, T.T. Koopmann, C.R. Bezzina, P. Loh, K. Zeppenfeld, P.G.A. Volders, and A.A.M. Wilde. 2011. Founder mutations in the Netherlands: familial idiopathic ventricular fibrillation and DPP6. *Neth. Heart J.* 19:290–296.
83. Ding, D.-B., L.-L. Fan, Z. Xiao, H. Huang, Y.-Q. Chen, S. Guo, Z.-H. Liu, and R. Xiang. 2018. A novel mutation of dipeptidyl aminopeptidase-like protein-6 in a family with suspicious idiopathic ventricular fibrillation. *QJM An Int. J. Med.* 111:373–377.
84. Adelman, J.P. 1995. Proteins that interact with the pore-forming subunits of voltage-gated ion channels. *Curr. Opin. Neurobiol.* 5:286–295.
85. Trimmer, J.S. 1998. Regulation of ion channel expression by cytoplasmic subunits. *Curr. Opin. Neurobiol.* 8:370–374.
86. Arikkath, J., and K.P. Campbell. 2003. Auxiliary subunits: essential components of the voltage-gated calcium channel complex. *Curr. Opin. Neurobiol.* 13:298–307.
87. Cannon, S.C. 2007. Physiologic principles underlying ion channelopathies. *Neurotherapeutics*. 4:174–183.
88. Yan, D., and S. Tomita. 2012. Defined criteria for auxiliary subunits of glutamate receptors. *J. Physiol.* 590:21–31.
89. Prado, P.A., S. Hafner, Y. Comoglio, B. Wdziekonski, C. Duranton, B. Attali, J. Barhanin, and G. Sandoz. 2021. KCNE1 is an auxiliary subunit of two distinct ion channel superfamilies. *Cell*. 184:534–544.
90. Jeworutzki, E., T. Lopez-Hernandez, X. Capdevila-Nortes, S. Sirisi, L. Bengtsson, M. Montolio, G. Zifarelli, T. Arnedo, C.S. Muller, U. Schulte, V. Nunes, A. Martinez, T.J. Jentsch, X. Gasull, M.

Pusch, and R. Estevez. 2012. GlialCAM, a protein defective in a Leukodystrophy, serves as a ClC-2 Cl– channel auxiliary subunit. *Neuron*. 73:951–961.

91. Taussig, M.J., C. Fonseca, J.S. Trimmer, and M. Biology. 2018. Antibody validation: a view from the mountains. *N Biotechnol*. 25:1–8.
92. Isom, L., K. De Jongh, D. Patton, B. Reber, J. Offord, H. Charbonneau, K. Walsh, A. Goldin, and W. Catterall. 1992. Primary structure and functional expression of the beta 1 subunit of the rat brain sodium channel. *Science (80-.).* 256:839–842.
93. Das, S., J. Gilchrist, F. Bosmans, and F. Van Petegem. 2016. Binary architecture of the Nav1.2-β2 signaling complex. *Elife*. 5.
94. Gilchrist, J., S. Das, F. Van Petegem, and F. Bosmans. 2013. Crystallographic insights into sodium-channel modulation by the β4 subunit. *Proc. Natl. Acad. Sci. U. S. A.* 110.
95. Namadurai, S., D. Balasuriya, R. Rajappa, M. Wiemhöfer, K. Stott, J. Klingauf, J.M. Edwardson, D.Y. Chirgadze, and A.P. Jackson. 2014. Crystal structure and molecular imaging of the Nav channel β3 subunit indicates a trimeric assembly. *J. Biol. Chem.* 289:10797–10811.
96. Marionneau, C., Y. Carrasquillo, A.J. Norris, R.R. Townsend, L.L. Isom, A.J. Link, and J.M. Nerbonne. 2012. The sodium channel accessory subunit Nav 1 regulates neuronal excitability through modulation of repolarizing voltage-gated K+ channels. *J. Neurosci.* 32:5716–5727.
97. Deschênes, I., A.A. Armoundas, S.P. Jones, and G.F. Tomaselli. 2008. Post-transcriptional gene silencing of KChIP2 and Navβ1 in neonatal rat cardiac myocytes reveals a functional association between Na and Ito currents. *J. Mol. Cell. Cardiol.* 45:336–346.
98. Deschenes, I., and G.F. Tomaselli. 2002. Modulation of Kv4.3 current by accessory subunits. *FEBS Lett.* 528:183–188.
99. Isom, L.L., D.S. Ragsdale, K.S. De Jongh, R.E. Westenbroek, B.F.X. Reber, T. Scheuer, and W.A. Catterall. 1995. Structure and function of the β2 subunit of brain sodium channels, a transmembrane glycoprotein with a CAM motif. *Cell*. 83:433–442.
100. Morgan, K., E.B. Stevens, B. Shah, P.J. Cox, A.K. Dixon, K. Lee, R.D. Pinnock, J. Hughes, P.J. Richardson, K. Mizuguchi, and A.P. Jackson. 2000. Beta 3: An additional auxiliary subunit of the voltage-sensitive sodium channel that modulates channel gating with distinct kinetics. *Proc. Natl. Acad. Sci. U. S. A.* 97:2308–2313.
101. Yu, F.H., R.E. Westenbroek, I. Silos-Santiago, K.A. McCormick, D. Lawson, P. Ge, H. Ferriera, J. Lilly, P.S. DiStefano, W.A. Catterall, T. Scheuer, and R. Curtis. 2003. Sodium channel beta4, a new disulfide-linked auxiliary subunit with similarity to beta2. *J. Neurosci.* 23:7577–85.
102. Raasakka, A., S. Ruskamo, J. Kowal, H. Han, A. Baumann, M. Myllykoski, A. Fasano, R. Rossano, P. Riccio, J. Bürck, A.S. Ulrich, H. Stahlberg, and P. Kursula. 2019. Molecular structure and function of myelin protein P0 in membrane stacking. *Sci. Rep.* 9:642.
103. Kazen-Gillespie, K.A., D.S. Ragsdale, M.R. D'Andreall, L.N. Mattei, K.E. Rogers, and L.L. Isom. 2000. Cloning, localization, and functional expression of sodium channel β1A subunits. *J. Biol. Chem.* 275:1079–1088.
104. Patton, D.E., L.L. Isom, W.A. Catterall, and A.L. Goldin. 1994. The adult rat brain beta 1 subunit modifies activation and inactivation gating of multiple sodium channel alpha subunits. *J. Biol. Chem.* 269:17649–55.
105. Calhoun, J.D., and L.L. Isom. 2014. The role of non-pore-forming β subunits in physiology and pathophysiology of voltage-gated sodium channels. *Handb. Exp. Pharmacol.* 221:51–89.
106. Sutkowski, E.M., and W.A. Catterall. 1990. β1 Subunits of sodium channels. Studies with subunit-specific antibodies. *J. Biol. Chem.* 265:12393–12399.

107. Blackburn-Munro, G., and S.M. Fleetwood-Walker. 1999. The sodium channel auxiliary subunits beta1 and beta2 are differentially expressed in the spinal cord of neuropathic rats. *Neuroscience*. 90:153–164.

108. Shah, B.S., E.B. Stevens, M.I. Gonzalez, S. Bramwell, R.D. Pinnock, K. Lee, and A.K. Dixon. 2000. Beta3, a novel auxiliary subunit for the voltage-gated sodium channel, is expressed preferentially in sensory neurons and is upregulated in the chronic constriction injury model of neuropathic pain. *Eur. J. Neurosci.* 12:3985–3990.

109. Zur, K.B., Y. Oh, S.G. Waxman, and J.A. Black. 1995. Differential up-regulation of sodium channel alpha- and beta 1-subunit mRNAs in cultured embryonic DRG neurons following exposure to NGF. *Brain Res. Mol. Brain Res.* 30:97–105.

110. Oh, Y., S. Sashihara, J.A. Black, and S.G. Waxman. 1995. Na+ channel beta 1 subunit mRNA: differential expression in rat spinal sensory neurons. *Brain Res. Mol. Brain Res.* 30:357–361.

111. Miyazaki, H., F. Oyama, R. Inoue, T. Aosaki, T. Abe, H. Kiyonari, Y. Kino, M. Kurosawa, J. Shimizu, I. Ogiwara, K. Yamakawa, Y. Koshimizu, F. Fujiyama, T. Kaneko, H. Shimizu, K. Nagatomo, K. Yamada, T. Shimogori, N. Hattori, M. Miura, and N. Nukina. 2014. Singular localization of sodium channel β4 subunit in unmyelinated fibres and its role in the striatum. *Nat. Commun.* 5:5525.

112. Sashihara, S., Y. Oh, J.A. Black, and S.G. Waxman. 1995. Na+ channel beta 1 subunit mRNA expression in developing rat central nervous system. *Brain Res. Mol. Brain Res.* 34:239–250.

113. Yan, J., and R.W. Aldrich. 2012. BK potassium channel modulation by leucine-rich repeat-containing proteins. *Proc. Natl. Acad. Sci. U. S. A.* 109:7917–7922.

114. Yan, J., and R.W. Aldrich. 2010. LRRC26 auxiliary protein allows BK channel activation at resting voltage without calcium. *Nature*. 466:513–516.

115. Yang, C., X.H. Zeng, Y. Zhou, X.M. Xia, and C.J. Lingle. 2011. LRRC52 (leucine-rich-repeat-containing protein 52), a testis-specific auxiliary subunit of the alkalization-activated Slo3 channel. *Proc. Natl. Acad. Sci. U. S. A.* 108:19419–19424.

116. Yang, C., V. Gonzalez-Perez, T. Mukaibo, J.E. Melvin, X.M. Xia, and C.J. Lingle. 2017. Knockout of the LRRC26 subunit reveals a primary role of LRRC26-containing BK channels in secretory epithelial cells. *Proc. Natl. Acad. Sci. U. S. A.* 114:E3739–E3747.

117. Egland, K.A., X.F. Liu, S. Squires, S. Nagata, Y.-G. Man, T.K. Bera, M. Onda, J.J. Vincent, R.L. Strausberg, B. Lee, and I. Pastan. 2006. High expression of a cytokeratin-associated protein in many cancers. *Proc. Natl. Acad. Sci.* 103:5929 LP – 5934.

118. Dolan, J., K. Walshe, S. Alsbury, K. Hokamp, S.O. Keeffe, T. Okafuji, S.F.C. Miller, G. Tear, and K.J. Mitchell. 2007. The extracellular Leucine-Rich Repeat superfamily; a comparative survey and analysis of evolutionary relationships and expression patterns. *BMC Genomics*. 8:1–24.

119. Zhang, Y.-Y., X. Han, Y. Liu, J. Chen, L. Hua, Q. Ma, Y.-Y.-X. Huang, Q.-Y. Tang, and Z. Zhang. 2018. +mRNA expression of LRRC55 protein (leucine-rich repeat-containing protein 55) in the adult mouse brain. *PLoS One*. 13:e0191749.

120. Lang, I., M. Jung, B.A. Niemeyer, P. Ruth, and J. Engel. 2019. Expression of the LRRC52 γ subunit (γ2) may provide Ca(2+)-independent activation of BK currents in mouse inner hair cells. *FASEB J.* 33:11721–11734.

121. Bishop, H.I., M.M. Cobb, M. Kirmiz, L.K. Parajuli, D. Mandikian, A.M. Philp, M. Melnik, J. Kuja-Panula, H. Rauvala, R. Shigemoto, K.D. Murray, and J.S. Trimmer. 2018. Kv2 ion channels determine the expression and localization of the associated AMIGO-1 cell adhesion molecule in adult brain neurons. *Front. Mol. Neurosci.* 11.

122. Homma, S., T. Shimada, T. Hikake, and H. Yaginuma. 2009. Expression pattern of LRR and Ig domain-containing protein (LRRIG protein) in the early mouse embryo. *Gene Expr. Patterns*. 9:1–26.

123. Chen, Y., S. Aulia, L. Li, and B.L. Tang. 2006. AMIGO and friends: An emerging family of brain-enriched, neuronal growth modulating, type I transmembrane proteins with leucine-rich repeats (LRR) and cell adhesion molecule motifs. *Brain Res. Rev.* 51:265–274.

124. Zhao, X., J. Kuja-Panula, M. Sundvik, Y.-C. Chen, V. Aho, M.A. Peltola, T. Porkka-Heiskanen, P. Panula, and H. Rauvala. 2014. Amigo adhesion protein regulates development of neural circuits in zebrafish brain. *J. Biol. Chem.* 289:19958–19975.

125. Dudem, S., R.J. Large, S. Kulkarni, H. Mcclafferty, I.G. Tikhonova, G.P. Sergeant, K.D. Thornbury, M.J. Shipston, B.A. Perrino, and M.A. Hollywood. 2020. LINGO1 is a regulatory subunit of large conductance , Ca2+-activated potassium channels. *Proc. Natl. Acad. Sci. U. S. A.* 117:2194–2200.

126. Mosyak, L., A. Wood, B. Dwyer, M. Buddha, M. Johnson, A. Aulabaugh, X. Zhong, E. Presman, S. Benard, K. Kelleher, J. Wilhelm, M.L. Stahl, R. Kriz, Y. Gao, Z. Cao, H. Ling, M.N. Pangalos, F.S. Walsh, and W.S. Somers. 2006. The structure of the Lingo-1 ectodomain, a module implicated in central nervous system repair inhibition. *J. Biol. Chem.* 281:36378–36390.

127. Llorens, F., V. Gil, S. Iraola, L. Carim-Todd, E. Martí, X. Estivill, E. Soriano, J.A. del Rio, and L. Sumoy. 2008. Developmental analysis of Lingo-1/Lern1 protein expression in the mouse brain: interaction of its intracellular domain with Myt1l. *Dev. Neurobiol.* 68:521–541.

128. Ozaki, Y., H. Matsui, H. Asou, A. Nagamachi, D. Aki, H. Honda, S. Yasunaga, Y. Takihara, T. Yamamoto, S. Izumi, M. Ohsugi, and T. Inaba. 2012. Poly-ADP ribosylation of Miki by tankyrase-1 promotes centrosome maturation. *Mol. Cell*. 47:694–706.

129. Gaudry, J., C. Arod, C. Sauvage, S. Busso, P. Dupraz, R. Pankiewicz, and B. Antonsson. 2008. Purification of the extracellular domain of the membrane protein GlialCAM expressed in HEK and CHO cells and comparison of the glycosylation. *Protein Expr. Purif.* 58:94–102.

130. López-Hernández, T., S. Sirisi, X. Capdevila-nortes, M. Montolio, V. Fernández-Dueñas, G.C. Scheper, M.S. van der Knaap, P. Casquero, F. Ciruela, I. Ferrer, V. Nunes, R. Estévez, T. Lo, G.C. Scheper, M.S. Van Der Knaap, P. Casquero, and V. Ferna. 2011. Molecular mechanisms of MLC1 and GLIALCAM mutations in megalencephalic leukoencephalopathy with subcortical cysts. *Hum. Mol. Genet.* 20:3266–3277.

131. Baldwin, K.T., C.X. Tan, S.T. Strader, C. Jiang, J.T. Savage, X. Elorza-Vidal, X. Contreras, T. Rülicke, S. Hippenmeyer, R. Estévez, R.-R. Ji, and C. Eroglu. 2021. HepaCAM controls astrocyte self-organization and coupling. *Neuron*. 109:2427-2442.e10.

132. Dolphin, A.C. 2013. The $\alpha 2\delta$ subunits of voltage-gated calcium channels. *Biochim. Biophys. Acta - Biomembr.* 1828:1541–1549.

133. Ellis, S.B., M.E. Williams, N.R. Ways, R. Brenner, A.H. Sharp, A.T. Leung, K.P. Campbell, E. McKenna, W.J. Koch, A. Hui, A. Schwartz, and M.M. Harpold. 1988. Sequence and expression of mRNAs encoding the alpha 1 and alpha 2 subunits of a DHP-sensitive calcium channel. *Science*. 241:1661–1664.

134. Barclay, J., N. Balaguero, M. Mione, S.L. Ackerman, V.A. Letts, J. Brodbeck, C. Canti, A. Meir, K.M. Page, K. Kusumi, E. Perez-Reyes, E.S. Lander, W.N. Frankel, R.M. Gardiner, A.C. Dolphin, and M. Rees. 2001. Ducky mouse phenotype of epilepsy and ataxia is associated with mutations in the Cacna2d2 gene and decreased calcium channel current in cerebellar Purkinje cells. *J. Neurosci.* 21:6095–6104.

135. Klugbauer, N., L. Lacinová, E. Marais, M. Hobom, and F. Hofmann. 1999. Molecular diversity of the calcium channel alpha2delta subunit. *J. Neurosci.* 19:684–691.

136. Qin, N., S. Yagel, M.-L. Momplaisir, E.E. Codd, and M.R. D'Andrea. 2002. Molecular cloning and characterization of the human voltage-gated calcium channel α2δ-4 subunit. *Mol. Pharmacol.* 62:485 LP – 496.

137. Whittaker, C.A., and R.O. Hynes. 2002. Distribution and evolution of von Willebrand/Integrin A domains: widely dispersed domains with roles in cell adhesion and elsewhere. *Mol. Biol. Cell*. 13:3369–3387.

138. Calderón-Rivera, A., A. Andrade, O. Hernández-Hernández, R. González-Ramírez, A. Sandoval, M. Rivera, J.C. Gomora, and R. Felix. 2012. Identification of a disulfide bridge essential for structure and function of the voltage-gated Ca(2+) channel α(2)δ-1 auxiliary subunit. *Cell Calcium*. 51:22–30.

139. Jay, S.D., A.H. Sharp, S.D. Kahl, T.S. Vedvick, M.M. Harpold, and K.P. Campbell. 1991. Structural characterization of the dihydropyridine-sensitive calcium channel alpha 2-subunit and the associated delta peptides. *J. Biol. Chem.* 266:3287–3293.

140. Cantí, C., M. Nieto-Rostro, I. Foucault, F. Heblich, J. Wratten, M.W. Richards, J. Hendrich, L. Douglas, K.M. Page, A. Davies, and A.C. Dolphin. 2005. The metal-ion-dependent adhesion site in the Von Willebrand factor-A domain of α2δ subunits is key to trafficking voltage-gated Ca2+ channels. *Proc. Natl. Acad. Sci. U. S. A.* 102:11230 LP – 11235.

141. Hendrich, J., A.T. Van Minh, F. Heblich, M. Nieto-Rostro, K. Watschinger, J. Striessnig, J. Wratten, A. Davies, and A.C. Dolphin. 2008. Pharmacological disruption of calcium channel trafficking by the α2δ ligand gabapentin. *Proc. Natl. Acad. Sci.* 105:3628 LP – 3633.

142. Gong, H.C., J. Hang, W. Kohler, L. Li, and T.Z. Su. 2001. Tissue-specific expression and gabapentin-binding properties of calcium channel alpha2delta subunit subtypes. *J. Membr. Biol.* 184:35–43.

143. Cole, R.L., S.M. Lechner, M.E. Williams, P. Prodanovich, L. Bleicher, M.A. Varney, and G. Gu. 2005. Differential distribution of voltage-gated calcium channel alpha-2 delta (alpha2delta) subunit mRNA-containing cells in the rat central nervous system and the dorsal root ganglia. *J. Comp. Neurol.* 491:246–269.

144. Hobom, M., S. Dai, E. Marais, L. Lacinova, F. Hofmann, and N. Klugbauer. 2000. Neuronal distribution and functional characterization of the calcium channel α2δ-2 subunit. *Eur. J. Neurosci.* 12:1217–1226.

145. Jerng, H.H., Y. Qian, and P.J. Pfaffinger. 2004. Modulation of Kv4. 2 channel expression and gating by dipeptidyl peptidase 10 (DPP10). *Biophys. J.* 87:2380–2396.

146. Strop, P., A.J. Bankovich, K.C. Hansen, K.C. Garcia, A.T. Brunger, J.H. Clark, and C. Drive. 2004. Structure of a human A-type potassium channel interacting protein DPPX, a member of the dipeptidyl aminopeptidase family. *J Mol Bio*. 343:1055–1065.

147. Nadal, M.S., Y. Amarillo, E.V. De Miera, Y. Ma, W. Mo, E.M. Goldberg, Y. Misumi, Y. Ikehara, T.A. Neubert, and B. Rudy. 2003. The CD26-related dipeptidyl aminopeptidase-like protein DPPX is a critical component of neuronal A-type K+ channels. *Neuron*. 37:449–461.

148. Lin, L., W. Sun, B. Throesch, F. Kung, J.T. Decoster, C.J. Berner, R.E. Cheney, B. Rudy, and D.A. Hoffman. 2013. DPP6 regulation of dendritic morphogenesis impacts hippocampal synaptic development. *Nat. Commun.* 4:2270.

149. Jerng, H.H., A.D. Lauver, and P.J. Pfaffinger. 2007. DPP10 splice variants are localized in distinct neuronal populations and act to differentially regulate the inactivation properties of Kv4-based ion channels. *Mol. Cell. Neurosci.* 35:604–624.

150. Nadal, M.S., Y. Amarillo, E.V. De Miera, and B. Rudy. 2006. Differential characterization of three

alternative spliced isoforms of DPPX. *Brain Res.* 94:1–12.

151. Zagha, E., A. Ozaita, S.Y. Chang, M.S. Nadal, U. Lin, M.J. Saganich, T. Mccormack, K.O. Akinsanya, S.Y. Qi, B. Rudy, and V. De Miera. 2005. DPP10 modulates Kv4-mediated A-type potassium channels. *J. Biol. Chem.* 280:18853–18861.
152. Ren, X., Y. Hayashi, N. Yoshimura, and K. Takimoto. 2005. Transmembrane interaction mediates complex formation between peptidase homologues and Kv4 channels. *Mol. Cell. Neurosci.* 29:320–332.
153. Jerng, H.H., and P.J. Pfaffinger. 2012. Incorporation of DPP6a and DPP6K variants in ternary Kv4 channel complex reconstitutes properties of A-type K current in rat cerebellar granule cells. *PLoS One*. 7:e38205.
154. Maffie, J., T. Blenkinsop, and B. Rudy. 2009. A novel DPP6 isoform (DPP6-E) can account for differences between neuronal and reconstituted A-type K+ channels. *Neurosci. Lett.* 449:189–194.
155. Du, J., Z. Fan, X. Ma, Y. Gao, Y. Wu, S. Liu, Y. Shen, M. Fan, and S. Wang. 2011. Expression of Dpp6 in mouse embryonic craniofacial development. *Acta Histochem.* 113:636–639.
156. Brody, M.J., and Y. Lee. 2016. The Role of Leucine-Rich Repeat Containing Protein 10 (LRRC10) in Dilated Cardiomyopathy. *Front. Physiol.* 7:337.
157. Ko, S.-H.H., P.W. Lenkowski, H.C. Lee, J.P. Mounsey, and M.K. Patel. 2005. Modulation of Nav1.5 by β1- and β3-subunit co-expression in mammalian cells. *Pflügers Arch.* 449:403–412.
158. Pan, X., Z. Li, X. Jin, Y. Zhao, G. Huang, and X. Huang. 2021. Comparative structural analysis of human Nav1.1 and Nav1.5 reveals mutational hotspots for sodium channelopathies. *PNAS*. 118:1–7.
159. Xu, H., T. Li, A. Rohou, C.P. Arthur, F. Tzakoniati, E. Wong, A. Estevez, C. Kugel, Y. Franke, J. Chen, C. Ciferri, D.H. Hackos, C.M. Koth, and J. Payandeh. 2019. Structural basis of Nav1.7 inhibition by a gating-modifier spider toxin. *Cell*. 176:702–715.
160. Kise, Y., G. Kasuya, H.H. Okamoto, D. Yamanouchi, K. Kobayashi, T. Kusakizako, T. Nishizawa, K. Nakajo, and O. Nureki. 2021. Structural basis of gating modulation of Kv4 channel complexes. *Nature*. 599:158–164.
161. Wu, J., Z. Yan, Z. Li, X. Qian, S. Lu, M. Dong, Q. Zhou, and N. Yan. 2016. Structure of the voltage-gated calcium channel Cav1. 1 at 3.6 Å resolution. *Nature*. 537:191–196.
162. Gao, S., X. Yao, and N. Yan. 2021. Structure of human Cav2. 2 channel blocked by the painkiller ziconotide. *Nature*. 596:143–147.
163. Long, S.B., E.B. Campbell, and R. Mackinnon. 2005. Crystal structure of a mammalian voltage-dependent Shaker family K+ channel. *Science*. 309:897–903.
164. Tao, X., and R. MacKinnon. 2019. Molecular structures of the human Slo1 K+ channel in complex with β4. *Elife*. 8:e51409.
165. Kang, C., C. Tian, F.D. Sönnichsen, J.A. Smith, J. Meiler, A.L. George Jr, C.G. Vanoye, H.J. Kim, and C.R. Sanders. 2008. Structure of KCNE1 and implications for how it modulates the KCNQ1 potassium channel. *Biochemistry*. 47:7999–8006.
166. Horrigan, F.T., and R.W. Aldrich. 2002. Coupling between voltage sensor activation, Ca2+ binding and channel opening in large conductance (BK) potassium channels. *J. Gen. Physiol.* 120:267–305.
167. Lingle, C.J., P.L. Martinez-Espinosa, A. Yang-Hood, L.E. Boero, S. Payne, D. Persic, B. V-Ghaffari, M. Xiao, Y. Zhou, X.M. Xia, S.J. Pyott, and M.A. Rutherford. 2019. LRRC52 regulates BK channel function and localization in mouse cochlear inner hair cells. *Proc. Natl. Acad. Sci. U. S. A.* 116:18397–18403.
168. Rockman, M.E., A.G. Vouga, and B.S. Rothberg. 2020. Molecular mechanism of BK channel

activation by the smooth muscle relaxant NS11021. *J. Gen. Physiol.* 152.

169. Zhu, W., T.L. Voelker, Z. Varga, A.R. Schubert, J.M. Nerbonne, and J.R. Silva. 2017. Mechanisms of noncovalent β subunit regulation of NaV channel gating. *J. Gen. Physiol.* 149:813–831.
170. Barro-Soria, R., M.E. Perez, and H.P. Larsson. 2015. KCNE3 acts by promoting voltage sensor activation in KCNQ1. *Proc. Natl. Acad. Sci. U. S. A.* 112:E7286–E7292.
171. Barro-Soria, R., R. Ramentol, S.I. Liin, M.E. Perez, R.S. Kass, and H.P. Larsson. 2017. KCNE1 and KCNE3 modulate KCNQ1 channels by affecting different gating transitions. *Proc. Natl. Acad. Sci. U. S. A.* 114:E7367–E7376.
172. Nakajo, K., and Y. Kubo. 2015. KCNQ1 channel modulation by KCNE proteins via the voltage-sensing domain. *J. Physiol.* 593:2617–2625.
173. Naranjo, D., H. Moldenhauer, M. Pincuntureo, and I. Díaz-Franulic. 2016. Pore size matters for potassium channel conductance. *J. Gen. Physiol.* 148:277–291.
174. Kaulin, Y.A., C.A. Rocha, M.S. Nadal, B. Rudy, and M. Covarrubias. 2009. The dipeptidyl-peptidase-like protein DPP6 determines the unitary conductance of neuronal Kv4.2 channels. *J. Neurosci.* 29:3242–3251.
175. Dougherty, K., M. Covarrubias, S.Y. Qi, B.R.J. Biol, and C. However. 2006. A dipeptidyl aminopeptidase – like protein remodels gating charge dynamics in Kv4.2 channels. *J. Gen. Physiol.* 128:745–753.
176. Dougherty, K., L. Tu, C. Deutsch, and M. Covarrubias. 2009. The dipeptidyl-aminopeptidase-like protein 6 is an integral voltage sensor-interacting β-subunit of neuronal KV4.2 channels. *Channels*. 3:122–128.
177. Sepela, R.J., R.G. Stewart, L.A. Valencia, P. Thapa, Z. Wang, B.E. Cohen, and J.T. Sack. 2021. The AMIGO1 adhesion protein activates Kv2.1 voltage sensors. *bioRxiv*. 2021.06.20.448455.
178. McCormick, K.A., J. Srinivasan, K. White, T. Scheuer, and W.A. Catterall. 1999. The extracellular domain of the beta1 subunit is both necessary and sufficient for beta1-like modulation of sodium channel gating. *J. Biol. Chem.* 274:32638–32646.
179. McCormick, K.A., L.L. Isom, D. Ragsdale, D. Smith, T. Scheuer, and W.A. Catterall. 1998. Molecular determinants of Na+ channel function in the extracellular domain of the beta1 subunit. *J. Biol. Chem.* 273:3954–3962.
180. Chen, C., and S.C. Cannon. 1995. Modulation of Na+ channel inactivation by the beta 1 subunit: a deletion analysis. *Pflugers Arch.* 431:186–195.
181. Spampanato, J., J.A. Kearney, G. De Haan, D.P. Mcewen, A. Escayg, I. Aradi, B.T. Macdonald, S.I. Levin, I. Soltesz, P. Benna, E. Montalenti, L.L. Isom, A.L. Goldin, and M.H. Meisler. 2004. A novel epilepsy mutation in the sodium channel SCN1A identifies a cytoplasmic domain for B subunit interaction. *J. Neurosci.* 24:10022–10034.
182. Yan, Z., Q. Zhou, L. Wang, Z. Yan, Q. Zhou, L. Wang, J. Wu, Y. Zhao, G. Huang, and W. Peng. 2017. Structure of the Nav 1.4-b1 complex from electrical eel. *Cell*. 170:470-475.e11.
183. Pan, X., Z. Li, Q. Zhou, H. Shen, K. Wu, X. Huang, J. Chen, J. Zhang, X. Zhu, J. Lei, W. Xiong, H. Gong, B. Xiao, and N. Yan. 2018. Structure of the human voltage-gated sodium channel Nav1.4 in complex with B1. *Science (80-.).* 362:1–9.
184. Shen, H., D. Liu, K. Wu, J. Lei, and N. Yan. 2019. Structures of human Nav1.7 channel in complex with auxiliary subunits and animal toxins. *Science (80-.).* 1308:1303–1308.
185. Shen, H., Q. Zhou, X. Pan, Z. Li, J. Wu, and N. Yan. 2017. Structure of a eukaryotic voltage-gated sodium channel at near-atomic resolution. *Science*. 355.
186. Vardanyan, V., and O. Pongs. 2012. Coupling of voltage-sensors to the channel pore: A

comparative view. *Front. Pharmacol.* 1–10.

187. Li, Q., X. Guan, K. Yen, J. Zhang, and J. Yan. 2016. The single transmembrane segment determines the modulatory function of the BK channel auxiliary γ subunit. *J. Gen. Physiol.* 147:337–351.
188. Wu, J., Z. Yan, Z. Li, C. Yan, S. Ly, M. Dong, and N. Yan. 2015. Structure of the voltage-gated calcium channel Cav1.1 complex. *Science (80-.).* 350:1–9.
189. Rutishauser, U., J.P. Thiery, R. Brackenbury, B.A. Sela, and G.M. Edelman. 1976. Mechanisms of adhesion among cells from neural tissues of the chick embryo. *Proc. Natl. Acad. Sci.* 73:577 LP – 581.
190. Ren, G., A.I. Roberts, and Y. Shi. 2011. Adhesion molecules: key players in mesenchymal stem cell-mediated immunosuppression. *Cell Adh. Migr.* 5:20–22.
191. Harjunpää, H., M.L. Asens, C. Guenther, and S.C. Fagerholm. 2019. Cell adhesion molecules and their roles and regulation in the immune and tumor microenvironment. *Front. Immunol.* 10:1–24.
192. Kobe, B., and A. V Kajava. 2001. The leucine-rich repeat as a protein recognition motif. *Curr. Opin. Struct. Biol.* 11:725–732.
193. Yoshihara, Y., S. Oka, J. Ikeda, and K. Mori. 1991. Immunoglobulin superfamily molecules in the nervous system. *Neurosci. Res.* 10:83–105.
194. Aricescu, A.R., and E.Y. Jones. 2007. Immunoglobulin superfamily cell adhesion molecules: zippers and signals. *Curr. Opin. Cell Biol.* 19:543–550.
195. Zinn, K., and O. Engin. 2017. Neural immunoglobulin superfamily interaction networks. *Curr. Opin. Neurobiol.* 45:99–105.
196. Ko, J., and E. Kim. 2007. Leucine-rich repeat proteins of synapses. *J. Neurosci. Res.* 2832:2824–2832.
197. Kobe, B., and J. Deisenhofer. 1994. The leucine-rich repeat: a versatile binding motif. *Trends Biomed. Sci.* 19:415–421.
198. Oxvig, C., and T.A. Springer. 1998. Experimental support for a β-propeller domain in integrin α-subunits and a calcium binding site on its lower surface. *Proc. Natl. Acad. Sci.* 95:4870 LP – 4875.
199. Springer, T.A. 1997. Folding of the N-terminal, ligand-binding region of integrin α-subunits into a β-propeller domain. *Proc. Natl. Acad. Sci.* 94:65 LP – 72.
200. Shimizu, H., A. Tosaki, N. Ohsawa, Y. Ishizuka-katsura, S. Shoji, H. Miyazaki, F. Oyama, T. Terada, M. Shirouzu, S. Sekine, N. Nukina, and S. Yokoyama. 2017. Parallel homodimer structures of the extracellular domains of the voltage-gated sodium channel B4 subunit explain its role in cell–cell adhesion. *J. Biol. Chem.* 292:13428–13440.
201. Kajander, T., J. Kuja-Panula, H. Rauvala, and A. Goldman. 2011. Crystal structure and role of glycans and dimerization in folding of neuronal leucine-rich repeat protein AMIGO-1. *J. Membr. Biol.* 413:1001–1015.
202. Guillemain, A., Y. Laouarem, L. Cobret, D. Štefok, W. Chen, S. Bloch, A. Zahaf, L. Blot, F. Reverchon, T. Normand, M. Decoville, C. Grillon, E. Traiffort, and S. Morisset-lopez. 2020. LINGO family receptors are differentially expressed in the mouse brain and form native multimeric complexes. *FASEB J.* 34:13641–13653.
203. Bezerra, G.A., E. Dobrovetsky, A. Seitova, S. Fedosyuk, S. Dhe-paganon, and K. Gruber. 2015. Structure of human dipeptidyl peptidase 10 (DPPY): a modulator of neuronal Kv4 channels. *Sci. Rep.* 5:1–9.
204. Brackenbury, W.J., and L.L. Isom. 2011. Na+ channel β subunits: Overachievers of the ion channel family. *Front. Pharmacol.* 2:1–11.
205. Davis, T.H., C. Chen, and L.L. Isom. 2004. Sodium channel beta1 subunits promote neurite outgrowth in cerebellar granule neurons. *J. Biol. Chem.* 279:51424–51432.

206. Moh, M.E.I.C., Q. Tian, T. Zhang, and L.A.Y.H. Lee. 2009. The immunoglobulin-like cell adhesion molecule hepaCAM modulates cell adhesion and motility through direct interaction with the actin cytoskeleton. *J. Cell. Physiol.* 219:382–391.

207. Moh, M.C., C. Zhang, C. Luo, L.H. Lee, and S. Shen. 2005. Structural and functional analyses of a novel Ig-like cell adhesion molecule, hepaCAM, in the human breast carcinoma MCF7 cells. *J. Biol. Chem.* 280:27366–27374.

208. Mohr, C.J., W. Schroth, S. Maier, B. Stegen, A. Dragoi, F.A. Steudel, S. Stehling, R. Hoppe, S. Madden, P. Ruth, and S.M. Huber. 2020. Subunits of BK channels promote breast cancer development and modulate responses to endocrine treatment in preclinical models. *Br J Pharmacol*. 1–19.

209. Zhou, Y., J. Xiang, A. Bhandari, J. Wen, B. Lin, L. Kong, and O. Wang. 2020. LRRC52-AS1 is associated with clinical progression and regulates cell migration and invasion in papillary thyroid cancer. *Clin. Exp. Pharmacol. Physiol.* 47:696–702.

210. Makkar, G., V. Shrivastava, B. Hlavay, M. Pretorius, B.D. Kyle, A.P. Braun, F.C. Lynn, and C. Huang. 2019. Lrrc55 is a novel prosurvival factor in pancreatic islets. *Am. J. Physiol. Endocrinol. Metab.* 317:E794–E804.

211. Weiss, N., and E. Ivanova. 2008. Does the voltage-gated calcium channel alpha2delta-1 subunit play a dual function in skeletal muscle? *J. Physiol.* 586:2035–2037.

212. Lau, L.A., F. Noubary, D. Wang, and C.G. Dulla. 2017. α2δ-1 signaling drives cell death, synaptogenesis, circuit reorganization, and gabapentin-mediated neuroprotection in a model of insult-induced cortical malformation. *eNeuro*. 4:ENEURO.0316-17.2017.

213. Meadows, L.S., J. Malhotra, A. Loukas, V. Thyagarajan, K.A. Kazen-Gillespie, M.C. Koopman, S. Kriegler, L.L. Isom, and D.S. Ragsdale. 2002. Functional and biochemical analysis of a sodium channel β1 subunit mutation responsible for generalized epilepsy with febrile seizures plus type 1. *J. Neurosci.* 22:10699 LP – 10709.

214. Malhotra, J.D., K. Kazen-Gillespie, M. Hortsch, and L.L. Isom. 2000. Sodium channel beta subunits mediate homophilic cell adhesion and recruit ankyrin to points of cell-cell contact. *J. Biol. Chem.* 275:11383–11388.

215. Yereddi, N.R., F.S. Cusdin, S. Namadurai, L.C. Packman, T.P. Monie, P. Slavny, J.J. Clare, A.J. Powell, and A.P. Jackson. 2013. The immunoglobulin domain of the sodium channel B3 subunit contains a surface-localized disulfide bond that is required for homophilic binding. *FASEB J.* 27:568–580.

216. Shimizu, H., H. Miyazaki, N. Ohsawa, S. Shoji, Y. Ishizuka-Katsura, A. Tosaki, F. Oyama, T. Terada, K. Sakamoto, M. Shirouzu, S.-I. Sekine, N. Nukina, and S. Yokoyama. 2016. Structure-based site-directed photo-crosslinking analyses of multimeric cell-adhesive interactions of voltage-gated sodium channel β subunits. *Sci. Rep.* 6:26618.

217. Elorza-vidal, X., E. Xicoy-espaulella, A. Pla-casillanis, M. Alonso-gardón, H. Gaitán-peñas, C. Engel-pizcueta, J. Fernández-recio, and R. Estévez. 2020. Structural basis for the dominant or recessive character of GLIALCAM mutations found in leukodystrophies. *Hum. Mol. Genet.* 29:1107–1120.

218. McEwen, D.P., and L.L. Isom. 2004. Heterophilic interactions of sodium channel beta1 subunits with axonal and glial cell adhesion molecules. *J. Biol. Chem.* 279:52744–52752.

219. Achour, L., M. Kamal, R. Jockers, and S. Marullo. 2011. Using quantitative BRET to assess g protein-coupled receptor homo- and heterodimerization. *Methods Mol Bio*. 756:183–200.

220. Cobret, L., M.L. De Tauzia, J. Ferent, E. Traiffort, I. Hénaoui, and F. Godin. 2014. Targeting the cis -

dimerization of LINGO-1 with low MW compounds affects its downstream. *Br. J. Pharmacol.* 172:841–856.

221. Salvage, X.S.C., W. Zhu, Z.F. Habib, S.S. Hwang, J.R. Irons, C.L.H. Huang, J.R. Silva, and X.A.P. Jackson. 2019. Gating control of the cardiac sodium channel Nav1.5 by its B3-subunit involves distinct roles for a transmembrane glutamic acid and the extracellular domain. *J. Biol. Chem.* 294:19752–19763.
222. Salvage, S.C., J.S. Rees, A. McStea, M. Hirsch, L. Wang, C.J. Tynan, M.W. Reed, J.R. Irons, R. Butler, A.J. Thompson, M.L. Martin-Fernandez, C.L.-H. Huang, and A.P. Jackson. 2020. Supramolecular clustering of the cardiac sodium channel Nav1.5 in HEK293F cells, with and without the auxiliary β3-subunit. *FASEB J.* 34:3537–3553.
223. Salvage, S.C., C.L. Huang, and A.P. Jackson. 2020. Cell-adhesion properties of β-subunits in the regulation of cardiomyocyte sodium channels. *Biomolecules*. 10:1–23.
224. Malhotra, J.D., V. Thyagarajan, C. Chen, and L.L. Isom. 2004. Tyrosine-phosphorylated and nonphosphorylated sodium channel β1 subunits are differentially localized in cardiac myocytes. *J. Biol. Chem.* 279:40748–40754.
225. Ratcliffe, C.F., R.E. Westenbroek, R. Curtis, and W.A. Catterall. 2001. Sodium channel β1 and β3 subunits associate with neurofascin through their extracellular immunoglobulin-like domain . *J. Cell Biol.* 154:427–434.
226. Srinivasan, J., M. Schachner, and W.A. Catterall. 1998. Interaction of voltage-gated sodium channels with the extracellular matrix molecules tenascin-C and tenascin-R. *Proc. Natl. Acad. Sci.* 95:15753 LP – 15757.
227. Xiao, Z.-C., D.S. Ragsdale, J.D. Malhotra, L.N. Mattei, P.E. Braun, M. Schachner, and L.L. Isom. 1999. Tenascin-R is a functional modulator of sodium channel B subunits. *J. Biol. Chem.* 274:26511–26517.
228. Jansson, K.H., D.G. Castillo, J.W. Morris, M.E. Boggs, K.J. Czymmek, E.L. Adams, L.P. Schramm, and R.A. Sikes. 2014. Identification of beta-2 as a key cell adhesion molecule in PCa cell neurotropic behavior: a novel ex vivo and biophysical approach. *PLoS One*. 9:e98408.
229. Eroglu, C., N.J. Allen, M.W. Susman, N.A. O'Rourke, C.Y. Park, E. Özkan, C. Chakraborty, S.B. Mulinyawe, D.S. Annis, and A.D. Huberman. 2009. Gabapentin receptor α2δ-1 is a neuronal thrombospondin receptor responsible for excitatory CNS synaptogenesis. *Cell*. 139:380–392.
230. McEwen, D.P., L.S. Meadows, C. Chen, V. Thyagarajan, and L.L. Isom. 2004. Sodium channel beta1 subunit-mediated modulation of Nav1.2 currents and cell surface density is dependent on interactions with contactin and ankyrin. *J. Biol. Chem.* 279:16044–16049.
231. Pan, Z., T. Kao, Z. Horvath, J. Lemos, J.-Y. Sul, S.D. Cranstoun, V. Bennett, S.S. Scherer, and E.C. Cooper. 2006. A common ankyrin-G-based mechanism retains KCNQ and NaV channels at electrically active domains of the axon. *J. Neurosci.* 26:2599 LP – 2613.
232. Ratcliffe, C.F., Y. Qu, K.A. McCormick, V.C. Tibbs, J.E. Dixon, T. Scheuer, and W.A. Catterall. 2000. A sodium channel signaling complex: modulation by associated receptor protein tyrosine phosphatase β. *Nat. Neurosci.* 3:437–444.
233. Park, H., S. Lee, P. Shrestha, J. Kim, J.A. Park, Y. Ko, Y.H. Ban, D.-Y. Park, S.-J. Ha, G.Y. Koh, V.S. Hong, N. Mochizuki, Y.-M. Kim, W. Lee, and Y.-G. Kwon. 2015. AMIGO2, a novel membrane anchor of PDK1, controls cell survival and angiogenesis via Akt activation. *J. Cell Biol.* 211:619–637.
234. Kim, D.Y., L.A.M. Ingano, B.W. Carey, W.H. Pettingell, and D.M. Kovacs. 2005. Presenilin/ y-secretase-mediated cleavage of the voltage-gated sodium channel B2-subunit regulates cell

adhesion. *J. Biol. Chem.* 280:23251–23261.

235. Wong, H., T. Sakurai, F. Oyama, K. Kaneko, K. Wada, H. Miyazaki, M. Kurosawa, B. De Strooper, P. Saftig, and N. Nukina. 2005. B subunits of voltage-gated sodium channels are novel substrates of B-site amyloid precursor protein-cleaving enzyme (BACE1) and y-secretase. *J. Biol. Chem.* 280:23009–23017.
236. Sirisi, S., X. Elorza-vidal, T. Arnedo, M. Armand-ug, G. Callejo, X. Capdevila-nortes, T. Lopez-Hernandez, U. Schulte, A. Barrallo-Gimeno, V. Nunes, X. Gasull, and R. Estevez. 2017. Depolarization causes the formation of a ternary complex between GlialCAM , MLC1 and ClC-2 in astrocytes: implications in megalencephalic leukoencephalopathy. *Hum. Mol. Genet.* 26:2436–2450.
237. Veeraraghavan, R., G.S. Hoeker, A. Alvarez-laviada, D. Hoagland, X. Wan, D.R. King, J. Sanchez-alonso, C. Chen, J. Jourdan, L.L. Isom, I. Deschenes, J.W. Smyth, J. Gorelik, S. Poelzing, and R.G. Gourdie. 2018. The adhesion function of the sodium channel beta subunit (b1) contributes to cardiac action potential propagation. 1–27.
238. Anastassiou, C.A., R. Perin, H. Markram, and C. Koch. 2011. Ephaptic coupling of cortical neurons. *Nat. Neurosci.* 14:217–223.
239. O'Connell, K.M.S., A.S. Rolig, J.D. Whitesell, and M.M. Tamkun. 2006. Kv2.1 potassium channels are retained within dynamic cell surface microdomains that are defined by a perimeter fence. *J. Neurosci.* 26:9609–9618.
240. Tamkun, M.M., K.M.S. O'connell, and A.S. Rolig. 2007. A cytoskeletal-based perimeter fence selectively corrals a sub-population of cell surface Kv2.1 channels. *J. Cell Sci.* 120:2413–23.
241. Deutsch, E., A. V Weigel, E.J. Akin, P. Fox, G. Hansen, C.J. Haberkorn, R. Loftus, D. Krapf, and M.M. Tamkun. 2012. Kv2.1 cell surface clusters are insertion platforms for ion channel delivery to the plasma membrane. *Mol. Biol. Cell*. 23:2917–2929.
242. Johnson, B., A.N. Leek, L. Solé, E.E. Maverick, T.P. Levine, and M.M. Tamkun. 2018. Kv2 potassium channels form endoplasmic reticulum/plasma membrane junctions via interaction with VAPA and VAPB. *Proc. Natl. Acad. Sci. U. S. A.* 115:E7331 LP-E7340.
243. Kirmiz, M., S. Palacio, P. Thapa, A.N. King, J.T. Sack, and J.S. Trimmer. 2018. Remodeling neuronal ER–PM junctions is a conserved nonconducting function of Kv2 plasma membrane ion channels. *Mol. Biol. Cell*. 29:2410–2432.
244. Glass, W.G., A.L. Duncan, and P.C. Biggin. 2020. Computational Investigation of Voltage-Gated Sodium Channel β3 Subunit Dynamics. *Front. Mol. Biosci.* 7:40.
245. Clatot, J., M. Hoshi, X. Wan, H. Liu, A. Jain, K. Shinlapawittayatorn, C. Marionneau, E. Ficker, T. Ha, and I. Deschênes. 2017. Voltage-gated sodium channels assemble and gate as dimers. *Nat. Commun.* 8:1–14.
246. Clatot, J., Y. Zheng, A. Girardeau, H. Liu, K.R. Laurita, C. Marionneau, and I. Deschênes. 2018. Mutant voltage-gated Na(+) channels can exert a dominant negative effect through coupled gating. *Am. J. Physiol. Heart Circ. Physiol.* 315:H1250–H1257.
247. Ono, T., N. Sekino-Suzuki, Y. Kikkawa, H. Yonekawa, and S. Kawashima. 2003. Alivin 1, a novel neuronal activity-dependent gene, inhibits apoptosis and promotes survival of cerebellar granule neurons. *J. Neurosci.* 23:5887 LP – 5896.
248. Vierra, N.C., S.C. O'Dwyer, C. Matsumoto, L.F. Santana, and J.S. Trimmer. 2021. Regulation of neuronal excitation–transcription coupling by Kv2.1-induced clustering of somatic L-type Ca2+ channels at ER-PM junctions. *Proc. Natl. Acad. Sci.* 118:e2110094118.
249. Rabenau, K.E., J.M. O'Toole, R. Bassi, H. Kotanides, L. Witte, D.L. Ludwig, and D.S. Pereira. 2004. DEGA/AMIGO-2, a leucine-rich repeat family member, differentially expressed in human gastric

adenocarcinoma: effects on ploidy, chromosomal stability, cell adhesion/migration and tumorigenicity. *Oncogene*. 23:5056–5067.

250. Cohen, S.A. 1996. Immunocytochemical localization of rH1 sodium channel in adult rat heart atria and ventricle. *Circulation*. 94:3083–3086.

251. Wildburger, N.C., S.R. Ali, W.-C.J. Hsu, A.S. Shavkunov, M.N. Nenov, C.F. Lichti, R.D. LeDuc, E. Mostovenko, N.I. Panova-Elektronova, M.R. Emmett, C.L. Nilsson, and F. Laezza. 2015. Quantitative proteomics reveals protein-protein interactions with fibroblast growth factor 12 as a component of the voltage-gated sodium channel 1.2 (nav1.2) macromolecular complex in Mammalian brain. *Mol. Cell. Proteomics*. 14:1288–1300.

252. Pan, X., Z. Li, X. Huang, G. Huang, S. Gao, H. Shen, L. Liu, J. Lei, and N. Yan. 2019. Molecular basis for pore blockade of human Na+ channel Nav1.2 by the u-conotoxin KIIIA. *Science (80-.).* 2:1309–1313.

253. Valdivia, C.R., A. Medeiros-domingo, B. Ye, W. Shen, T.J. Algiers, M.J. Ackerman, and J.C. Makielski. 2010. Loss-of-function mutation of the SCN3B -encoded sodium channel b3 subunit associated with a case of idiopathic ventricular fibrillation. *Cardiovasc. Res.* 6:392–400.

254. Kanellopoulos, A.H., J. Koenig, H. Huang, M. Pyrski, Q. Millet, S. Lolignier, T. Morohashi, S.J. Gossage, M. Jay, J.E. Linley, G. Baskozos, B.M. Kessler, J.J. Cox, A.C. Dolphin, F. Zufall, J.N. Wood, and J. Zhao. 2018. Mapping protein interactions of sodium channel NaV 1. 7 using epitope-tagged gene-targeted mice. *EMBO J.* 37:427–445.

255. Evanson, K.W., J.P. Bannister, M.D. Leo, and J.H. Jaggar. 2014. LRRC26 is a functional BK channel auxiliary γ subunit in arterial smooth muscle cells. *Circ. Res.* 115:423–431.

256. Noda, S., Y. Suzuki, H. Yamamura, W.R. Giles, and Y. Imaizumi. 2019. Roles of LRRC26 as an auxiliary γ1-subunit of large-conductance Ca2+-activated K+ channels in bronchial smooth muscle cells. *Am. J. Physiol. Cell. Mol. Physiol.* 318:L366–L375.

257. Takahashi, M., M.J. Seagar, J.F. Jones, B.F. Reber, and W.A. Catterall. 1987. Subunit structure of dihydropyridine-sensitive calcium channels from skeletal muscle. *Proc. Natl. Acad. Sci. U. S. A.* 84:5478–5482.

258. Müller, C.S., A. Haupt, W. Bildl, J. Schindler, H.-G. Knaus, M. Meissner, B. Rammner, J. Striessnig, V. Flockerzi, B. Fakler, and U. Schulte. 2010. Quantitative proteomics of the Cav2 channel nano-environments in the mammalian brain. *Proc. Natl. Acad. Sci.* 107:14950 LP – 14957.

259. Seikel, E., and J.S. Trimmer. 2009. Convergent modulation of Kv4.2 channel a subunits by structurally distinct DPPX and KChIP auxiliary subunits. *Biochemistry*. 48:5721–5730.

260. Jerng, H.H., K. Kunjilwar, and P.J. Pfaffinger. 2005. Multiprotein assembly of Kv4.2, KChIP3, and DPP10 produces ternary channel complexes with ISA-like properties. *J Physiol*. 3:767–788.

261. Belau, F., K. Metzner, T. Christ, U. Ravens, M. Schaefer, S. Künzel, W. Li, E. Wettwer, D. Dobrev, A. El-armouche, and S. Kämmerer. 2019. DPP10 is a new regulator of Nav1.5 channels in human heart. *Int. J. Cardiol.* 284:68–73.

262. Kazarinova-Noyes, K., J.D. Malhotra, D.P. McEwen, L.N. Mattei, E.O. Berglund, B. Ranscht, S.R. Levinson, M. Schachner, P. Shrager, L.L. Isom, and Z.C. Xiao. 2001. Contactin associates with Na+ channels and increases their functional expression. *J. Neurosci.* 21:7517–7525.

263. Webb, J., F. Wu, and S.C. Cannon. 2009. Slow inactivation of the NaV1.4 sodium channel in mammalian cells is impeded by co-expression of the beta1 subunit. *Pflugers Arch.* 457:1253–1263.

264. Zhao, J., M.E. O'Leary, and M. Chahine. 2011. Regulation of Nav1.6 and Nav1.8 peripheral nerve Na+ channels by auxiliary β-subunits. *J. Neurophysiol.* 106:608–619.

265. Laedermann, C.J., N. Syam, M. Pertin, I. Decosterd, and H. Abriel. 2013. β1- and β3- voltage-gated

sodium channel subunits modulate cell surface expression and glycosylation of Nav1.7 in HEK293 cells. *Front. Cell. Neurosci.* 7:137.

266. Bao, Y., B.C. Willis, C.R. Frasier, L.F. Lopez-, X. Lin, R. Ramos-mondragón, S. David, C. Chen, Z. Wang, and J. Anumonwo. 2016. Scn2b deletion in mice results in ventricular and atrial arrhythmias. *Circ Arrhythm Electrophysiol*. 9:734–763.

267. Vijayaragavan, K., A.J. Powell, I.J. Kinghorn, and M. Chahine. 2004. Role of auxiliary β1-, β2-, and β3-subunits and their interaction with Nav1.8 voltage-gated sodium channel. *Biochem. Biophys. Res. Commun.* 319:531–540.

268. Ransdell, J.L., E. Dranoff, B. Lau, W. Lo, D.L. Donermeyer, P.M. Allen, and J.M. Nerbonne. 2017. Loss of NavB4-mediated regulation of sodium currents in adult Purkinje neurons disrupts firing and impairs motor coordination and balance. *Cell Rep.* 19:532–544.

269. Fuller-Bicer, G.A., G. Varadi, S.E. Koch, M. Ishii, I. Bodi, N. Kadeer, J.N. Muth, G. Mikala, N.N. Petrashevskaya, M.A. Jordan, S.-P. Zhang, N. Qin, C.M. Flores, I. Isaacsohn, M. Varadi, Y. Mori, W.K. Jones, and A. Schwartz. 2009. Targeted disruption of the voltage-dependent calcium channel alpha2/delta-1-subunit. *Am. J. Physiol. Heart Circ. Physiol.* 297:H117-24.

270. Kim, J., M.S. Nadal, A.M. Clemens, M. Baron, S. Jung, Y. Misumi, B. Rudy, D.A. Hoffman, J. Kim, N. Ms, C. Am, M. Baron, J. S-c, and Y. Misumi. 2008. Kv4 accessory protein DPPX (DPP6) is a critical regulator of membrane excitability in hippocampal CA1 pyramidal neurons. *J Neurophysiol*. 100:1835–1847.

271. Patino, G.A., L.R.F. Claes, L.F. Lopez-Santiago, E.A. Slat, R.S.R. Dondeti, C. Chen, H.A. O'Malley, C.B.B. Gray, H. Miyazaki, N. Nukina, F. Oyama, P. De Jonghe, and L.L. Isom. 2009. A functional null mutation of SCN1B in a patient with Dravet syndrome. *J. Neurosci.* 29:10764–10778.

272. Qu, Y., R. Curtis, D. Lawson, K. Gilbride, P. Ge, P.S. DiStefano, I. Silos-Santiago, W.A. Catterall, and T. Scheuer. 2001. Differential Modulation of Sodium Channel Gating and Persistent Sodium Currents by the β1, β2, and β3 Subunits. *Mol. Cell. Neurosci.* 18:570–580.

273. Ferrera, L., and O. Moran. 2006. β1-subunit modulates the Nav1.4 sodium channel by changing the surface charge. *Exp. Brain Res.* 172:139–150.

274. Islas, A.A., A. Sánchez-Solano, T. Scior, L. Millan-PerezPeña, and E.M. Salinas-Stefanon. 2013. Identification of Navβ1 Residues Involved in the Modulation of the Sodium Channel Nav1.4. *PLoS One*. 8:e81995.

275. Valdivia, C.R., T. Nagatomo, and J.C. Makielski. 2002. Late Na Currents Affected by α Subunit Isoform and β1 Subunit Co-expression in HEK293 Cells. *J. Mol. Cell. Cardiol.* 34:1029–1039.

276. Watanabe, H., D. Darbar, D.W. Kaiser, K. Jiramongkolchai, S. Chopra, B.S. Donahue, P.J. Kannankeril, and D.M. Roden. 2009. Mutations in sodium channel β1- and β2-subunits associated with atrial fibrillation. *Circ. Arrhythm. Electrophysiol.* 2:268–275.

277. Bouza, A.A., J.M. Philippe, N. Edokobi, A.M. Pinsky, J. Offord, J.D. Calhoun, M. Lopez-Florán, L.F. Lopez-Santiago, P.M. Jenkins, and L.L. Isom. 2020. Sodium channel β1 subunits are post-translationally modified by tyrosine phosphorylation, S-palmitoylation, and regulated intramembrane proteolysis. *J. Biol. Chem.* 295:10380–10393.

278. Casini, S., H.L. Tan, I. Demirayak, C.A. Remme, A.S. Amin, B.P. Scicluna, H. Chatyan, J.M. Ruijter, C.R. Bezzina, A.C.G. van Ginneken, and M.W. Veldkamp. 2010. Tubulin polymerization modifies cardiac sodium channel expression and gating. *Cardiovasc. Res.* 85:691–700.

279. Watanabe, H., T.T. Koopmann, S. Le Scouarnec, T. Yang, C.R. Ingram, J.-J. Schott, S. Demolombe, V. Probst, F. Anselme, and D. Escande. 2008. Sodium channel β1 subunit mutations associated with Brugada syndrome and cardiac conduction disease in humans. *J. Clin. Invest.* 118:2260–2268.

280. Herfst, L.J., F. Potet, C.R. Bezzina, W.A. Groenewegen, H. Le Marec, T.M. Hoorntje, S. Demolombe, I. Baró, D. Escande, H.J. Jongsma, A.A.M. Wilde, and M.B. Rook. 2003. Na^+ channel mutation leading to loss of function and non-progressive cardiac conduction defects. *J. Mol. Cell. Cardiol.* 35:549–557.

281. Fahmi, A.I., M. Patel, E.B. Stevens, A.L. Fowden, J.E. 3rd John, K. Lee, R. Pinnock, K. Morgan, A.P. Jackson, and J.I. Vandenberg. 2001. The sodium channel beta-subunit SCN3b modulates the kinetics of SCN5a and is expressed heterogeneously in sheep heart. *J. Physiol.* 537:693–700.

282. Mercier, A., R. Clément, T. Harnois, N. Bourmeyster, J.-F. Faivre, I. Findlay, M. Chahine, P. Bois, and A. Chatelier. 2012. The β1-subunit of Na(v)1.5 cardiac sodium channel is required for a dominant negative effect through α-α interaction. *PLoS One*. 7:e48690–e48690.

283. Wilson, M.J., M.M. Zhang, L. Azam, B.M. Olivera, G. Bulaj, and D. Yoshikami. 2011. Navβ subunits modulate the inhibition of Nav1.8 by the analgesic gating modifier μO-conotoxin MrVIB. *J. Pharmacol. Exp. Ther.* 338:687–693.

284. Chen, C., J.D. Calhoun, Y. Zhang, L. Lopez-Santiago, N. Zhou, T.H. Davis, J.L. Salzer, and L.L. Isom. 2012. Identification of the cysteine residue responsible for disulfide linkage of Na+ channel α and β2 subunits. *J. Biol. Chem.* 287:39061–39069.

285. Llongueras, P., S. Das, J. De Waele, and L. Capulzini. 2020. Biophysical investigation of sodium channel interaction with b-subunit variants associated with arrhythmias. *Bioelectricity*. 2:269–278.

286. Cusdin, F.S., D. Nietlispach, J. Maman, T.J. Dale, A.J. Powell, J.J. Clare, and A.P. Jackson. 2010. The sodium channel {beta}3-subunit induces multiphasic gating in NaV1.3 and affects fast inactivation via distinct intracellular regions. *J. Biol. Chem.* 285:33404–33412.

287. Aman, T.K., T.M. Grieco-Calub, C. Chen, R. Rusconi, E.A. Slat, L.L. Isom, and I.M. Raman. 2009. Regulation of Persistent Na Current by Interactions between β Subunits of Voltage-Gated Na Channels. *J. Neurosci.* 29:2027 LP – 2042.

288. Medeiros-Domingo, A., T. Kaku, D.J. Tester, P. Iturralde-Torres, A. Itty, B. Ye, C. Valdivia, K. Ueda, S. Canizales-Quinteros, M.T. Tusié-Luna, J.C. Makielski, and M.J. Ackerman. 2007. SCN4B-encoded sodium channel β4 subunit in congenital long-QT syndrome. *Circulation*. 116:134–142.

289. Guan, X., Q. Li, and J. Yan. 2017. Relationship between auxiliary gamma subunits and mallotoxin on BK channel modulation. *Sci. Rep.* 7:1–10.

290. Li, Q., F. Fan, H.R. Kwak, and J. Yan. 2015. Molecular basis for differential modulation of BK channel voltage-dependent gating by auxiliary γ subunits. *J. Gen. Physiol.* 145:543–554.

291. Lacinová, L., and N. Klugbauer. 2004. Modulation of gating currents of the Ca(v)3.1 calcium channel by alpha 2 delta 2 and gamma 5 subunits. *Arch. Biochem. Biophys.* 425:207–213.

292. Dougherty, K., and M. Covarrubias. 2006. A dipeptidyl aminopeptidase-like protein remodels gating charge dynamics in Kv4.2 channels. *J. Gen. Physiol.* 128:745–753.

293. Li, H., Y. Qu, Y.C. Lu, V.E. Bondarenko, S. Wang, I.M. Skerrett, M.J. Morales, Y. Qu, Y.C. Lu, V.E. Bon-, S. Wang, I.M. Skerrett, and M.J. Mo-. 2006. DPP10 is an inactivation modulatory protein of Kv4. 3 and Kv1. 4. *Am. J. Physiol. - Cell Physiol.* 291:966–976.

294. Chowdhury, S., and B. Chanda. 2013. Free-energy relationships in ion channels activated by voltage and ligand. *J. Gen. Physiol.* 141:11–28.

295. Bezanilla, F. 2008. How membrane proteins sense voltage. *Nat. Rev. Mol. Cell Biol.* 9:323–332.

296. Long, S.B., X. Tao, E.B. Campbell, and R. MacKinnon. 2007. Atomic structure of a voltage-dependent K+ channel in a lipid membrane-like environment. *Nature*. 450:376–382.

297. Aggarwal, S.K., and R. MacKinnon. 1996. Contribution of the S4 segment to gating charge in the Shaker K+ channel. *Neuron*. 16:1169–1177.

298. Seoh, S.A., D. Sigg, D.M. Papazian, and F. Bezanilla. 1996. Voltage-sensing residues in the S2 and S4 segments of the Shaker K+ channel. *Neuron*. 16:1159–1167.

299. Islas, L.D., and F.J. Sigworth. 1999. Voltage sensitivity and gating charge in Shaker and Shab family potassium channels. *J. Gen. Physiol.* 114:723–742.

300. Armstrong, C.M., and F. Bezanilla. 1973. Currents related to movement of the gating particles of the sodium channels. *Nature*. 242:459—461.

301. Zagotta, W.N., T. Hoshi, J. Dittman, and R.W. Aldrich. 1994. Shaker potassium channel gating. II: Transitions in the activation pathway. *J. Gen. Physiol.* 103:279–319.

302. Tao, X., A. Lee, W. Limapichat, D.A. Dougherty, and R. MacKinnon. 2010. A gating charge transfer center in voltage sensors. *Science (80-.).* 328:67–73.

303. Tanabe, T., K.G. Beam, J.A. Powell, and S. Numa. 1988. Restoration of excitation—contraction coupling and slow calcium current in dysgenic muscle by dihydropyridine receptor complementary DNA. *Nature*. 336:134.

304. Kaczmarek, L.K. 2006. Non-conducting functions of voltage-gated ion channels. *Nat. Rev. Neurosci.* 7:761–771.

305. Murakoshi, H., G. Shi, R.H. Scannevin, and J.S. Trimmer. 1997. Phosphorylation of the Kv2.1 K+ channel alters voltage-dependent activation. *Mol. Pharmacol.* 52:821–8.

306. Plant, L.D., E.J. Dowdell, I.S. Dementieva, J.D. Marks, and S.A.N. Goldstein. 2011. SUMO modification of cell surface Kv2.1 potassium channels regulates the activity of rat hippocampal neurons. *J. Gen. Physiol.* 137:441–54.

307. MacDonald, P.E., A.M.F. Salapatek, and M.B. Wheeler. 2003. Temperature and redox state dependence of native Kv2.1 currents in rat pancreatic beta-cells. *J. Physiol.* 546:647–653.

308. Ramu, Y., Y. Xu, and Z. Lu. 2006. Enzymatic activation of voltage-gated potassium channels. *Nature*. 442:696–699.

309. Gordon, E., T.K. Roepke, and G.W. Abbott. 2006. Endogenous KCNE Subunits Govern Kv2 . 1 K 1 Channel Activation Kinetics in Xenopus Oocyte Studies. *Biophys. J.* 90:1223–1231.

310. Bocksteins, E. 2016. Kv5, Kv6, Kv8, and Kv9 subunits: No simple silent bystanders. *J. Gen. Physiol.* 147:105–125.

311. Schneider, M.F., and W.K. Chandler. 1973. Voltage Dependent Charge Movement in Skeletal Muscle: a Possible Step in Excitation–Contraction Coupling. *Nature*. 242:244.

312. Schoppa, N.E., and F.J. Sigworth. 1998. Activation of Shaker potassium channels. I. Characterization of voltage-dependent transitions. *J. Gen. Physiol.* 111:271–294.

313. Hoshi, T., W.N. Zagotta, and R.W. Aldrich. 1994. Shaker potassium channel gating. I: Transitions near the open state. *J. Gen. Physiol.* 103:249–278.

314. Ledwell, J.L., and R.W. Aldrich. 1999. Mutations in the S4 region isolate the final voltage-dependent cooperative step in potassium channel activation. *J. Gen. Physiol.* 113:389–414.

315. Pathak, M.M., V. Yarov-yarovoy, G. Agarwal, B. Roux, P. Barth, S. Kohout, F. Tombola, and E.Y. Isacoff. 2007. Article Closing In on the Resting State of the Shaker K + Channel. *Neuron*. 56:124–140.

316. Larsson, H.P., O.S. Baker, D.S. Dhillon, and E.Y. Isacoff. 1996. Transmembrane Movement of the Shaker K ⁺ Channel S4. *Neuron*. 16:387–397.

317. Liu, Y., M. Holmgren, M.E. Jurman, and G. Yellen. 1997. Gated Access to the Pore of a Voltage-Dependent K ⁺ Channel. *Neuron*. 19:175–184.

318. Lin, M.Z., and M.J. Schnitzer. 2016. Genetically encoded indicators of neuronal activity. *Nat. Neurosci.* 19:1142–1153.

319. Zhang, G., S. Zheng, H. Liu, and P.R. Chen. 2015. Illuminating biological processes through site-specific protein labeling. *Chem. Soc. Rev.* 44:3405–3417.

320. Tilley, D.C., J.M. Angueyra, K.S. Eum, H. Kim, L.H. Chao, A.W. Peng, and J.T. Sack. 2019. The tarantula toxin GxTx detains K+ channel gating charges in their resting conformation. *J. Gen. Physiol.* 151:292–315.

321. Thapa, P., R. Stewart, R.J. Sepela, O. Vivas, L.K. Parajuli, M. Lillya, S. Fletcher-taylor, B.E. Cohen, K. Zito, and J.T. Sack. 2021. EVAP: A two-photon imaging tool to study conformational changes in endogenous Kv2 channels in live tissues. *J. Gen. Physiol.* 153:1–24.

322. Fletcher-Taylor, S., P. Thapa, R.J. Sepela, R. Kaakati, V. Yarov-Yarovoy, J.T. Sack, and B.E. Cohen. 2020. Distinguishing potassium channel resting state conformations in live cells with environment-sensitive fluorescence. *Am. Chem. Soc. Chem. Neurosci.* 11.

323. Catterall, W.A., S. Cestèle, V. Yarov-Yarovoy, F.H. Yu, K. Konoki, and T. Scheuer. 2007. Voltage-gated ion channels and gating modifier toxins. *Toxicon*. 49:124–141.

324. Herrington, J., Y.P. Zhou, R.M. Bugianesi, P.M. Dulski, Y. Feng, V.A. Warren, M.H.M. Smith, M.G. Kohler, V.M. Garsky, M. Sanchez, M. Wagner, K. Raphaelli, P. Banerjee, C. Ahaghotu, D. Wunderler, B.T. Priest, J.T. Mehl, M.L. Garcia, O.B. McManus, G.J. Kaczorowski, and R.S. Slaughter. 2006. Blockers of the delayed-rectifier potassium current in pancreatic Beta-cells enhance glucose-dependent insulin secretion. *Diabetes*. 55:1034–1042.

325. Gupta, K., M. Zamanian, C. Bae, M. Milescu, D. Krepkiy, D.C. Tilley, J.T. Sack, V. Yarov-Yarovoy, J. Il Kim, and K.J. Swartz. 2015. Tarantula toxins use common surfaces for interacting with Kv and ASIC ion channels. *Elife*. 4:1–20.

326. Legant, W.R., L. Shao, J.B. Grimm, T.A. Brown, D.E. Milkie, B.B. Avants, L.D. Lavis, and E. Betzig. 2016. High-density three-dimensinoal localization microscopy across large volumes. *Nat. Methods*. 13:359–365.

327. Macgregor, R.B., and G. Weber. 1986. Estimation of the polarity of the protein interior by optical spectroscopy. *Nature*. 319:70–73.

328. Sackett, D.L., and J. Wolff. 1987. Nile red as a polarity-sensitive fluorescent probe of hydrophobic protein surfaces. *Anal. Biochem.* 167:228–234.

329. E., C.B., M.T. B., P.E. Sun, J.Y. Nung, B.S. G., and J.L. Yeh. 2002. Probing Protein Electrostatics with a Synthetic Fluorescent Amino Acid. *Science (80-.).* 296:1700–1703.

330. Pierce, D.W., and S.G. Boxer. 1992. Dielectric relaxation in a protein matrix. *J. Phys. Chem.* 96:5560–5566.

331. Cohen, B.E., A. Pralle, X. Yao, G. Swaminath, C.S. Gandhi, Y.N. Jan, B.K. Kobilka, E.Y. Isacoff, and L.Y. Jan. 2005. A fluorescent probe designed for studying protein conformational change. *Proc. Natl. Acad. Sci. U. S. A.* 102:965–970.

332. Zito, K., G. Knott, G.M.G. Shepherd, S. Shenolikar, K. Svoboda, and N. Carolina. 2004. Induction of Spine Growth and Synapse Formation by Regulation of the Spine Actin Cytoskeleton. *Neuron*. 44:321–334.

333. Scholle, A., S. Dugarmaa, T. Zimmer, M. Leonhardt, R. Koopmann, B. Engeland, O. Pongs, and K. Benndorf. 2004. Rate-limiting reactions determining different activation kinetics of Kv1.2 and Kv2.1 channels. *J. Membr. Biol.* 198:103–12.

334. Jara-Oseguera, A., I.G. Ishida, G.E. Rangel-Yescas, N. Espinosa-Jalapa, J.A. Pérez-Guzmán, D. Elías-Viñas, R. Le Lagadec, T. Rosenbaum, and L.D. Islas. 2011. Uncoupling charge movement from channel opening in voltage-gated potassium channels by ruthenium complexes. *J. Biol. Chem.* 286:16414–16425.

335. Lee, H.C., J.M. Wang, and K.J. Swartz. 2003. Interaction between extracellular hanatoxin and the resting conformation of the voltage-sensor paddle in Kv channels. *Neuron*. 40:527–536.

336. Mann, V.R., A.S. Powers, D.C. Tilley, J.T. Sack, and B.E. Cohen. 2018. Azide-Alkyne Click Conjugation on Quantum Dots by Selective Cooper Coordination. *ACS Nano*. 12:4469–4477.

337. Titus, J.A., R. Haugland, S.O. Sharrow, and D.M. Segal. 1982. Texas red, a hydrophilic, red-emitting flourophore for use with flourescein in dual parameter flow microfluorometric and fluorescence microscopic studies. *J. Immunol. Methods*. 50:193–204.

338. Antonucci, D.E., S.T. Lim, S. Vassanelli, and J.S. Trimmer. 2001. Dynamic localization and clustering of dendritic Kv2.1 voltage-dependent potassium channels in developing hippocampal neurons. *Neuroscience*. 108:69–81.

339. Jha, S.K., M. Ji, K.J. Gaffney, and S.G. Boxer. 2011. Direct measurement of the protein response to an electrostatic perturbation that mimics the catalytic cycle in ketosteroid isomerase. *Proc. Natl. Acad. Sci.* 108:16612 LP – 16617.

340. Greathouse, J.A., R.T. Cygan, R.W. Bradshaw, E.H. Majzoub, and B.A. Simmons. 2007. Computational and Spectroscopic Studies of Dichlorofluoroethane Hydrate Structure and Stability. *J. Phys. Chem. C*. 111:16787–16795.

341. Tilley, D.C., K.S. Eum, S. Fletcher-Taylor, D.C. Austin, C. Dupre, L.A. Patron, R.L. Garcia, K. Lam, V. Yarov-Yarovoy, B.E. Cohen, and J.T. Sack. 2014. Chemoselective tarantula toxins report voltage activation of wild-type ion channels in live cells. *Proc. Natl. Acad. Sci. U. S. A.* 111:E4789–E4796.

342. Hodgkin, A.L., and A.F. huxley. 1952. A quantitative description of membrane current and its application to conduction and excitation in nerve. *J Physiol*. 117:500–544.

343. Sun, J., and R. MacKinnon. 2020. Structural Basis of Human KCNQ1 Modulation and Gating. *Cell*. 180:340-347.e9.

344. Malin, S.A., and J.M. Nerbonne. 2002. Delayed rectifier K currents, IK, are encoded by Kv2-subunits and regulate tonic firing in mammalian sympathetic neurons. *Mol. Biol.* 22:10094–10105.

345. O'Connell, K.M.S., R. Loftus, and M.M. Tamkun. 2010. Localization-dependent activity of the Kv2.1 delayed-rectifier K+ channel. *Proc. Natl. Acad. Sci. U. S. A.* 107:12351–12356.

346. Singer-lahat, D., A. Sheinin, D. Chikvashvili, S. Tsuk, D. Greitzer, R. Friedrich, L. Feinshreiber, U. Ashery, M. Benveniste, E.S. Levitan, and I. Lotan. 2007. K+ Channel Facilitation of Exocytosis by Dynamic Interaction with Syntaxin. *J. Neurosci.* 27:1651–1658.

347. Feinshreiber, L., D. Singer-Lahat, R. Friedrich, U. Matti, A. Sheinin, O. Yizhar, R. Nachman, D. Chikvashvili, J. Rettig, U. Ashery, and I. Lotan. 2010. Non-conducting function of the Kv2.1 channel enables it to recruit vesicles for release in neuroendocrine and nerve cells. *J. Cell Sci.* 123:1940–1947.

348. Fox, P.D., C.J. Haberkorn, A. V Weigel, J.L. Higgins, E.J. Akin, M.J. Kennedy, D. Krapf, and M.M. Tamkun. 2013. Plasma membrane domains enriched in cortical endoplasmic reticulum function as membrane protein trafficking hubs. *Mol. Biol. Cell*. 24:2703–2713.

349. Kirmiz, M., N.C. Vierra, S. Palacio, and J.S. Trimmer. 2018. Identification of VAPA and VAPB as Kv2 channel-interacting proteins defining endoplasmic reticulum–plasma membrane junctions in mammalian brain neurons. *J. Neurosci.* 38:7562–7584.

350. Vierra, N.C., M. Kirmiz, D. van der List, L.F. Santana, and J.S. Trimmer. 2019. Kv2.1 mediates spatial and functional coupling of L-type calcium channels and ryanodine receptors in mammalian neurons. *Elife*. 8.

351. Turner, M., D.E. Anderson, P. Bartels, M. Nieves-Cintron, A.M. Coleman, P.B. Henderson, K.N.M. Man, P.-Y. Tseng, V. Yarov-Yarovoy, D.M. Bers, M.F. Navedo, M.C. Horne, J.B. Ames, and J.W.

Hell. 2020. α-Actinin-1 promotes activity of the L-type Ca(2+) channel Ca(v) 1.2. *EMBO J.* 39:e102622.

352. Fox, P.D., R.J. Loftus, and M.M. Tamkun. 2013. Regulation of Kv2.1 K(+) conductance by cell surface channel density. *J. Neurosci.* 33:1259–70.

353. Dai, X.Q., J.E. Manning Fox, D. Chikvashvili, M. Casimir, G. Plummer, C. Hajmrle, A.F. Spigelman, T. Kin, D. Singer-Lahat, Y. Kang, A.M.J. Shapiro, H.Y. Gaisano, I. Lotan, and P.E. Macdonald. 2012. The voltage-dependent potassium channel subunit Kv2.1 regulates insulin secretion from rodent and human islets independently of its electrical function. *Diabetologia*. 55:1709–1720.

354. Park, K.-S., D.P. Mohapatra, H. Misonou, and J.S. Trimmer. 2006. Graded regulation of the Kv2.1 potassium channel by variable phosphorylation. *Science (80-.).* 313:976–979.

355. Cerda, O., and J.S. Trimmer. 2011. Activity-dependent phosphorylation of neuronal Kv2.1 potassium channels by CDK5. *J. Biol. Chem.* 286:28738–28748.

356. Mccord, M.C., and E. Aizenman. 2013. Convergent Ca 2 + and Zn 2 + signaling regulates apoptotic Kv2 . 1 K + currents. *PNAS*. 110:13988–12993.

357. Dai, X.Q., J. Kolic, P. Marchi, S. Sipione, and P.E. MacDonald. 2009. SUMOylation regulates Kv2.1 and modulates pancreatic β-cell excitability. *J. Cell Sci.* 122:775–779.

358. McCord, M.C., and E. Aizenman. 2013. Convergent Ca2+ and Zn2+ signaling regulates apoptotic Kv2.1 K+ currents. *Proc. Natl. Acad. Sci. U. S. A.* 110:13988–93.

359. McCrossan, Z.A., A. Lewis, G. Panaghie, P.N. Jordan, D.J. Christini, D.J. Lerner, and G.W. Abbott. 2003. MinK-related peptide 2 modulates Kv2.1 and Kv3.1 potassium channels in mammalian brain. *J. Neurosci.* 23:8077–8091.

360. Kang, S.K., C.G. Vanoye, S.N. Misra, D.M. Echevarria, J.D. Calhoun, J.B. O'Connor, K.L. Fabre, D. McKnight, L. Demmer, P. Goldenberg, L.E. Grote, I. Thiffault, C. Saunders, K.A. Strauss, A. Torkamani, J. van der Smagt, K. van Gassen, R.P. Carson, J. Diaz, E. Leon, J.E. Jacher, M.C. Hannibal, J. Litwin, N.R. Friedman, A. Schreiber, B. Lynch, A. Poduri, E.D. Marsh, E.M. Goldberg, J.J. Millichap, A.L.J. George, and J.A. Kearney. 2019. Spectrum of K(v) 2.1 dysfunction in KCNB1-associated neurodevelopmental disorders. *Ann. Neurol.* 86:899–912.

361. Vacher, H., D.P. Mohapatra, and J.S. Trimmer. 2008. Localization and targeting of voltage-dependent ion channels in mammalian central neurons. *Physiol. Rev.* 88:1407–1447.

362. Yang, W., and R. Yuste. 2017. In vivo imaging of neural activity. *Nat. Methods*. 14.

363. McDonough, S.I., R. a Lampe, R. a Keith, and B.P. Bean. 1997. Voltage-dependent inhibition of N- and P-type calcium channels by the peptide toxin omega-grammotoxin-SIA. *Mol. Pharmacol.* 52:1095–104.

364. Sack, J.T., R.W. Aldrich, and W.F. Gilly. 2004. A gastropod toxin selectively slows early transitions in the Shaker K channel's activation pathway. *J. Gen. Physiol.* 123:685–96.

365. Swartz, K.J. 2007. Tarantula toxins interacting with voltage sensors in potassium channels. *Toxicon*. 49:213–230.

366. Trapani, J.G., and S.J. Korn. 2003. Control of ion channel expression for patch clamp recordings using an inducible expression system in mammalian cell lines. *BMC Neurosci.* 4.

367. Matt, L., K. Kim, A.C. Hergarden, M.C. Horne, J.B. Ames, J.W. Hell, L. Matt, K. Kim, A.C. Hergarden, T. Patriarchi, Z.A. Malik, and D.K. Park. 2018. a -Actinin Anchors PSD-95 at Postsynaptic Sites Article a -Actinin Anchors PSD-95 at Postsynaptic Sites. *Neuron*. 97:1094–1109.

368. Kihira, Y., T.O. Hermanstyne, and H. Misonou. 2010. Formation of heteromeric Kv2 channels in mammalian brain neurons. *J. Biol. Chem.* 285:15048–15055.

369. Hönigsperger, C., M.J. Nigro, and J.F. Storm. 2017. Physiological roles of Kv2 channels in entorhinal cortex layer II stellate cells revealed by Guangxitoxin-1E. *J. Physiol.* 595:739–757.
370. Romer, S.H., A.S. Deardorff, and R.E.W. Fyffe. 2019. A molecular rheostat: Kv2.1 currents maintain or suppress repetitive firing in motoneurons. *J. Physiol.* 597:3769–3786.
371. Torkamani, A., K. Bersell, B.S. Jorge, R.L. Bjork, J.R. Friedman, C.S. Bloss, J. Cohen, S. Gupta, S. Naidu, C.G. Vanoye, A.L. George, and J.A. Kearney. 2014. De novo KCNB1 mutations in epileptic encephalopathy. *Ann. Neurol.* 76:529–540.
372. Thiffault, I., D.J. Speca, D.C. Austin, M.M. Cobb, K.S. Eum, N.P. Safina, L. Grote, E.G. Farrow, N. Miller, S. Soden, S.F. Kingsmore, J.S. Trimmer, C.J. Saunders, and J.T. Sack. 2015. A novel epileptic encephalopathy mutation in KCNB1 disrupts Kv2.1 ion selectivity, expression, and localization. *J. Gen. Physiol.* 146:399–410.
373. Aras, M.A., R.A. Saadi, and E. Aizenman. 2009. Zn2+ regulates Kv2.1 voltage-dependent gating and localization following ischemia. *Eur. J. Neurosci.* 30:2250–2257.
374. Misonou, H., S.M. Thompson, and X. Cai. 2008. Dynamic regulation of the Kv2.1 voltage-gated potassium channel during brain ischemia through neuroglial interaction. *J. Neurosci.* 28:8529–38.
375. Peltola, M.A., J. Kuja-Panula, J. Liuhanen, V. Võikar, P. Piepponen, T. Hiekkalinna, T. Taira, S.E. Lauri, J. Suvisaari, N. Kulesskaya, T. Paunio, and H. Rauvala. 2015. AMIGO-Kv2.1 potassium channel complex is associated with schizophrenia-related phenotypes. *Schizophr. Bull.* 42:105.
376. Chen, Y., H.H. Hor, and B.L. Tang. 2012. AMIGO is expressed in multiple brain cell types and may regulate dendritic growth and neuronal survival. *J. Cell. Physiol.* 227:2217–2229.
377. Cregg, R., B. Laguda, R. Werdehausen, J.J. Cox, J.E. Linley, J.D. Ramirez, I. Bodi, M. Markiewicz, K.J. Howell, Y.C. Chen, K. Agnew, H. Houlden, M.P. Lunn, D.L.H. Bennett, J.N. Wood, and M. Kinali. 2013. Novel mutations mapping to the fourth sodium channel domain of nav1.7 result in variable clinical manifestations of primary erythromelalgia. *NeuroMolecular Med.* 15:265–278.
378. Huang, J., M. Estacion, P. Zhao, F.B. Dib-Hajj, B. Schulman, A. Abicht, I. Kurth, K. Brockmann, S.G. Waxman, and S.D. Dib-Hajj. 2019. A Novel Gain-of-Function Nav1.9 Mutation in a Child With Episodic Pain. *Front. Neurosci.* 13:1–11.
379. Abriel, H., C. Cabo, X.H.T. Wehrens, I. Rivolta, H.K. Motoike, M. Memmi, C. Napolitano, S.G. Priori, and R.S. Kass. 2001. Novel arrhythmogenic mechanism revealed by a long-QT syndrome mutation in the cardiac Na+ channel. *Circ. Res.* 88:740–745.
380. Zhang, J., and J. Yan. 2014. Regulation of BK channels by auxiliary γ subunits. *Front. Physiol.* 5:401.
381. Ponce, A., A. Castillo, L. Hinojosa, J. Martinez-Rendon, and M. Cereijido. 2018. The expression of endogenous voltage-gated potassium channels in HEK293 cells is affected by culture conditions. *Physiol. Rep.* 6:e13663.
382. Yu, S.P., and G.A. Kerchner. 1998. Endogenous voltage-gated potassium channels in human embryonic kidney (HEK293) cells. *J. Neurosci. Res.* 52:612–7.
383. Gamper, N., J.D. Stockand, and M.S. Shapiro. 2005. The use of Chinese hamster ovary (CHO) cells in the study of ion channels. *J. Pharmacol. Toxicol. Methods*. 51:177–185.
384. Mardinly, A.R., I.A. Oldenburg, N.C. Pégard, S. Sridharan, E.H. Lyall, K. Chesnov, S.G. Brohawn, L. Waller, and H. Adesnik. 2018. Precise multimodal optical control of neural ensemble activity. *Nat. Neurosci.* 21:881–893.
385. Manders, E.M.M., J. Stap, G.J. Brakenhoff, R. Van Driel, and J.A. Aten. 1992. Dynamics of three-dimensional replication patterns during the S-phase, analysed by double labelling of DNA and confocal microscopy. *J. Cell Sci.* 103:857–862.
386. Dunn, K.W., M.M. Kamocka, and J.H. McDonald. 2011. A practical guide to evaluating

colocalization in biological microscopy. *Am. J. Physiol. Cell Physiol.* 300:C723-742.

387. Cobb, M.M., D.C. Austin, J.T. Sack, and J.S. Trimmer. 2016. Cell cycle-dependent changes in localization and phosphorylation of the plasma membrane Kv2.1 K+ channel impact endoplasmic reticulum membrane contact sites in COS-1 cells. *J. Biol. Chem.* 291:5527.
388. Milescu, M., F. Bosmans, S. Lee, A.A. Alabi, J. Il Kim, and K.J. Swartz. 2009. Interactions between lipids and voltage sensor paddles detected with tarantula toxins. *Nat. Struct. Mol. Biol.* 16:1080–1085.
389. Green, W.N., and O.S. Andersen. 1991. Surface charges and ion channel function. *Annu. Rev. Physiol.* 53:341–359.
390. Ednie, A.R., and E.S. Bennett. 2012. Modulation of voltage-gated ion channels by sialylation. *Compr. Physiol.* 2:1269–1301.
391. Johnson, D., M.L. Montpetit, P.J. Stocker, and E.S. Bennett. 2004. The sialic acid component of the β1 subunit modulates voltage-gated sodium channel function. *J. Biol. Chem.* 279:44303–44310.
392. Elinder, F., and P. Århem. 2003. Metal ion effects on ion channel gating. *Q. Rev. Biophys.* 36:373–427.
393. Broomand, A., F. Österberg, T. Wardi, and F. Elinder. 2007. Electrostatic domino effect in the Shaker K channel turret. *Biophys. J.* 93:2307–2314.
394. Ikematsu, N., M.L. Dallas, F.A. Ross, R.W. Lewis, J.N. Rafferty, J.A. David, R. Suman, C. Peers, D.G. Hardie, and A.M. Evansc. 2011. Phosphorylation of the voltage-gated potassium channel Kv2.1 by AMP-activated protein kinase regulates membrane excitability. *Proc. Natl. Acad. Sci. U. S. A.* 108:18132–18137.
395. Bar, C., M. Kuchenbuch, G. Barcia, A. Schneider, M. Jennesson, G. Le Guyader, G. Lesca, C. Mignot, M. Montomoli, E. Parrini, H. Isnard, A. Rolland, B. Keren, A. Afenjar, N. Dorison, L.G. Sadleir, D. Breuillard, R. Levy, M. Rio, S. Dupont, S. Negrin, A. Danieli, E. Scalais, A. De Saint Martin, S. El Chehadeh, J. Chelly, A. Poisson, A.-S. Lebre, A. Nica, S. Odent, T. Sekhara, V. Brankovic, A. Goldenberg, P. Vrielynck, D. Lederer, H. Maurey, G. Terrone, C. Besmond, L. Hubert, P. Berquin, T. Billette de Villemeur, B. Isidor, J.L. Freeman, H.C. Mefford, C.T. Myers, K.B. Howell, A. Rodríguez-Sacristán Cascajo, P. Meyer, D. Genevieve, A. Guët, D. Doummar, J. Durigneux, M.F. van Dooren, M.C.Y. de Wit, M. Gerard, I. Marey, A. Munnich, R. Guerrini, I.E. Scheffer, E. Kabashi, and R. Nabbout. 2020. Developmental and epilepsy spectrum of KCNB1 encephalopathy with long-term outcome. *Epilepsia*. 61:2461–2473.
396. Baver, S.B., and K.M.S. O'Connell. 2012. The C-terminus of neuronal Kv2.1 channels is required for channel localization and targeting but not for NMDA-receptor-mediated regulation of channel function. *Neuroscience*. 217:56–66.
397. Aréchiga-Figueroa, I.A., M. Delgado-Ramírez, R. Morán-Zendejas, and A.A. Rodríguez-Menchaca. 2015. Modulation of Kv2.1 channels inactivation by curcumin. *Pharmacol. Reports*. 67:1273–1279.
398. Delgado-Ramírez, M., J.J. De Jesús-Pérez, I.A. Aréchiga-Figueroa, J. Arreola, S.K. Adney, C.A. Villalba-Galea, D.E. Logothetis, and A.A. Rodríguez-Menchaca. 2018. Regulation of Kv2.1 channel inactivation by phosphatidylinositol 4,5-bisphosphate. *Sci. Rep.* 8:1769.
399. Aréchiga-Figueroa, I.A., R. Morán-Zendejas, M. Delgado-Ramírez, and A.A. Rodríguez-Menchaca. 2017. Phytochemicals genistein and capsaicin modulate Kv2.1 channel gating. *Pharmacol. Reports*. 69:1145–1153.
400. Liu, R., G. Yang, M.-H. Zhou, Y. He, Y.-A. Mei, and Y. Ding. 2016. Flotillin-1 downregulates K(+) current by directly coupling with Kv2.1 subunit. *Protein Cell*. 7:455–60.
401. David, J.-P., J.I. Stas, N. Schmitt, and E. Bocksteins. 2015. Auxiliary KCNE subunits modulate both

homotetrameric Kv2.1 and heterotetrameric Kv2.1/Kv6.4 channels. *Sci. Rep.* 5:12813.

402. Li, X.-T., X.-Q. Li, X.-M. Hu, and X.-Y. Qiu. 2015. The inhibitory effects of Ca2+ channel blocker nifedipine on rat Kv2.1 potassium channels. *PLoS One*. 10:e0124602.
403. Liu, X., Y. Fu, H. Yang, T. Mavlyutov, J. Li, C.R. McCurdy, L.-W. Guo, and B.R. Pattnaik. 2017. Potential independent action of sigma receptor ligands through inhibition of the Kv2.1 channel. *Oncotarget*. 8:59345–59358.
404. Eichel, C.A., E.B. Ríos-Pérez, F. Liu, M.B. Jameson, D.K. Jones, J.J. Knickelbine, and G.A. Robertson. 2019. A microtranslatome coordinately regulates sodium and potassium currents in the human heart. *Elife*. 8.
405. Nagaya, N., and D.M. Papazian. 1997. Potassium channel alpha and beta subunits assemble in the endoplasmic reticulum. *J. Biol. Chem.* 272:3022–3027.
406. Gonzalez-Perez, V., X.-M. Xia, and C.J. Lingle. 2014. Functional regulation of BK potassium channels by γ1 auxiliary subunits. *Proc. Natl. Acad. Sci. U. S. A.* 111:4868–4873.
407. Gonzalez-Perez, V., M. Ben Johny, X.M. Xia, and C.J. Lingle. 2018. Regulatory γ1 subunits defy symmetry in functional modulation of BK channels. *Proc. Natl. Acad. Sci. U. S. A.* 115:9923–9928.
408. Wang, Y.W., J.P. Ding, X.M. Xia, and C.J. Lingle. 2002. Consequences of the stoichiometry of Slo1, α and auxiliary β subunits on functional properties of large-conductance Ca2+-activated K+ channels. *J. Neurosci.* 22:1550–1561.
409. Mandikian, D., E. Bocksteins, L.K. Parajuli, H.I. Bishop, O. Cerda, R. Shigemoto, and J.S. Trimmer. 2014. Cell type-specific spatial and functional coupling between mammalian brain Kv2.1 K+ channels and ryanodine receptors. *J. Comp. Neurol.* 522:3555–3574.
410. Newkirk, G.S., D. Guan, N. Dembrow, W.E. Armstrong, and R.C. Foehring. 2021. Kv2 . 1 Potassium Channels Regulate Repetitive Burst Firing in Extratelencephalic Neocortical Pyramidal Neurons. 1–22.
411. Bishop, H.I., D. Guan, E. Bocksteins, L.K. Parajuli, K.D. Murray, M.M. Cobb, H. Misonou, K. Zito, R.C. Foehring, and J.S. Trimmer. 2015. Distinct cell- and layer-specific expression patterns and independent regulation of Kv2 channel subtypes in cortical pyramidal neurons. *J. Neurosci.* 35:14922–14942.
412. Guan, D., W.E. Armstrong, and R.C. Foehring. 2013. Kv2 channels regulate firing rate in pyramidal neurons from rat sensorimotor cortex. *J. Physiol.* 591:4807–25.
413. Stewart, R., B.E. Cohen, and J.T. Sack. 2021. Fluorescent toxins as ion channel activity sensors. *Methods Enzymol.* 1–24.
414. Liu, X., S.N. Constantinescu, Y. Sun, J.S. Bogan, D. Hirsch, R.A. Weinberg, and H.F. Lodish. 2000. Generation of mammalian cells stably expressing multiple genes at predetermined levels. *Anal. Biochem.* 280:20–28.
415. Sack, J.T., and R.W. Aldrich. 2006. Binding of a gating modifier toxin induces intersubunit cooperativity early in the Shaker K channel's activation pathway. *J. Gen. Physiol.* 128:119–132.
416. Lopatin, A.N., E.N. Makhina, and C.G. Nichols. 1994. Potassium channel block by cytoplasmic polyamines as the mechanism of intrinsic rectification. *Nature*. 372:366–369.
417. Chowdhury, S., and B. Chanda. 2012. Estimating the voltage-dependent free energy change of ion channels using the median voltage for activation. *J. Gen. Physiol.* 139:3–17.
418. Schindelin, J., I. Arganda-Carreras, E. Frise, V. Kaynig, M. Longair, T. Pietzsch, S. Preibisch, C. Rueden, S. Saalfeld, B. Schmid, J.-Y. Tinevez, D.J. White, V. Hartenstein, K. Eliceiri, P. Tomancak, and A. Cardona. 2012. Fiji: An open-source platform for biological-image analysis. *Nat. Methods*. 9:676–682.

419. Sheets, P.L., J.O.J. Ii, S.G. Waxman, S.D. Dib-hajj, and R. Cummins. 2007. A Nav1.7 channel mutation associated with hereditary erythromelalgia contributes to neuronal hyperexcitability and displays reduced lidocaine sensitivity. *J Physiol*. 3:1019–1031.

420. Lopez-Rodriguez, A., and M. Holmgren. 2018. Deglycosylation of Shaker Kv channels affects voltage sensing and the open–closed transition. *J. Gen. Physiol.* 150:1025–1034.

421. Mohapatra, D.P., and J.S. Trimmer. 2006. The Kv2.1 C terminus can autonomously transfer Kv2.1-like phosphorylation-dependent localization, voltage-dependent gating, and muscarinic modulation to diverse Kv channels. *J. Neurosci.* 26:685–695.

422. R., H.I., P. Jimin, B. Minkyung, K. Aditya, A. Ivan, O. Sergey, Z. Jing, N.T. J., B. Sudeep, B.S. R., S.V. G., L. Xiao-Han, L. Kaixian, Z. Zhi, B.D. J., R. Upasana, K. Jochen, F.I. S., S. Barnabas, B. Dana, R. Josep, K. Caroline, G.E. C., B. Sue, K. Scott, M.E. A., F.J. Christopher, H.T. L., C. Qian, and B. David. 2021. Computed structures of core eukaryotic protein complexes. *Science (80-.).* 0:eabm4805.

423. J., S.A., Y. Chung-Yang, O.B. N., P.O. J., H.M. P., M. Aubin, K. Rajesh, S. Dandan, J.J. A., and A. Elias. 2021. Targeted disruption of Kv2.1-VAPA association provides neuroprotection against ischemic stroke in mice by declustering Kv2.1 channels. *Sci. Adv.* 6:eaaz8110.

424. Kobrinsky, E., L. Stevens, Y. Kazmi, D. Wray, and N.M. Soldatov. 2006. Molecular rearrangements of the Kv2.1 potassium channel termini associated with voltage gating. *J. Biol. Chem.* 281:19233–19240.

425. Kobrinsky, E., L. Stevens, Y. Kazmi, D. Wray, and N.M. Soldatov. 2006. Molecular rearrangements of the Kv2.1 potassium channel termini associated with voltage gating. *J. Biol. Chem.* 281:19233–19240.

426. Wang, C., B.C. Chung, H. Yan, S.-Y. Lee, and G.S. Pitt. 2012. Crystal structure of the ternary complex of a NaV C-terminal domain, a fibroblast growth factor homologous factor, and calmodulin. *Structure*. 20:1167–1176.

427. Kimm, T., Z.M. Khaliq, and B.P. Bean. 2015. Differential regulation of action potential shape and burst-frequency firing by BK and Kv2 channels in substantia nigra dopaminergic neurons. *J. Neurosci.* 35:16404–17.

428. Abbott, G.W. 2020. KCNQs: Ligand- and voltage-gated potassium channels. *Front. Physiol.* 11:583.

429. Staff, N.P., H.Y. Jung, T. Thiagarajan, M. Yao, and N. Spruston. 2000. Resting and active properties of pyramidal neurons in subiculum and CA1 of rat hippocampus. *J. Neurophysiol.* 84:2398–2408.

430. Karczewski, K.J., L.C. Francioli, G. Tiao, B.B. Cummings, J. Alföldi, Q. Wang, R.L. Collins, K.M. Laricchia, A. Ganna, D.P. Birnbaum, L.D. Gauthier, H. Brand, M. Solomonson, N.A. Watts, D. Rhodes, M. Singer-Berk, E.M. England, E.G. Seaby, J.A. Kosmicki, R.K. Walters, K. Tashman, Y. Farjoun, E. Banks, T. Poterba, A. Wang, C. Seed, N. Whiffin, J.X. Chong, K.E. Samocha, E. Pierce-Hoffman, Z. Zappala, A.H. O'Donnell-Luria, E.V. Minikel, B. Weisburd, M. Lek, J.S. Ware, C. Vittal, I.M. Armean, L. Bergelson, K. Cibulskis, K.M. Connolly, M. Covarrubias, S. Donnelly, S. Ferriera, S. Gabriel, J. Gentry, N. Gupta, T. Jeandet, D. Kaplan, C. Llanwarne, R. Munshi, S. Novod, N. Petrillo, D. Roazen, V. Ruano-Rubio, A. Saltzman, M. Schleicher, J. Soto, K. Tibbetts, C. Tolonen, G. Wade, M.E. Talkowski, C.A. Aguilar Salinas, T. Ahmad, C.M. Albert, D. Ardissino, G. Atzmon, J. Barnard, L. Beaugerie, E.J. Benjamin, M. Boehnke, L.L. Bonnycastle, E.P. Bottinger, D.W. Bowden, M.J. Bown, J.C. Chambers, J.C. Chan, D. Chasman, J. Cho, M.K. Chung, B. Cohen, A. Correa, D. Dabelea, M.J. Daly, D. Darbar, R. Duggirala, J. Dupuis, P.T. Ellinor, R. Elosua, J. Erdmann, T. Esko, M. Färkkilä, J. Florez, A. Franke, G. Getz, B. Glaser, S.J. Glatt, D. Goldstein, C. Gonzalez, L. Groop, C. Haiman, C. Hanis, M. Harms, M. Hiltunen, M.M. Holi, C.M. Hultman, M. Kallela, J. Kaprio, S. Kathiresan, B.J. Kim, Y.J. Kim, G. Kirov, J. Kooner, S. Koskinen, H.M.

Krumholz, S. Kugathasan, S.H. Kwak, M. Laakso, T. Lehtimäki, R.J.F. Loos, S.A. Lubitz, R.C.W. Ma, D.G. MacArthur, J. Marrugat, K.M. Mattila, S. McCarroll, M.I. McCarthy, D. McGovern, R. McPherson, J.B. Meigs, O. Melander, A. Metspalu, B.M. Neale, P.M. Nilsson, M.C. O'Donovan, D. Ongur, L. Orozco, M.J. Owen, C.N.A. Palmer, A. Palotie, K.S. Park, C. Pato, A.E. Pulver, N. Rahman, A.M. Remes, J.D. Rioux, S. Ripatti, D.M. Roden, D. Saleheen, V. Salomaa, N.J. Samani, J. Scharf, H. Schunkert, M.B. Shoemaker, P. Sklar, H. Soininen, H. Sokol, T. Spector, P.F. Sullivan, J. Suvisaari, E.S. Tai, Y.Y. Teo, T. Tiinamaija, M. Tsuang, D. Turner, T. Tusie-Luna, E. Vartiainen, H. Watkins, R.K. Weersma, M. Wessman, J.G. Wilson, R.J. Xavier, B.M. Neale, M.J. Daly, and D.G. MacArthur. 2020. The mutational constraint spectrum quantified from variation in 141,456 humans. *Nature*. 581:434–443.

431. Benndorf, K., R. Koopmann, C. Lorra, and O. Pongs. 1994. Gating and conductance properties of a human delayed rectifier K+ channel expressed in frog oocytes. *J. Physiol.* 477:1–14.
432. O'Connell, K.M.S., R. Loftus, and M.M. Tamkun. 2010. Localization-dependent activity of the Kv2.1 delayed-rectifier K+ channel. *Proc. Natl. Acad. Sci.* 107:12351–12356.
433. Hoegg-beiler, M.B., D. Heredia, V. Nunes, C. Vilches, M. Lo, M. Auberson, and K. Go. 2014. Disrupting MLC1 and GlialCAM and ClC-2 interactions in leukodystrophy entails glial chloride channel dysfunction. *Nat. Commun.* 5:1–16.
434. Muennich, E.A.L., and R.E.W. Fyffe. 2004. Focal aggregation of voltage-gated, Kv2.1 subunit-containing, potassium channels at synaptic sites in rat spinal motoneurones. *J. Physiol.* 554:673–685.
435. Yu, F.H., V. Yarov-Yarovoy, G. a Gutman, and W. a Catterall. 2005. Overview of molecular relationships in the voltage-gated ion channel superfamily. *Pharmacol. Rev.* 57:387–395.
436. Nerbonne, J.M. 2000. Molecular basis of functional voltage-gated K+ channel diversity in the mammalian myocardium. *J. Physiol.* 525 Pt 2:285–98.
437. Bell, A.G. 1880. On the production and reproduction of sound by light. *J. Soc. Telegr. Eng.* 9:404–426.
438. Yao, J., and L. V Wang. 2013. Photoacoustic Microscopy. *Laser Photon. Rev.* 7:758–778.
439. Wang, L. V., and S. Hu. 2012. Photoacoustic Tomography: In Vivo Imaging from Organelles to Organs. *Science (80-.).* 335:1458–1462.
440. Yao, J., and L. V Wang. 2014. Photoacoustic brain imaging: from microscopic to macroscopic scales. *Neurophotonics*. 1:011003.
441. Yao, J., L. Wang, J.-M. Yang, K.I. Maslov, T.T.W. Wong, L. Li, C.-H. Huang, J. Zou, and L. V Wang. 2015. High-speed label-free functional photoacoustic microscopy of mouse brain in action. *Nat. Methods*. 12:407–10.
442. Fatakdawala, H., S. Poti, F. Zhou, Y. Sun, J. Bec, J. Liu, D.R. Yankelevich, S.P. Tinling, R.F. Gandour-Edwards, D.G. Farwell, and L. Marcu. 2013. Multimodal in vivo imaging of oral cancer using fluorescence lifetime, photoacoustic and ultrasound techniques. *Biomed. Opt. Express*. 4:1724.
443. Tilley, D.C., K.S. Eum, S. Fletcher-Taylor, D.C. Austin, C. Dupre, L.A. Patron, R.L. Garcia, K. Lam, V. Yarov-Yarovoy, B.E. Cohen, J.T. Sack, C. Dupré, L.A. Patrón, R.L. Garcia, K. Lam, V. Yarov-Yarovoy, B.E. Cohen, and J.T. Sack. 2014. Chemoselective tarantula toxins report voltage activation of wild-type ion channels in live cells. *Proc Natl Acad Sci U S A*. 111:E4789–E4796.
444. Sun, Y., D.N. Stephens, J. Park, Y. Sun, L. Marcu, J.M. Cannata, and K.K. Shung. 2008. Development of a multi-modal tissue diagnostic system combining high frequency ultrasound and photoacoustic imaging with lifetime fluorescence spectroscopy. In: 2008 IEEE Ultrasonics Symposium. . pp. 570–573.

445. Phillips, L.R., M. Milescu, Y. Li-Smerin, J.A. Mindell, J. Il Kim, and K.J. Swartz. 2005. Voltage-sensor activation with a tarantula toxin as cargo. *Nature*. 436:857–60.
446. Swartz, K.J., and R. MacKinnon. 1997. Mapping the receptor site for hanatoxin, a gating modifier of voltage-dependent K+ channels. *Neuron*. 18:675–682.
447. Li-Smerin, Y., and K.J. Swartz. 2000. Localization and molecular determinants of the Hanatoxin receptors on the voltage-sensing domains of a K(+) channel. *J. Gen. Physiol.* 115:673–684.
448. Hoi, J.J., Y.L. Ju, H.K. Su, Y.J. Eu, Y.S. Song, M. Milescu, K.J. Swartz, and I.K. Jae. 2005. Solution structure and lipid membrane partitioning of VSTx1, an inhibitor of the KvAP potassium channel. *Biochemistry*. 44:6015–6023.
449. Milescu, M., J. Vobecky, S.H. Roh, S.H. Kim, H.J. Jung, J. Il Kim, and K.J. Swartz. 2007. Tarantula toxins interact with voltage sensors within lipid membranes. *J. Gen. Physiol.* 130:497–511.
450. Klemic, K.G., C. Shieh, G.E. Kirsch, and S.W. Jones. 1998. Inactivation of Kv2 . 1 Potassium Channels. *Biophys. J.* 74:1779–1789.
451. Mohapatra, D.P., D.F. Siino, and J.S. Trimmer. 2008. Interdomain Cytoplasmic Interactions Govern the Intracellular Trafficking, Gating, and Modulation of the Kv2.1 Channel. *J. Neurosci.* 28:4982–4994.
452. Madej, M.G., and C.M. Ziegler. 2018. Dawning of a new era in TRP channel structural biology by cryo-electron microscopy. *Pflügers Arch. - Eur. J. Physiol.* 470:213–225.
453. Barros, F., L.A. Pardo, P. Domínguez, L.M. Sierra, and P. de la Peña. 2019. New structures and gating of voltage-dependent potassium (Kv) channels and their relatives: a multi-domain and dynamic question. *Int. J. Mol. Sci.* 20:248.
454. Choveau, F.S., N. Rodriguez, F. Abderemane Ali, A.J. Labro, T. Rose, S. Dahimène, H. Boudin, C. Le Hénaff, D. Escande, D.J. Snyders, F. Charpentier, J. Mérot, I. Baró, and G. Loussouarn. 2011. KCNQ1 channels voltage dependence through a voltage-dependent binding of the S4-S5 linker to the pore domain. *J. Biol. Chem.* 286:707–716.
455. Choveau, F.S., F. Abderemane-Ali, F.C. Coyan, Z. Es-Salah-Lamoureux, I. Baró, and G. Loussouarn. 2012. Opposite effects of the S4-S5 linker and PIP(2) on voltage-gated channel function: KCNQ1/KCNE1 and other channels. *Front. Pharmacol.* 3:125.
456. Ju, M., L. Stevens, E. Leadbitter, and D. Wray. 2003. The roles of N- and C-terminal determinants in the activation of the Kv2.1 Potassium channel. *J. Biol. Chem.* 278:12769–12778.
457. Misonou, H. 2010. Homeostatic regulation of neuronal excitability by K+ channels in normal and diseased brains. *Neuroscientist*. 16:51–64.
458. Mohapatra, D.P., H. Misonou, S.J. Pan, J.E. Held, D.J. Surmeier, and J.S. Trimmer. 2009. Regulation of intrinsic excitability in hippocampal neurons by activity-dependent modulation of the Kv2.1 potassium channel. *Channels*. 3:46–56.
459. Costes, S. V., D. Daelemans, E.H. Cho, Z. Dobbin, G. Pavlakis, and S. Lockett. 2004. Automatic and quantitative measurement of protein-protein colocalization in live cells. *Biophys. J.* 86:3993–4003.
460. McDonald, J.H., and K.W. Dunn. 2013. Statistical tests for measures of colocalization in biological microscopy. *J. Microsc.* 252:295–302.
461. Gruber, A.D., R.C. Elble, H.L. Ji, K.D. Schreur, C.M. Fuller, and B.U. Pauli. 1998. Genomic cloning, molecular characterization, and functional analysis of human CLCA1, the first human member of the family of Ca2+-activated Cl- channel proteins. *Genomics*. 54:200–214.
462. Sala-Rabanal, M., Z. Yurtsever, C.G. Nichols, and T.J. Brett. 2015. Secreted CLCA1 modulates TMEM16A to activate Ca2+-dependent chloride currents in human cells. *Elife*. 4:e05875.
463. Sala-Rabanal, M., Z. Yurtsever, K.N. Berry, C.G. Nichols, and T.J. Brett. 2017. Modulation of

TMEM16A channel activity by the von Willebrand factor type A (VWA) domain of the calcium-activated chloride channel regulator 1 (CLCA1). *J. Biol. Chem.* 292:9164–9174.

464. Zhu, D.Z., C.F. Cheng, and B.U. Pauli. 1991. Mediation of lung metastasis of murine melanomas by a lung-specific endothelial cell adhesion molecule. *Proc. Natl. Acad. Sci. U. S. A.* 88:9568–9572.

465. Elble, R.C., V. Walia, H.-C.C. Cheng, C.J. Connon, L. Mundhenk, A.D. Gruber, and B.U. Pauli. 2006. The putative chloride channel hCLCA2 has a single C-terminal transmembrane segment. *J. Biol. Chem.* 281:29448–29454.

466. Loewen, M.E., and G.W. Forsyth. 2005. Structure and function of CLCA proteins. *Physiol. Rev.* 85:1061–1092.

467. Gibson, A., A.P. Lewis, K. Affleck, A.J. Aitken, E. Meldrum, and N. Thompson. 2005. hCLCA1 and mCLCA3 are secreted non-integral membrane proteins and therefore are not ion channels. *J. Biol. Chem.* 280:27205–27212.

468. Lange, P.F., L. Wartosch, T.J. Jentsch, and J.C. Fuhrmann. 2006. ClC-7 requires Ostm1 as a B-subunit to support bone resorption and lysosomal function. *Nat. Lett.* 440:7–10.

469. Leisle, L., C.F. Ludwig, F.A. Wagner, T.J. Jentsch, and T. Stauber. 2011. ClC-7 is a slowly voltage-gated 2Cl-/1H+ exhcanger and requires Ostm1 for transport activity. *EMBO J.* 30:2140–2152.

470. Kornak, U., D. Kasper, M.R. Bo, E. Kaiser, M. Schweizer, A. Schulz, W. Friedrich, and T.J. Jentsch. 2001. Loss of the ClC-7 chloride channel leads to osteopetrosis in mice and man. *Cell*. 104:205–215.

471. Zeng, X.-H., C. Yang, X.-M. Xia, M. Liu, and C.J. Lingle. 2015. SLO3 auxiliary subunit LRRC52 controls gating of sperm KSPER currents and is critical for normal fertility. *Proc. Natl. Acad. Sci.* 112:2599 LP – 2604.

472. Goder, V., and M. Spiess. 2001. Topogenesis of membrane proteins: determinants and dynamics. *FEBS Lett.* 504:87–93.

473. Lodish, H.F., A. Berk, S.L. Zipursky, P. Matsudaira, D. Baltimore, and J. Darnell. 2000. Molecular Cell Biology. 4th ed. New York: .

474. Lander, E.S., L.M. Linton, B. Birren, C. Nusbaum, M.C. Zody, J. Baldwin, K. Devon, K. Dewar, M. Doyle, W. FitzHugh, R. Funke, D. Gage, K. Harris, A. Heaford, J. Howland, L. Kann, J. Lehoczky, R. LeVine, P. McEwan, K. McKernan, J. Meldrim, J.P. Mesirov, C. Miranda, W. Morris, J. Naylor, C.C. Raymond, M. Rosetti, R. Santos, A. Sheridan, C. Sougnez, N. Stange-Thomann, N. Stojanovic, A. Subramanian, D. Wyman, J. Rogers, J. Sulston, R. Ainscough, S. Beck, D. Bentley, J. Burton, C. Clee, N. Carter, A. Coulson, R. Deadman, P. Deloukas, A. Dunham, I. Dunham, R. Durbin, L. French, D. Grafham, S. Gregory, T. Hubbard, S. Humphray, A. Hunt, M. Jones, C. Lloyd, A. McMurray, L. Matthews, S. Mercer, S. Milne, J.C. Mullikin, A. Mungall, R. Plumb, M. Ross, R. Shownkeen, S. Sims, R.H. Waterston, R.K. Wilson, L.W. Hillier, J.D. McPherson, M.A. Marra, E.R. Mardis, L.A. Fulton, A.T. Chinwalla, K.H. Pepin, W.R. Gish, S.L. Chissoe, M.C. Wendl, K.D. Delehaunty, T.L. Miner, A. Delehaunty, J.B. Kramer, L.L. Cook, R.S. Fulton, D.L. Johnson, P.J. Minx, S.W. Clifton, T. Hawkins, E. Branscomb, P. Predki, P. Richardson, S. Wenning, T. Slezak, N. Doggett, J.-F. Cheng, A. Olsen, S. Lucas, C. Elkin, E. Uberbacher, M. Frazier, R.A. Gibbs, D.M. Muzny, S.E. Scherer, J.B. Bouck, E.J. Sodergren, K.C. Worley, C.M. Rives, J.H. Gorrell, M.L. Metzker, S.L. Naylor, R.S. Kucherlapati, D.L. Nelson, G.M. Weinstock, Y. Sakaki, A. Fujiyama, M. Hattori, T. Yada, A. Toyoda, T. Itoh, C. Kawagoe, H. Watanabe, Y. Totoki, T. Taylor, J. Weissenbach, R. Heilig, W. Saurin, F. Artiguenave, P. Brottier, T. Bruls, E. Pelletier, C. Robert, P. Wincker, A. Rosenthal, M. Platzer, G. Nyakatura, S. Taudien, A. Rump, D.R. Smith, L. Doucette-Stamm, M. Rubenfield, K. Weinstock, H.M. Lee, J. Dubois, H. Yang, J. Yu, J. Wang, G. Huang, J. Gu, L. Hood, L. Rowen, A. Madan, S. Qin, R.W. Davis, N.A. Federspiel, A.P. Abola, M.J. Proctor, B.A. Roe, F. Chen, H. Pan, J. Ramser, H. Lehrach, R. Reinhardt, W.R. McCombie, M. de la Bastide,

N. Dedhia, H. Blöcker, K. Hornischer, G. Nordsiek, R. Agarwala, L. Aravind, J.A. Bailey, A. Bateman, S. Batzoglou, E. Birney, P. Bork, D.G. Brown, C.B. Burge, L. Cerutti, H.-C. Chen, D. Church, M. Clamp, R.R. Copley, T. Doerks, S.R. Eddy, E.E. Eichler, T.S. Furey, J. Galagan, J.G.R. Gilbert, C. Harmon, Y. Hayashizaki, D. Haussler, H. Hermjakob, K. Hokamp, W. Jang, L.S. Johnson, T.A. Jones, S. Kasif, A. Kaspryzk, S. Kennedy, W.J. Kent, P. Kitts, E. V Koonin, I. Korf, D. Kulp, D. Lancet, T.M. Lowe, A. McLysaght, T. Mikkelsen, J. V Moran, N. Mulder, V.J. Pollara, C.P. Ponting, G. Schuler, J. Schultz, G. Slater, A.F.A. Smit, E. Stupka, J. Szustakowki, D. Thierry-Mieg, J. Thierry-Mieg, L. Wagner, J. Wallis, R. Wheeler, A. Williams, Y.I. Wolf, K.H. Wolfe, S.-P. Yang, R.-F. Yeh, F. Collins, M.S. Guyer, J. Peterson, A. Felsenfeld, K.A. Wetterstrand, R.M. Myers, J. Schmutz, M. Dickson, J. Grimwood, D.R. Cox, M. V Olson, R. Kaul, C.C. Raymond, N. Shimizu, K. Kawasaki, S. Minoshima, G.A. Evans, M. Athanasiou, R. Schultz, A. Patrinos, M.J. Morgan, I.H.G.S. Consortium, C. for G.R. Whitehead Institute for Biomedical Research, T.S. Centre:, W.U.G.S. Center, U.S.D.O.E.J.G. Institute:, B.C. of M.H.G.S.B.G.I.G. Center:, R.G.S. Center:, G. and C. UMR-8030:, I. of M.B. Department of Genome Analysis, G.T.C.S. Center:, B.C. of M.H.G.S.B.G.I.G. Center:, T.I. for S.B. Multimegabase Sequencing Center, S.G.T.H.G. Center:, U. of O.A.C. for G. Technology:, M.P.I. for M. Genetics:, L.A.H.G.C. Cold Spring Harbor Laboratory, G.R.C. for Biotechnology:, also includes individuals listed under other headings): *Genome Analysis Group (listed in alphabetical order, U.S.N.I. of H. Scientific management: National Human Genome Research Institute, S.G.T.H.G. Center:, U. of W.G. Center:, K.U.S. of M. Department of Molecular Biology, U. of T.S.M.C. at Dallas:, U.S.D. of E. Office of Science, and T.W. Trust: 2001. Initial sequencing and analysis of the human genome. *Nature*. 409:860–921.

475. Zhang, Q.C., D. Petrey, L. Deng, L. Qiang, Y. Shi, C.A. Thu, and B. Bisikirska. 2012. Structure-based prediction of protein-protein interactions on a genome-wide scale. *Nature*. 490:1–7.

476. Bella, J., K.L. Hindle, P.A. Mcewan, and S.C. Lovell. 2008. The leucine-rich repeat structure. *Cell Mol Life Sci*. 65:2307–2333.

477. Schroeder, A., J. Vanderlinden, K. Vints, and N. V Gounko. 2018. A modular organization of LRR protein-mediated synaptic adhesion defines synapse identity. *Neuron*. 99:329–344.

478. Dahimene, S., K.M. Page, I. Kadurin, L. Ferron, D.Y. Ho, G.T. Powell, W.S. Pratt, S.W. Wilson, and A.C. Dolphin. 2018. The α(2)δ-like protein Cachd1 increases N-type calcium currents and cell surface expression and competes with α(2)δ-1. *Cell Rep.* 25:1610-1621.e5.

479. Cottrell, G.S., C.H. Soubrane, J.A. Hounshell, H. Lin, V. Owenson, M. Rigby, P.J. Cox, B.S. Barker, M. Ottolini, S. Ince, C.C. Bauer, E. Perez-Reyes, M.K. Patel, E.B. Stevens, and G.J. Stephens. 2018. CACHD1 is an α2δ-like protein that modulates Ca(V)3 voltage-gated calcium channel activity. *J. Neurosci.* 38:9186–9201.

480. Hoffman, D.A., J.C. Magee, C.M. Colbert, and D. Johnston. 1997. K+ channel regulation of signal propagation in dendrites of hippocampal pyramidal neurons. *Nature*. 387:869–875.

481. Chen, X., and D. Johnston. 2004. Properties of single voltage-dependent K+ channels in dendrites of CA1 pyramidal neurones of rat hippocampus. *J. Physiol.* 559:187–203.

482. Jerng, H.H., M. Shahidullah, and M. Covarrubias. 1999. Inactivation gating of Kv4 potassium channels: molecular interactions involving the inner vestibule of the pore. *J. Gen. Physiol.* 113:641–660.

483. Beck, E.J., M. Bowlby, W.F. An, K.J. Rhodes, and M. Covarrubias. 2002. Remodelling inactivation gating of Kv4 channels by KChIP1, a small-molecular-weight calcium-binding protein. *J. Physiol.* 538:691–706.

484. Holmqvist, M.H., J. Cao, R. Hernandez-Pineda, M.D. Jacobson, K.I. Carroll, M.A. Sung, M. Betty, P. Ge, K.J. Gilbride, M.E. Brown, M.E. Jurman, D. Lawson, I. Silos-Santiago, Y. Xie, M.

Covarrubias, K.J. Rhodes, P.S. Distefano, and W.F. An. 2002. Elimination of fast inactivation in Kv4 A-type potassium channels by an auxiliary subunit domain. *Proc. Natl. Acad. Sci. U. S. A.* 99:1035–1040.

485. Maffie, J., and B. Rudy. 2008. Weighing the evidence for a ternary protein complex mediating A-type K+ currents in neurons. *J. Physiol.* 586:5609–5623.
486. Amarillo, Y., J.A. De Santiago-Castillo, K. Dougherty, J. Maffie, E. Kwon, M. Covarrubias, and B. Rudy. 2008. Ternary Kv4.2 channels recapitulate voltage-dependent inactivation kinetics of A-type K+ channels in cerebellar granule neurons. *J. Physiol.* 586:2093–2106.
487. Rettig, J., S.H. Heinemann, F. Wunder, C. Lorra, D.N. Parcej, J.O. Dolly, and O. Pongs. 1994. Inactivation properties of voltage-gated K+ channels altered by presence of beta-subunit. *Nature*. 369:289–294.
488. Solaro, C.R., and C.J. Lingle. 1992. Trypsin-sensitive, rapid inactivation of a calcium-activated potassium channel. *Science*. 257:1694–1698.
489. Makita, N., P.B. Bennett, and A.L.G. Jr. 1996. Molecular determinants of B1 subunit-induced gating modulation in voltage-dependent Na+ channels. *J. Neurosci.* 16:7117–7127.
490. 2021. Chapter 7 - Cell adhesion and the extracellular matrix. In: Goodman SRBT-GMCB (Fourth E, editor. . Academic Press. pp. 203–247.
491. Malhotra, J.D., M.C. Koopmann, K.A. Kazen-Gillespie, N. Fettman, M. Hortsch, and L.L. Isom. 2002. Structural requirements for interaction of sodium channel beta 1 subunits with ankyrin. *J. Biol. Chem.* 277:26681–26688.
492. Davies, A., I. Kadurin, A. Alvarez-Laviada, L. Douglas, M. Nieto-Rostro, C.S. Bauer, W.S. Pratt, and A.C. Dolphin. 2010. The alpha2delta subunits of voltage-gated calcium channels form GPI-anchored proteins, a posttranslational modification essential for function. *Proc. Natl. Acad. Sci. U. S. A.* 107:1654–1659.
493. Kim, D.Y., B.W. Carey, H. Wang, L.A.M. Ingano, A.M. Binshtok, M.H. Wertz, W.H. Pettingell, P. He, V.M. Lee, C.J. Woolf, and D.M. Kovacs. 2007. BACE1 regulates voltage-gated sodium channels and neuronal activity. *Nat. Cell Biol.* 9.
494. Gutstein, D.E., G.E. Morley, H. Tamaddon, D. Vaidya, M.D. Schneider, J. Chen, K.R. Chien, H. Stuhlmann, and G.I. Fishman. 2001. Conduction slowing and sudden arrhythmic death in mice with cardiac-restricted inactivation of connexin43. *Circ. Res.* 88:333–339.
495. Shibayama, J., W. Paznekas, A. Seki, S. Taffet, E.W. Jabs, M. Delmar, and H. Musa. 2005. Functional characterization of connexin43 mutations found in patients with oculodentodigital dysplasia. *Circ. Res.* 96:e83-91.
496. Gorelik, J., Y. Gu, H.A. Spohr, A.I. Shevchuk, M.J. Lab, S.E. Harding, C.R.W. Edwards, M. Whitaker, G.W.J. Moss, D.C.H. Benton, D. Sánchez, A. Darszon, I. Vodyanoy, D. Klenerman, and Y.E. Korchev. 2002. Ion channels in small cells and subcellular structures can be studied with a smart patch-clamp system. *Biophys. J.* 83:3296–3303.
497. Zaydman, M.A., and J. Cui. 2014. PIP2 regulation of KCNQ channels: biophysical and molecular mechanisms for lipid modulation of voltage-dependent gating. *Front. Physiol.* 5:195.
498. Alexander, S., A. Mathie, J. Peters, E. Veale, J. Striessnig, K. Armstrong, E. Faccenda, S. Harding, A. Pawson, J. Sharman, C. Southan, and J. Davies. 2019. The consise guide to pharmacology 2019/20: ion channels. *Br J Pharmacol*. 176:S142-228.